



TECHNISCHE
UNIVERSITÄT
WIEN
Vienna University of Technology

Coupling a single trapped atom to a whispering-gallery-mode microresonator

DISSERTATION

zur Erlangung des akademischen Grades

Doktor der Naturwissenschaften

eingereicht von

Elisa Will

Matrikelnummer 01428270
Hörnesgasse 4/16, 1030 Wien

an der
Fakultät für Physik der Technischen Universität Wien

Betreuung: Prof. Dr. Arno Rauschenbeutel, HU Berlin

Diese Dissertation haben begutachtet:

(Prof. Dr. Arno
Rauschenbeutel)

(Prof. Dr. Pepijn Pinkse)

(Prof. Dr. Tracy Northup)

Wien, 04.02.2022

(Elisa Will)



TECHNISCHE
UNIVERSITÄT
WIEN
Vienna University of Technology

Coupling a single trapped atom to a whispering-gallery-mode microresonator

DISSERTATION

submitted in partial fulfillment of the requirements for the degree of

Doktor der Naturwissenschaften

by

Elisa Will

Registration Number 01428270

Hörnesgasse 4/16, 1030 Wien

to the Faculty of Physics
at the TU Wien

Advisor: Prof. Dr. Arno Rauschenbeutel, HU Berlin

The dissertation has been reviewed by:

(Prof. Dr. Arno
Rauschenbeutel)

(Prof. Dr. Pepijn Pinkse)

(Prof. Dr. Tracy Northup)

Wien, 04.02.2022

(Elisa Will)

Für meine Familie

*Roswitha, Josef, Sebastian,
Isabell & Maximilian*

&

Für Alice

Abstract

The interaction between single atoms and single photons can be significantly enhanced by strongly confining the photons inside a microresonator with high quality factor, and by coupling the atoms to the resonator mode. This approach lies at the heart of cavity quantum electrodynamics, and it is an essential ingredient for many applications in quantum information science and technology. Whispering-gallery-mode microresonators are particularly interesting in this regard, as they are compatible with integration on optical chips and offer chiral, i.e. propagation direction-dependent, light-matter interaction, which enables novel protocols for processing light on the quantum level. In order to achieve a stable and controlled interaction – a crucial prerequisite for deterministically operating quantum protocols – the atom has to be localized in the resonator mode. While atom trapping is an established technique in cavity quantum electrodynamics with optical Fabry-Pérot cavities, it has so far not been demonstrated with whispering-gallery-mode resonators.

In this thesis, I present the first realization of strong coupling between a *trapped* single atom and a whispering-gallery-mode microresonator. In order to trap single rubidium atoms close to such a resonator, we employ a red-detuned tightly focused laser beam, which is retroreflected from the resonator surface. This creates a standing-wave optical dipole trap along the beam axis, with the first potential minimum being located at a distance of about 200 nm from the resonator surface. We detect an atom in the trap via the observation of fluorescence photons or by the modification of the resonator field. To characterize the single trapped atoms, we measure their average lifetime and temperature in the trap. The trap light induces a position-dependent light shift, which detunes the atomic transition frequency from the resonator mode. In order to counteract this shift we employ a two-color light shift compensation scheme, in which the trapping beam is superimposed with a second laser beam. The parameters of this additional laser beam are chosen such that it reduces the excited state energy of the atom until the unperturbed transition frequency is recovered. We demonstrate that we reach the strong coupling regime of cavity quantum electrodynamics with a trapped atom by measuring a vacuum Rabi splitting in the excitation spectrum of the coupled system.

The results presented in this thesis are a crucial step toward harnessing the full potential of this class of resonators, thereby making strong chiral atom-light coupling available for fundamental research and applications in optical quantum technologies.

Kurzfassung

Die Wechselwirkung zwischen einzelnen Atomen und einzelnen Photonen kann wesentlich verstärkt werden, indem man die Photonen in einen Mikroresonator mit hohem Gütefaktor "einsperrt" und die Atome an die Resonatormode koppelt. Dieser Ansatz ist das grundlegende Konzept der Resonator-Quantenelektrodynamik und ist Voraussetzung für viele Anwendungen in der Quanteninformationsverarbeitung und Quantentechnologie. Flüstergaleriemoden-Mikroresonatoren sind in dieser Hinsicht besonders interessant, da sie mit optischer Chip-Technologie kompatibel sind und in ihnen eine chirale, d.h. propagationsrichtungs-abhängige, Licht-Materie-Wechselwirkung auftritt. Dies ermöglicht die Implementierung neuartiger Protokolle für die Verarbeitung von Lichtsignalen auf der Quantenebene. Voraussetzung für deterministische Quantenprotokolle ist eine stabile und kontrollierte Atom-Resonator-Wechselwirkung. Dazu muss das Atom in der Resonatormode räumlich fixiert werden. In der Resonator-Quantenelektrodynamik mit optischen Fabry-Pérot-Resonatoren ist das Fangen von einzelnen Atomen eine etablierte Methode. Im Fall von Flüstergaleriemoden-Resonatoren ist dies jedoch bisher nicht gelungen.

Die vorliegende Arbeit präsentiert die erste experimentelle Realisierung einer starken Kopplung zwischen einem einzelnen *gefangenen* Atom und einem Flüstergaleriemoden-Resonator. Um einzelne Rubidium-Atome nahe der Oberfläche eines solchen Resonators zu fangen, verwenden wir einen rot-verstimmten stark fokussierten Lichtstrahl, der an der Resonatoroberfläche reflektiert wird. Dadurch entsteht entlang der Strahlachse eine optische Stehwellen-Falle, deren erstes Potentialminimum in einem Abstand von etwa 200 nm zur Resonatoroberfläche liegt. Wir detektieren Atome in der Falle durch die Registrierung von Fluoreszenzphotonen und alternativ durch die Modifikation des Resonator-Lichtfelds. Zur Charakterisierung der einzelnen gefangenen Atome, messen wir deren mittlere Lebensdauer und Temperatur in der Falle. Das Fallenlicht induziert eine positionsabhängige Verschiebung der atomaren Übergangsfrequenz, die das Atom bezüglich der Resonatormode verstimmt. Um diese Verschiebung rückgängig zu machen, setzen wir im Experiment eine Zweifarben-Kompensationsmethode ein, bei der der Fallenstrahl mit einem zweiten Laserstrahl räumlich überlagert wird. Die Parameter des zweiten Laserstrahls sind so gewählt, dass er die Energie des angeregten Zustands so weit reduziert, dass der atomare Übergang wieder seine ursprüngliche Frequenz erhält. Wir zeigen schließlich, durch Messung eines Vakuum-Rabispittings im Anregungsspektrum des gekoppelten Systems, dass wir das Regime der starken Licht-Atom-Wechselwirkung mit einem gefangenen Atom erreichen.

Die im Rahmen dieser Arbeit erzielten Ergebnisse stellen einen wichtigen Schritt dar, um in Zukunft das volle Potential dieser Resonatorklasse nutzen zu können. Dies ist, insbesondere im Hinblick auf die Wichtigkeit der chiralen Atom-Licht-Kopplung, sowohl für Grundlagenforschung als auch die Entwicklung optischer Quantentechnologien relevant.

List of Publications

In the process of working on this thesis, the following articles have been published in peer-reviewed journals:

- E. Will, L. Masters, A. Rauschenbeutel, M. Scheucher, and J. Volz.
Coupling a single trapped atom to a whispering-gallery-mode microresonator.
Phys. Rev. Lett. 126, 233602 (2021).
- M. Scheucher, A. Hilico, E. Will, J. Volz, and A. Rauschenbeutel.
Quantum optical circulator controlled by a single chirally coupled atom.
Science 354, 1577-1580 (2016).

Contents

1	Introduction	1
2	Bottle resonator CQED experiment	5
2.1	Single-atom cavity quantum electrodynamics	6
2.2	The bottle microresonator	9
2.3	Basic theory of atom–light interaction in resonators	18
2.4	Experimental setup	24
2.5	Experimental cycle	33
2.6	Data acquisition and analysis	39
3	Retroreflected optical tweezer trap	43
3.1	Optical dipole potentials	44
3.2	Options for an optical dipole trap close to a WGM resonator	46
3.3	Design considerations for the optical dipole trap	51
3.4	Light shift of a multilevel atom in a light field with arbitrary polarization	51
3.5	Trap-induced light shift of the ^{85}Rb D_2 -transition	53
3.6	Modeling the trapping potential	57
3.7	Experimental implementation of the optical dipole trap	65
4	Trapping single atoms close to the bottle resonator	75
4.1	Experimental setup for atom trapping	76
4.2	Trap loading	77
4.3	Basic trapping sequence and data analysis	79
4.4	Investigation of trap loading and re-detection	83
4.5	Fluorescence detection and probing of a trapped atom	87
4.6	Characterization of the single trapped atoms	94
5	Compensation of the trap-induced light shift	105
5.1	Principle of light shift compensation	106
5.2	Calculation of the two-color light shifts	108
5.3	Residual mismatch of the intensity distributions and resulting position dependence of the two-color light shifts	111
5.4	Compensation laser setup and offset-lock	114

5.5	Experimental verification of the light shift compensation	119
5.6	Spectroscopy of the atom–resonator system	125
6	Summary and Outlook	131
	Appendices	135
A.1	<i>Supplementary Information:</i> Trapping single atoms close to the bottle resonator	137
A.2	Resonator heating effect	140
A.3	Position distribution of the trapped atoms	143
A.4	<i>Supplementary Information:</i> Compensation of the trap-induced light shift . . .	145
	List of Acronyms	149
	Bibliography	151

Introduction

Cavity quantum electrodynamics (CQED) is a sub-research field of atomic physics and quantum optics and has already a long history. Experimental CQED emerged in the 1980s when it was verified that the spontaneous emission rate of an atom is modified when placing it between mirrors (or in a cavity), as compared to its behavior in free space [1]. It was experimentally demonstrated from the microwave to the optical domain that the atomic decay rate can be both inhibited [2–7] and enhanced [5–8] in the presence of such boundary conditions.

This field of research was propelled forward by the ability to produce cavities with large quality factors Q , i.e. long photon lifetimes in the cavity. In a low- Q cavity, the photon emitted by an atom leaves the cavity rapidly, such that the emission is irreversible, just as in free space. However, with the advent of high- Q cavities a fundamentally new regime was entered, in which the emitted photon stays in the cavity long enough such that there is a large probability for reabsorption of the photon by the atom. In this regime, spontaneous emission becomes a *reversible* process, resulting in so-called Rabi oscillations [9].

The first experiments making use of the longer photon storage time were, e.g., the one-atom maser [10, 11] and the two-photon maser [12]. These experiments used a thermal beam of so-called Rydberg atoms traveling through a closed superconducting microwave cavity. With this CQED system, the interaction of single atoms with a single mode of the electromagnetic field in the cavity could be studied for the first time. Subsequent experiments were mostly performed with Fabry-Pérot (FP) cavities for microwaves, composed of two superconducting niobium mirrors [13]. These Rydberg-atom microwave CQED systems are very successful, and they demonstrated, e.g., the quantization of the electromagnetic field by observing quantum Rabi oscillations [14] or exploring the quantum-to-classical boundary by generating a Schrödinger cat state [15]. Apart from such fundamental studies of quantum physics, this system also provided a platform for the development of new quantum technologies in the realm of quantum information processing. Examples are the demonstration of a quantum phase gate [16] and the non-destructive detection of a single photon [17]. This and further work led to the award of the Nobel Prize in physics to Serge Haroche (and David J. Wineland) in 2012.

In parallel, experiments have been performed with optical FP cavities designed to study the interaction with atoms via *optical* transitions. Here, the first experiments likewise used thermal atomic beams. The first demonstration of strong atom–light coupling in these cavities was achieved by the observation of a vacuum Rabi splitting in the excitation spectrum of the coupled system with an average atom number of only 1 [18].

Based on the advances in laser cooling and trapping [19] a striving for longer atom–light interaction times in optical cavities started, as it would facilitate studies of the coherent dynamics of a coupled atom–cavity system as well as manipulations of the system, particularly aiming at applications in quantum information science. The first techniques to provide slower atoms for CQED experiments were to release cold atoms from a magneto-optical trap (MOT) [20,21] and to use an atomic fountain with the cavity at the turning point of the atoms, yielding interaction times of $\sim 100 \mu\text{s}$ [22]. A significant increase of the atom–light interaction time by $10^2 - 10^3$ as well as a more stable coupling strength were then achieved by optically trapping single atoms in the cavity mode [23]. An even higher level of control over the atomic motion was reached by employing techniques for fast and efficient cooling of the trapped atom [24–26]. The first experiment to demonstrate cooling for single trapped atoms strongly coupled to a cavity reported a trapping time of ~ 1 s, even under continuous observation of the atom [27]. Such long trap lifetimes allowed CQED experiments to be performed with one-and-the-same atom [28], e.g., the deterministic generation of single photons [29] and the observation of a vacuum Rabi splitting for just one atom [30].

Within the recent years, such CQED systems have provided the basis for cutting-edge research, in particular aimed toward the realization of quantum networks [31]. Outstanding achievements with respect to distribution and processing of quantum information include, e.g., the demonstration of an elementary quantum network [32], a photon–photon quantum gate [33] and, most recently, a nonlocal quantum gate between distant quantum network modules [34].

In the above-mentioned experiments and demonstrations, both in the microwave and the optical domain, FP cavities have been the workhorse. The fabrication and further improvement of ultrahigh reflectance mirrors, in particular for the optical FP cavities [35], is however an involved and costly process. Furthermore, large-scale quantum networks require to interconnect many ”quantum nodes”, e.g., in form of coupled atom–cavity systems, via ”quantum channels”, which could, e.g., be optical waveguides. Therefore, there have been efforts to develop alternative resonator structures that can be well integrated into such a network architecture [36,37]. By now, different waveguide-integrated resonator types have been successfully employed in single-atom CQED, such as optical fiber-based Fabry-Pérot cavities [38–41], photonic crystal cavities [42,43], optical nanofiber-based cavities [44,45] and whispering-gallery-mode microresonators [36,46,47]. The key element of the work presented in this thesis is a special type of whispering-gallery-mode microresonator. Therefore, in the following, we will only focus on this class of resonators.

The principle of light confinement in whispering-gallery-mode (WGM) resonators is conceptually different from that in FP cavities. These resonators are dielectric, monolithic structures, where the light circulates inside the resonator material by the principle of total internal reflection. Due to the latter, WGM resonators also exhibit an evanescent field outside the sur-

face that can couple to atoms or other quantum emitters. Atom–light interaction mediated by a WGM microresonator was first demonstrated at the end of the 1990s using atoms in a dilute vapor [48]. Strong coupling between one atom and a WGM resonator was observed in 2006 using free-falling atoms from a MOT above the resonator [36]. These resonators attracted a lot of interest, as they offer high quality factors in conjunction with a small mode volume. The latter leads to a strong electric field per photon inside the resonator and, therefore, contributes to the enhancement of the atom–light interaction strength. Furthermore, when WGM resonators are interfaced with tapered optical fibers, close-to-perfect in- and out-coupling efficiencies can be achieved based on the principle of frustrated total internal reflection. Thus, these resonators are ideal for routing and processing photons with low loss, making them particularly interesting for applications in quantum information science in fiber-integrated networks. Most interestingly, it was discovered in 2013 [46] that WGM resonators provide spin–momentum locking of light [49, 50]. This means, that the polarization of the light in the resonator depends on its propagation direction and, therefore, offers chiral light–matter interaction [46, 51]. This special form of light–matter interaction enables novel protocols and functionalities for processing light on the quantum level. Achievements in this direction include the experimental demonstration of photon routing [47, 52], ultra-strong photon–photon interactions [53], non-reciprocal integrated optical devices [54, 55] and photon–atom state transfer [56].

Besides the above-mentioned beneficial features, WGM resonators have, however, the major drawback that trapping a single atom in the resonator mode is technically very challenging. As these resonators are solid structures, the resonator mode is only accessible from the outside via its evanescent field, which decays exponentially with the distance from the resonator surface on a length scale of ~ 100 nm. On this length scale, surface forces, such as the van der Waals and the Casimir-Polder force, act on a coupled atom. Moreover, the optical access for trapping beams is very limited. For these reasons, so far, all the experiments using WGM resonators were still conducted with free-falling atoms, just like the early experiments with FP cavities. This brings along the shortcomings of a limited interaction time, only a probabilistic operation and a fluctuating atom–light coupling strength. Obviously, this limits the performance and applicability of operations with these resonators as the ones mentioned above and hampers future developments. Gaining the ability to trap single atoms inside the whispering-gallery mode is the essential prerequisite for overcoming the current limitations and, therefore, has been on the agenda in the field of single-atom CQED for over 20 years.

This work presents the first observation of strong coupling of a *trapped* single atom to a WGM microresonator. Specifically, we optically trap single ^{85}Rb atoms inside the WGM of a so-called bottle microresonator [57] using a red-detuned tightly focused laser beam, which is retroreflected from the resonator surface [42]. This creates a one-dimensional optical lattice along the beam axis, with the first potential minimum being located at a distance of about 200 nm from the resonator surface. The trap light induces a position-dependent light shift on both the ground state and the excited state of the atom. In general, the two states shift into opposite directions, thereby detuning the atomic transition frequency from the resonator mode. One way to circumvent this problem is to operate the trap at a so-called magic wavelength, in which case the ground and excited states are shifted in the same direction. However, for rubidium no suited

magic wavelength exists in the red-detuned regime. Therefore, we counteract the trap-induced light shift by means of a two-color magic wavelength scheme [58]. In that, the trapping beam is superposed with a second laser beam, the so-called compensation laser. By suitably choosing the parameters of the compensation laser, the atomic transition is shifted back into resonance with the resonator mode. This allows us to observe a vacuum Rabi splitting in the excitation spectrum of the coupled atom–resonator system.

The thesis is organized as follows: In chapter 2, I will introduce the characteristics of the bottle microresonator as well as the theoretical basics of single-atom CQED with whispering-gallery-mode resonators. Furthermore, I will thoroughly describe our CQED setup that is the basis for all measurements with trapped atoms presented in the course of this thesis.

The theoretical description of the employed optical dipole trap and its experimental implementation into the existing setup are subject to chapter 3. We calculate the trap-induced light shift of the ground and excited state of the ^{85}Rb atom, which also yields the modification of the atomic transition frequency. Based on the light shift calculation we can model the trapping potential for our experimental parameters. In the experimental part, the trap optics and the techniques used to position the trapping beam on the resonator surface are described.

In chapter 4, I present first characterization and optimization measurements with single atoms trapped close to the resonator surface. We investigate the detection of trapped atoms via the observation of fluorescence photons that couple into the resonator mode. Furthermore, we measure the average lifetime and temperature of the trapped single atoms and discuss different mechanisms that potentially lead to heating of an atom in the trap.

Chapter 5 is dedicated to the two-color light shift compensation scheme. In the measurements presented up to this point, the trapped atoms were not resonant to the resonator mode due to the trap-induced light shift. Here, first, the effect of the compensation laser beam on the energy levels of an atom in the dipole trap is calculated. The optical setup and the frequency stabilization of the compensation laser are described. With this infrastructure at hand, we experimentally verify the working principle of the light shift compensation scheme. This, finally, allows us to observe strong coupling between the trapped single atoms and the resonator, which is revealed by the measurement of a vacuum Rabi splitting in the excitation spectrum of the coupled atom–resonator system.

Bottle resonator CQED experiment

This chapter is dedicated to introducing our cavity quantum electrodynamics (CQED) experiment, which has been upgraded in the framework of this thesis by adding to it an optical dipole trap for single rubidium atoms. The core functions of the experiment have been retained. Thus, the present chapter will provide the basis for the following chapters, which will present the implementation of the dipole trap and the way to strong coupling between a trapped atom and a specific type of whispering-gallery-mode (WGM) microresonator, a so-called bottle resonator.

The experiment has been designed and set up about a decade ago with the idea of generating strong atom–photon interaction in a fiber-integrated fashion [59, 60]. Whispering-gallery-mode resonators are ideal for this purpose, as – on the one hand – they have the ability to strongly enhance the interaction between single atoms and single photons and – on the other hand – they can be very efficiently coupled to optical fibers. As such, this system has a great potential for fundamental investigations and applications in the field of quantum information science.

The main driving force in this field is the vision of scalable quantum networks [37], which includes applications in quantum computing [61], quantum communication [62] and quantum metrology [63]. Quantum networks are envisioned to consist of spatially separated nodes, which are interconnected by quantum communication channels. The nodes are supposed to store and process quantum information in form of stationary matter quantum bits (qubits), e.g. provided by single atoms in a cavity [32, 64]. On the other hand, photonic channels are the most promising candidate to efficiently distribute the quantum information over long distances between the network nodes, and they are compatible with existing telecommunication fiber technology [32].

Many applications in the above context also require the photons to interact with each other, e.g. to prepare and probe entanglement or to perform quantum logic operations. Photons do not directly interact with each other in free space. However, effective photon–photon interactions can be mediated – again – by coupling the photons to quantum emitters, such as neutral atoms. Such an effective photon–photon interaction has been achieved in our setup in form of the demonstration of a nonlinear π phase shift for coincident photons [53, 65].

In the course of the first observations of atom–light interaction with our setup, my predecessors found that the light confined in WGM resonators has peculiar polarization proper-

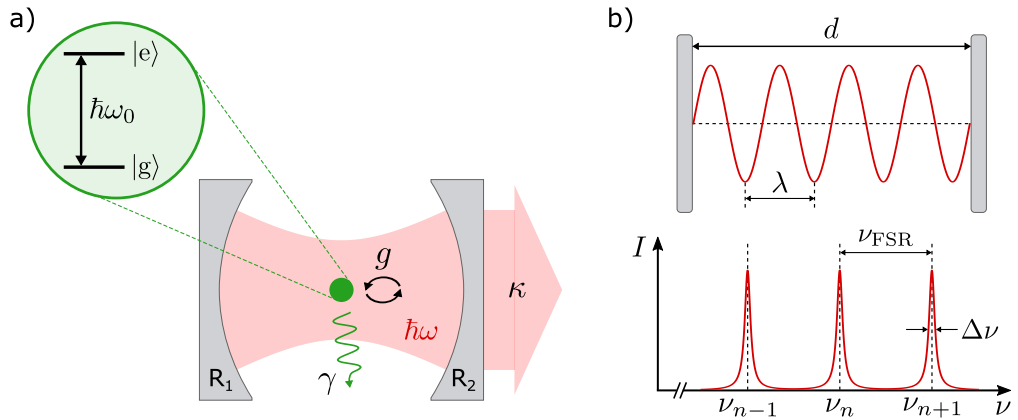


Figure 2.1: a) Typical CQED setting: A single neutral atom is located in the optical mode of a Fabry-Pérot (FP) cavity with angular frequency ω . The important rates that characterize the system are the atom-light coupling rate g , the atomic decay rate γ and the total cavity decay rate κ . The atom is assumed to exhibit only two energy levels, a ground state $|g\rangle$ and an excited state $|e\rangle$. The energy difference between the two levels is given by $\hbar\omega_0$. b) Illustration of the resonance frequencies supported by a FP cavity, see details in the text. Figures in panel (b) adapted from Ref. [66].

ties [46, 60], which were not considered in the description of WGMs until that point. In particular, they give rise to chiral, i.e. propagation direction-dependent light-matter interaction. The latter has direct implications for controlling the propagation of light in optical fibers by means of a quantum system. We were able to exploit this effect for the realization of non-reciprocal devices, such as an optical isolator [54] and a quantum optical circulator [55, 65].

In this chapter, I will describe the characteristics of whispering-gallery-mode resonators in general and the bottle microresonator in particular. I will outline the theoretical basics of CQED, including a qualitative description of chiral atom-light interaction in WGM resonators. Subsequently, I will describe in detail our experimental setup and the basic measurement techniques.

2.1 Single-atom cavity quantum electrodynamics

Single-atom cavity quantum electrodynamics terms the field of research that investigates the interaction between a single atom and single photons in a cavity. The typical textbook setting in this respect is illustrated in Fig. 2.1 a). A neutral atom (green dot) is located between two mirrors that form an optical resonator, in this case a so-called Fabry-Pérot (FP) cavity. Light can bounce back and forth between the cavity mirrors and is, therefore, both spatially and temporally confined and can interact with the atom.

In the following, we will first introduce some general properties of optical resonators, mostly following Refs. [9, 66]. Afterwards we will introduce the characteristic parameters that define atom-light interaction in optical resonators. A quantum mechanical treatment of atom-light interaction in resonators will be given in Sec. 2.3.

2.1.1 Optical resonators

In an optical resonator, light can be stored at certain discrete frequencies, which are called resonance frequencies. In case of a FP cavity, the resonance frequencies are determined by the distance, d , between the mirrors that form the cavity, as illustrated in Fig. 2.1 b). Since the electric field has to vanish at the mirror surfaces, the cavity supports such light modes, for which an integer multiple of half the optical wavelength, λ , exactly corresponds to the mirror distance: $d = n \lambda/2$ with $n \in \{1, 2, \dots\}$. In this case, the light bouncing back and forth in the cavity is in phase during each round trip. Using the relation between the wavelength and frequency of the light, $c = \lambda \nu$, the resonance frequencies can be expressed as

$$\nu_n = n \frac{c}{2d}, \quad (2.1)$$

where c is the speed of light. From this expression is apparent that the resonance frequencies can be tuned by changing the distance d between the mirrors. Furthermore, the resonance frequencies are equally spaced with a mode spacing of

$$\nu_{\text{FSR}} = \frac{c}{2d}, \quad (2.2)$$

which is called the *free spectral range* (FSR), see Fig. 2.1 b). The situation described above is an ideal one, where the cavity mirrors perfectly reflect the light (reflectivities $R_1 = R_2 = 1$) and, thus, the light is stored forever in the cavity. In practice, however, the reflectivities slightly differ from 1, and often at least one mirror is deliberately partially transmitting [66] such that the system properties can be studied by means of the outcoupled light field. In this case, the number of round-trips the light can perform in the cavity before it is lost, is determined by the finesse [31]

$$\mathcal{F} = \frac{\pi(R_1 R_2)^{1/4}}{1 - \sqrt{R_1 R_2}}. \quad (2.3)$$

Additionally, intrinsic cavity losses due to, e.g., absorption and scattering, further reduce the finesse and shorten the lifetime of the light in the cavity. Both mentioned effects, thus, result in a spectral broadening of the resonance frequencies, as depicted in Fig. 2.1 b). The spectral width is given by

$$\Delta\nu = \frac{\nu_{\text{FSR}}}{\mathcal{F}} = \frac{1}{2\pi\tau_{\text{ph}}}, \quad (2.4)$$

where τ_{ph} is the photon lifetime in the cavity.

In order to describe other – more general – types of resonators, including WGM resonators, it is helpful to introduce the *quality factor*. It simply gives the photon lifetime τ_{ph} in the resonator in units of the optical period $T_{\text{opt}} = 2\pi/\omega$

$$Q = 2\pi \frac{\tau_{\text{ph}}}{T_{\text{opt}}} = \frac{\omega}{\Delta\omega}, \quad (2.5)$$

where we now assumed a specific resonator mode of angular frequency $\omega = 2\pi\nu$. Furthermore, the relation between the quality factor and the finesse is given by

$$Q = \frac{\nu}{\nu_{\text{FSR}}} \mathcal{F}. \quad (2.6)$$

One can conclude, that the quality factor and the finesse describe the temporal confinement of light in a resonator: the larger Q (or \mathcal{F}), the longer a photon lives inside the resonator and the narrower the resonances are in the frequency domain.

The second important property of a resonator is the spatial confinement of the light. It is typically described by the mode volume V , which we define as the spatial integral over the normalized intensity distribution [57]

$$V = \int n^2(\mathbf{r}) \frac{I(\mathbf{r})}{I_{\max}} d\mathbf{r}. \quad (2.7)$$

Here, $n(\mathbf{r})$ is the position-dependent refractive index and I_{\max} is the peak intensity of the resonator mode.

2.1.2 Strong coupling regime of CQED

In order to couple an atom to the light field confined in an optical resonator, one of the resonator modes has to coincide – or, in practice, be tuned into resonance – with the atomic transition frequency ω_0 . Under this condition, the atom and the resonator can interact, i.e. exchange photons in a resonant way [9]. When the interaction is strong enough, the atom can perform cycles of absorption and re-emission of a photon from and into the cavity mode, which are called Rabi oscillations. The rate at which this coherent energy exchange occurs is called the single-photon Rabi frequency or coupling strength, and it is given by [67]

$$g(\mathbf{r}) = \frac{d_{ge} \mathcal{E}_0}{\hbar} \Psi(\mathbf{r}) = \sqrt{\frac{d_{ge}^2 \omega}{2\hbar\epsilon_0 V}} \Psi(\mathbf{r}) = g_0 \Psi(\mathbf{r}), \quad (2.8)$$

where $\mathcal{E}_0 = \sqrt{\hbar\omega/\epsilon_0 V}$ is the field per photon with the permittivity of the vacuum ϵ_0 . Moreover, $d_{ge} = \langle g | \hat{d} | e \rangle$ denotes the dipole matrix element of the two-level atom, and it is a measure of the transition strength. The quantity $\Psi(\mathbf{r})$ is the resonator-mode function, which is normalized such that the resonator-mode volume is $V = \int |\Psi(\mathbf{r})|^2 d\mathbf{r}$. The smaller the mode volume V , the larger the field per photon. That means, when the light is strongly confined in the resonator, the intra-resonator intensity and with it the atom–photon interaction is enhanced. Furthermore, the coupling strength g also depends on the position \mathbf{r} of the atom in the resonator mode via the spatial dependence of the mode function $\Psi(\mathbf{r})$.

Now, whether Rabi oscillations can be observed in an experiment, does not only depend on the value of the coupling strength. This is because the interaction can be hampered by two mechanisms. First, when the atom absorbs a photon, it can emit the photon not only back into the resonator mode, but also into the continuum of free-space modes with the spontaneous decay rate [68]

$$\gamma = \frac{d_{ge}^2 \omega_0^3}{12\pi\epsilon_0 \hbar c^3} = \frac{1}{2\tau}, \quad (2.9)$$

see Fig. 2.1 a). Here, τ is the lifetime of the excited state $|e\rangle$ of the atom. Second, the photons in the resonator have a finite lifetime, τ_{ph} , as discussed in the previous section. Meaning, when the atom emits a photon into the resonator, it has a chance to be lost from there before it can

be reabsorbed by the atom. The resonator loss rate κ is identical to the half-width $\Delta\omega/2$ of the resonant mode, such that

$$\kappa = \frac{\omega}{2Q} \quad (2.10)$$

according to Eq. (2.5). In order to enter the so-called *strong coupling regime*, the coupling rate g must be larger than the loss rates of the system

$$2C = \frac{g^2}{\kappa\gamma} \gg 1, \quad (2.11)$$

where C is called the single-atom cooperativity. Inserting Eqs. (2.9) and (2.10) into Eq. (2.11) yields

$$\frac{g^2}{\kappa\gamma} \propto \frac{Q}{V}, \quad (2.12)$$

which shows that the cooperativity is effectively determined by the resonator properties. In particular, it is independent of the atomic transition strength. The steady improvement of the quality factor and the miniaturization of different kinds of optical resonators over the past decades, has made it possible to experimentally realize the simple model system described here in numerous experimental setups.

2.2 The bottle microresonator

The heart of our CQED experiment is a so-called bottle microresonator [57, 69, 70], which belongs to the class of whispering-gallery-mode (WGM) microresonators. In the following, we will first describe how light is confined inside WGM resonators and specifically in the bottle resonator. An important consequence of the confinement is the emergence of longitudinal polarization components, which makes WGM resonators fundamentally different from Fabry-Pérot and conventional ring-resonators. Afterwards, we briefly explain how light can be efficiently coupled into and out of the resonator using tapered optical fibers.

2.2.1 Whispering-gallery-mode microresonators

Whispering-gallery modes were first discovered in the nineteenth century in the acoustic domain, from where they received their peculiar name. Lord Rayleigh had observed in the gallery of St. Paul's cathedral – and later theoretically described – how sound waves travel along the inner curved surface of the gallery [72]. The optical equivalent of this phenomenon can be observed in optical microresonators, such as the ones depicted in Fig. 2.2 a) from left to right: microspheres [73, 74], microdisks [75] (not shown), microtoroids [76, 77] and bottle microresonators. The latter is a special type of WGM microresonator that owes its name to its prolate shape [78]. As will be seen, this property distinguishes the bottle resonator in certain aspects from other WGM resonators and offers a couple of advantages.

WGM microresonators are dielectric monolithic structures. In contrast to Fabry-Pérot cavities, where the light bounces back and forth between two highly reflective mirrors, here the light is guided inside the resonator material. In radial direction (r), the light is confined by total



Figure 2.2: a) Different types of WGM resonators, from left to right: a microsphere, a microtoroid and a bottle microresonators. Part of the figure taken from Ref. [71]. b) Radial confinement of light in WGM resonators in a ray path picture (cross section through the equatorial plane). Light is guided along the resonator circumference via total internal reflection, which is a consequence of the relation between the refractive indices $n_1 > n_2$ of the surrounding vacuum ($n_2 = 1$) and the resonator material ($n_1 > 1$).

internal reflection, as illustrated in Fig. 2.2 b) in a ray path picture. This effect occurs at the interface between a thicker (refractive index n_1) and a thinner (n_2) medium, when the light initially propagates in the thicker medium and hits the interface with an incidence angle larger than a critical angle $\Theta > \Theta_c = \arcsin n_2/n_1$ [66]. For grazing incidence, i.e. $\Theta \rightarrow \pi/2$, the distance between two reflections at the interface becomes infinitesimally small. In this case, one speaks of continuous total internal reflection [79] and an optical whispering-gallery wave is formed that is guided near the resonator surface.

WGM microresonators combine ultra-high quality factors $Q \approx 10^8 - 10^9$ and very small mode volumes V [80, 81], which according to Eq. (2.12) makes them very good platforms for atom–light interaction in the realm of CQED.

2.2.2 Fabrication of the bottle microresonator

A schematic of a bottle microresonator is depicted in Fig. 2.3. The resonator used in our experiment was fabricated from a standard optical glass fiber in a heat-and-pull process using a fiber pulling rig, which is described in detail in Ref. [82]. In the first step, the diameter of the fiber is reduced to the desired resonator diameter over a few millimeters-long fiber section [70]. This is done by linearly translating the fiber relative to the heat source – either a hydrogen-oxygen flame or a CO_2 laser with a focal spot size of 100-120 μm [60] – and simultaneously pulling the fiber. In the second step, this tapered fiber is locally heated at two spots with a mutual distance of about 150 μm by the focused CO_2 -laser beam, while at the same time being further stretched [70]. This creates two micro-tapers, in between which a bulge is formed – the bottle resonator.

In the case of our resonator, the entire pulling process was performed with the CO_2 -laser. The positions, the length and the diameter of the micro-tapers determine the curvature of the resonator, which can be characterized with the help of an optical microscope in the fiber-pulling rig [70]. The bottle resonator that was used for the experiments in this thesis is the same as in

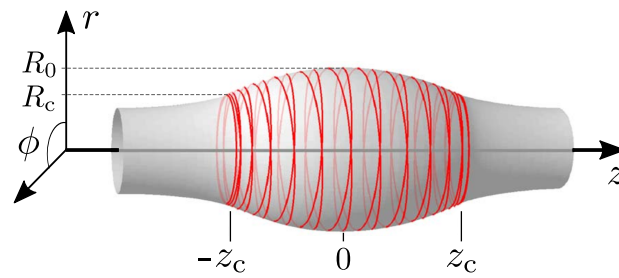


Figure 2.3: Axial confinement of light in the bottle microresonator in a ray path picture. Due to the bulgy shape of the resonator the light spirals around the resonator axis (z) between two turning points at $\pm z_c$, where the light intensity is enhanced. The resonator radius at these so-called caustics is denoted as $R_c = R(\pm z_c)$, and the central radius of the resonator is denoted as $R_0 = R(z = 0)$. Figure adapted from Ref. [57].

Refs. [59, 60, 65]. Since it was installed inside the vacuum chamber it was not replaced until the experiment had to be disassembled for the move to a new laboratory. The central radius of the resonator was measured to be $R_0 \approx 18.5 \mu\text{m}$ (cf. Fig. 2.3) and the curvature was determined to be $\Delta k = 0.014 \mu\text{m}^{-1}$ [60]. The quality factor $Q \approx 5 \times 10^7$ of the typically used resonator mode was approximately constant over the years, which we attribute to the two-chamber design of the setup (cf. Sec. 2.4.2).

2.2.3 Storage of light in the bottle microresonator

The principle of light confinement in the bottle resonator in radial direction is the same as for other WGM resonators. Due to the prolate shape of the bottle resonator, the light spirals around the symmetry axis (z) between two turning points, the so-called caustics, which is illustrated in Fig. 2.3 in a ray path picture. The light cannot leave along the z -axis due to an angular momentum barrier. This is similar to the confinement of charged particles in a magnetic bottle [57]. It causes the light to perform many loops in azimuthal direction (ϕ) until one full round trip – from one caustic to the other and back – is completed. This has implications on the spectral properties of the bottle resonator, as we will see later.

Bottle resonator modes

The ray path picture above provides an intuitive understanding of the confinement of light in the bottle resonator. However, to obtain the mode structure we have to solve the wave equation for the bottle resonator. In the following, I will only summarize the important steps of the derivation of the bottle modes and give the results. More detailed derivations can be found in [57, 60, 70].

Both the electric field \mathcal{E} and the magnetic field \mathcal{H} of the resonator eigenmodes have to fulfill the Helmholtz equation [66]

$$(\nabla^2 + k^2) \Psi = 0 \quad (2.13)$$

with $\Psi = \mathcal{E}, \mathcal{H}$. Furthermore, $k = |\mathbf{k}| = nk_0 = n2\pi/\lambda_0$ is the wave number of the mode with the vacuum wave number k_0 and the vacuum wavelength λ_0 , where n is the refractive index of the medium in which the light is propagating.

Due to the cylindrical symmetry of the bottle resonator, it is convenient to describe the problem in cylindrical coordinates (r, ϕ, z) , as defined in Fig. 2.3. As a consequence of the cylindrical symmetry, one can separate the azimuthal (ϕ) part of the wave equation, whose solutions are proportional to $\exp(im\phi)$, with the angular momentum quantum number m . The latter counts the number of wavelengths around the resonator circumference. In what follows, we assume that the bottle resonator can approximately be described by a parabolic axial profile

$$R(z) \approx R_0 \left(1 - \frac{(\Delta k z)^2}{2} \right), \quad (2.14)$$

where $R_0 = R(z = 0)$ is the central radius (cf. Fig. 2.3) and Δk is the curvature of the resonator. Furthermore, the curvature is assumed to be small, i.e. $dR/dz \ll 1$. Based on this adiabatic approximation [57], the radial component of the wave vector can be neglected, such that $k \approx \sqrt{k_\phi^2 + k_z^2}$. Moreover, one can make the assumption that the remaining r - and z -dependent part of the wave function is of the form $\Phi(r, R(z))Z(z)$ [57]. Using the ansatz for the full solution, $\Psi(r, \phi, z) = \Phi(r, R(z))Z(z) \exp(im\phi)$, the Helmholtz equation, Eq. (2.13), separates into a radial and an axial wave equation [57]

$$\left(\partial_r^2 + \frac{1}{r} \partial_r + k_\phi^2 - \frac{m^2}{r^2} \right) \Phi = 0, \quad (2.15)$$

$$(\partial_z^2 + k^2 - k_\phi^2) Z = 0, \quad (2.16)$$

which can be solved independently. The value of the axial component of the wave vector, k_z , vanishes at the resonator caustics with radius $R_c = R(\pm z_c)$, i.e. $k_\phi(\pm z_c) = k$. Thus, the azimuthal component of the wave vector is given by $k_\phi = k \cdot R_c/R(z) = 2\pi n R_c/\lambda_0 R(z)$ [70].

The radial wave equation (2.15) is of the form of a Bessel differential equation. Hence, the corresponding solutions are linear combinations of the Bessel functions of first and second kind J_m and Y_m , respectively. From the asymptotic behavior of the Bessel functions and the restriction to modes localized near the resonator surface, one can infer that the radial wave functions will be of the form [60]

$$\Phi_l(r, z) = \begin{cases} A_l \cdot J_m \left(\frac{2\pi n R_c}{\lambda_0 R(z)} \cdot r \right), & \text{for } r \leq R(z) \\ B_l \cdot Y_m \left(\frac{2\pi R_c}{\lambda_0 R(z)} \cdot r \right), & \text{for } r > R(z), \end{cases} \quad (2.17)$$

where the index l indicates the respective vector component and it is assumed that the resonator is surrounded by vacuum [60].

The bottle resonator supports WGMs with two types of polarization. For transverse-electric (TE) modes, the electric field points along the resonator axis and, thus, the electromagnetic field is solely described by the components $\mathcal{E}_z, \mathcal{H}_r$ and \mathcal{H}_ϕ . On the other hand, for transverse-magnetic (TM) modes only the components $\mathcal{H}_z, \mathcal{E}_r$ and \mathcal{E}_ϕ are non-vanishing. One can derive

resonance conditions from Eq. (2.17) for both types of polarizations [60], when the respective boundary conditions of the field components at the resonator surface ($r = R(z)$) are respected. Using these resonance conditions we can find resonant solutions of the radial wave equation for a bottle resonator with central radius $R_0 \approx 18.5 \mu\text{m}$, as used in our experiment. In doing so, one can either choose a fixed resonance wavelength λ_0 and derive radial modes of different orders with corresponding caustic radii R_c , or vice versa. We choose a fixed wavelength $\lambda_0 = 780 \text{ nm}$, as it approximately matches the transition wavelength of the D_2 line of the ^{85}Rb atom (cf. Fig. 2.10 b)). Furthermore, we set the azimuthal quantum number to $m = 206$, such that the caustic radius R_c of the fundamental radial mode roughly coincides with the central resonator radius R_0 [60].

In Fig. 2.4 a), we plot the squared radial wave functions $|\mathcal{E}_{\mathcal{P}}(r)|^2$ for the four lowest-order radial modes with quantum numbers $p = \{0, 1, 2, 3\}$, for both ($\mathcal{P}=\text{TM}$)-polarization (light blue) and ($\mathcal{P}=\text{TE}$)-polarization (dark blue). As can be seen, the radial quantum number, p , counts the nodes of the intensity distribution along the radial direction. The TM-polarized modes are discontinuous at the resonator surface originating from the boundary conditions of electric fields perpendicular to an interface. Outside the resonator, the intensity decays approximately exponentially in form of an evanescent field, which allows one to access the resonator mode from the outside. This plays the key role for coupling light into and out of the resonator as well as for coupling single atoms to the resonator mode.

Resulting from the assumption of the parabolic resonator profile, Eq. (2.14), the axial wave equation (2.16) turns out to be identical to the differential equation of the harmonic oscillator. Its solution is given by

$$Z_{m,q}(z) = C_{mq} \cdot H_q \left(\sqrt{\frac{\Delta E_m}{2}} \cdot z \right) \exp \left(-\frac{\Delta E_m}{4} z^2 \right), \quad (2.18)$$

where $C_{mq} = \sqrt[4]{\Delta E_m / (\pi 2^{2q+1} (q!)^2)}$ and H_q is a Hermite polynomial. This means, that the parabolic shape of the resonator creates a harmonic potential for the light, which thus forms eigenmodes according to Eq. (2.18) with discrete energy eigenvalues. These are given by $E_{mq} = (q + 1/2)\Delta E_m$, where $\Delta E_m = 2m\Delta k / (c_r R_0)$ and q is the axial quantum number. One can also derive an expression for the allowed eigenvalues of the wave number [60]

$$k_{m,q} = \sqrt{\frac{m^2}{(c_r R_0)^2} + \left(q + \frac{1}{2} \right) \frac{2m\Delta k}{c_r R_0}}. \quad (2.19)$$

Here, c_r is a correction factor, accounting for the fact that the bottle modes do not have a well-defined radius, but exhibit a radial intensity distribution [60, 70].

The squared axial wave functions $|Z_{m,q}(z)|^2$ for the four lowest-order axial modes with quantum numbers $q = \{0, 1, 2, 3\}$ are plotted in Fig. 2.4 b), where q gives the number of intensity nodes along z . For each mode, the outer two maxima exhibit the largest intensity, which are called the caustics. The axial wave function is responsible for the characteristic ring structure of the bottles modes, when seen in three dimensions.

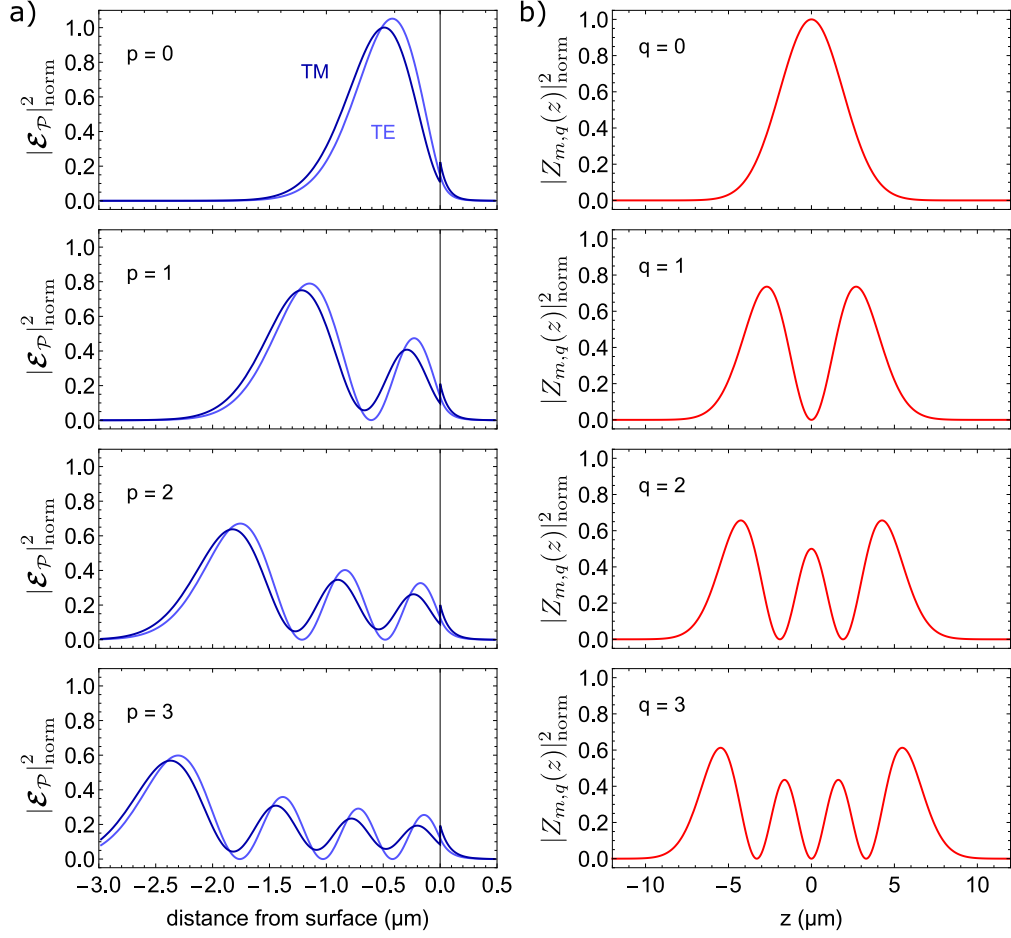


Figure 2.4: Spatial distribution of bottle resonator modes in a) radial (r) and b) axial (z) direction. a) The normalized radial distribution $|\mathcal{E}_{\mathcal{P}}(r)|^2_{\text{norm}} = |\mathcal{E}_{\mathcal{P}}(r)|^2 / \int_0^\infty n(r)^2 |\mathcal{E}_{\mathcal{P}}(r)|^2 r dr \max(|\mathcal{E}_{\text{TM}}(r)|^2_{p=0})$ is plotted for the four lowest-order radial modes, both for ($\mathcal{P} = \text{TE}$)-polarization (light blue) and ($\mathcal{P} = \text{TM}$)-polarization (dark blue), where $|\mathcal{E}_{\text{TE}}(r)|^2 = |\mathcal{E}_z(r)|^2$ and $|\mathcal{E}_{\text{TM}}(r)|^2 = |\mathcal{E}_r(r)|^2 + |\mathcal{E}_\phi(r)|^2$. The modes shown have radial quantum numbers $p = \{0, 1, 2, 3\}$ with corresponding caustic radii $R_c^{\text{TE}} = \{18.42, 19.15, 19.76, 20.30\} \mu\text{m}$ and $R_c^{\text{TM}} = \{18.48, 19.21, 19.82, 20.36\} \mu\text{m}$. b) The normalized axial distribution $|Z_{m,q}(z)|^2_{\text{norm}} = |Z_{m,q}(z)|^2 / \max(|Z_{m,q=0}(z)|^2)$ is plotted for the four lowest-order axial modes with quantum numbers $q = \{0, 1, 2, 3\}$ and corresponding caustic radii $R_c = \{18.48, 18.46, 18.44, 18.42\} \mu\text{m}$. All modes in panels (a) and (b) are plotted for an azimuthal quantum number $m = 206$ and a resonance wavelength of $\lambda_0 \approx 780 \text{ nm}$, for a resonator with central radius $R_0 = 18.5 \mu\text{m}$, curvature $\Delta k = 0.014 \mu\text{m}^{-1}$ and refractive index $n = 1.454$.

Mode volume

From the intensity distribution of the bottle resonator mode we can determine the corresponding mode volume V by integrating over the axial and the radial coordinates [60]

$$V_{m,q} \approx 2\pi \cdot \int_{-\infty}^{\infty} \left(\frac{Z_{m,q}(z)}{\max(Z_{m,q}(z))} \right)^2 dz \cdot \int_0^{r_{\text{rad}}} n(r)^2 \left(\frac{|\mathcal{E}(r)|^2}{\max(|\mathcal{E}(r)|^2)} \right) r dr. \quad (2.20)$$

Here, the integration over the azimuthal coordinate has already been performed, leading to the factor of 2π . Depending on whether the mode volume is calculated for TE- or TM-polarized modes, the electric field intensity is given by $|\mathcal{E}_{\text{TE}}(r)|^2 = |\mathcal{E}_z(r)|^2$ or $|\mathcal{E}_{\text{TM}}(r)|^2 = |\mathcal{E}_r(r)|^2 + |\mathcal{E}_\phi(r)|^2$, respectively. In radial direction, the integration is performed up to the so-called radiation caustic r_{rad} [60]. The mode volumes of the axial modes shown in Fig. 2.4 range between $\sim 830 \mu\text{m}^3$ for $q = 0$ and $\sim 1350 \mu\text{m}^3$ for $q = 3$.

Spectral properties

By approximating the wave number in Eq. (2.19) for small resonator curvatures ($\Delta k R_0 \ll 1$) via a Taylor expansion to first order, we obtain for the axial and the azimuthal free spectral ranges (FSR) [60]

$$\Delta\nu_m = \frac{c}{2\pi n} \cdot (k_{m+1,q} - k_{m,q}) \approx \frac{c}{2\pi n} \frac{1}{c_r R_0}, \quad (2.21)$$

$$\Delta\nu_q = \frac{c}{2\pi n} \cdot (k_{m,q+1} - k_{m,q}) \approx \frac{c}{2\pi n} \Delta k. \quad (2.22)$$

The azimuthal FSR is determined by the central radius R_0 of the resonator, while the axial FSR is determined by the resonator curvature Δk . Thus, the axial FSR can be engineered to be much smaller than the azimuthal FSR [59]. For the bottle resonator used in this thesis with central radius $R_0 \approx 18.5 \mu\text{m}$, curvature $\Delta k = 0.014 \mu\text{m}^{-1}$ and refractive index of $n = 1.454$, the axial and the azimuthal FSR amount to $\Delta\nu_q \approx 0.46 \text{ THz}$ and $\Delta\nu_m = 1.83 \text{ THz}$, respectively. The small axial FSR has the advantage compared to other WGM resonators, that the resonance frequency of the bottle resonator can easily be tuned over a full axial FSR [57]. This feature is essential, when the resonator needs to be tuned to an arbitrary frequency, e.g., to match the frequency of an atomic transition in the context of atom–resonator coupling. Frequency tuning requires to change the optical path length, which in WGM resonators is typically done by varying the resonator temperature. The bottle resonator has the additional advantage that, due to the geometry, mechanical strain can be applied to the two ends of the fiber, thereby changing the resonator radius as well as the refractive index [70].

2.2.4 Polarization properties of WGMs

In the previous section, we have seen how light can propagate in a bottle microresonator. In this context, it is a valid question to ask, which influence such a strong confinement has on the properties of a light field. It turns out that, for strongly confined beams, the standard approximation of paraxial optics is not valid anymore, i.e. the light field can no longer be described as a fully

transverse-polarized wave [83]. We want to illustrate this first for a general setting, before we will qualitatively describe the consequences for WGMs.

We consider a monochromatic beam of frequency ω , propagating in $+z$ -direction

$$\mathbf{E}(\mathbf{r}) = \mathcal{E}(\mathbf{r})e^{i(kz - \omega t)} \quad (2.23)$$

with the complex vector amplitude $\mathcal{E}(\mathbf{r}) = (\mathcal{E}_x, \mathcal{E}_y, \mathcal{E}_z)$ and the wave number $k = |\mathbf{k}| = 2\pi/\lambda$. According to Gauss's law, in a charge- and current-free medium, the divergence of the electric field vanishes

$$\nabla \cdot \mathbf{E} = (\partial_x E_x + \partial_y E_y + \partial_z E_z) = 0. \quad (2.24)$$

Under the assumption that the complex vector amplitude varies only slowly along the propagation direction, it follows from Eq. (2.24) for the longitudinal field component

$$\mathcal{E}_z \approx -i \frac{1}{k} (\partial_x \mathcal{E}_x + \partial_y \mathcal{E}_y). \quad (2.25)$$

According to this expression, the longitudinal field component is proportional to the divergence of the transverse field component $\mathcal{E}_t = (\mathcal{E}_x, \mathcal{E}_y)$. This means, if \mathcal{E}_t varies significantly on the length scale of $1/k = \lambda/2\pi$, the longitudinal field component can become as large as $|\mathcal{E}_t|$. Furthermore, the factor $-i$ indicates that there is a phase difference of $\pi/2$ between \mathcal{E}_z and \mathcal{E}_t . As a consequence, if \mathcal{E}_t is a fully linearly polarized field, the superposition of the longitudinal and transverse field components leads to local elliptical polarization, and in the special case $\mathcal{E}_z = |\mathcal{E}_t|$ to circular polarization. Note, that this elliptical polarization lies in the plane of the propagation direction, and is therefore fundamentally different from elliptical polarization of a paraxial light field, where the electric field vector rotates around the propagation direction. Moreover, Eq. (2.25) reveals the most interesting feature of the considered light beam: when its propagation direction is reversed from $+z$ to $-z$, i.e. $\mathbf{k} \rightarrow -\mathbf{k}$, the sign of the longitudinal field component and, thus, the sense of rotation of the local elliptical polarization flips. This intrinsic link between the polarization and the propagation direction has also been investigated theoretically in Refs. [49, 50], and has been termed *spin-momentum locking*.

Strong transverse field gradients can occur in all situations where light is strongly confined, e.g., in tightly focused Gaussian beams or – most important for us – evanescent fields. For a long time this effect has not been considered in the description of whispering-gallery modes, until our group found in 2013 that the measured transmission spectra for TM-polarized bottle modes can only be explained by taking into account the longitudinal field component [46, 60]. It turns out that the exponential decay of the evanescent field of the WGM on a length scale of ~ 100 nm leads to a longitudinal field component almost as large as the transverse field component [60]. As WGM resonators are ring resonators, they always support two degenerate modes, a clockwise propagating (cw) and a counter-clockwise propagating mode (ccw), as illustrated in Fig. 2.5. If we choose the resonator axis (z) as our quantization axis, such that we can define the basis polarization states $e_{\sigma^\pm} = (e_r \pm ie_\phi)/\sqrt{2}$ and $e_\pi = e_z$, then the overlap of the polarization of the ccw- and cw-mode with σ^+ - and σ^- -polarization, respectively, is given by

$$\frac{|\mathcal{E}^{\text{ccw}} \cdot e_{\sigma^+}^*|^2}{|\mathcal{E}^{\text{ccw}}|^2} = \frac{|\mathcal{E}^{\text{cw}} \cdot e_{\sigma^-}^*|^2}{|\mathcal{E}^{\text{cw}}|^2} = 0.97 \quad (2.26)$$

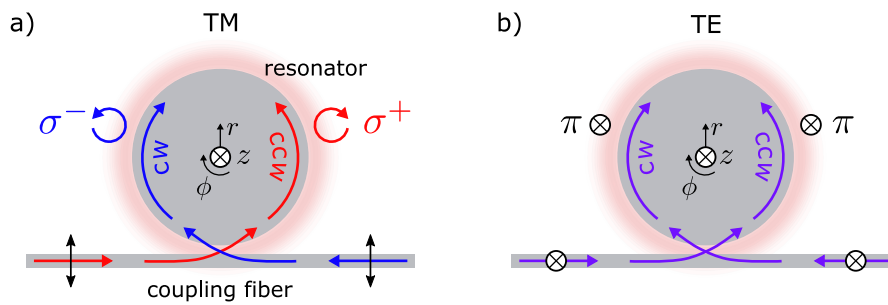


Figure 2.5: Illustration of the local polarization properties in the evanescent field of a) a TM-polarized and b) a TE-polarized WGM. A WGM resonator always supports two degenerate modes, a clockwise (cw) and a counter-clockwise (ccw) propagating mode. In the case of TM-polarization, the two propagation directions are intrinsically linked with the mutually orthogonal circular polarizations, σ^+ and σ^- , of the evanescent fields, which is called spin–momentum locking. In the case of TE-polarization, the two counter-propagating modes have identical linear polarization.

near the resonator surface. Hence, the evanescent field of the ccw (cw) mode is nearly perfectly σ^+ (σ^-)-polarized, as illustrated in Fig. 2.5 a). Note, that this effect is only present for TM-polarized modes, as they exhibit a non-vanishing longitudinal electric field component \mathcal{E}_ϕ (cf. Sec. 2.2.3). As a consequence, the two counter-propagating TM-polarized modes are almost perfectly orthogonally polarized to each other and, hence, do not interfere. Accordingly, they do not build up a standing-wave mode structure inside the resonator. As we will see in Sec. 2.3.3, these polarization properties of WGMs have implications on the interaction with single atoms and allow one to enter a new regime of CQED.

For completeness, in the case of TE-polarized WGMs, the two counter-propagating modes are both linearly polarized along the z -axis, see Fig. 2.5 b). In this case, a WGM resonator is equivalent to a conventional ring-resonator.

2.2.5 Evanescent coupling to WGMs with tapered fiber couplers

A distinct feature of WGM resonators is that light can be coupled into these resonators with nearly 100% efficiency [84] by using tapered optical fibers [82]. The latter can be fabricated from standard optical single-mode fibers in a heat-and-pull process [82]. This process can be engineered such that – within a few millimeter-long section – the fiber is adiabatically tapered down to diameters smaller than the wavelength of the light. The resulting waist of the tapered fiber is also called *nanofiber*. The adiabaticity condition ensures that the light remains in the fiber-guided mode and, thus, a fiber transmission close to unity can be maintained [85, 86]. In the nanofiber section, a significant fraction of the light intensity is guided outside of the fiber in form of an evanescent field.

Now, such a tapered fiber can be used to couple light into and out of a WGM resonator via the effect of frustrated total internal reflection [79]. For this, the fiber and the resonator have to be interfaced with each other such that their fields overlap. To achieve a high coupling efficiency,

the spatial mode overlap should be large, the fiber mode and the resonator mode should be resonant with each other and their wave vectors should match. The latter corresponds to a phase-matching condition, which has to be fulfilled to enable constructive interference between the fields of the fiber coupler and the resonator at the coupling junction [87].

As a consequence of the evanescent coupling, the fiber–resonator coupling rate can be tuned simply by changing the fiber–resonator distance, thereby changing the overlap of the electric fields. We denote the fiber–resonator coupling rate with κ_{ext} , see Fig. 2.7 a). One distinguishes three coupling regimes depending on the fiber–resonator distance and the corresponding relation between the external coupling rate κ_{ext} and the intrinsic resonator field decay rate κ_0 : under-coupling ($\kappa_{\text{ext}} < \kappa_0$), critical coupling ($\kappa_{\text{ext}} = \kappa_0$) and over-coupling ($\kappa_{\text{ext}} > \kappa_0$). The experiments presented in this thesis were all performed under the condition of critical coupling. In this regime on resonance, the amplitudes of the incident light and the light that couples back from the resonator into the fiber are equal. The latter, however, experiences a π phase shift such that the two light fields interfere destructively. As a consequence, the fiber transmission is zero, which means that the complete light power is transferred into the resonator and is dissipated there [60]. This setting is essential for our atom-detection scheme, as will be seen in Sec. 2.5.2. However, there exists another detection technique, when the system is operated in the over-coupled regime [65], as used, e.g., in the experiment described in Ref. [53].

In the special case of the bottle microresonator, the elongated mode structure along the resonator axis allows the coupling of two tapered fiber couplers to the resonator mode without the spatial constraint inherent to equatorial WGMs [59, 81]. In this way, the bottle resonator can be employed as a four-port device, which we exploited, e.g., for the demonstration of a quantum optical circulator [55].

2.3 Basic theory of atom–light interaction in resonators

In the following, we will describe the resonant coherent interaction between a single atom and a single quantized mode of the electromagnetic field, which can be selected from the continuum of free-space modes by imposing boundary conditions using an optical microresonator. A fully quantum mechanical treatment of this situation has been provided by Jaynes and Cummings in 1963 [88]. To this day, this model receives a great deal of attention, and it has been extended and generalized to describe, e.g., multi-level atoms [89] and multi-modes [90]. However, it does not treat the dissipation mechanisms present in a real system. This can be included into the Jaynes-Cummings description using the so-called master equation approach [91], as we will see in Sec. 2.3.2.

2.3.1 Jaynes-Cummings model

We consider a two-level atom with a ground state $|g\rangle$ and an excited state $|e\rangle$, as depicted in Fig. 2.1 a). The single quantized field mode is characterized by the number of photons in the field $|n\rangle$. The Jaynes-Cummings Hamiltonian that describes the total system consists of three parts

$$\hat{H}_{\text{JC}} = \hat{H}_{\text{a}} + \hat{H}_{\text{r}} + \hat{H}_{\text{int}}, \quad (2.27)$$

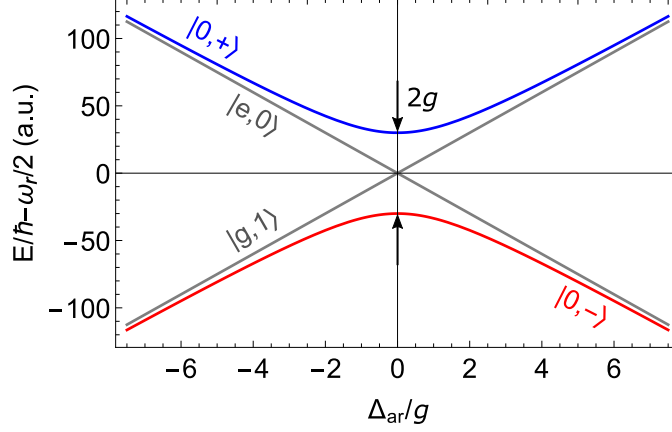


Figure 2.6: Energy eigenvalues of the dressed states $|n, \pm\rangle$ according to Eq. (2.32) for the case of an empty resonator mode ($n = 0$), as a function of the atom–resonator detuning Δ_{ar} . On resonance ($\Delta_{\text{ar}} = 0$), an avoided crossing occurs with a splitting of width $2g$. For comparison, the eigenenergies of the bare states $|g, 1\rangle$ and $|e, 0\rangle$ are plotted in gray.

where the first term describes the free atom

$$\hat{H}_a = \frac{1}{2} \hbar \omega_a \hat{\sigma}_z, \quad (2.28)$$

with the atomic transition frequency ω_a and the atomic inversion operator $\hat{\sigma}_z = |e\rangle\langle e| - |g\rangle\langle g|$. Here, we chose the point of zero energy to lie exactly in between the ground and the excited state. The second term in Eq. (2.27) describes the free field with frequency ω_r . It can be shown that a single mode of the electromagnetic field is formally equivalent to the quantum harmonic oscillator and, thus, the corresponding Hamiltonian is given by

$$\hat{H}_r = \hbar \omega_r \hat{a}^\dagger \hat{a}. \quad (2.29)$$

Here, \hat{a}^\dagger and \hat{a} are the creation and annihilation operators of a photon, respectively. The zero-point energy $(1/2)\hbar\omega_r$ was set to zero in this expression, as it does not contribute to the dynamics [92]. Finally, the interaction between the atom and the field mode can be written in the dipole and rotating-wave approximations [92, 93] as

$$\hat{H}_{\text{int}} = \hbar g (\hat{a}^\dagger \hat{\sigma}_- + \hat{a} \hat{\sigma}_+), \quad (2.30)$$

where g is the atom–light coupling strength (cf. Eq. (2.8)), and $\hat{\sigma}_+ = |e\rangle\langle g|$ and $\hat{\sigma}_- = |g\rangle\langle e|$ are the atomic excitation and deexcitation operators, respectively. The Hamiltonian \hat{H}_{JC} only couples the states $|e\rangle \otimes |n\rangle \leftrightarrow |g\rangle \otimes |n+1\rangle$ [92]. The product states $|e, n\rangle = |e\rangle \otimes |n\rangle$ and $|g, n+1\rangle = |g\rangle \otimes |n+1\rangle$ are the eigenstates of the uncoupled system ($g = 0$), often referred to as *bare states*.

In order to obtain the eigenstates of the coupled system ($g \neq 0$), we have to diagonalize the total Hamiltonian, yielding the so-called *dressed states* [92]

$$\begin{aligned} |n, +\rangle &= \cos(\Phi_n/2) |e, n\rangle + \sin(\Phi_n/2) |g, n+1\rangle, \\ |n, -\rangle &= -\sin(\Phi_n/2) |e, n\rangle + \cos(\Phi_n/2) |g, n+1\rangle, \end{aligned} \quad (2.31)$$

where $\Phi_n = \tan^{-1}(2g\sqrt{n+1}/\Delta_{\text{ar}})$ with the atom–resonator detuning $\Delta_{\text{ar}} = \omega_a - \omega_r$. The corresponding energy eigenvalues are

$$E_{n,\pm} = \left(n + \frac{1}{2}\right) \hbar\omega_r \pm \frac{1}{2}\hbar\Omega_n(\Delta_{\text{ar}}), \quad (2.32)$$

with the Rabi frequency $\Omega_n(\Delta_{\text{ar}}) = \sqrt{4g^2(n+1) + \Delta_{\text{ar}}^2}$. The energies of the dressed states $|n, \pm\rangle$ are plotted in Fig. 2.6 for the case of $n = 0$ as a function of the atom–resonator detuning Δ_{ar} . Setting $g = 0$ in Eq. (2.32) gives the bare state energies for comparison, shown in gray in Fig. 2.6. One can see that for large detuning the dressed states asymptotically approach the bare states. On resonance ($\Delta_{\text{ar}} = 0$), however, they exhibit an avoided crossing. The corresponding energy splitting arises due to the resonant atom–resonator interaction and the width of the splitting is given by $\Omega_n(0) = 2g\sqrt{n+1}$. The fact that the Rabi frequency is non-zero for $n = 0$, reflects that the atom undergoes Rabi oscillations even in an empty resonator, which are induced by the electromagnetic vacuum. The energy splitting in this case is referred to as *vacuum Rabi splitting* [94].

2.3.2 Master equation: losses and driving

In the previous section, we discussed the situation of an atom exclusively interacting with a quantized field mode, e.g. a resonator mode. However, in order to describe a realistic system, we also want to include into the theory the dissipation mechanisms discussed in Sec. 2.1.2. Furthermore, to be able to retrieve information from the system, we want to introduce an external coupling channel between the atom and the resonator field. For WGM resonators, this can be the optical mode of a tapered fiber coupler, as explained in Sec. 2.2.5 and illustrated in Fig. 2.7 a).

Such a so-called open quantum system can be theoretically treated using the master equation approach [91], which we will outline here. In this approach, the dissipation of a system of interest S is described by its interaction with a large reservoir R . The state of the combined system $S \otimes R$ is represented by the density operator $\hat{\rho}_{SR}$ and its time evolution is described by the Schrödinger equation $d\hat{\rho}_{SR}/dt = -i/\hbar [\hat{H}_{SR}, \hat{\rho}_{SR}]$. The objective now is to derive the equations of motion for the system only. The reduced density operator for the system can be obtained by taking the trace over the states of the reservoir, i.e. $\hat{\rho}_S(t) = \text{Tr}_R[\hat{\rho}_{SR}(t)]$ [93]. Using the Born-Markov approximation [91] one can derive the master equation, which reads in Lindblad form

$$\frac{d\hat{\rho}_S}{dt} = -\frac{i}{\hbar}[\hat{H}_S, \hat{\rho}_S] + \mathcal{L}\hat{\rho}_S, \quad (2.33)$$

where \mathcal{L} is the Lindblad superoperator.

For our system, the total system Hamiltonian is now given by

$$\hat{H}_S = \hat{H}_{\text{JC}} + \hat{H}_{\text{drive}}, \quad (2.34)$$

where we now also added a driving term in order to include probing of the atom–resonator system. Furthermore, the Jaynes-Cummings Hamiltonian has been transformed into a frame that rotates with the frequency ω_{probe} of the probe field

$$\hat{H}_{\text{JC}}/\hbar = \Delta_{\text{ap}}\hat{\sigma}_+\hat{\sigma}_- + \Delta_{\text{rp}}\hat{a}^\dagger\hat{a} + g(\hat{a}^\dagger\hat{\sigma}_- + \hat{a}\hat{\sigma}_+). \quad (2.35)$$

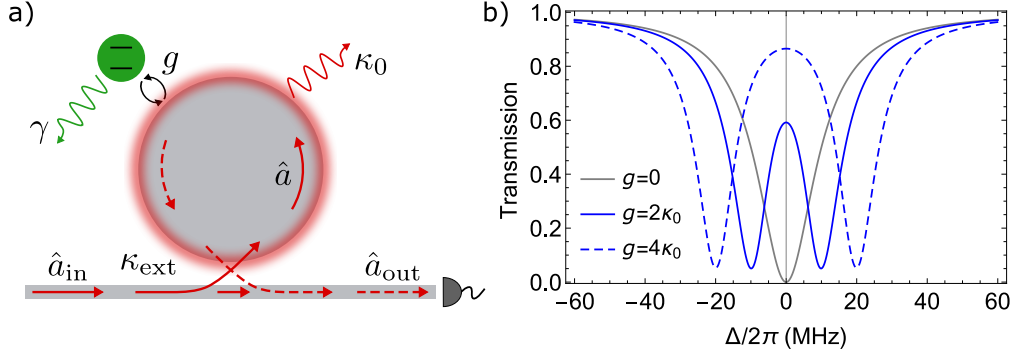


Figure 2.7: a) Illustration of a single two-level atom (green dot) coupled to a WGM resonator, which is interfaced with a fiber coupler. The resonator mode \hat{a} is driven via the fiber-guided input field \hat{a}_{in} . The total resonator decay rate κ_{tot} consists of the intrinsic resonator decay rate κ_0 and the coupling rate to the fiber κ_{ext} . b) Calculated transmission spectrum according to Eq. (2.39) as a function of the detuning $\Delta_{\text{ap}} = \Delta_{\text{rp}} = \Delta$, for three different values of the coupling strength g . Here, we assumed critical coupling for the empty resonator with $\kappa_0 = \kappa_{\text{ext}} = 2\pi \times 5$ MHz and inserted the spontaneous decay rate of the ^{85}Rb atom of $\gamma = 2\pi \times 3$ MHz.

Here, $\Delta_{\text{ap}} = \omega_a - \omega_{\text{probe}}$ is the atom–probe detuning and $\Delta_{\text{rp}} = \omega_r - \omega_{\text{probe}}$ is the resonator–probe detuning. The Lindblad superoperator is given by

$$\mathcal{L} = \kappa_{\text{tot}}(2\hat{a}\hat{\rho}\hat{a}^\dagger - \hat{a}^\dagger\hat{a}\hat{\rho} - \hat{\rho}\hat{a}^\dagger\hat{a}) + \gamma(2\hat{\sigma}_-\hat{\rho}\hat{\sigma}_+ - \hat{\sigma}_+\hat{\sigma}_-\hat{\rho} - \hat{\rho}\hat{\sigma}_+\hat{\sigma}_-) \quad (2.36)$$

where $\kappa_{\text{tot}} = \kappa_0 + \kappa_{\text{ext}}$ with the intrinsic decay rate of the resonator κ_0 and the fiber–resonator coupling rate κ_{ext} , and γ is the atomic dipole decay rate.

There are two possibilities to probe the coupled atom–resonator system: either by sending a probe light field onto the atom (“atom-drive”) or onto the resonator (“resonator-drive”). At this point, we will only address the latter case. However, in Sec. 5.5 a measurement is presented that uses the atom-drive setting and the corresponding formulas will be given in Sec. 5.5.1. The driving-Hamiltonian for driving the resonator with a coherent light pulse is given by

$$\hat{H}_{\text{drive}}/\hbar = i\epsilon(\hat{a} - \hat{a}^\dagger), \quad (2.37)$$

where $\epsilon = \sqrt{2\kappa_{\text{ext}}}\langle\hat{a}_{\text{in}}\rangle$ and \hat{a}_{in} is the amplitude of the incident field. In our experiment, we retrieve information from the system, independent of the type of driving, by analyzing the light in the fiber output mode \hat{a}_{out} . In the case of the resonator drive this output field is a superposition of the input field \hat{a}_{in} and the field that couples back from the resonator mode \hat{a} into the output mode (cf. Fig. 2.7 a))

$$\hat{a}_{\text{out}} = \hat{a}_{\text{in}} - i\sqrt{2\kappa_{\text{ext}}}\hat{a}. \quad (2.38)$$

We want to determine the steady-state transmission through the coupling fiber, which is given by $T = |\langle\hat{a}_{\text{out}}\rangle / \langle\hat{a}_{\text{in}}\rangle|^2$. For this, we have to determine the resonator field $\langle\hat{a}\rangle$, which we can do by solving the master equation in steady state ($d\hat{\rho}_S/dt = 0$) under the assumption of weak driving and considering that the expectation value of a system operator can be computed as

$\hat{O} = \text{Tr}[\hat{\rho}_S \hat{O}]$. Thus, by inserting Eqs. (2.34) and (2.36) into Eq. (2.33), we can find an analytic expression for the transmission through the coupling fiber

$$T = \left| \frac{g^2 + (\gamma + i\Delta_{\text{ap}})(\kappa_0 - \kappa_{\text{ext}} + i\Delta_{\text{rp}})}{g^2 + (\gamma + i\Delta_{\text{ap}})(\kappa_0 + \kappa_{\text{ext}} + i\Delta_{\text{rp}})} \right|^2. \quad (2.39)$$

Figure 2.7 b) shows transmission spectra according to Eq. (2.39) for three different values of the coupling strength g as a function of the detuning $\Delta_{\text{ap}} = \Delta_{\text{rp}} = \Delta$. For the cases depicted by the blue lines, a vacuum Rabi splitting with a width of $2g$ is predicted.

2.3.3 Chiral atom–light interaction in WGM resonators

In Sec. 2.2.4 we discussed that WGM resonators support two degenerate counter-propagating modes. Thus, the previous treatment of the interaction of an atom with a single resonator mode is, in general, not a complete description for WGM resonators. In order to describe the system including two modes \hat{a} and \hat{b} , the Hamiltonian needs to be modified to

$$\begin{aligned} \hat{H}_S/\hbar = & \Delta_{\text{ap}}\hat{\sigma}_+\hat{\sigma}_- \\ & + \Delta_{\text{rp}}(\hat{a}^\dagger\hat{a} + \hat{b}^\dagger\hat{b}) + (h\hat{a}^\dagger\hat{b} + h^*\hat{b}^\dagger\hat{a}) \\ & + (g_a^*\hat{a}^\dagger\hat{\sigma}_- + g_a\hat{a}\hat{\sigma}_+) + (g_b\hat{b}^\dagger\hat{\sigma}_- + g_b^*\hat{b}\hat{\sigma}_+) \\ & + i\epsilon_a(\hat{a} - \hat{a}^\dagger) + i\epsilon_b(\hat{b} - \hat{b}^\dagger). \end{aligned} \quad (2.40)$$

The first two terms describe again the free atom and the free field modes, respectively. The third term in the Hamiltonian now takes into account the possibility of coupling between the two resonator modes [95]. Such an exchange of energy between the modes with the rate h can be caused by bulk or surface imperfections of the resonator, thereby lifting the degeneracy between the two modes. The coupling rate from mode \hat{a} to mode \hat{b} is assumed to be equal to the rate of the reverse process. The fourth and fifth term describe the interaction between an atom and each of the modes with coupling strengths g_a and g_b , respectively. The latter are in general not equal ($g_a \neq g_b$). In the most general case, the system can be driven via both modes, which is described by the last two terms in Eq. (2.40), where $\epsilon_a = \sqrt{2\kappa_{\text{ext}}}\langle\hat{a}_{\text{in}}\rangle$ and $\epsilon_b = \sqrt{2\kappa_{\text{ext}}}\langle\hat{b}_{\text{in}}\rangle$. The master equation for this system is then given by

$$\begin{aligned} \frac{d\hat{\rho}_S}{dt} = & -\frac{i}{\hbar}[\hat{H}_S, \hat{\rho}_S] \\ & + \kappa_{\text{tot}}(2\hat{a}\hat{\rho}\hat{a}^\dagger - \hat{a}^\dagger\hat{a}\hat{\rho} - \hat{\rho}\hat{a}^\dagger\hat{a}) \\ & + \kappa_{\text{tot}}(2\hat{b}\hat{\rho}\hat{b}^\dagger - \hat{b}^\dagger\hat{b}\hat{\rho} - \hat{\rho}\hat{b}^\dagger\hat{b}) \\ & + \gamma(2\hat{\sigma}_-\hat{\rho}\hat{\sigma}_+ - \hat{\sigma}_+\hat{\sigma}_-\hat{\rho} - \hat{\rho}\hat{\sigma}_+\hat{\sigma}_-). \end{aligned} \quad (2.41)$$

Equations (2.40) and (2.41) are generally valid both for conventional ring-resonators, which support two counter-propagating modes with identical polarization, and for WGM resonators. In WGM resonators the two modes can have different polarizations, as we have seen in Sec. 2.2.4. Furthermore, different polarization components of the resonator modes drive different transitions in the magnetic sub-structure of the atomic levels and, thus, the atom cannot be treated as a

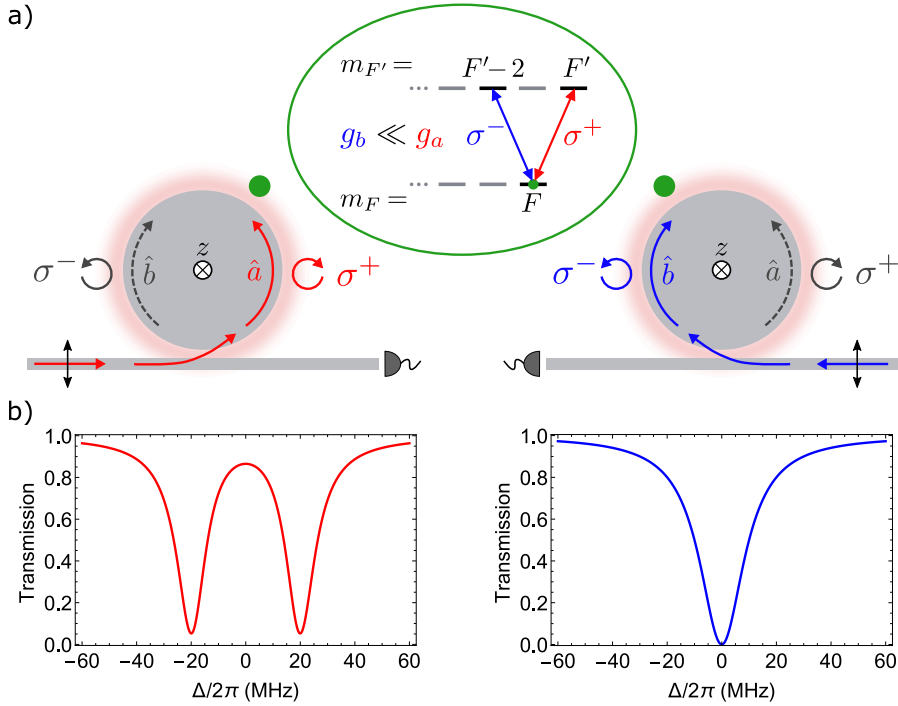


Figure 2.8: Chiral atom–light interaction in a WGM resonator. a) Coupling between an atom, which is prepared in its outermost Zeeman state of the hyperfine ground state, and TM-polarized WGMs. Two cases are considered, where either mode \hat{a} (left) or mode \hat{b} (right) is driven via an input field in the coupling fiber. b) Calculated transmission spectra according to Eq. (2.39) for the two cases illustrated in panel (a). The coupling strength to mode \hat{a} (mode \hat{b}) is assumed to be $g_a = 4\kappa_0$ ($g_b = 0$). Furthermore, we assumed critical coupling for the empty resonator with $\kappa_{\text{ext}} = \kappa_0 = 2\pi \times 5$ MHz and inserted the spontaneous decay rate of the ^{85}Rb atom of $\gamma = 2\pi \times 3$ MHz. Figure adapted from Ref. [83].

two-level system anymore. An accurate formalism for the description of atom–light interaction with WGMs, which treats the resonator fields as vector quantities and takes the complex atomic level structure into account, can be found in Refs. [60, 65, 83].

Here, we want to qualitatively address one particularly interesting case. We consider TM-polarized counter-propagating resonator modes, i.e. the light in mode \hat{a} (mode \hat{b}) is almost perfectly σ^+ (σ^-)-polarized, as shown in Fig. 2.8 a). Furthermore, we assume the atom to be a polarization-dependent scatterer, i.e. it does not couple equally to both of the modes or – in the extreme case – couples to only one of the modes. The latter situation can approximately be realized by preparing, e.g., an alkali atom in one of the outermost Zeeman sublevels of the hyperfine ground state F , e.g. in $m_F = +F$. Then, the resonator fields drive an effective V-level system, as illustrated in Fig. 2.8 a). In alkali atoms, the transition strength of the $(m_F = F) \rightarrow (m_{F'} = F + 1)$ transition is significantly larger than that of the $(m_F = F) \rightarrow (m_{F'} = F - 1)$

transition. As a consequence, the atom almost exclusively couples to mode \hat{a} ($g_b \ll g_a$) which, thus, drives the closed cycling transition, thereby reducing the complex atomic level structure to an effective two-level system. If only mode \hat{a} is driven and in the absence of mode–mode coupling ($h = 0$), the Hamiltonian in Eq. (2.40) reduces to the Jaynes-Cummings Hamiltonian given in Eq. (2.35). If only mode \hat{b} is driven and if $h = 0$, the system behaves much like an empty resonator. The corresponding calculated transmission spectra are depicted in Fig. 2.8 b), where we assumed critical coupling of the empty resonator ($\kappa_{\text{ext}} = \kappa_0$), and the coupling strengths between the atom and the two resonator modes to be $g_a = 4\kappa_0$ and $g_b = 0$, respectively, as well as $h = 0$.

In our experiment, the scenario on the left side of Fig. 2.8 constitutes the basis for the real-time detection of atoms in the resonator mode, as we will see in Sec. 2.5.2. Most interestingly, however, in the described setting, the response of the system depends on the propagation direction of the input light field. This so-called chiral atom–light interaction is a consequence of the spin–momentum locked light fields in the resonator. In our group, we exploited this effect for the realization of two non-reciprocal devices: an optical isolator [54] and a quantum optical circulator [55].

If TE-polarized WGMs are used or if the atom couples equally to both resonator modes, the system behaves symmetrically, i.e. independent of the propagation direction. Hence, WGM resonators can be operated in both the chiral and the non-chiral regime.

2.4 Experimental setup

2.4.1 Concept of the bottle resonator CQED experiment

The ideal scenario for interfacing a single atom with a resonator is to localize the atom inside the resonator mode for a substantial amount of time, as it allows for deterministic coherent atom–light interaction with a stable coupling strength. Some systems, as e.g. single atoms coupled to Fabry-Pérot cavities, have already come quite close to this ideal situation by optically trapping and cooling atoms inside the cavity mode [26]. In the case of WGM resonators, the atom needs to be trapped very close to the resonator surface in the evanescent field, which will be the subject of chapters 3 and 4. Until now, however, only free-falling atoms have been coupled to WGMs. This is done either by releasing a cold atomic cloud from a magneto-optical trap (MOT) from a few millimeters above the resonator [36, 96], such that their velocity is relatively low when they fall through the evanescent field, or by delivering a cold atomic cloud via the atomic fountain principle [97–99].

In our experiment, the latter approach has been implemented. A cold cloud of ^{85}Rb atoms is formed inside a magneto-optical trap (MOT), which is then vertically launched toward the resonator. The fountain parameters are chosen such that the turning point of the ballistic trajectory of the atomic cloud lies near the resonator. Here, its center-of-mass velocity is zero and, thus, the atom–light interaction time is maximized within the limits of this method. On the way to the resonator, the atomic cloud expands due to its finite temperature. When the cloud is near the resonator, its density is so low that every now and then a single atom falls through the evanescent field of the resonator mode. We detect such a single-atom transit event in real time and rapidly

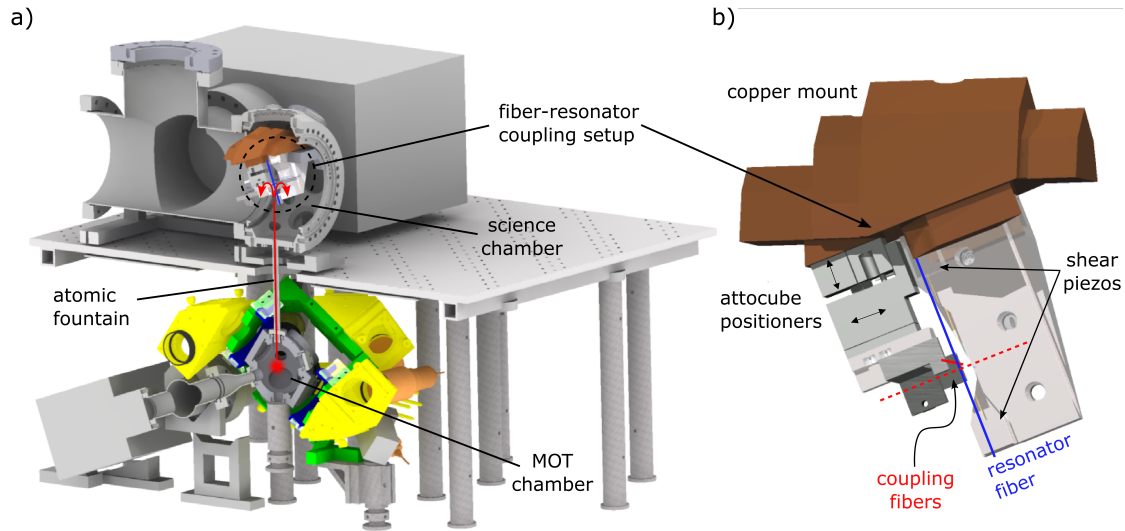


Figure 2.9: Experimental apparatus. a) Cross section of the vacuum chamber with a two-chamber design, consisting of the lower MOT chamber and the upper science chamber. In the MOT chamber a cold cloud of rubidium atoms is formed in a magneto-optical trap (MOT). The pair of magnetic field coils in anti-Helmholtz configuration is marked in blue. Furthermore, the fiber-coupled collimators for the cooling beams (orange) as well as the optics to adjust the beams and overlap them with each other in the center of the chamber (yellow) are shown. The cold atomic cloud is launched via an atomic fountain into the upper chamber, where the resonator with the two coupling fibers is located. b) Fiber-resonator coupling setup mounted onto a 2kg copper block, which rests on four viton rings for vibration isolation [59]. The resonator-fiber (blue line) is tilted by $\approx 17^\circ$ to the vertical. Coupling fiber 1 (red solid line) is shown including its U-shaped holder, which is attached to two attocube linear translators (see text). The orientation of coupling fiber 2 is indicated by the red dashed line, without showing the holder and attocube positioners for clarity. Figures adapted from [59, 100].

react to it using a field programmable gate array (FPGA)-based detection and control system. This enables us to observe signatures of the atom-resonator interaction within the short time, in which the atom couples to the resonator.

In this section, the main parts of the bottle resonator CQED experiment will be described. More details on the various parts explained here as well as further information can be found in Refs. [59, 60, 100].

2.4.2 Vacuum chamber

The vacuum chamber housing the main components of the experiment is shown in Fig. 2.9 a). It consists of two chambers, which are connected by a differential pumping tube of about 30 cm length. In the lower chamber, a cold cloud of ^{85}Rb atoms is formed in a MOT. The heart of the upper chamber is an assembly of the bottle resonator and two coupling fibers, which is shown

in Fig. 2.9 b) and described in the next section. The fibers are guided into the vacuum chamber via dedicated feed-throughs¹ that allow to maintain the ultra-high vacuum. The two chamber design has the advantage that the bottle resonator is not located close to the rubidium dispensers (cf. Sec. 2.4.4), as otherwise atoms would stick to its surface, leading to a degradation of the quality factor [101]. The atomic cloud is launched through the differential pumping tube into the upper chamber to the resonator. Here, the actual experiments take place, which is why it is called *science chamber*.

2.4.3 Fiber–resonator coupling setup

The resonator fiber, indicated by the blue solid line in Fig. 2.9, is mounted in the upper chamber with an angle of $\approx 17^\circ$ to the vertical. Each side of it is glued onto a shear piezo, which allows strain-tuning of the resonance frequency. The bottle resonator is interfaced with two coupling fibers with the orientations depicted in Fig. 2.9 b). The two fibers each exhibit a nanofiber section with a minimal diameter of 500 nm. Each fiber is glued onto a U-shaped fiber holder². The fiber holders are each mounted onto a stack of two linear nanopositioners³ that allow to adjust the fiber–resonator distance and to move the fiber along the resonator axis, respectively. In the framework of this thesis only coupling fiber 1 was used, which is marked by the red solid line.

The fiber–resonator coupling setup is mounted to a massive gold-coated copper piece, which rests on two metal beams in the science chamber, see Fig. 2.9. Viton rings between the beams and the copper block isolate the resonator and the fibers from vibrations of the setup [60]. The copper block exhibits a hole along the vertical to grant optical access to the resonator through the top viewport of the science chamber. We make use of this, when we apply the heating laser, which will be described in Sec. A.2.

2.4.4 Atom preparation

Magneto-optical trap

As the first step of the atomic fountain, a cold cloud of ^{85}Rb atoms is formed in a magneto-optical trap (MOT). This trapping mechanism was first demonstrated in [102]. A MOT provides laser-cooling and trapping of atoms by a hybrid approach that combines a linear gradient magnetic field with optical molasses cooling [103, 104]. While optical molasses cooling only generates a velocity-dependent damping force, the magnetic field gradient in conjunction with the polarization of the laser beams adds a position-dependent restoring force that provides confinement of the atoms.

The configuration of our MOT is illustrated in Fig. 2.10 a). A pair of current-carrying coils in the so-called anti-Helmholtz configuration generates a quadrupole magnetic field: it is zero at the center of the coils and its magnitude increases linearly in all directions from the coil center for small displacements [105]. The orientation of the anti-Helmholtz coils in our setup is visible

¹swagelok adapters, Vacom GmbH

²For better visibility, only the fiber-holder of coupling fiber 1 is shown.

³ANPx101/NUM and ANPz101/NUM, attocube systems

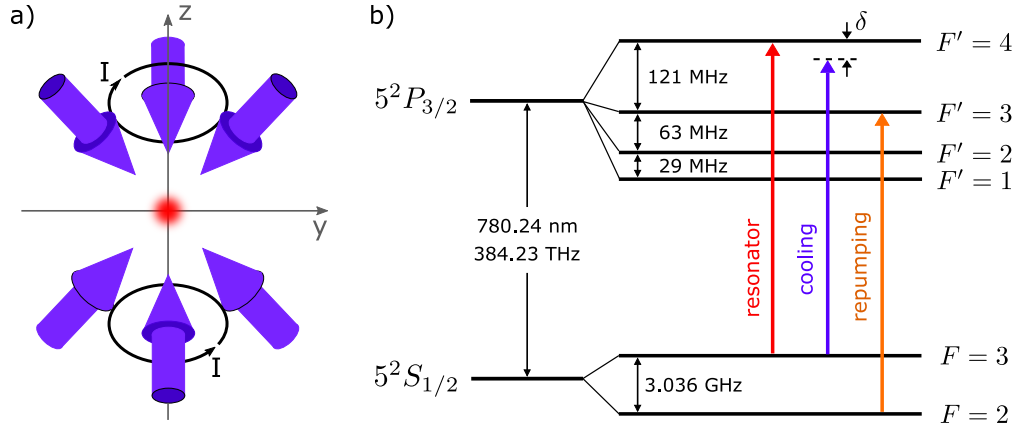


Figure 2.10: a) Illustration of the MOT. The six cooling beams are arranged in a (1,1,1)-configuration. The electric current through the pair of anti-Helmholtz coils is indicated by the black arrows. b) Energy level scheme of the D_2 line of the ^{85}Rb atom. The purple and orange arrows indicate the cooling and repumping transitions for the MOT, respectively. The resonance frequency of the bottle resonator is locked to the $F = 3 \rightarrow F' = 4$ transition (red arrow). Figure adapted from [65].

in Fig. 2.9 a) (blue coils) and the flow direction of the electric current, I , through the coils is indicated in Fig. 2.10 a). We use a current of 6 A, yielding a magnetic field gradient of 5 G/cm along the axis pointing through the coils, and 2.5 G/cm along the perpendicular axes [60].

Additionally, three pairs of mutually orthogonal counter-propagating cooling-laser beams are sent toward the coil center. In our setup, the beams are aligned in the so-called (1,1,1)-configuration, i.e. all beams have an angle of 54.7° to the vertical. This provides a free path along the vertical ($+z$ -direction) for the atomic fountain [106]. The cooling beams each have a power of about 20 mW and their frequency is red-detuned by $|\delta| = 2\Gamma \approx 12$ MHz, with respect to the $(5S_{1/2}, F = 3) \rightarrow (5P_{3/2}, F' = 4)$ transition of the ^{85}Rb atom, see Fig. 2.10 b). The source of rubidium atoms is a Rb-dispenser, which is supplied with a current of ~ 3 A and continuously emits hot atoms into the MOT chamber. Thus, atoms can be trapped and cooled in the MOT from the background gas.

While cooling the atoms, they are eventually pumped into the $F = 2$ ground state. Although this process is forbidden by the selection rules, it happens due to off-resonant excitation to the $F' = 3$ state. To bring the atoms back into the cooling cycle, we shine a repump beam into the MOT chamber, which is resonant to the $F = 2 \rightarrow F' = 3$ transition, as indicated in Fig. 2.10 b) by the orange arrow.

With the above described parameters a cloud of cold atoms with a diameter of about 1 mm is formed in the center of the MOT. The loading rate is about 1.88×10^8 atoms/s, resulting in a typical maximal number of ^{85}Rb atoms of about 5×10^7 , which is mainly limited due to collisions with the background gas [60].

MOT laser system

The cooling beams are provided by a powerful laser source⁴, consisting of an external cavity diode laser (ECDL) as a master laser tuned to a wavelength of about 780 nm, which is used to seed a tapered amplifier (TA) laser diode. Several milliwatts from the master laser output power are branched off and sent through a commercial saturated absorption spectroscopy unit⁵ in order to stabilize the laser to the $(5S_{1/2}, F = 3) \rightarrow (5P_{3/2}, F' = 3, 4)$ crossover transition⁶. To stabilize the laser frequency with the help of the spectroscopy signal, we use a frequency modulation (FM) locking scheme.

The main beam from the master laser is injected into the TA laser diode, where it is amplified to an optical power of 1 W, which is split into two equal portions by a beam-splitter (BS) cube. The two beams provide the light for the upper and lower set of the fountain beams, respectively. Each of the beams is guided through an acousto-optical modulator (AOM) in double-pass configuration [107] and coupled into a polarization-maintaining (PM) optical fiber. The frequency of the cooling beams is controlled by the above mentioned AOMs, which are driven by direct digital synthesizer (DDS) sources⁷. In particular, these sources allow to drive the frequency ramps required for the atomic fountain phase (cf. Sec. 2.5.1). The double-pass configuration has the big advantage that efficient fiber-coupling can be maintained during those frequency ramps. The PM fibers guide the two beams from the laser table to the experiment table, where each of them is coupled into a fiber-port cluster⁸. Here, each beam is again split into three portions. Each cluster exhibits a built-in photodiode, which provides a signal for intensity stabilization of each beam. Each of the six cluster outputs is connected via a PM fiber to a fiber-coupled collimator outside the MOT chamber, which are highlighted in Fig. 2.9 a) in orange color. Here, the beams are widened to a beam diameter of about 27 mm and are subsequently sent into the MOT region.

Repump laser system

Our repump laser source is a grating-stabilized ECDL⁹ running at 780 nm with an output power of about 50 mW. The output beam is divided into two parts, each of which is sent through an AOM in double-pass configuration. One of the beams is used to stabilize the frequency of the laser to the $F = 2 \rightarrow F' = 3$ transition. For this purpose, the beam is sent through a CoSy spectroscopy unit. Since the requirements for the frequency stability of the repump laser are not so strict, we use the side-of-fringe locking technique here, where the slope of the spectroscopy line itself serves as an error signal for giving feedback to the diffraction grating. The main beam, which carries most of the power is coupled into a PM-fiber, which guides the light to the experiment table. There, it is sent through a viewport into the MOT region using a collimator, which widens the beam to a diameter of about 13.5 mm. Typically, a power of about 10 mW is used for repumping.

⁴TA pro, Toptica Photonics

⁵CoSy, TEM Messtechnik

⁶Crossover transitions are an artefact of this spectroscopy technique, but they have the advantage of providing strong absorption lines.

⁷AODS 20160 STD, Crystal Technology

⁸1 → 3-port cluster, Schäfter+Kirchhoff

⁹DL 100, Toptica Photonics

2.4.5 Atom detection and probing

Resonator laser setup

In order to investigate the interaction between single atoms and WGMs of the bottle resonator, several resonant light fields are required. Specifically, we need a light field to which the resonator frequency can be stabilized as well as light fields for detecting and probing the atom via the evanescent field of the resonator mode. As only small optical powers are needed for these tasks, we derive these beams from the same laser source. We use an ECDL¹⁰, which provides an output power of about 100 mW. The laser is locked to the $(5S_{1/2}, F = 3) \rightarrow (5P_{3/2}, F' = 4)$ atomic transition (cf. Fig. 2.10 b)) by FM spectroscopy, where we use saturated absorption spectroscopy provided by a commercial spectroscopy unit¹¹. For the latter, a few milliwatts of power are branched off from the main laser output beam and sent through an AOM in double-pass configuration before entering the spectroscopy unit.

For each of the above mentioned tasks, a certain amount of power is again branched off from the main beam. All beams are sent through AOMs in double-pass configuration, respectively, which – on the one hand – compensate for the frequency offset of $2 \times \nu_{\text{SatAbs}}$ introduced by the AOM in the spectroscopy branch and, on the other hand, allow for independent frequency adjustment of the individual beams. After the double-pass, the light is coupled into PM fibers to guide it to the experiment table. Here, the PM fibers are connected to the fiber network around the science chamber, which is depicted in Fig. 2.11 and will be described in the next section.

Fiber network

The task of the fiber network is to prepare and process the light fields during the experimental sequence in a fiber-integrated fashion. As mentioned in Sec. 2.4.3, our experiment exhibits two fibers with nanofiber waists that can be coupled to the bottle resonator. The two ends of each fiber provide in total four ports, which are numbered in Fig. 2.11. In all measurements presented in this thesis, Port 1 is used as the input port for all light fields. All ports, including Port 1, serve as output ports that can be equipped with detectors for light analysis, depending on the application.

Upon being coupled into the fiber network, the *resonator stabilization light* is divided into two branches by a 50:50 fiber-beamsplitter (FBS). One half is sent onto a photodiode (PD), which is used for active intensity stabilization of this light field. A PID controller continuously compares the measured intensity with a set value, and gives according feedback to the AOM in the stabilization beam path of the resonator laser setup. The other half is the main beam, which first passes a paddle polarization controller that allows to adjust the polarization of the stabilization light to the eigenpolarization of the resonator mode. The transmission of the stabilization light through coupling fiber 1 is measured by the avalanche photodiode (APD) 1 in Port 2.

After reaching the experiment table, the *detection light* and the *probe light* first pass through fiber-integrated Mach-Zehnder (MZ) intensity modulators¹². These interferometric devices allow intensity modulation with a bandwidth of 10 GHz, controlled by a voltage applied to an

¹⁰DL pro, Toptica Photonics

¹¹CoSy, TEM Messtechnik

¹²NIR-MX800-LN-10, Photline

2. BOTTLE RESONATOR CQED EXPERIMENT

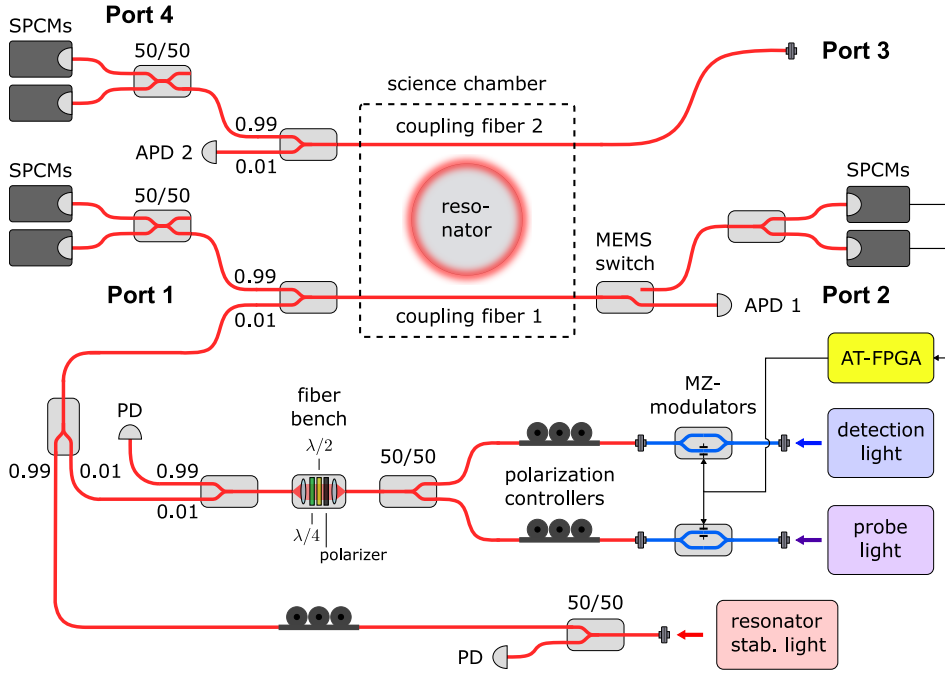


Figure 2.11: Fiber network surrounding the bottle microresonator. The task of the fiber network is to prepare the resonator stabilization light, the detection light and the probe light for investigating the interaction of single atoms with a WGM. Furthermore, it provides the infrastructure to detect the outcoupled light fields that contain information about the atom–resonator interaction. The polarization of the light fields can be independently adjusted by polarization controllers or by free-space components in a fiber bench. The Mach-Zehnder (MZ) modulators allow very fast on/off-switching of the detection and probe light. The photodiodes (PD) provide feedback signals for intensity stabilization. Before entering the vacuum chamber the optical paths of all the light fields are combined via fiber-integrated beamsplitters into a single path that connects to coupling fiber 1. In the transmission port of coupling fiber 1 (Port 2) a MEMS switch is used to route the transmitted light either to an avalanche photodiode (APD) or single-photon counting modules (SPCMs). A field-programmable gate array (AT-FPGA) allows real time detection of atom transits and accordingly triggers the detection and probe light fields. Figure adapted from Ref. [60].

electro-optical material in one of the arms of the MZ interferometer. In our experiment, their purpose is to provide fast on/off-switching of the two light fields. Subsequently, the detection and probe lights both pass through a polarization controller, before their light paths are combined on a 50:50 FBS. Then, by passing through a fiber bench¹³, the polarization of the light fields is cleaned with a thin-film polarizer followed by two waveplates for polarization adjustment. The PD in the 99 % port of the following FBS is used for stabilization of the detection light intensity. Subsequently, the detection and probe light path merges the one of the stabilization light at a

¹³Fiber-to-fiber U-bench, Thorlabs

99:1 FBS, before entering the vacuum chamber. The light transmitted through coupling fiber 1 can be switched upon a trigger signal between two output branches in Port 2 by a fiber-integrated MEMS switch¹⁴. This arrangement prevents the stabilization light, which has a relatively high power of several nanowatts, to be sent onto the single-photon counting modules¹⁵ (SPCM). The purpose of having two SPCMs in one output port is two-fold. On the one hand, less photons are missed due to the dead time of 30 ns of the detectors than if there was only one detector, and on the other hand it allows for Hanbury-Brown-Twiss-type measurements.

As will be explained in Sec. 2.5.2, a field-programmable gate array (AT-FPGA) reacts in real time to the transmission increase of the detection light, registered by the SPCMs in Port 2, which occurs when an atom strongly couples to the resonator mode. Upon atom detection, the FPGA triggers the detection light to switch off and the probe light to switch on via the MZ-modulators, see also Fig. 2.16. The probe light may have other properties than the detection light, as e.g. different power, detuning or polarization. Since there is not enough time to change the properties of the detection light during the short atom transit, we use a separately prepared light field for this purpose.

Resonator lock

In order to observe resonant atom–resonator interaction, we have to actively stabilize the frequency of the bottle resonator mode to the frequency of the $(5S_{1/2}, F = 3) \rightarrow (5P_{3/2}, F' = 4)$ atomic transition. For this, we use the stabilization light introduced before. The coupling fiber is critically coupled to the empty resonator and several nanowatts of stabilization laser power are sent through the coupling fiber. When the resonator frequency is scanned across the fixed frequency of the stabilization light, we observe the Lorentzian resonance of the bottle resonator in the transmission spectrum on APD 1. We use the Pound-Drever-Hall (PDH) locking technique to generate an error signal from this resonance [108]. To implement this technique, an electro-optical modulator (EOM), driven at a frequency of 42.8 MHz by a local oscillator (LO), is used to modulate frequency sidebands onto the stabilization light, before it is sent onto the resonator. As the RF driving frequency is larger than the resonator linewidth, these frequency sidebands are off-resonant with respect to the resonator and, thus, serve as a phase reference. By mixing the measured APD signal with the LO and low-pass filtering the mixer output, one yields the error signal. A PID servo loop uses the error signal to give feedback to the shear piezos to which the bottle resonator fiber is glued for strain-tuning of the resonator mode frequency (cf. Sec. 2.4.3).

Fiber–resonator distance adjustment

Besides the frequency stabilization of the resonator mode, it is important to maintain the critical coupling condition throughout a measurement (cf. Sec. 2.2.5). Therefore, in the initial design of the experiment, an active stabilization of the fiber–resonator distance was implemented via the PDH technique [60]. The setup, however, turned out to be extremely stable even without this stabilization. Over the typical measurement times of many hours, we only observe a slow change

¹⁴MEMS OSW12, Thorlabs

¹⁵SPCM-AQRH-14-FC, Excelitas Technologies

of the fiber–resonator distance, such that an active stabilization is not needed. Instead, a calibration of the fiber–resonator distance is automatically performed every 500 cycles (see Sec. 2.5), corresponding to about every 15 min. For this, the fiber is moved by the attocube translator over the point of critical coupling and the transmission of the stabilization light through the coupling fiber is measured. Then, the fiber is positioned at the point of minimum transmission.

2.4.6 Resonator mode

For all experiments within this thesis, we used the same TM-polarized resonator mode that features a small intrinsic resonator field decay rate of $\kappa_0 \approx 2\pi \times 5$ MHz. However, we do not exactly know its quantum numbers $\{m, p, q\}$ (cf. Sec. 2.2.3), as they cannot be exclusively obtained from the frequency spectrum of the resonator [60]. The azimuthal quantum number m can in principle be estimated from knowing the resonance wavelength and the resonator circumference, if the radial quantum number p is known. To experimentally determine the latter, one would have to count the radial intensity nodes. This is not possible, as they are located inside the resonator. However, calculations based on coupled mode theory suggest that the bottle modes we excite in our experiments are fundamental radial modes [109], i.e. they have radial quantum number $p = 0$. From this follows, that the azimuthal quantum numbers are close to $m \approx 200$ [60].

The axial quantum number q , on the other hand, is in principle measurable, as it corresponds to the number of axial intensity nodes (cf. Sec. 2.2.3). In principle, the axial ring structure can be visible from the outside due to light scattering into free space. Due to the high quality of the resonator, the scattering losses naturally are, however, too low to observe the rings. Another option is to count the intensity minima by moving one of the coupling fibers along the resonator axis and monitor the transmission through the fiber, as it becomes maximal at the points of the intensity minima. This procedure, however, cannot be straightforwardly performed in our experiment. The predominant reason is, that the attocube nanopositioners (cf. Fig. 2.9) do not allow continuous movement of the coupling fiber over the full axial width of the resonator mode. Nevertheless, by attempting such a measurement we were able to narrow down the range of possible axial quantum numbers for the used mode to $0 < q < 5$ [65] and therefore use the most likely value of $q = 3$ for the theoretical descriptions.

2.4.7 Spatial dependence of the coupling strength

According to Eq. (2.8), the coupling strength $g(\mathbf{r})$ between a given dipole emitter and a single photon in a certain resonator mode depends on the position \mathbf{r} of the atom via the mode function $\Psi(\mathbf{r})$. Here, we want to derive the spatial dependence of the coupling strength between a ^{85}Rb atom and the TM-polarized bottle resonator mode used in our experiment with estimated quantum numbers $\{m = 200, q = 3, p = 0\}$ (cf. Sec. 2.4.6). To determine the maximum coupling strength, g_0 , for our experimental system, we have to insert the mode volume, which can be calculated via Eq. (2.20), as well as the dipole matrix element d_{ge} . For the latter, we assume that the atom–light interaction takes place via the $(5S_{1/2}, F = 3, m_F = 3) \rightarrow (5P_{3/2}, F' = 4, m_{F'} = 4)$ cycling transition. However, as we can only access the evanescent field of the bottle resonator mode, we are mostly interested in the coupling strength close to the resonator surface g_{surf} [57].

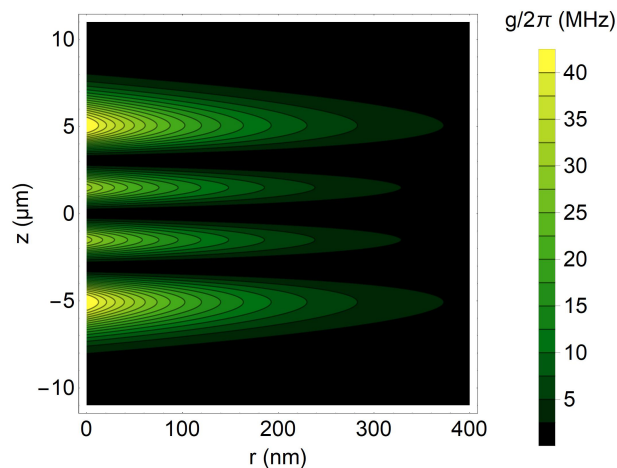


Figure 2.12: Spatial dependence of the coupling strength $g(r, z)$ according to Eq. (2.42), for the resonator mode used in all experiments within this thesis. The azimuthal, radial and axial quantum numbers of this mode are estimated to be $\{m = 200, q = 3, p = 0\}$, see Sec. 2.4.6. The coupling strength at the resonator surface ($r = 0$) and at the caustic is $g_{\text{surf}} = 2\pi \times 43.8$ MHz.

For the considered mode we find $g_{\text{surf}} = 2\pi \times 43.8$ MHz at the axial position of the caustic. With that, the spatial distribution of the coupling strength outside the resonator surface can be approximated by

$$g(r, z) = g_{\text{surf}} \exp(-r/\delta) |Z_{m,q}(z)|^2. \quad (2.42)$$

For simplicity, in radial direction we assume an exponential decay with decay length $\delta \approx 130$ nm. $Z_{m,q}(z)$ is the axial wave function given in Eq. (2.18). The spatial dependence of the coupling strength according to Eq. (2.42) is plotted in Fig. 2.12. It will be used in the derivation of the theoretical models to describe the measured data in Sec. 5.5 and Sec. 5.6.

2.5 Experimental cycle

The experimental cycle describes the sequence of tasks of the different experimental components required to launch the cold atomic cloud to the resonator and subsequently probe single atom coupling events. The execution of the tasks is triggered by a central control software. This software addresses numerous analog and digital output channels to supply, e.g., AOM drivers, piezo-electric actuators and optical switches with preset control voltages and TTL signals. For the main components of the setup the temporal sequence of tasks is illustrated in Fig. 2.13.

The experimental cycle takes about 1.7 s in total and can be divided into two parts, a preparation phase and a detection window. The preparation phase starts with loading ^{85}Rb atoms into the MOT and laser-cooling them for about 1.3 s. Simultaneously, the MZ modulators of the detection beam and the probe beam are calibrated so as to provide optimal switching contrast during the detection window. Afterwards, the cloud of cold atoms is launched towards the bottle resonator. During the whole preparation phase, the resonator is locked to the stabilization light

2. BOTTLE RESONATOR CQED EXPERIMENT

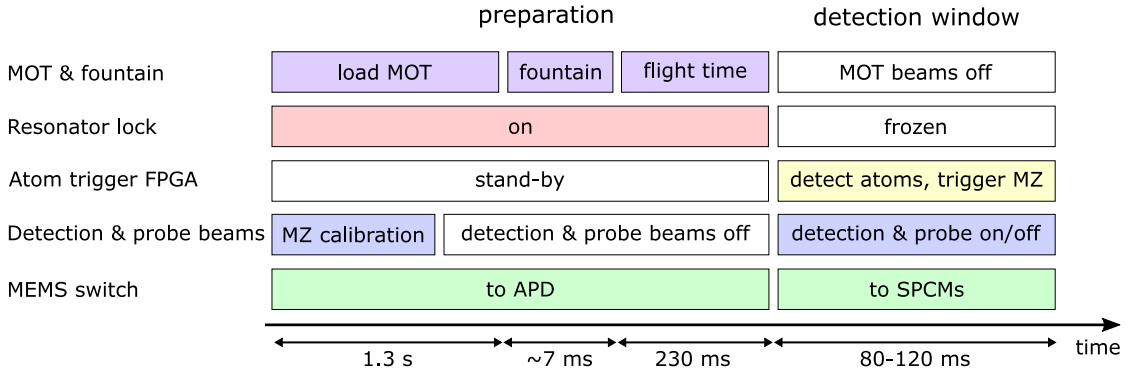


Figure 2.13: Experimental cycle of the CQED apparatus. Shown are the tasks of the key components of the setup as a function of time. The cycle consists of two main parts, a preparation phase and a detection phase, which take in total about 1.7 s to be executed. Details about the different parts are given in the main text.

and, thus, to the $(5S_{1/2}, F = 3) \rightarrow (5P_{3/2}, F' = 4)$ atomic transition. The MEMS switch directs the stabilization light onto the APD 1, see Fig. 2.11. The cold atomic cloud spends about 100 ms in close vicinity to the resonator, which defines the length of the *detection window*, in which single atom transits can be registered.

During this time, the MOT beams are switched off by AOMs and mechanical shutters, in order to prevent stray light from reaching the science chamber. Furthermore, the resonator stabilization is frozen, and the stabilization light is switched off during the detection of atoms. At the start of this detection window, the detection light is switched on and the atom-trigger (AT) FPGA receives a trigger signal from the control software (*sequence trigger*) to look out for atom transit events. The MEMS switch directs the light to the SPCMs. Whenever an atom is detected, the FPGA triggers the detection light to switch off and the probe light to switch on to interrogate the atom. Since in one experimental cycle we detect only about 10 atoms that are strongly coupled to the resonator mode, we typically repeat the cycle several ten thousand times to complete a measurement.

In the following, the atomic fountain principle and the real time detection of single atom transits will be described in more detail.

2.5.1 Atom delivery using an atomic fountain

The temporal sequence for the atomic fountain is depicted in Fig. 2.14. After a cloud of cold atoms has been formed in the MOT, as described in Sec. 2.4.4, the magnetic field is switched off, converting the MOT into an optical molasses. In this moment the atomic fountain sequence begins and, consequently, the atomic cloud is accelerated toward the resonator. This is done by blue-detuning (red-detuning) the lower (upper) set of cooling beams with respect to the initial cooling frequency, see Fig. 2.14. The frequencies are changed in linear ramps until a final relative detuning of $2\Delta\omega$ is reached. This transforms the optical molasses into a moving molasses:

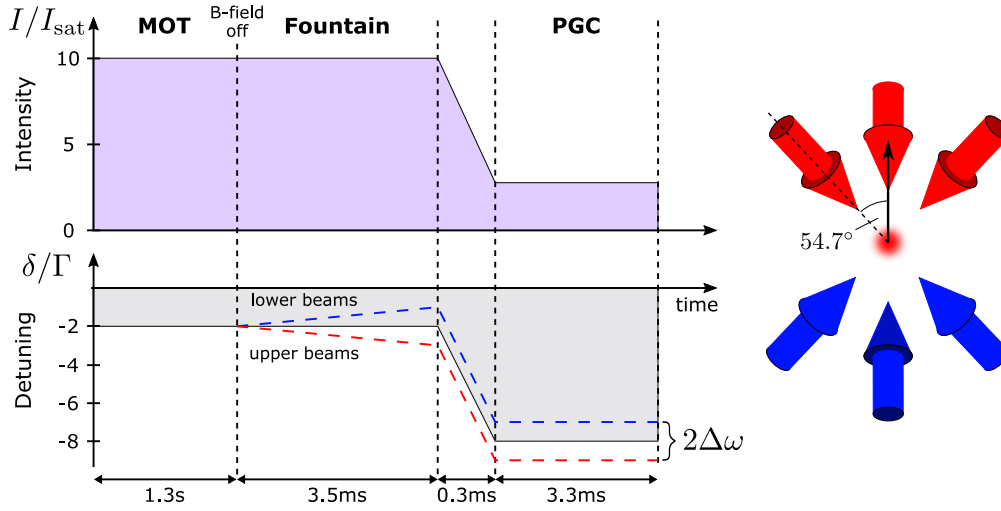


Figure 2.14: Temporal sequence of the atomic fountain (adapted from Ref. [100]), as described in detail in the main text, with an illustration of the frequency detuning between the upper and lower set of cooling beams.

the Doppler shift compensates for the velocity-induced detuning,

$$\Delta\omega - \mathbf{k} \cdot \mathbf{v}_0 = 0 \Leftrightarrow \Delta\omega - k v_0 \underbrace{\cos(54.7^\circ)}_{\approx 1/\sqrt{3}} = 0, \quad (2.43)$$

such that the atoms still experience the optical molasses cooling, but now in a reference frame moving along the vertical axis with the velocity

$$v_0 = \sqrt{3} \frac{\Delta\omega}{k}, \quad (2.44)$$

where $\cos(54.7^\circ) \approx 1/\sqrt{3}$ is the angle between the vertical axis and the cooling beams due to the (1,1,1)-beam configuration (cf. Sec. 2.4.4). Now, the start velocity of the atomic cloud has to be chosen such that the turning point of the fountain trajectory lies near the resonator, which has a distance from the center of the MOT of ~ 30 cm. In the experiment, we therefore use a detuning of $\Delta\omega = \pm 2\pi \cdot 1.77$ MHz, corresponding to a start velocity of $v_0 = 2.4$ m/s according to Eq. (2.44). The linear frequency ramps are driven by the DDS sources (cf. Sec. 2.4.4), with a slope of 0.5 MHz/ms. Accordingly, the acceleration of the cloud takes 3.54 ms.

The temperature of the atomic cloud determines the magnitude of the transverse velocity components. Thus, in order to achieve long atom–resonator interaction times, the atomic cloud should be as cold as possible. Therefore, besides laser-cooling in the MOT, a polarization gradient cooling (PGC)¹⁶ phase is added to the fountain sequence. It finishes after about 3 ms,

¹⁶The PGC or Sisyphus cooling [105,110] exploits the multilevel-structure of the atoms in a way that non-uniform level population – caused by optical pumping processes – in conjunction with polarization gradients in the cooling beams lead to a larger imbalance of the scattering forces exerted by the counter-propagating beams and, thus, colder atoms.

when the atomic cloud exits the cooling beams. For PGC, the intensity of the cooling beams, I , and their mean detuning, δ , is ramped down, while maintaining their relative detuning $2\Delta\omega$, see Fig. 2.14. The dependence of the temperature of the atoms on these two parameters has been investigated for our experiment in Ref. [100]. To measure the temperature, a time-of-flight method has been used, as described in [59, 60, 100]. A minimum temperature of about $6 \mu\text{K}$ has been reached for a detuning $|\delta|/\Gamma = 7 - 9$ with $\Gamma = 2\gamma$ and an intensity of $I/I_{\text{sat}} \approx 4$, where $I_{\text{sat}} = 1.67 \text{ mW/cm}^2$ is the saturation intensity for the D_2 cooling transition in ^{85}Rb , for σ^\pm -polarized light [111].

After the atomic cloud has exited the cooling beams, it takes $v_0/g \approx 240 \text{ ms}$ to reach the resonator. In this time, the cloud expands due to its finite temperature. The time dependence of the cloud diameter, σ , for a given temperature, T , is given by [100]

$$\sigma(t) = \sqrt{D^2 + \frac{k_{\text{B}}T}{m_{\text{Rb}}}t^2}, \quad (2.45)$$

where $D \approx 1 \text{ mm}$ is the initial diameter of the atomic cloud in the MOT and m_{Rb} is the mass of a ^{85}Rb atom. According to this expression, the atomic cloud expands during the time of flight to the resonator to a diameter of about 6 mm . Assuming, that all atoms are transferred from the MOT to the moving molasses, the maximum cloud density at the position of the resonator amounts to $4.4 \times 10^8 \text{ atoms/cm}^3$.

2.5.2 Real-time atom detection

Due to the probabilistic coupling of single atoms to the resonator mode within the detection window, we need to detect the presence of an atom in real time. For this, we exploit that – under properly chosen conditions – the resonant atom–resonator interaction leads to a significant transmission increase of the detection light through the coupling fiber, to which the atom-trigger FPGA system can react.

We send the resonant detection light through the coupling fiber 1 and monitor the transmitted power on the SPCMs in Port 2, as depicted in Fig. 2.11 and again sketched in Fig. 2.15 a). The quasi-linear polarization of the detection light is chosen to be orthogonal to the resonator surface, such that it excites a TM-polarized resonator mode. In this case, the evanescent field of the resonator is almost perfectly circularly polarized (cf. Sec. 2.2.4). For the quantization axis pointing along the z -axis, the evanescent field polarization, thus, almost fully coincides with the σ^+ -eigenpolarization of the atom. When an atom now falls through the resonator mode, the detection light predominantly drives $\Delta m = +1$ -transitions between the Zeeman sub-levels and, thus, the atomic population is optically pumped into the outermost $F = 3, m_F = +3$ Zeeman state, see Fig. 2.15 b). This process takes up to $\sim 2 \mu\text{s}$ [60] and, subsequently, the atom is predominantly driven on the closed cycling transition. Hence, the atom now effectively acts like a two-level system interacting with a single resonator mode – the ideal CQED situation, as theoretically described in Sec. 2.3. As a consequence, a vacuum Rabi splitting occurs in the excitation spectrum of the coupled atom–resonator system, as plotted in Fig. 2.7 b). This means, that the transmission through the coupling fiber strongly depends on the presence of an atom in the resonator mode. In order to obtain optimal contrast between the transmission in

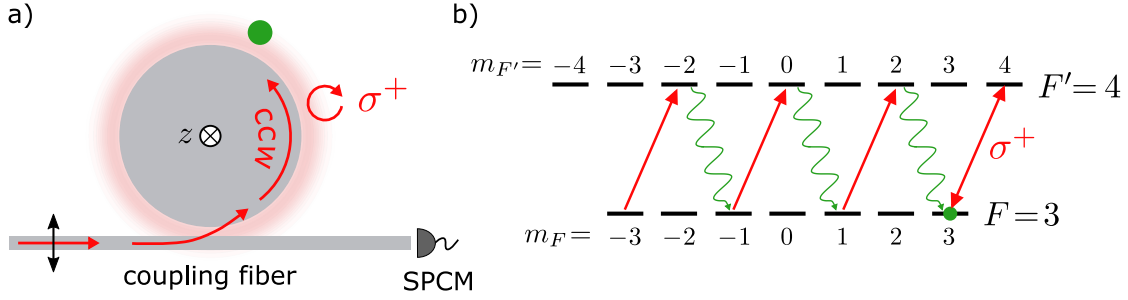


Figure 2.15: a) Illustration of the excitation of the counter-clockwise propagating TM-polarized resonator mode. b) When a ^{85}Rb atom – illustrated in a) as green dot and assumed to be in the $F = 3$ ground state of the D_2 line – enters the evanescent field of the resonator mode, the atomic population is optically pumped in the outermost Zeeman state, $m_F = 3$, from where it can cycle only between the $m_F = 3$ and the $m_{F'} = 4$ Zeeman states. The complicated energy level structure is, thus, effectively reduced to a two-level system.

absence and presence of an atom, respectively, the detection light is chosen to be resonant with the atom and the resonator ($\Delta = 0$). Ideally, the transmission should be zero in absence of an atom (gray line in Fig. 2.7 b)). This is achieved by operating the empty resonator in the regime of critical coupling (cf. Sec. 2.2.5). In practice, we typically have a residual transmission of 1-2 %. When an atom couples to the resonator mode, this transmission increases to ~ 70 % and the transmitted photons are registered by the SPCMs with a quantum efficiency of about 60 %. Then, the SPCMs forward the corresponding output pulses to the atom-trigger FPGA, where they are processed as described in the following.

Atom-trigger FPGA

The atom detection and control system is illustrated in Fig. 2.16 a). The *atom-trigger FPGA*¹⁷ (AT-FPGA) has eight digital channels, which can be programmed either as input or output channels. During the detection window, the FPGA receives the photon clicks from the SPCMs on two inputs and decides whether an atom is strongly coupled to the resonator, depending on the photon count rate. To make this decision, the FPGA continuously counts the photons within a running time window of length $\Delta t_{\text{trig}} = 1.28 \mu\text{s}$. If the number of detected photons reaches a preset threshold value $n \geq n_{\text{thr}}$ within this time, the FPGA decides that an atom is coupled to the resonator. In this case, it sends trigger signals via two outputs to the MZ modulators to run a pre-programmed pulse sequence of the detection and probe beams, which is shown in Fig. 2.16 b) and will be described below. A detailed description of the programming of the atom-trigger FPGA can be found in [59, 112].

The trigger threshold value n_{thr} is chosen such, that the number of detected atoms per cycle is maximized, while ensuring a low probability for false detection events. Such false events can occur, when the transmission through the coupling fiber increases for other reasons than a

¹⁷XEM3010, OpalKelly; Field programmable gate arrays are programmable fast logic circuits. Our FPGA operates with a clock frequency of 100 MHz.

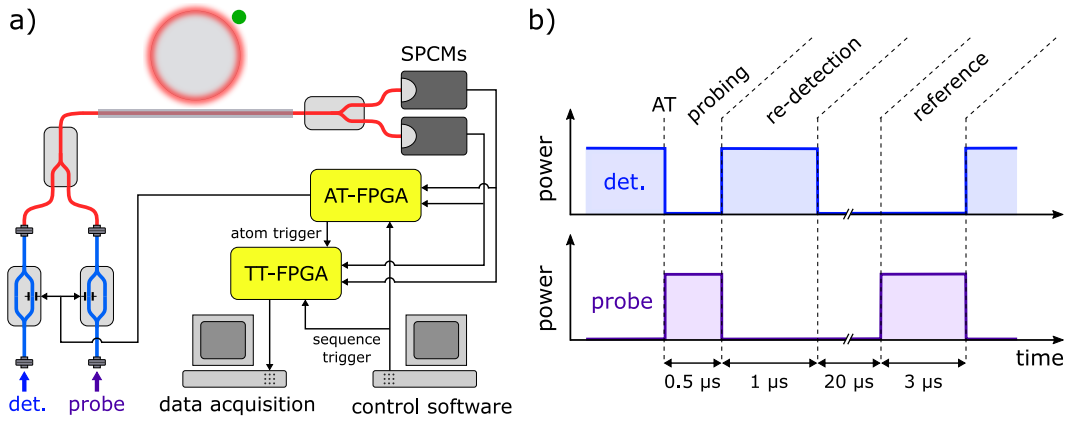


Figure 2.16: a) Simplified scheme of the setup for the real-time atom detection and data acquisition. At the start of each detection window, the control software sends a sequence trigger to the atom-trigger (AT) FPGA to initiate counting of the photon clicks coming in from the SPCMs. When a single atom enters the resonator mode, the concomitant transmission increase of the detection light through the coupling fiber is registered by the SPCMs, which transfer all photon clicks to both FPGAs. When the atom-trigger FPGA evaluates the trigger criterion “ n_{thr} photons in Δt_{trig} ” to be true, it initiates the pulse sequence of the detection and the probe light depicted in panel (b). Both the sequence trigger and the atom trigger are sent to the time-tagger (TT) FPGA, to enable data sorting after the measurement. b) Switching sequence of the detection and the probe light after the detection of an atom (AT). The re-detection pulse allows one to post-select atom transit events, that couple to the resonator mode through the full probing window. The reference pulse is sent much later than the interaction time and, thus, serves to determine the transmission in absence of the atom for reference. Figure adapted from [65].

strongly coupled atom. This can be, e.g., a drift of the resonance frequency of the resonator, as the latter is not locked during the detection window, or a spatial drift of the fiber that changes the fiber–resonator distance. In the experiment, we set the trigger threshold typically to $n_{\text{thr}} = 6$.

Atom interrogation sequence

When the atom-trigger FPGA detects an atom coupling event, it initiates the typical pulse sequence of the detection and probe beams depicted in Fig. 2.16 b). First, the detection beam is switched off and the probe beam is switched on. The total delay between the time when the atom-trigger FPGA receives the n_{thr} -th photon and the time when the probe light reaches the resonator amounts to about 180 ns [60]. The atom is probed for about $0.5 \mu\text{s}$. During this time, the atom is transiting through the resonator mode, i.e. the atom–resonator coupling strength varies with time. Some atoms come very close to the resonator surface or even crash into the resonator. In this case, interactions with the surface shift the atomic levels, such that the atom is effectively lost. For this reason, a re-detection pulse is sent through the coupling fiber for $1 \mu\text{s}$. Evaluating the transmission in this window, allows to decide whether an atom strongly coupled to the resonator mode during the full probing window. After a time that is long compared to the

atom transit time, e.g. $20 \mu\text{s}$, a resonant reference probe pulse is sent, which allows to determine the transmitted counts in absence of the atom.

2.6 Data acquisition and analysis

The experimental cycle is repeated many times, leading to hundreds of thousands of atom coupling events. During the detection window in each cycle, the SPCMs continuously detect the transmitted photons of both the detection and the probe light. The temporal distribution of the photon clicks contains information about the atom–resonator interaction. In order to be able to post-analyse the atom–resonator interaction, each photon is assigned a time stamp. This task is performed by a second FPGA, as described in the following.

2.6.1 Time-tagger FPGA and data selection

The *time-tagger FPGA*¹⁸ (TT-FPGA) receives at its inputs three different signals: a trigger signal from the control software at every new experimental cycle (*sequence trigger*), a trigger signal from the atom-trigger FPGA whenever an atom is detected (*atom trigger*), as well as all photon clicks registered by the transmission SPCMs, see Fig. 2.16 a). The time-tagger FPGA gives time tags to both the atom trigger events and the photons clicks relative to the time of the sequence trigger with a resolution of 128 ps. Such a fine resolution is achieved by making use of internal hardware delays on the chip [60]. Then, the FPGA sends all the data to a computer. However, only the photon clicks within a certain time window around the time of an atom trigger event potentially contain interesting information. Hence, to limit the amount of data, all other clicks are discarded. This is done on-the-fly by a computer program, which sorts out the photon clicks within a *photon recording window* before and after an atom trigger event and saves the data in a file. We typically record the photon clicks within $\pm 25 \mu\text{s}$ around an atom trigger event. However, for the experiments with trapped atoms (cf. Ch. 4) a longer photon recording window and a lower time tagging resolution was used.

2.6.2 Experimental results

Atom arrival histogram

Using the time tags provided by the time-tagger FPGA, we can histogram the arrival times of atoms within the detection window, as shown by the solid line in Fig. 2.17 a). We observe two maxima at about 25 ms and 70 ms after the sequence trigger, corresponding to velocity classes of atoms that couple to the resonator on their way up and down, respectively. The dashed line corresponds to the histogram of false detection events, when the atomic cloud is not launched toward the resonator. Ideally, in this case, one would expect no trigger events at all. However, during the detection window the resonator is not locked, see Fig. 2.13. As a consequence, the resonance frequency of the resonator slightly drifts during the 120 ms-long window. Due to this effect, we set the frequency of the stabilization light such that the average transmission

¹⁸XEM3005, OpalKelly

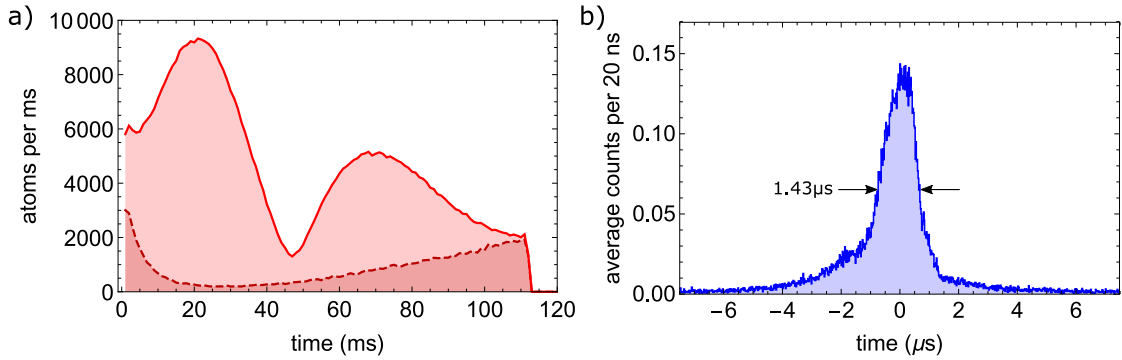


Figure 2.17: a) Histogram of the arrival times of atom trigger events. The solid (dashed) line shows the result for the case that an atomic cloud was launched (was not launched). b) Transmission of the detection light around the arrival time of a trigger event, averaged over ~ 3500 events, originally published in Ref. [60]. Here, the time axis of each single-atom trace has been aligned such that the time $t = 0$ lies at the mean value of the photon distribution.

is minimized. The difference between the areas below the solid and the dashed curve, thus, corresponds to the total number of genuine atom detection events.

Atom transits

We can also plot the transmission of the detection light averaged over ~ 3500 atom transit events, as shown in Fig. 2.17 b). Note, that for this measurement – in contrast to the sequence shown in Fig. 2.16 b) – the detection light is kept on after the detection of an atom and we do not switch to the probe laser. Accordingly, no post-selection is being applied to filter only strongly coupled atoms. Furthermore, the time axes of all the photon traces corresponding to atom transit events have been aligned such that the time $t = 0$ always lies at the mean value of the photon distribution.

We observe a peak with a FWHM of $1.43 \mu\text{s}$, corresponding to the average interaction time between a single atom and the resonator mode. Furthermore, the peak exhibits an asymmetry: the transmission slowly increases for negative times, while there is a steep slope for positive times. This confirms that for a certain fraction of atoms the atom–resonator interaction abruptly ends, as the atoms come too close to the resonator.

Spectroscopy of the atom–resonator system

My predecessors on this experiment performed spectroscopy of the coupled atom–resonator system, using the probing sequence in Fig. 2.16 b), see also Ref. [46, 60]. This has been done both for a TM- and a TE-polarized bottle mode. Here, I want to show the result obtained for the TM-polarized mode described in Sec. 2.4.6, which we will later compare to the same measurement performed with trapped atoms instead of transiting atoms.

In the measurement, a magnetic bias field of 4.5 G was applied along the resonator axis, which defines the quantization axis such that the evanescent field polarization has an over-

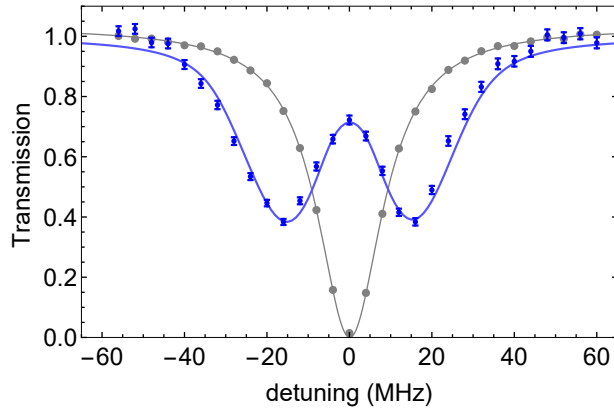


Figure 2.18: Normalized transmission spectrum of the coupled atom-resonator system. The blue data points show the spectrum in presence of coupled atoms, revealing a vacuum Rabi splitting, and the gray data points show the empty resonator spectrum. Both the data and the fit results were originally published in Ref. [46].

lap with the atomic σ^+ -eigenpolarization of $\sim 97\%$ (cf. Sec. 2.2.4). Accordingly, the resonator frequency has to be adjusted so as to be on resonance with the $(F = 3, m_F = 3) \rightarrow (F' = 4, m_{F'} = 4)$ cycling transition. The fiber-resonator distance is set to critical coupling for the empty resonator. The photon flux of the detection light was 1.2×10^7 photons/s, corresponding to an intra-resonator photon number of 0.19. To perform spectroscopy, the resonator-probe detuning $\Delta_{\text{rp}}/2\pi$ is scanned step-wise over a range of ± 60 MHz.

A second trigger criterion was applied to the photon counts within the $1 \mu\text{s}$ -long re-detection window, in order to filter strongly coupled atom events. For each setting of the detuning, the transmission within the probing window was analysed for ~ 1000 atom coupling events. The result is shown in Fig. 2.18. The blue data points show the transmission spectrum in presence of the coupled atoms and the gray data points show the empty resonator spectrum. In the former case, the data reveals a vacuum Rabi splitting with a transmission increase on resonance of about 70%. The solid blue line is a fit to the data based on a theoretical model, which takes into account the polarization properties of the evanescent field and, consequently, the full Zeeman sub-structure of the $F = 3 \rightarrow F' = 4$ atomic transition [60]. The model is used to calculate theoretical transmission spectra for different coupling strengths. As the atoms are free falling through the resonator mode, the coupling strengths vary both in time and between different atom coupling events. Realistic coupling strengths $g/2\pi$ are assumed to range from 7.5 MHz to 30 MHz. Then, the individual spectra are averaged using weighting factors corresponding to a normal distribution of the coupling strengths. Finally, this average transmission spectrum is fitted to the data with the mean \bar{g} and the standard deviation σ_g of the normal distribution as free parameters. The fit yields $\bar{g}/2\pi = 17$ MHz and $\sigma_g/2\pi = 6$ MHz. Considering the spatial dependence of the coupling strength for the estimated bottle mode given in Fig. 2.12, this corresponds to a mean distance of the atoms from the resonator surface of ~ 125 nm.

Retroreflected optical tweezer trap

We have seen in the last chapter, that the probabilistic coupling of single atoms to the resonator mode is accompanied by short atom–light interaction times and time-varying coupling strengths. Both effects severely limit the performance of applications with WGM resonators and hamper future developments, e.g. involving quantum protocols for optical quantum information processing. Therefore, trapping single atoms close to WGM resonators has been a long-standing goal.

In the history of neutral atom trapping, different techniques have been developed on the basis of different physical mechanisms [113]: radiation pressure traps based on near-resonant atom–light interaction [102], magnetic traps based on state-dependent forces on the magnetic dipole moment in an inhomogeneous field [105, 114] and optical dipole traps [19, 113], which rely on the electric dipole interaction with far-detuned light. The latter have become a key element in numerous atomic physics and quantum optics experiments that require localization of single atoms. Two frequently used ways to realize a dipole trapping potential for single atoms are optical tweezers and optical standing waves. Optical tweezers use a tightly focused Gaussian beam, where an atom is trapped at the intensity maximum [115, 116]. Standing waves on the other hand yield periodic intensity modulations which generate one-dimensional (1D) optical lattices [117], thereby providing stronger confinement in axial direction. In the context of single-atom cavity quantum electrodynamics with Fabry-Pérot type microresonators, most commonly, standing-wave dipole traps are used. Here, atoms are either trapped in the field of a cavity mode [23] or in a cavity-independent trap [26, 118–120].

When coupling atoms to micro- or nanophotonic structures, as e.g. WGM resonators, a challenge is imposed by the fact that the atoms have to be trapped very close (~ 100 nm) to a dielectric surface in order to couple strongly to the optical mode confined in that structure. In an early proposal for WGM resonators, the idea was to employ the evanescent field of WGMs itself for two-color dipole trapping of atoms [121, 122]. A related approach is to trap single atoms close to a nanofiber in a two-color dipole trap [123, 124], and to bring this fiber close to the resonator. However, both ideas are technically very challenging. A more promising way to trap a single atom close to a nanoscale optical cavity has been demonstrated by Thompson et al. [42].

Here, a standing-wave optical dipole trap for a single atom is created by retroreflecting an optical tweezer beam from the surface of a nanoscale photonic crystal waveguide. By now, this approach has also been adopted into other systems, like, e.g., nanofiber-based cavities [45] and on-chip waveguides and microring resonators [125, 126]. We apply this technique for trapping a single ^{85}Rb atom close to our bottle resonator.

In this chapter, we will first provide the theoretical background of optical dipole traps and give a qualitative overview of the above mentioned options to implement a dipole trap close to a WGM resonator. Then, we describe a formalism that allows one to calculate the energy shift of a multilevel atom in a light field with arbitrary polarization [127]. Using this formalism, we calculate the trap light-induced energy shift of both the ground and the excited state of the ^{85}Rb atom for our experimental trap parameters. Based on these calculations, we then model the standing-wave dipole potential of the retroreflected optical tweezer and determine the effect of the trap light on the atomic transition frequency. Furthermore, the experimental implementation of the trapping potential will be presented.

3.1 Optical dipole potentials

Optical dipole traps rely on the interaction of an atom with far-detuned laser light. First, we want to give a classical explanation, following Ref. [113]. Here, both the light field and the atom are described classically. The electric field of the laser is

$$\mathbf{E} = \mathcal{E}e^{-i\omega t} + c.c., \quad (3.1)$$

where ω is the angular frequency of the light and $\mathcal{E} = \mathcal{E}\mathbf{u}$ is the positive-frequency electric field, with \mathcal{E} and \mathbf{u} being the field amplitude and the polarization vector, respectively. The electric field \mathbf{E} induces an electric dipole moment $\mathbf{d} = d\mathbf{u}e^{-i\omega t} + c.c.$ in the atom, which oscillates at the driving frequency ω and whose amplitude is given by

$$d = \alpha\mathcal{E}. \quad (3.2)$$

The proportionality factor α is the complex polarizability of the atom. The interaction energy of this dipole in the electric field

$$U \propto -\langle \mathbf{d} \cdot \mathbf{E} \rangle \propto -\text{Re}(\alpha)|\mathcal{E}|^2 \propto -\text{Re}(\alpha)I \quad (3.3)$$

is proportional to the real part of the polarizability, which describes the component of the dipole oscillation that is in phase with the electric field. Here, $\langle \cdot \rangle$ denotes the time average over the fast oscillation. The $|\mathcal{E}|^2$ -dependence in Eq. (3.3) is the reason why the literature often refers to this atom–light interaction as *quadratic Stark effect*. For oscillating electric fields, such as light fields it is called *AC Stark effect*. We will see in the following sections that this interaction manifests itself in a shift of the atomic energy levels, the so-called *AC Stark shift* or *light shift*. I will stick to the latter term throughout this thesis.

The imaginary part of the polarizability, which describes the out-of-phase component of the dipole oscillation, is related to the scattering rate of the atom

$$\Gamma_{\text{sc}} \propto -\text{Im}(\alpha)I. \quad (3.4)$$

As visible from Eq. (3.3) and (3.4), key to finding the interaction energy and the scattering rate is to know the atomic polarizability. For a classical damped oscillator one can derive the ω -dependent polarizability as [113]

$$\alpha(\omega) = 6\pi\epsilon_0 c^3 \frac{\Gamma/\omega_0^2}{\omega_0^2 - \omega^2 - i(\omega^3/\omega_0^2)\Gamma}. \quad (3.5)$$

Here, ϵ_0 is the vacuum permittivity, c is the speed of light, ω_0 is the eigenfrequency of the dipole oscillation and Γ the energy damping rate due to the dipole's radiation. It turns out, however, that the same result can be obtained with a semiclassical approach, where the atom is described as a two-level quantum emitter interacting with a classical light field. Then, in Eq. (3.5), ω_0 denotes the atomic transition frequency and Γ the damping rate associated with the spontaneous decay rate of the excited level.

Using the above expression for the polarizability, the interaction energy and the scattering rate can be derived for the case of large detuning and negligible saturation as [113]

$$U_{\text{dip}}(\mathbf{r}) = -\frac{3\pi c^2}{2\omega_0^3} \left(\frac{\Gamma}{\omega_0 - \omega} + \frac{\Gamma}{\omega_0 + \omega} \right) I(\mathbf{r}), \quad (3.6)$$

$$\Gamma_{\text{sc}}(\mathbf{r}) = \frac{3\pi c^2}{2\hbar\omega_0^3} \left(\frac{\omega}{\omega_0} \right)^3 \left(\frac{\Gamma}{\omega_0 - \omega} + \frac{\Gamma}{\omega_0 + \omega} \right)^2 I(\mathbf{r}). \quad (3.7)$$

In the case of $\Delta = \omega - \omega_0 \ll \omega_0$, the so-called rotating-wave approximation [68, 128] can be applied, which neglects the counter-rotating terms resonant at $\omega = -\omega_0$. Then the two previous expressions simplify to

$$U_{\text{dip}}(\mathbf{r}) = \frac{3\pi c^2}{2\omega_0^3} \frac{\Gamma}{\Delta} I(\mathbf{r}), \quad (3.8)$$

$$\Gamma_{\text{sc}}(\mathbf{r}) = \frac{3\pi c^2}{2\hbar\omega_0^3} \left(\frac{\Gamma}{\Delta} \right)^2 I(\mathbf{r}). \quad (3.9)$$

These formulas describe the basic physics of optical dipole trapping in a compact form. The expression in Eq. (3.8) can also be derived by second-order time-independent perturbation theory, where it comes out as the light-induced energy shift of the ground state of a two-level atom [113]. As this shift is proportional to the light intensity, an appropriately shaped intensity distribution $I(\mathbf{r})$ enables to form a trapping potential for a neutral atom. Here, the sign of the atom–light detuning, Δ , matters. When $\Delta < 0$, i.e. the light is red-detuned with respect to the atomic transition, the potential energy decreases with increasing intensity. In other words, potential minima, which serve for atom trapping, are formed at positions of maximum intensity. In contrast, if $\Delta > 0$, atoms can be trapped in regions of minimum intensity, while they are repelled from higher-intensity regions. Furthermore, we can see in the above expressions that the potential depth scales with $1/\Delta$, while the scattering rate scales with $1/\Delta^2$. That is, for an increased detuning Δ , the scattering is more strongly reduced than the potential depth.

The dipole potential and the scattering rate can be calculated more accurately than with Eqs. (3.8) and (3.9) by taking the atomic fine-structure splitting into account. For linearly polarized light and under the condition that the detuning Δ is much larger than the hyperfine splitting

of the excited state, the corresponding expressions are [113]

$$U_{\text{dip}}(\mathbf{r}) = \frac{\pi c^2 \Gamma}{2\omega_0^3} \left(\frac{2}{\Delta_{2,F}} + \frac{1}{\Delta_{1,F}} \right) I(\mathbf{r}), \quad (3.10)$$

$$\Gamma_{\text{sc}}(\mathbf{r}) = \frac{\pi c^2 \Gamma^2}{2\hbar\omega_0^3} \left(\frac{2}{\Delta_{2,F}^2} + \frac{1}{\Delta_{1,F}^2} \right) I(\mathbf{r}), \quad (3.11)$$

where $\Delta_{2,F}$ and $\Delta_{1,F}$ are the detunings of the trap light with respect to the D_2 and D_1 transition of an alkali atom, starting from the $^2S_{1/2}, F$ ground state. Here, the line strength factor of 2/3 for the D_2 line and 1/3 for the D_1 line are taken into account [113].

3.2 Options for an optical dipole trap close to a WGM resonator

We have seen in Ch. 2, that atoms have to be brought as close as ~ 100 nm to the resonator surface in order to efficiently couple to the evanescent field of a WGM. Trapping an atom at such a small distance to a dielectric surface is experimentally challenging. In the following, we will explain different approaches for creating an optical dipole potential close to a dielectric surface and discuss which are most easy to implement for WGM resonators.

3.2.1 Two-color evanescent field traps

Creating a trap for neutral atoms based on the dipole forces exerted by evanescent fields of a dielectric structure was first proposed in Ref. [129]. When a light field experiences total internal reflection at a dielectric–vacuum interface, an exponentially decaying field penetrates into the vacuum, which is called *evanescent field*, see e.g. Secs. 2.2.3 and 2.2.4. Considering Eq. (3.8), this exponentially decaying field will exert a force that pulls an atomic dipole either toward (attractive) or away (repulsive) from the region with higher light intensity, depending on the detuning, Δ , of the light field with respect to the atomic transition.

Now, the idea for generating a trap potential is to superimpose the evanescent field of a red-detuned and a blue-detuned light field [130]. The decay length of the evanescent field depends on the wavelength of the incident light, λ , as $\lambda/2\pi/\sqrt{n_1^2 - 1}$ (for grazing incidence, i.e. for an incidence angle of $\Theta = 90^\circ$), where n_1 is the refractive index of the dielectric medium. Thus, the blue-detuned evanescent field decays faster than the red-detuned field. In this way, the repulsive potential associated with the blue-detuned field dominates at shorter distances (blue curve in Fig. 3.1 a)), whereas the attractive force associated with the red-detuned field dominates at larger distances (red curve in Fig. 3.1 a)), thereby giving rise to a total potential (black curve in Fig. 3.1 a)), which can be used for trapping an atom close to the dielectric surface. An additional attraction toward the surface is caused by the van der Waals force [131], which is significant only at very short distance to the surface. The blue-detuned evanescent field can counteract both attractive forces, when the powers of the light fields are tuned appropriately with respect to each other.

In the following, we will consider two possible ways to make use of the described technique in order to yield a single atom trap close to a WGM resonator, and we will qualitatively discuss the requirements and challenges that come with each approach.

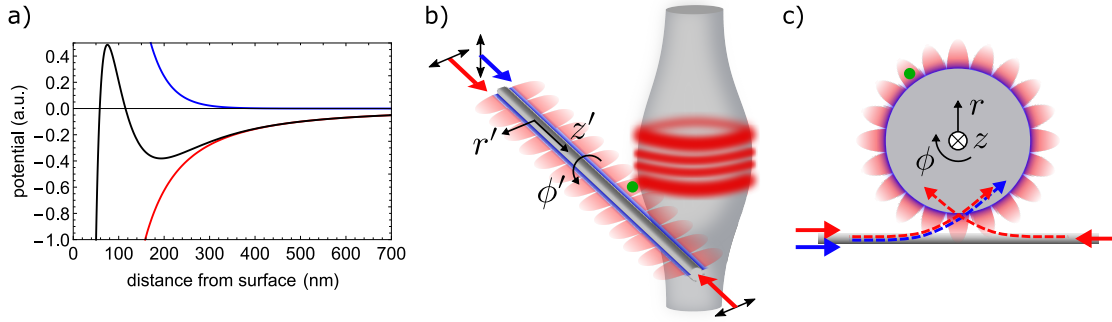


Figure 3.1: a) Principle of a two-color evanescent field trap. The black curve shows the total potential as a function of the distance from a dielectric surface, resulting from a two-color evanescent field plus the van der Waals surface potential. b) Illustration of a nanofiber two-color dipole trap based on the principle in (a), which is interfaced with a bottle resonator. c) Illustration of a two-color dipole trap based on the principle in (a) using the evanescent fields of a WGM resonator.

Approach 1: Nanofiber trap close to a WGM resonator

The first option is to trap an atom in a two-color evanescent field trap along an optical nanofiber, which has been proposed in Ref. [123], and then bring the nanofiber with the trapped atom close to a WGM resonator. The idea is illustrated in Fig. 3.1 b).

The nanofiber two-color dipole trap itself was first experimentally realized in our group, namely for neutral cesium atoms [132]. By now it is well established also in other research groups for atomic physics/quantum optics experiments with Cs atoms [133–135] and with ^{87}Rb atoms [136]. With the evanescent field technique described above, a confining potential in radial (r') direction of the nanofiber can be formed. The shape of the potential in azimuthal (ϕ') direction is determined by the polarization of the light fields. When the red- and blue-detuned light fields are quasi-circularly polarized, the potential has the form of a cylinder around the nanofiber. In contrast, if the two light fields have orthogonal linear polarizations, this yields trapping potentials in form of two parallel lines in the transverse plane of the nanofiber. We are considering the latter case, as it provides additional azimuthal confinement of the atoms. Depending on the exact parameters as, e.g., the diameter of the nanofiber and the used wavelengths, one can typically trap atoms at a radial distance from the fiber surface of about 200 nm. Three-dimensional (3D) confinement is achieved by sending an additional counter-propagating red-detuned field. In this way, the red-detuned fields form a standing wave, resulting in two 1D lattices on each side of the nanofiber, as shown in Fig. 3.1 b).

Typically, atoms are loaded and cooled into such a nanofiber trap from a cold atomic cloud in a MOT surrounding the fiber [132]. Due to the effect of collisional blockade [137] at most one atom is trapped per lattice site. When the nanofiber trap is supposed to be operated close to a WGM resonator, the loading of atoms into the nanofiber trap would have to be performed sufficiently far away from the resonator, both to grant optical access to the cooling beams and to

not degrade the resonator's quality factor. A single atom trapped in one of the nanofiber lattice sites could then be transported into the resonator mode, e.g., via the optical conveyor belt technique [138], i.e. moving the standing wave along the nanofiber by detuning the two red-detuned trapping fields with respect to each other.

The coupling of nanofiber-trapped atoms to a WGM resonator has so far not been experimentally demonstrated, although, at first glance, it might seem rather straightforward. A theoretical analysis of this scenario using nanofiber-trapped Cs atoms and a microtoroidal resonator has been performed in Ref. [139]. The first requirement for a successful implementation is that the scheme should yield a sufficiently large atom–resonator coupling strength. Considering the distance of the trapped atoms to the nanofiber of about 200 – 300 nm, the nanofiber–resonator distance should, therefore, not be larger than ~ 300 nm. For our bottle resonator, at such a small distance the fiber is already in the over-coupled regime (cf. Sec. 2.2.5), as it is critically coupled at a distance of about 600–700 nm [59, 70].

As a second requirement, the nanofiber should ideally only act as a "holder" for single atoms. This means, that the full intensity of the trapping fields should stay in the fiber, i.e. not couple into the resonator, in order to yield the desired trap potential. One way to achieve this would be to move the fiber sufficiently far away from the resonator, which, however, compromises the fulfillment of the first requirement. Thus, to prevent the trapping light fields from coupling into the resonator one has to detune their frequencies from resonances of the resonator. Let us assume that we can afford an intra-resonator intensity that amounts to no more than 1% of the intensity in the nanofiber ($I_{\text{res}} \leq 0.01 I_{\text{fiber}}$). At the point of critical fiber–resonator coupling and on resonance, i.e. for a light–resonator detuning $\Delta_{\text{lr}} = 0$, the full power of the trapping field, P_{fiber} , would couple into the resonator. For $\Delta_{\text{lr}} \neq 0$, the in-coupled power is given by $P_{\text{coupled}} \approx (\kappa/\Delta_{\text{lr}})^2 P_{\text{fiber}}$ with the total resonator field decay rate κ . The in-coupled power is, however, enhanced by the resonator to an intra-resonator power of

$$P_{\text{res}} = \frac{\mathcal{F}}{\pi} P_{\text{coupled}} \approx \left(\frac{\mathcal{F}}{\pi}\right) \left(\frac{\kappa}{\Delta_{\text{lr}}}\right)^2 P_{\text{fiber}}, \quad (3.12)$$

where \mathcal{F} is the finesse of the resonator. For typical WGM resonators we have a finesse of $\mathcal{F} \approx 10^5$ and a total resonator field decay rate of $\kappa/2\pi = 10$ MHz. In order to fulfill the 1% starting condition above, the detuning to all resonator modes would have to be $\Delta_{\text{lr}} \gtrsim 20$ GHz. This is much larger than the typical measured frequency separation between resonator modes of ~ 1 GHz in our system, i.e. it is practically impossible to prevent trapping light to couple into the resonator.

Nevertheless, it might be possible to find a configuration of the frequencies and powers of the trapping fields that leads to a stable trapping potential, when taking into account a non-zero intra-resonator intensity. However, if a single atom is supposed to be moved toward the resonator via the optical conveyor belt technique, as suggested above, a stable trap potential configuration needs to be achieved not only at the position of the smallest fiber–resonator distance, but for all positions along the nanofiber. Moreover, due to the exponential dependence of the evanescent field and, therefore, of the fiber–resonator coupling on the fiber–resonator distance, even small changes of the latter, e.g. due to drifts of the nanofiber transverse or longitudinal with respect to the resonator, are expected to strongly modify the potential.

Approach 2: Resonator field trap

The two-color trapping scheme can in principle also be implemented using the evanescent fields of WGMs, as illustrated in Fig. 3.1 c). In fact, this scheme was originally envisioned for coupling neutral atoms to WGM resonators [121, 122]. A more recent theoretical analysis has been performed for microtoroids in Refs. [139, 140], but to date this trapping scheme has not been experimentally realized.

In this scheme, in addition to the radial (r) confinement of atoms, confinement along the z -axis of the resonator is required. The latter depends on the choice of axial modes (cf. Sec. 2.2.3) for the red- and blue-detuned trapping fields. If only fundamental axial modes are used, no proper z -confinement is obtained, for most types of WGM resonators. While in *microdisks* the axial width of the resonator mode only depends on the disk height [141], in *microspheres*, *microtoroids* and *bottle microresonators* the width increases with increasing wavelength. Thus, for the latter three resonator types, the attractive potential will be broader than the repulsive one, if only fundamental axial modes are used. As a result, the atom can escape to both sides in axial direction. To circumvent this problem, one option is to choose a higher-order red-detuned mode, as suggested in Ref. [139]. Another possibility is to use two blue-detuned resonator modes, namely a fundamental axial mode and an additional two-ring mode, where the latter provides a repulsive potential along the resonator axis in both directions.

In this way, one obtains a trap potential in form of a ring (or *atom gallery* [121]), in which the atom orbits around the resonator. If, however, the atom is supposed to be localized azimuthally (ϕ), this can be achieved equivalently to the axial (z') confinement in the nanofiber trap by sending a second red-detuned light field, which circulates in the resonator in counter-propagating direction.

The two-color dipole trap potentials depend on a stable balance of the red- and blue-detuned fields: small changes in the trap intensities will result in strong changes in the trap potential. Achieving this stable balance is particularly challenging in the case of the resonator field trap. First, all trapping light fields are coupled into the resonator via a single nanofiber. Spatial drifts of the fiber will, thus, change the fiber–resonator coupling rates for the different modes in different ways and, thereby, modify the intra-resonator intensities of the trapping fields relative to each other. Second, the trapping fields have to be resonant with the chosen resonator modes. Consequently, changes in the resonator mode frequencies, e.g. due to a temperature change, will again lead to changing ratios of the trap light intensities.

3.2.2 Retroreflected optical tweezer trap

An alternative way to optically trap a single atom close to a dielectric surface is a retroreflected optical tweezer trap. This scheme has been first experimentally demonstrated in Ref. [42] for a nanoscale photonic crystal waveguide. The implementation of this idea for our bottle resonator system is illustrated in Fig. 3.2. A laser beam with a wavelength λ_{trap} is tightly focused onto the bottle resonator and retroreflected from its surface. Interference between the incident and the reflected beam forms a standing-wave pattern with a periodicity of $\sim \lambda_{\text{trap}}/2$ along the x -axis, which is orthogonal to the resonator axis (z -axis). The intensity pattern of the standing wave exhibits an antinode closest to the resonator surface at a distance of $\sim \lambda_{\text{trap}}/4$. To trap an atom

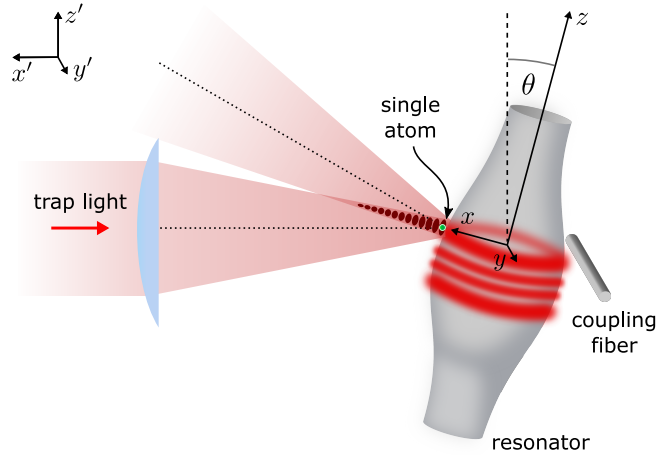


Figure 3.2: Retroreflected optical tweezer trap. A red-detuned tightly focused laser beam is retroreflected from the surface of the bottle resonator. The interference between the incident and the reflected beam forms a standing-wave pattern along the x -axis. A single atom is trapped in the first potential minimum at a distance of $\sim \lambda_{\text{trap}}/4$. The resonator-centered coordinate system (x, y, z) and a laboratory-centered coordinate system (x', y', z') are defined as indicated.

at this intensity maximum, the trap light field needs to be red-detuned with respect to the atomic transition.

The bottle resonator is made from silica glass and, therefore, reflects about 4 % of the incident light intensity. As a consequence, the standing wave is only partially modulated with a modulation contrast of $1 - I_{\text{min}}/I_{\text{max}}$. Due to the tilt of the resonator fiber in our experiment (cf. Sec. 2.4), the incoming beam hits the resonator surface at an angle of about 17° . This has the advantage that it prevents unwanted interference between the incident beam and its reflection from the back-surface of the resonator. In section 3.6, we will model the expected intensity distribution including these experimental details.

We decided to implement this trapping scheme in our system, as it has several advantages compared to the two-color trapping schemes. First of all, only one trapping field is required. Furthermore, the retroreflected trap potential is neither sensitive to drifts of the fiber–resonator distance, nor to drifts of the light frequency or the resonator frequency. In contrast to the case of the nanofiber trap close to the resonator, the location of the trapping site has a fixed distance to the resonator surface and, therefore, the scheme intrinsically offers a more stable atom–light coupling strength. Another advantage is – in particular, compared to the resonator field trap – that there is only one trapping site within the resonator mode, such that one precisely knows the atom’s location¹. This allows one to externally address the atom, e.g., for fluorescence detection, which we will see in Sec. 4.5.

¹Atoms trapped in the other standing-wave antinodes have a distance to the resonator surface of $\frac{3}{4}\lambda$, $\frac{5}{4}\lambda$, and so on. For these distances, the coupling to the resonator mode is negligibly small and, thus, only atoms in the first antinode can interact with the WGM.

3.3 Design considerations for the optical dipole trap

Our trap potential needs a trap depth in the millikelvin regime to be able to capture free-falling atoms from the cold atomic cloud and to counteract Van der Waals forces [131] exerted by the resonator surface on the atom (cf. Sec. 3.6.2). In accordance with Eq. (3.8), the potential depth is proportional to

$$U_{\text{dip}} \propto \frac{P_{\text{trap}}}{w_0^2 \Delta_{\text{trap}}}, \quad (3.13)$$

where w_0 is the waist radius of the Gaussian trapping beam [66], P_{trap} is the optical power of the trapping light field and Δ_{trap} is the detuning to the $5S_{1/2} \rightarrow 5P_{3/2}$ (D_2) transition of the ^{85}Rb atom. For the beam waist we choose a value of $w_0 \approx 3 \mu\text{m}$. In this case, the focus size is relatively small compared to the resonator diameter and, thus, the build-up of the standing wave is not much affected by the resonator curvature in azimuthal direction. With the waist radius given, the trap depth is determined by the ratio $P_{\text{trap}}/\Delta_{\text{trap}}$. It is advisable to choose a large detuning in order to reduce the atomic scattering rate (cf. Eq.(3.9)) from the trap field and, thus, limit heating of the trapped atom. Additionally, it allows efficient suppression of trap photon background on our SPCMs using band-pass filters. A large detuning also reduces the trap depth, which in principle can be compensated by a larger power. We are, however, limited in the power that we can afford to send onto the bottle resonator: when our trapping beam impinges on the resonator, it slightly heats the resonator material, resulting in an unwanted shift of the resonance frequency (cf. Sec. A.2). As a trade-off, we thus choose a power of $P_{\text{trap}} \approx 20 \text{ mW}$ and a trap wavelength of $\lambda_{\text{trap}} = 783.68 \text{ nm}$, corresponding to a detuning with respect to the Rb D_2 transition ($\lambda_0 = 780.24 \text{ nm}$ [111]) of $\Delta_{\text{trap}} = 2\pi \times 1.68 \text{ THz}$. This choice of parameter values results in a depth of the optical potential created by the partial standing wave of roughly 3 mK.

3.4 Light shift of a multilevel atom in a light field with arbitrary polarization

For a rigorous treatment of the interaction between a classical light field and real atoms, one has to describe the atom as a quantum system with – in general – many energy levels. The formalism described in the following provides a tool to calculate the light shift of a certain fine-structure state $|nJ\rangle$ of an atom interacting with a far-detuned light field of arbitrary polarization [127], as given in Eq. (3.1). Here, n is the principal quantum number and J is the quantum number for the total angular momentum \mathbf{J} of the electron. We will only give the final expressions relevant for the present work, more details can be found in [127].

The formalism is valid for cases where the Stark interaction energy is small compared to the fine structure splitting, such that J remains a good quantum number. The interaction between the atom and the light field is now described by the operator

$$V_{\text{Stark}} = -\mathbf{E} \cdot \mathbf{d}, \quad (3.14)$$

where \mathbf{d} is the operator for the electric dipole of the atom. If the light field is far-detuned one can show that the matrix elements of the Stark operator in the basis of the hyperfine structure

states, $V_{\text{Stark}}^{FMF'M'} = \langle (nJ)FM | V_{\text{Stark}} | (nJ)F'M' \rangle$, can be expressed as

$$\begin{aligned}
 V_{\text{Stark}}^{FMF'M'} &= |\mathcal{E}|^2 \sum_{q=-K, \dots, K}^{K=0,1,2} \alpha_{n,J}^{(K)} \{ \mathbf{u}^* \otimes \mathbf{u} \}_{Kq} \\
 &\quad \times (-1)^{J+I+K+q-M} \sqrt{(2F+1)(2F'+1)} \\
 &\quad \times \begin{pmatrix} F & K & F' \\ M & q & -M' \end{pmatrix} \begin{Bmatrix} F & K & F' \\ J & I & J \end{Bmatrix}. \tag{3.15}
 \end{aligned}$$

Here, F is the quantum number of the total angular momentum $\mathbf{F} = \mathbf{J} + \mathbf{I}$ of the atom and M is the quantum number of the projection F_z of \mathbf{F} onto the quantization axis z . I is the quantum number of the nuclear spin. Note that in Eq. (3.15) the sets of quantum numbers $\{F, M\}$ and $\{F', M'\}$ denote two different levels within the hyperfine manifold of the same fine-structure state $|nJ\rangle$. To indicate the ground state levels and excited state levels, we use the common notation $\{F, m_F\}$ and $\{F', m_{F'}\}$, respectively.

The dynamical polarizability, $\alpha_{n,J}^{(K)}$, of a certain fine-structure state $|nJ\rangle$ in Eq. (3.15) is given by

$$\begin{aligned}
 \alpha_{n,J}^{(K)} &\approx (-1)^{K+J+1} \sqrt{2K+1} \\
 &\quad \times \sum_{n'J'} (-1)^{J'} \begin{Bmatrix} 1 & K & 1 \\ J & J' & J \end{Bmatrix} |\langle n'J' || \mathbf{d} || nJ \rangle|^2 \\
 &\quad \times \frac{1}{\hbar} \text{Re} \left(\frac{1}{\omega_{n'J'nJ} - \omega} + \frac{(-1)^K}{\omega_{n'J'nJ} + \omega} \right). \tag{3.16}
 \end{aligned}$$

Here and also in Eq. (3.15), $K = 0, 1, 2$ indicates the reduced dynamical scalar, vector and tensor polarizability of an atom in the fine-structure level $|nJ\rangle$, respectively. Furthermore, $\omega_{n'J'nJ}$ is the angular frequency of the $|nJ\rangle \rightarrow |n'J'\rangle$ transition, and ω is the angular frequency of the light field according to Eq. (3.1). In both Eqs. (3.15) and (3.16) we used the notations

$\begin{pmatrix} j_1 & j_2 & j \\ m_1 & m_2 & m \end{pmatrix}$ and $\begin{Bmatrix} j_1 & j_2 & j_3 \\ j_4 & j_5 & j_6 \end{Bmatrix}$ for the Wigner 3-j and 6-j symbols, respectively.

Finally, the compound tensor components $\{ \mathbf{u}^* \otimes \mathbf{u} \}_{Kq}$ in Eq. (3.15) are defined as

$$\begin{aligned}
 \{ \mathbf{u}^* \otimes \mathbf{u} \}_{Kq} &= \sum_{\mu, \mu'=0, \pm 1} (-1)^{q+\mu'} u_\mu u_{-\mu'}^* \\
 &\quad \times \sqrt{2K+1} \begin{pmatrix} 1 & K & 1 \\ \mu & -q & \mu' \end{pmatrix}, \tag{3.17}
 \end{aligned}$$

with the spherical tensor components of the polarization vector \mathbf{u} in the Cartesian coordinate frame $\{x, y, z\}$: $u_{-1} = (u_x - iu_y)/\sqrt{2}$, $u_0 = u_z$, and $u_1 = -(u_x + iu_y)/\sqrt{2}$.

In Eq. (3.15) the important part is again the atomic polarizability. It depends on the reduced matrix elements $\langle n'J' || \mathbf{d} || nJ \rangle$ of the electric dipole. These can be obtained from the transition rates given by

$$A_{n'J'nJ} = \frac{\omega_{n'J'nJ}^3}{3\pi\epsilon_0\hbar c^3} \frac{1}{2J'+1} |\langle n'J' || \mathbf{d} || nJ \rangle|^2. \tag{3.18}$$

The transition rates of many transitions can be found in the literature. The spontaneous decay rate of a certain excited state $|nJ\rangle$ can be obtained by summing over the probabilities of all relevant transitions $|nJ\rangle \rightarrow |n'J'\rangle$

$$\Gamma_{nJ} = \sum_{n'J'} A_{n'J'nJ}. \quad (3.19)$$

3.5 Trap-induced light shift of the ^{85}Rb D_2 -transition

In this section, we will use the formalism introduced in Sec. 3.4 to calculate the light shift of the D_2 -transition of the ^{85}Rb atom, induced by the dipole trap light. The atomic energy level scheme for the D_2 -transition is shown in Fig. 3.3 a). We have to calculate the light shifts for the ground state, $5^2S_{1/2}$, and the excited state, $5^2P_{3/2}$, separately. In Sec. 3.1 we already mentioned that the trap light is linear polarized, which brings a simplification into the formalism that is valid for both the ground and the excited state. For a linearly polarized light field, the polarization vector \mathbf{u} can be taken as a real vector, in which case $[\mathbf{u}^* \times \mathbf{u}]$ vanishes [127]. Consequently, the contribution of the vector polarizability to the light shift is zero, $\alpha_{n,J}^{(K=1)} = 0$, and only the terms of the sum $\sum_{K=0,1,2}$ in Eq. (3.15) corresponding to $K = 0$ and $K = 2$ remain.

3.5.1 Light shift of the $5^2S_{1/2}$ ground state

First, we want to calculate the light shift for the ground state $5^2S_{1/2}$. In conjunction with the intensity pattern of the standing wave, which will be determined in Sec. 3.6, this will allow us to model the dipole trap potential expected for our experimental trap parameters.

For the ground state, the total electron angular momentum quantum number is $J = 1/2$, which brings another simplification: for $J = 1/2$ and $K = 2$, the Wigner 6- j symbol in Eq. (3.16) is zero, which leads to $\alpha_{5,1/2}^{(2)} = 0$. Hence, also the contribution of the tensor polarizability to the light shift vanishes and only the contribution of the scalar polarizability ($K = 0$) remains. This simplifies Eq. (3.15) to

$$\begin{aligned} V_{\text{Stark}}^{FMF'M'}(5^2S_{1/2}) &= -\frac{|\mathcal{E}|^2}{\sqrt{3}} \alpha_{5,1/2}^{(0)} \\ &\quad \times (-1)^{3-M} \sqrt{(2F+1)(2F'+1)} \\ &\quad \times \begin{pmatrix} F & 0 & F' \\ M & 0 & -M' \end{pmatrix} \begin{Bmatrix} F & 0 & F' \\ 1/2 & 5/2 & 1/2 \end{Bmatrix}, \end{aligned} \quad (3.20)$$

where we inserted the nuclear spin of the ^{85}Rb -atom of $I = 5/2$, and the linear polarization vector $\mathbf{u} = (0, 0, 1)$ such that $\{\mathbf{u}^* \otimes \mathbf{u}\}_{00} = -1/\sqrt{3}$. Now, the matrix elements of the Stark operator only depend – apart from the Zeeman quantum numbers $\{F, M, F', M'\}$ – on the scalar polarizability, $\alpha_{5,1/2}^{(0)}$, and the trap light intensity $I_{\text{trap}} = 2\epsilon_0 c |\mathcal{E}|^2$.

The polarizability of a fine-structure state $|nJ\rangle$ only depends on the states $|n'J'\rangle$ that it can couple to, and one has to sum over all these states, see Eq. (3.16). For the ground state, as $L = 0$ and $J = 1/2$, the selection rules for electric dipole transitions ($\Delta L = \pm 1$, $\Delta J = 0, \pm 1$) allow

Table 3.1: Transition wavelengths $\lambda_{n'J'nJ}$ and dipole matrix elements $\langle n'J' | \mathbf{d} | nJ \rangle$ of the rubidium atom. The dipole matrix elements are calculated according to Eq. (3.18) using the transition wavelength $\lambda_{n'J'nJ}$ and probabilities $A_{n'J'nJ}$ given in Ref. [142]. As Ref. [142] gives only the air wavelengths, they were converted into vacuum wavelengths using Eq. 3.21.

$5S_{1/2} \rightarrow n'P_{J'}$	$\lambda_{n'J'nJ}$ [nm]	$A_{n'J'nJ}$ [10^6 s^{-1}]	$\langle n'J' \mathbf{d} nJ \rangle$ [ea_0]
$5S_{1/2} \rightarrow 5P_{3/2}$	780.2414	38.1	5.977
$5S_{1/2} \rightarrow 5P_{1/2}$	794.9789	36.1	4.231
$5S_{1/2} \rightarrow 6P_{3/2}$	420.2976	1.77	0.509
$5S_{1/2} \rightarrow 6P_{1/2}$	421.6711	1.50	0.333
$5S_{1/2} \rightarrow 7P_{3/2}$	358.8074	0.396	0.190
$5S_{1/2} \rightarrow 7P_{1/2}$	359.2597	0.289	0.115
$5S_{1/2} \rightarrow 8P_{3/2}$	334.9659	0.137	0.101
$5S_{1/2} \rightarrow 8P_{1/2}$	335.1775	0.0891	0.058

the coupling to the fine-structure states $n'P_{1/2}$ and $n'P_{3/2}$, where $n' \geq 5$. We take into account the states up to $n' = 8$. However, because the trap light with wavelength $\lambda_{\text{trap}} = 783.68 \text{ nm}$ has the smallest detunings to the $5S_{1/2} \rightarrow 5P_{1/2}$, $5P_{3/2}$ transitions, the coupling to those transitions has the biggest contribution to the light shift of the ground state.

Table 3.1 contains all quantities that are needed to compute the polarizability $\alpha_{5,1/2}^{(0)}$ for the selected transitions $5S_{1/2} \rightarrow n'P_{J'}$. The transition probabilities $A_{n'J'nJ}$ with corresponding wavelengths $\lambda_{n'J'nJ}$ are given in Ref. [142]. The latter are given only as air wavelengths and were, thus, converted into vacuum wavelengths via $\lambda_{\text{vac}} = \lambda_{\text{air}} n(\lambda_{\text{air}})$, where the wavelength-dependent refractive index was calculated using the Sellmeier equation for atmospheric air [143]

$$n(\lambda_{\text{air}}) \approx 1 + \sum_{j=1,2} \frac{B_j}{C_j - \lambda_{\text{air}}^{-2}}, \quad (3.21)$$

with $B_1 = 0.05792105 \mu\text{m}^{-2}$, $B_2 = 0.05792105 \mu\text{m}^{-2}$, $C_1 = 238.0185 \mu\text{m}^{-2}$, $C_2 = 57.362 \mu\text{m}^{-2}$. The dipole matrix elements $\langle n'J' | \mathbf{d} | nJ \rangle$ for all considered transitions were calculated according to Eq. (3.18) using the transition probabilities and the vacuum wavelengths from Tab. 3.1. With that, we have all necessary information to calculate the scalar polarizability for the ground state.

Now, we only need to insert the intensity of the trap light in order to calculate the Stark matrix. For an atom in the center of the beam waist of a Gaussian beam [66], the intensity is given by $I_{\text{trap}} = 2P_{\text{trap}}/\pi w_{\text{trap}}^2$. If the Stark interaction energy is small compared to the hyperfine splitting, the Stark matrix is diagonal, i.e. only the matrix elements $\langle (nJ)FM | V_{\text{Stark}} | (nJ)FM \rangle$ will be non-zero. The latter is normally fulfilled for the ground state, as the hyperfine splitting is on the order of several GHz [111], compared to the few 10 MHz due to the Stark interaction. Furthermore, because the contributions of the vector and tensor polarizability vanish, all Zeeman sublevels of the ground state hyperfine manifold, $|Fm_F\rangle$, experience the same light

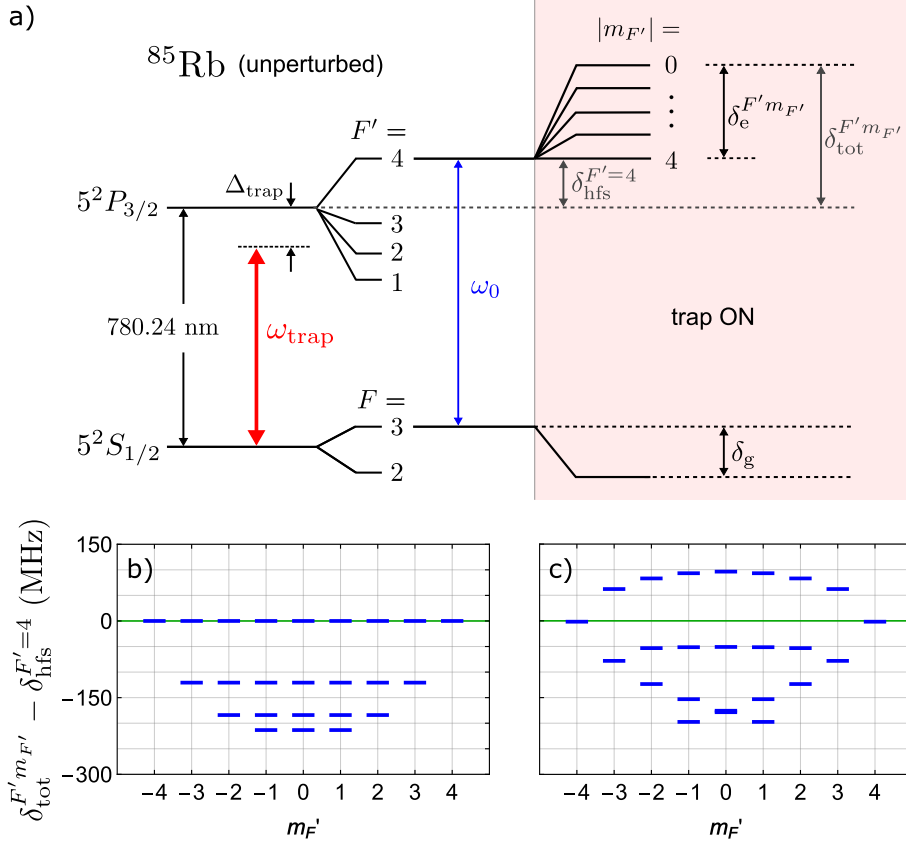


Figure 3.3: a) Energy level scheme of the D_2 -line of the ^{85}Rb atom: in the case of no interaction with a light field (left) and in the presence of a linearly polarized trap light field (right; red-shaded area). b) and c) Energies of the levels of the $5P_{3/2}$ state manifold, taken with respect to the energy of the $5P_{3/2}$, $F' = 4$ state for the unperturbed case and in presence of the trap light, respectively, calculated for the parameter values $\{P_{\text{trap}}, w_{\text{trap}}, \Delta_{\text{trap}}/2\pi\} = \{19 \text{ mW}, 3.5 \mu\text{m}, 1.68 \text{ THz}\}$.

shift, δ_g . We insert our experimental parameters² for the trap light: $\{P_{\text{trap}}, w_{\text{trap}}, \Delta_{\text{trap}}/2\pi\} = \{19 \text{ mW}, 3.5 \mu\text{m}, 1.68 \text{ THz}\}$ (cf. Sec. 3.3). Here, Δ_{trap} is defined as the detuning to the $5S_{1/2} \rightarrow 5P_{3/2}$ transition, as depicted in Fig. 3.3 a). The resulting light shift for the ground state thus amounts to

$$\delta_g \approx -91 \text{ MHz}, \quad (3.22)$$

where the minus sign indicates that all levels are shifted toward lower energy values.

²The given value for the beam waist w_{trap} , which is slightly larger than the measured beam waist (cf. Sec. 3.7.3), accounts for imperfect alignment of the trap optics and drifts of the latter.

3.5.2 Light shift of the $5^2P_{3/2}$ state

In the previous section, we calculated the trap-induced light shift of the atomic ground state, which is the basis for forming a trap potential for an atom detected in the evanescent field of the resonator mode. Here, we also want to calculate the light shift of the $5^2P_{3/2}$ excited state, using the same formalism, which allows us to determine the modification of the $5S_{1/2} \rightarrow 5P_{3/2}$ transition frequency resulting from the light shifts.

For a total electron angular momentum of $J = 3/2$, only the vector polarizability vanishes in the Stark operator in Eq. (3.15), such that both the scalar and the tensor polarizabilities contribute to the light shift. The tensor component leads to a $m_{F'}$ -dependent light shift for all F' -states and is depicted in Fig. 3.3 a) for the $F' = 4$ -manifold. From the selection rules for electric dipole transitions follows that the $5^2P_{3/2}$ state can couple not only to $n'S_{1/2}$ states, but also to $n'D_{3/2}$ and $n'D_{5/2}$ states. In the case of $n'S_{1/2}$ we take the fine-structure states with principle quantum number $n' = \{5, 6, 7, 8, 9, 10\}$ into account, and for $n'D_{3/2}$ and $n'D_{5/2}$ the ones with principle quantum number $n' = \{4, 5, 6, 7, 8, 9\}$. Thus, in total we consider the coupling of the $5^2P_{3/2}$ state to 18 different fine-structure states. However, the trap light predominantly couples to the $5P_{3/2} \rightarrow 5S_{1/2}$ and $5P_{3/2} \rightarrow 5D_{3/2}, 5D_{5/2}$ transitions, which therefore contribute the most to the light shift of the excited state. In order to calculate the scalar polarizability $\alpha_{5,3/2}^{(0)}$ and the tensor polarizability $\alpha_{5,3/2}^{(2)}$ of the $5P_{3/2}$ state, we need the vacuum wavelengths and the dipole matrix elements of each of the considered transitions. This time we take them directly from Tab. I in Ref. [144].

When computing the matrix elements of the Stark operator according to Eq. (3.15), we find that for our experimental parameters the Stark matrix is not diagonal. This arises because the trap-induced light shift is not small compared to the hyperfine structure (hfs) splitting of the $5P_{3/2}$ excited state and, thus, F' and $m_{F'}$ are not good quantum numbers anymore. To find the new energy eigenvalues, we thus have to diagonalize the combined interaction Hamiltonian that describes both the hyperfine and the atom–light interaction,

$$H_{\text{int}} = V_{\text{Stark}} + V_{\text{hfs}} . \quad (3.23)$$

The hyperfine interaction operator V_{hfs} is diagonal in the basis of the hyperfine structure states $\{|(nJ)FM\rangle\}$ and the non-zero matrix elements are given by [127]

$$\begin{aligned} \langle (nJ)FM | V_{\text{hfs}} | (nJ)FM \rangle &= \frac{1}{2} \hbar A_{\text{hfs}} G \\ &+ \hbar B_{\text{hfs}} \frac{\frac{3}{2}G(G+1) - 2I(I+1)J(J+1)}{2I(2I-1)2J(2J-1)} , \end{aligned} \quad (3.24)$$

where $G = F(F+1) - I(I+1) - J(J+1)$. A_{hfs} and B_{hfs} are the hyperfine structure constants which depend on the fine-structure level $|nJ\rangle$. For the $5P_{3/2}$ excited state, the values of these constants are $A_{\text{hfs}}/2\pi = 25.0020$ MHz and $B_{\text{hfs}}/2\pi = 25.790$ MHz [111].

As the total interaction Hamiltonian in Eq. (3.23) is no longer diagonal in the $\{|(nJ)FM\rangle\}$ hyperfine basis, we have to transfer it into the new eigenbasis. The new eigenstates are then superpositions of the hyperfine basis states. However, to still be able to name the shifted atomic

energy levels in the following, we assign those hyperfine basis states to the new energy eigenvalues that contribute most to the corresponding new eigenstates. This being said, the new eigenvalues of the full interaction matrix corresponding to Eq. (3.23) now give the total frequency offset for each $|F' m_{F'}\rangle$ level with respect to the $5P_{3/2}$ state in the absence of Stark and hyperfine interaction

$$\delta_{\text{tot}}^{F' m_{F'}}(I_{\text{trap}}) = \delta_{\text{hfs}}^{F'} + \delta_{\text{e}}^{F' m_{F'}}(I_{\text{trap}}), \quad (3.25)$$

consisting of the F' -dependent frequency shift, $\delta_{\text{hfs}}^{F'}$, due to the hyperfine interaction and the F' - and $m_{F'}$ -dependent light shift $\delta_{\text{e}}^{F' m_{F'}}$. These shifts are illustrated in Fig. 3.3 a), exemplarily for the $F' = 4$ manifold. In our experiment, the resonator is locked to the $F = 3 \rightarrow F' = 4$ transition. Hence, we are interested in the shift of each $|F' m_{F'}\rangle$ level relative to the unperturbed $5P_{3/2}, F' = 4$ hyperfine state, which is given by

$$\delta_{\text{tot}}^{F' m_{F'}}(I_{\text{trap}}) - \delta_{\text{hfs}}^{F'=4}. \quad (3.26)$$

Figure 3.3 b) and c) show the energy shifts for all excited state Zeeman levels for the unperturbed atom and in the presence of the trap light, respectively. In the latter case, we have used the parameter values $\{P_{\text{trap}}, w_{\text{trap}}, \Delta_{\text{trap}}/2\pi\} = \{19 \text{ mW}, 3.5 \mu\text{m}, 1.68 \text{ THz}\}$ and assumed the intensity of a Gaussian beam in the center of the beam waist $I_{\text{trap}} = 2P_{\text{trap}}/\pi w_{\text{trap}}^2$. One can see that the energy shifts of the excited state are F' - and $|m_{F'}|$ -dependent. The $F' = 4$ Zeeman manifold is shifted toward higher energies with respect to the unperturbed $5P_{3/2}, F' = 4$ state. The $(F' = 4, m_{F'} = 0)$ level experiences the largest shift of ≈ 96 MHz. Note, that the outermost Zeeman levels, $(F' = 4, m_{F'} = \pm 4)$, do not shift, as they do not couple to the π -polarized trap light field. Consequently, the cycling transition is only shifted out of resonance with the resonator due to the light shift of the ground state.

Taking both the ground state light shifts from the preceding section and the excited state shifts into account, the total detuning of the atomic transition frequency for each $m_{F'}$ -level with respect to the frequency, $\omega_0/2\pi$, of the unperturbed $(5S_{1/2}, F = 3) \rightarrow (5P_{3/2}, F' = 4)$ transition is given by

$$\delta\nu(I_{\text{trap}}) = \delta_{\text{tot}}^{F' m_{F'}}(I_{\text{trap}}) - \delta_{\text{hfs}}^{F'=4} - \delta_{\text{g}}(I_{\text{trap}}). \quad (3.27)$$

For the $(F' = 4, m_{F'} = 0)$ level the total detuning to the unperturbed transition frequency is the largest and amounts to $\delta\nu \approx 187$ MHz. The cycling transitions $(F = 3, m_F = \pm 3) \rightarrow (F' = 4, m_{F'} = \pm 4)$ are only shifted due to the ground state shift of about 90 MHz. From this, it is evident, that an atom trapped in our dipole potential will be strongly detuned with respect to the resonator, which is locked to the frequency ω_0 .

3.6 Modeling the trapping potential

3.6.1 Trap light intensity distribution near the resonator surface

In this section, we want to model the three-dimensional spatial intensity distribution of the trap light field $I(\mathbf{r})$ that is depicted in the schematic in Fig. 3.2. In combination with the results

of the light shift calculation this will allow us to model the trapping potential expected for our experimental parameters.

The characteristics of a laser beam are well described by a Gaussian beam with complex electric field amplitude $\mathcal{E}(\mathbf{r})$ [66]. The spatial intensity distribution of a Gaussian beam of power, P , propagating in x -direction is given by

$$I(\rho, x) = |\mathcal{E}(\mathbf{r})|^2 = \frac{2P}{\pi w^2(x)} \exp\left(-\frac{2\rho^2}{w^2(x)}\right). \quad (3.28)$$

Here, $\rho = \sqrt{y^2 + z^2}$ is the radial coordinate and $w(x)$ is the beam radius given by

$$w(x) = w_0 \sqrt{1 + \left(\frac{x}{x_R}\right)^2}. \quad (3.29)$$

It is defined as the radial distance from the optical axis (x), at which the beam intensity has decreased from its peak value $2P/\pi w^2(x)$ at $\rho = 0$ to $1/e^2$ of it. The beam radius is minimal in the focal plane of the beam at $x = 0$ and is called beam waist, $w_0 = w(x = 0)$. Furthermore, $x_R = \pi w_0^2/\lambda$ is the Rayleigh length, defined as the axial distance from the waist, at which the beam radius is increased to $\sqrt{2}w_0$. As can be seen from Eq. (3.28), the radial intensity profile of the Gaussian beam in a plane at $x = x'$ is described by a Gaussian function with FWHM-width of $\sqrt{2 \ln 2} w(x')$. Inserting the expression for $w(x)$ into Eq. (3.28) one finds the intensity profile in axial direction to be a Lorentzian function.

Now, for modeling the intensity distribution of our trap light field, we use the resonator-centered coordinate system as depicted in Fig. 3.2. We assume that the trap beam is focused onto the resonator such that the beam waist lies on the resonator surface. We are only interested in the intensity distribution near the resonator surface over the extent of our trap potential in x -direction of just a few hundred nanometer. This allows us to separate the description of the axial (x) and the transverse (y respective z) dependence of the intensity distribution, which provides a simple analytic expression accurate enough for our purposes.

We can approximate the beam radius $w(x)$ over the extent of our trap potential by the beam waist w_0 . Furthermore, we neglect the influence of the angle 2θ between the incoming and the reflected beam due to the resonator tilt (cf. Fig. 3.2) on the radial beam profile. Thus, in radial direction we assume the Gaussian intensity profile

$$I(\rho) = I_0 \exp\left(\frac{-2\rho^2}{w_0^2}\right), \quad (3.30)$$

where we also included the intensity magnitude given by $I_0 = 2P_{\text{trap}}/\pi w_0^2$.

In order to model the partial standing-wave intensity pattern along the axial (x) direction we describe the incoming beam as well as the beam reflected from the resonator surface by plane waves. Thereby, we neglect the slow variation of the intensity profile along the optical axis characteristic for a Gaussian beam. Furthermore, we approximate the interface between vacuum and the bottle resonator by a planar interface, as illustrated in Fig. 3.4 a). The latter

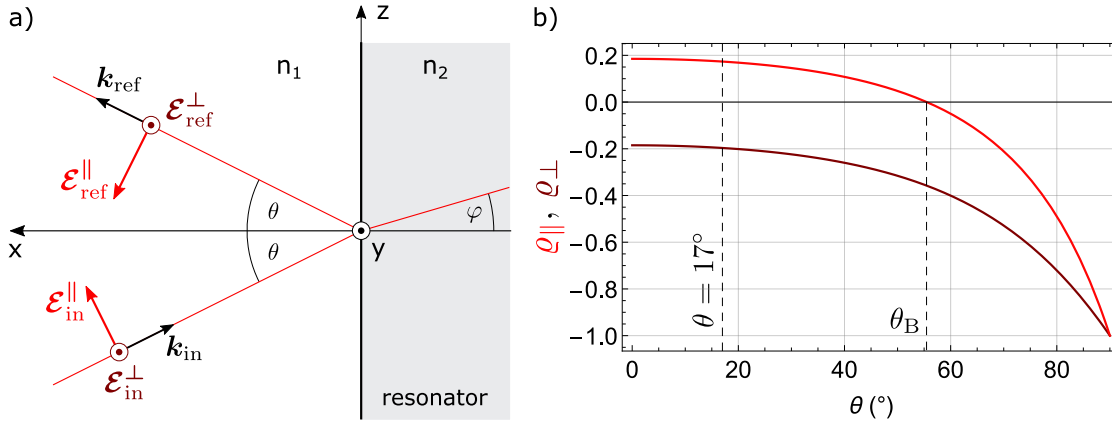


Figure 3.4: a) Reflection and transmission of a plane wave at a planar interface between vacuum ($n_1 = 1$) and fused silica ($n_2 = 1.454$ for a light wavelength of ~ 780 nm). Two types of polarization of the light field are distinguished: parallel (\parallel) and perpendicular (\perp) to the plane of incidence (x - z -plane). b) Reflection coefficients $\rho_p(\theta)$ for both types of polarization $p = \{\perp, \parallel\}$. The dashed lines indicate our specific case, where the angle of incidence is fixed by the tilt of the bottle resonator fiber, $\theta = 17^\circ$, and the Brewster angle θ_B , respectively.

approximation is justified because the trap waist is small compared to the resonator diameter. Note that, for simplicity, we shifted the origin of coordinates in x -direction to the intersection point of the incoming beam with the resonator surface. As we will see, the interference between the incident and the reflected beam depends on the polarization. In most of the experiments with single trapped atoms presented in this thesis, we aligned the linear polarization of the trap light field along the y -direction, i.e. perpendicular (\perp) to the plane of incidence (x - z -plane). Only the spectroscopy of the coupled atom-resonator system (cf. Sec. 5.6) was performed with the polarization vector lying in the plane of incidence (\parallel). Nevertheless, we will address both cases in the following.

We describe the incoming trap light field by a plane wave with angular frequency $\omega_{\text{trap}} = 2\pi c/\lambda_{\text{trap}}$ propagating in the $x - z$ -plane

$$\mathbf{E}_{\text{in}}(\mathbf{r}, t) = \mathcal{E}_{\text{in}} \exp(i\mathbf{k}_{\text{in}} \cdot \mathbf{r}) \exp(-i\omega_{\text{trap}}t) + c.c., \quad (3.31)$$

where \mathcal{E}_{in} is the vector amplitude of the electric field and $\mathbf{k}_{\text{in}} = k(-\cos\theta, 0, \sin\theta)$ is the wave vector with $k = 2\pi/\lambda_{\text{trap}}$. We distinguish between the two types of polarization described above, for which we can express the corresponding vector amplitudes in Cartesian coordinates as (cf. Fig. 3.4 a))

$$\mathcal{E}_{\text{in}}^{\perp} = \mathcal{E}_{\text{in}} \hat{\mathbf{p}}_{\text{in}}^{\perp} = \begin{pmatrix} 0 \\ \mathcal{E}_{\text{in}} \\ 0 \end{pmatrix} \quad \text{and} \quad \mathcal{E}_{\text{in}}^{\parallel} = \mathcal{E}_{\text{in}} \hat{\mathbf{p}}_{\text{in}}^{\parallel} = \begin{pmatrix} \mathcal{E}_{\text{in}} \sin\theta \\ 0 \\ \mathcal{E}_{\text{in}} \cos\theta \end{pmatrix}, \quad (3.32)$$

respectively, where $\hat{\mathbf{p}}_{\text{in}}^{\perp}$ and $\hat{\mathbf{p}}_{\text{in}}^{\parallel}$ are unit vectors. Note, that the scalar amplitude \mathcal{E}_{in} is the same in both cases, as it is related to the intensity of the incoming field $I \propto |\mathcal{E}_{\text{in}}|^2$, which is independent

of the polarization. Upon incidence on the dielectric interface, the wave is partially transmitted with the angle of refraction φ and partially reflected with the angle $-\theta$. We are only interested in the reflected part of the electric field, given by

$$\mathbf{E}_{\text{ref}}(\mathbf{r}, t) = \mathcal{E}_{\text{ref}} \exp(i\mathbf{k}_{\text{ref}} \cdot \mathbf{r}) \exp(-i\omega_{\text{trap}} t), \quad (3.33)$$

with the wave vector $\mathbf{k}_{\text{ref}} = k(\cos\theta, 0, \sin\theta)$ and the vector amplitudes

$$\mathcal{E}_{\text{ref}}^{\perp} = \mathcal{E}_{\text{ref}}^{\perp} \hat{\mathbf{p}}_{\text{ref}}^{\perp} = \begin{pmatrix} 0 \\ \mathcal{E}_{\text{ref}}^{\perp} \\ 0 \end{pmatrix} \quad \text{and} \quad \mathcal{E}_{\text{ref}}^{\parallel} = \mathcal{E}_{\text{ref}}^{\parallel} \hat{\mathbf{p}}_{\text{ref}}^{\parallel} = \begin{pmatrix} \mathcal{E}_{\text{ref}}^{\parallel} \sin\theta \\ 0 \\ -\mathcal{E}_{\text{ref}}^{\parallel} \cos\theta \end{pmatrix}. \quad (3.34)$$

The ratios between the reflected and the incident field amplitudes for both types of polarization are described by the Fresnel equations [145]:

$$\varrho_{\perp} = \frac{\mathcal{E}_{\text{ref}}^{\perp}}{\mathcal{E}_{\text{in}}^{\perp}} = \frac{n_1 \cos\theta - n_2 \cos\varphi}{n_1 \cos\theta + n_2 \cos\varphi}, \quad \varrho_{\parallel} = \frac{\mathcal{E}_{\text{ref}}^{\parallel}}{\mathcal{E}_{\text{in}}^{\parallel}} = \frac{n_2 \cos\theta - n_1 \cos\varphi}{n_2 \cos\theta + n_1 \cos\varphi}. \quad (3.35)$$

By replacing the angle of refraction φ in Eq. (3.35) using Snell's law [145]

$$n_1 \sin\theta = n_2 \sin\varphi \quad (3.36)$$

we can plot the reflection coefficients $\varrho_{\perp}(\theta)$ and $\varrho_{\parallel}(\theta)$ as a function of the angle of incidence, see Fig. 3.4 b), where we inserted the refractive indices for the vacuum $n_1 = 1$ and the resonator material $n_2 = 1.454$. The power reflectance $R_p(\theta) = \varrho_p^2(\theta)$, where $p = \{\perp, \parallel\}$, indicates the ratio of the reflected intensity to the one of the incoming wave. For $\theta = 0$ it amounts to $R_p(0) = 0.034$ for both types of polarization, i.e. 3.4 % of the incoming optical intensity is reflected. In our specific case of $\theta = 17^\circ$, the reflection coefficients are $\varrho_{\parallel} = 0.173$ and $\varrho_{\perp} = -0.197$, and thus the corresponding reflectances are $R_{\parallel} = 3.0\%$ and $R_{\perp} = 3.9\%$. We will see that this difference has a considerable effect on the depth of the resulting trap potential. Another interesting configuration can be seen in Fig. 3.4 b): for the so-called Brewster's angle, θ_B , the reflection coefficient $\varrho_{\parallel}(\theta_B) = 0$. This means that a \parallel -polarized wave incident under this angle has no reflected component, but is only transmitted. For us, however, this setting is not of relevance, as the angle of incidence is fixed by the resonator tilt to $\theta = 17^\circ$.

We can now calculate the standing-wave intensity pattern using Eqs. (3.31)-(3.36) by superposing the incoming and the reflected fields, and we obtain

$$|\mathbf{E}_{\text{in}}^p + \mathbf{E}_{\text{ref}}^p|^2 = |\mathcal{E}_{\text{in}}|^2 f_p(x), \quad (3.37)$$

with the following functions that describe the x -dependence of the intensity modulation of the standing wave for the two polarization cases:

$$f_{\perp}(x) = 1 + \varrho_{\perp}^2 + 2\varrho_{\perp} \cos(2kx \cos\theta), \quad (3.38)$$

$$f_{\parallel}(x) = 1 + \varrho_{\parallel}^2 - 2\varrho_{\parallel} \cos(2\theta) \cos(2kx \cos\theta). \quad (3.39)$$

Here, we used the notation $\varrho_{\parallel} \equiv \varrho_{\parallel}(\theta)$ and $\varrho_{\perp} \equiv \varrho_{\perp}(\theta)$. The two functions are plotted in Fig. 3.5 for $\theta = 17^\circ$. One can see that we only get a partial standing wave, as only a small

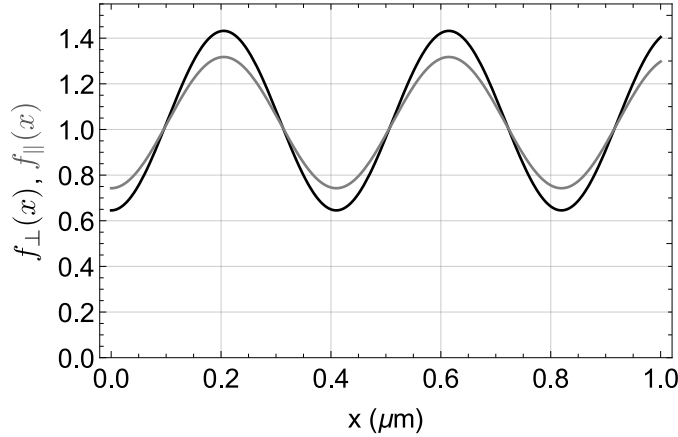


Figure 3.5: Standing-wave pattern according to Eqs. (3.38) and (3.39) formed by the incoming and reflected waves, for \perp - and \parallel -polarization, respectively.

fraction of the incident light is reflected. The standing-wave contrast is reduced in the case of \parallel -polarization, as the modulus of the reflection coefficient is smaller and only the z -components of the incident and reflected polarization vectors interfere. The periodicity of the standing wave depends on the angle of incidence, $\lambda_{\text{trap}}/(2 \cos \theta)$, as does the location of the first intensity maximum, $\lambda_{\text{trap}}/(4 \cos \theta)$, where we want to trap our single atoms. For $\theta = 17^\circ$ and $\lambda_{\text{trap}} = 783.68$ nm, the trap center is thus located at $\lambda_{\text{trap}}/(4 \cos \theta) \approx 205$ nm, where $f_{\perp}(205 \text{ nm}) = 1.43$ and $f_{\parallel}(205 \text{ nm}) = 1.31$ for the two polarization cases, respectively.

Taking Eq. (3.30) into account, we finally obtain the three-dimensional intensity distributions, that also depends on the choice of polarization

$$I_p(x, \rho) = I_0 f_p(x) e^{-2\rho^2/w_0^2}. \quad (3.40)$$

The corresponding optical dipole potential is then simply given by

$$U_{\text{dip}}(x, \rho) = U'_0 f_p(x) e^{-2\rho^2/w_0^2}, \quad (3.41)$$

where $U'_0 = h\delta_g$ with δ_g being the ground state light shift from Eq. (3.22). Note, that the latter quantity does not describe the depth of the final potential, but the potential depth that would correspond to the non-reflected Gaussian beam (cf. Sec. 3.5.1).

3.6.2 Surface forces

In the preceding sections, we described how a trapping potential for neutral atoms can be build by means of an external detuned electromagnetic field that interacts with the induced electric dipole moment of the atom. The purpose of the trapping potential is to place the atom as close as a few hundred nanometer to the resonator surface, such that it can interact with the resonator mode. However, when placing an atom so close to a dielectric surface, it inevitably experiences

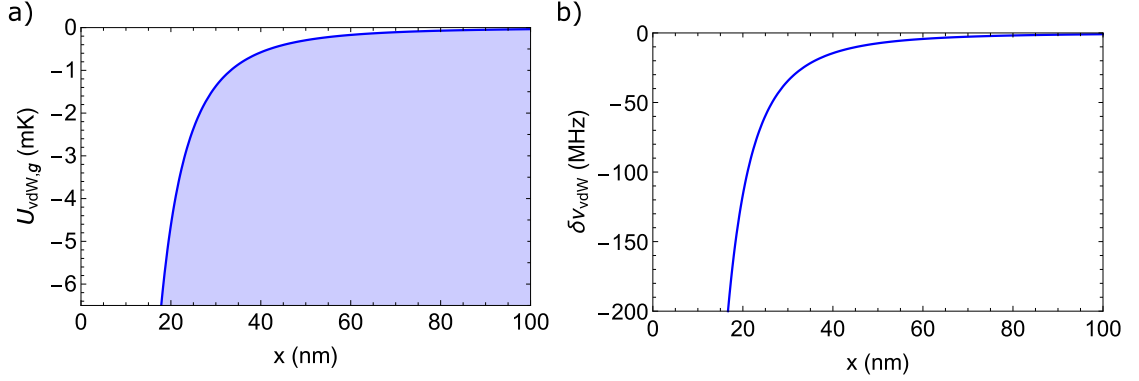


Figure 3.6: a) Surface potential for the atomic ground state ($5^2S_{1/2}$) caused by the radiative interaction of the atom with the resonator surface. b) Corresponding frequency shift, $\delta\nu_{\text{vdW}} = (-C_3(5P_{3/2})/x^3 + C_3(5S_{1/2})/x^3) / h$, of the $5^2S_{1/2} \rightarrow 5^2P_{3/2}$ atomic transition.

forces that have to be taken into account. These forces are similar in origin to the dipole force, except that they cannot be fully understood by classical physics: quantum fluctuations in the electromagnetic vacuum near the dielectric surface induce fluctuations of the atomic electric dipole moment. In the literature, the fluctuation-induced interaction between an atom and a surface is commonly termed Casimir-Polder interaction. This effect is closely related to the famous Casimir effect that describes the force between two conducting plates, predicted by Casimir in 1948 [146].

The Casimir-Polder forces give rise to a conservative potential that is in general attractive. Its exact shape depends on the material properties, the atomic polarizability and the atom–surface distance x . For distances $x \lesssim 0.1 \mu\text{m}$, the potential is called van der Waals potential and scales as $1/x^3$, for larger distances it is called Casimir-Polder potential and it scales as $1/x^4$ [147]. The van der Waals potential experienced by an atom near the surface can be understood as resulting from the interaction between the fluctuating dipole moment of the atom and its electrical image in the dielectric [131].

To describe the atom–surface interaction in our system, we will use a sufficiently accurate approximation, that is valid for short distances. We can regard our bottle resonator as a flat-surface bulk-medium, such that we can approximate the van der Waals potential by [123]

$$U_{\text{vdW}}(x) = -\frac{C_3}{x^3}. \quad (3.42)$$

The coefficient C_3 is proportional to the energy level shift. It has been calculated in [59] for the D_2 -line of ^{85}Rb atoms, taking into account the material constants of silica and the transition strengths of rubidium atoms [142]. This calculation yielded

$$C_3(5S_{1/2}) = h \times 770 \text{ Hz } \mu\text{m}^3 \text{ and } C_3(5P_{3/2}) = h \times 1.7 \text{ kHz } \mu\text{m}^3 \quad (3.43)$$

for the $5^2S_{1/2}$ ground state and the $5^2P_{3/2}$ excited state, respectively. Figure 3.6 a) shows the potential for the ground state. The calculated C_3 constants are both positive, which implies that

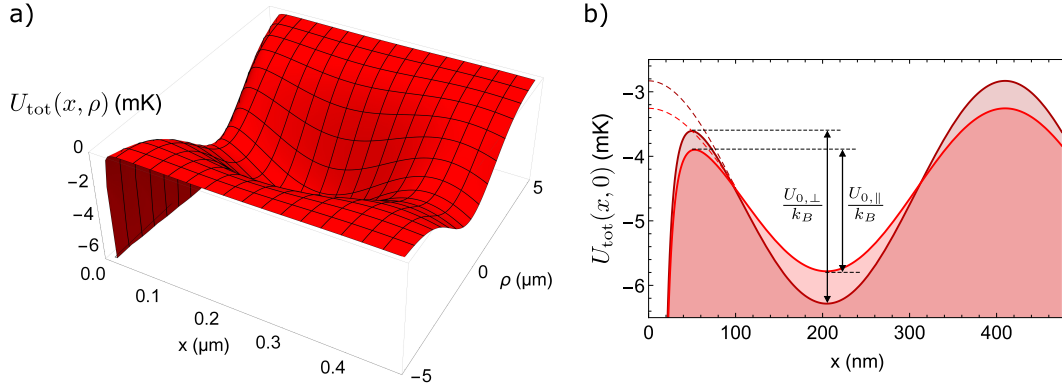


Figure 3.7: Model of the trap potential according to Eq. (3.44), for the trap parameters $\{P_{\text{trap}}, w_{\text{trap}}, \Delta_{\text{trap}}/2\pi\} = \{19 \text{ mW}, 3.5 \mu\text{m}, 1.68 \text{ THz}\}$ in our experiment. a) Potential landscape plot for the case of \perp -polarized trap light. b) Trap potential along the x -direction for both \perp - and \parallel -polarized trap light. The dashed lines indicate the optical potential according to Eq. (3.41). The trap depths of the total potentials are defined as indicated and amount to $U_0^\perp/k_B \approx 2.7 \text{ mK}$ and $U_0^\parallel/k_B \approx 1.9 \text{ mK}$, respectively.

the corresponding interaction potentials are attractive. The fact that the excited state C_3 constant is larger means that the excited state is subject to a larger energy shift and thus the atom–surface interaction reduces the atomic transition frequency with respect to the unperturbed transition, see Fig. 3.6 b).

3.6.3 Trapping potential

With the results from the preceding sections, we can now model the full potential seen by a ^{85}Rb atom. In x -direction, we sum up the optical potential and the van der Waals potential, where we assume that in radial direction the potential is approximately not affected by the surface forces:

$$\begin{aligned}
 U_{\text{tot}}(x, \rho) &= (U_{\text{dip}}(x, 0) + U_{\text{vdW}}(x)) e^{-2\rho^2/w_0^2} \\
 &= \left(U_0' f_p(x) - \frac{C_3}{x^3} \right) e^{-2\rho^2/w_0^2}. \tag{3.44}
 \end{aligned}$$

Figure 3.7 shows the full trap potential according to Eq. (3.44) for the parameter values of the trap light field in our experiment $\{P_{\text{trap}}, w_{\text{trap}}, \Delta_{\text{trap}}/2\pi\} = \{19 \text{ mW}, 3.5 \mu\text{m}, 1.68 \text{ THz}\}$. In panel (a) the potential is represented along the axial and radial directions for the \perp -polarized case. In panel (b) its dependence along the x -axis is shown for both polarization cases. The dashed lines indicate the shapes of the corresponding optical potentials $U_{\text{dip}}(x, 0)$ neglecting surface forces according to Eq. (3.41). The trap depths in each case are defined by the respective energy differences between the local trap minimum at $x \approx 205 \text{ nm}$ and the height of the potential barrier toward the resonator surface. The trap depths for the given experimental parameters

amount to $U_0^\perp/k_B \approx 2.7$ mK and $U_0^\parallel/k_B \approx 1.9$ mK, respectively, that is the trap depth of the \parallel -polarized trap is only about 70 % of the trap depth of the \perp -polarized trap.

Trap frequencies

We want to determine the oscillation frequencies of an atom trapped in the potential in Fig. 3.7. The knowledge of the characteristic trap frequencies is important, e.g., in the context of heating mechanisms which can limit the lifetime of an atom in the trap, as will be discussed in Sec. 4.6.3. A typical way of measuring trap frequencies exploits the loss of atoms by modulating the trapping potential close to the trap frequency.

Here, we want to obtain a theoretical estimate for the oscillation frequencies in our dipole trap. For this purpose, we harmonically approximate the trap potential by Taylor expansion of Eq. (3.41). By comparing the result to the cylindrically symmetric harmonic potential $U_{\text{harmonic}} = \frac{1}{2}m(\omega_x^2 x^2 + \omega_y^2 y^2 + \omega_z^2 z^2)$ we recover the known expressions for standing-wave optical potentials [113]

$$\omega_x = \frac{2\pi \cos \theta}{\lambda_{\text{trap}}} \sqrt{\frac{2U_{0,x}}{m}} \quad \text{and} \quad \omega_{y/z} = \sqrt{\frac{4U_{0,y/z}}{mw_0^2}}. \quad (3.45)$$

It is plausible that the incidence angle θ also enters in the axial trap frequency, as it modifies the periodicity of the standing wave. Because our standing wave is not fully modulated, the parameters U_0 , however, differ in axial and radial direction and are given by

$$U_{0,x}^\perp = 4\varrho_\perp U_0' \quad \text{and} \quad U_{0,y/z}^\perp = (1 - \varrho_\perp)^2 U_0' \quad (3.46)$$

for \perp -polarized trap light and

$$U_{0,x}^\parallel = 4\varrho_\parallel \cos(2\theta) U_0' \quad \text{and} \quad U_{0,y/z}^\parallel = (1 + \varrho_\perp^2 + 2\varrho_\perp \cos(2\theta))^2 U_0', \quad (3.47)$$

for \parallel -polarized trap light, where $U_0' = h\delta_g$ with the ground state light shift δ_g from Eq. (3.22). Using the above equations we can calculate the trap frequencies and obtain $\{\omega_x, \omega_{y/z}\} = 2\pi \times \{1.00$ MHz, 71 kHz $\}$ and $\{\omega_x, \omega_{y/z}\} = 2\pi \times \{0.86$ MHz, 68 kHz $\}$ for \perp -polarized and \parallel -polarized trap light, respectively.

3.6.4 Position-dependent shift of the atomic transition frequency

In Fig. 3.7 we showed the trapping potential, which is based on the position dependence of the ground state light shift of the atom. We have seen in Sec. 3.5.2 that also the levels of the $5P_{3/2}$ excited state experience a light shift, which is of course also position dependent due to the spatial intensity distribution of the trap light field. In this section, we want to evaluate the position dependence of the transition frequency of a trapped atom, where we also include the van der Waals energy shift of both the ground and the excited state.

The detuning of the ground state with respect to the unperturbed energy of the $5S_{1/2}, F = 3$ state is given by

$$\Delta\nu_{g,p}(x) = (U_{\text{dip}}(x, 0) + U_{\text{vdW}}(x))/h = \delta_g f_p(x) - \frac{C_3(5S_{1/2})}{hx^3}. \quad (3.48)$$

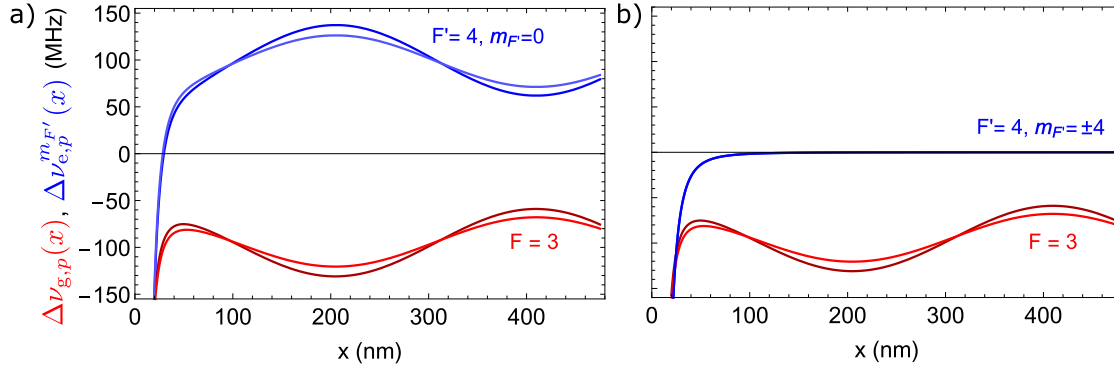


Figure 3.8: Position-dependent detuning along the x -axis, for the ground state (red) and for a) the $(5P_{3/2}, F' = 4, m_{F'} = 0)$ excited state and b) the $(5P_{3/2}, F' = 4, m_{F'} = \pm 4)$ excited state (blue) of a trapped atom. The darker (lighter) colors show the prediction for $\perp(\parallel)$ -polarization.

with the ground state light shift δ_g from Eq. (3.22) and the standing-wave pattern $f_p(x)$ from Eq. (3.38) respective (3.39). The detuning of an excited state Zeeman level with respect to the unperturbed energy of the $5P_{3/2}, F' = 4$ state is given by

$$\Delta\nu_{e,p}^{m_{F'}}(x) = \delta_e^{F'=4, m_{F'}} f_p(x) - \frac{C_3(5P_{3/2})}{hx^3}. \quad (3.49)$$

Figure 3.8 shows the $m_{F'}$ -independent ground state detuning, $\Delta\nu_{g,p}(x)$ (red) and the excited state detuning $\Delta\nu_{e,p}^{m_{F'}}(x)$ (blue) for the two extreme cases of a) the $m_{F'} = 0$ level and b) the $m_{F'} = \pm 4$ levels. The darker (lighter) colors show the case of $\perp(\parallel)$ -polarization. The red solid lines for the ground state are thus equivalent to the ones in Fig. 3.7 b).

As the excited state light shifts are of opposite sign compared to the ground state light shift, our trap light intensity distribution results in a repulsive potential for the excited state levels with $|m_{F'}| < 4$, see Fig. 3.8 a). As we have seen in Sec. 3.5.2, the $|m_{F'}| = \pm 4$ levels are not shifted under the influence of linear polarized trap light. Thus, the frequencies of the cycling transitions to the $|m_{F'}| = \pm 4$ levels are only shifted due to the ground state light shift and the atom-surface interaction, see Fig. 3.8 b). In both cases, however, an atom moving in the trap potential experiences a substantial and varying shift of its transition frequency. As a consequence, it cannot couple to the resonator mode anymore. In Ch. 5 we will show, how we can counteract the position-dependent light shift of the atomic transition by means of a second light field that shifts the excited state back into resonance.

3.7 Experimental implementation of the optical dipole trap

In this section, we will first describe the experimental components needed to create the dipole trap, from the trap laser source to the focusing optics. Another essential ingredient to obtain the desired trapping potential is the proper positioning of the beam focus on the resonator surface, which will be explained afterwards.

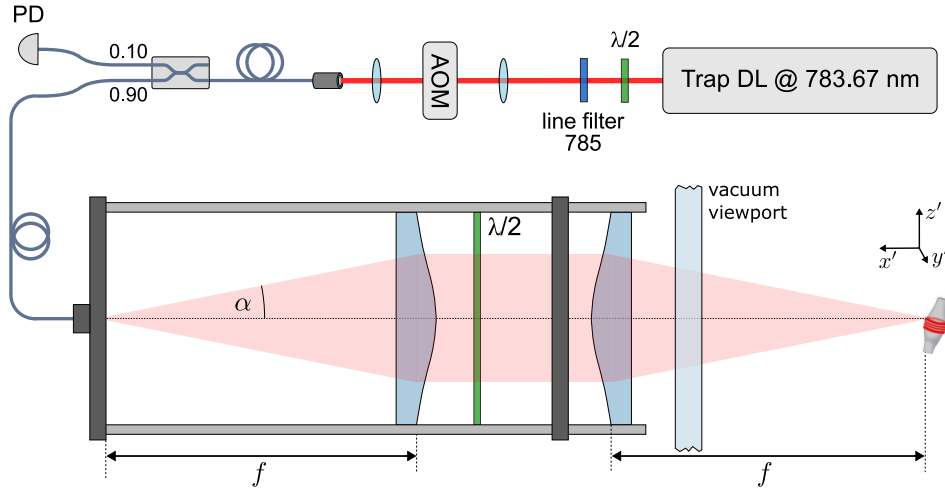


Figure 3.9: Schematic of the trap laser path from the laser source to the bottle resonator. The trap optics assembly is positioned in front of the main viewport of the science chamber and consists of two aspheric lenses and a $\lambda/2$ -waveplate in between (details in the main text).

3.7.1 Trap laser setup

A simplified scheme of the trap laser path from the laser source to the bottle resonator is depicted in Fig. 3.9. The laser source is a commercial laser diode³, which is implemented into a home-built diode laser setup. The laser diode is a single-mode diode with a typical lasing wavelength of 785 nm, which can be tuned to the desired value of $\lambda_{\text{trap}} = 783.68$ nm by tuning and stabilizing the diode temperature. The specified typical output power of the laser diode is > 400 mW, which ensures that at least the required 20 mW are available for the dipole trap. The requirements on frequency stability of this laser are not very strict, as it is far-detuned from the atomic resonance ($\Delta\lambda_{\text{trap}} = 3.44$ nm). As our trap laser is free-running, the laser wavelength drifts slowly, typically in a range of $\delta\lambda \leq 5 \times 10^{-4}$ nm. This represents a relative change of the detuning from the D_2 transition of $\delta\lambda/\Delta\lambda_{\text{trap}} \approx 1.5 \times 10^{-4}$, resulting in a change in trap depth of $\sim 4 \times 10^{-4}$ mK and is, therefore, negligible.

After exiting the diode, the trap light passes a $\lambda/2$ -waveplate for polarization adjustment and a line filter⁴ to suppress the spectrally broad amplified spontaneous emission (ASE) background from the laser diode. In particular, spurious light with a wavelength near the resonant 780.24 nm is to be minimized in order to avoid heating of an atom in the dipole trap and additional background counts on the SPCMs. Afterwards, the trap light passes through an acousto-optical modulator (AOM), which allows for triggered on/off-switching of the trap light. Finally, the trapping beam is coupled into a single-mode fiber-based beamsplitter⁵ with a splitting ratio of about 90:10. The 90%-port is connected to the trap optics, which will be described in the following section, while the 10%-port allows for measuring the trap power. Note, that the trap

³LD785-SE400, Thorlabs

⁴785 nm MaxLine laser clean-up filter, Semrock

⁵FC780-90B-APC, Thorlabs

light path depicted in Fig. 3.9 is simplified for clarity. For the measurements with trapped atoms presented in this thesis, we sent several light fields along with the dipole trap light through the trap optics. The full laser setup is depicted in Fig. 4.2.

3.7.2 Trap optics

In this section, we describe the optics assembly that we use to focus the dipole trap laser beam onto the bottle resonator, see Fig. 3.9. The starting criterion for its configuration was that it should produce a Gaussian beam waist of about $3 \mu\text{m}$, i.e. much smaller than the resonator diameter. The best optical access to the resonator is granted by the large vacuum viewport at the front of the science chamber (cf. Sec. 2.4.2), which has, however, a relatively large distance to the resonator of $D \approx 120 \text{ mm}$. This distance imposes a lower limit for the focal length of the focusing lens to be used.

To image the trap light onto the resonator, we chose two identical aspheric lenses with a focal length of $f = 150 \text{ mm}$ ⁶. Aspheric lenses have the advantage of strongly reducing the effect of spherical aberrations [148]. The lenses are mounted in a Thorlabs 60 mm cage system, which ensures proper axial alignment of the optical components with respect to each other, while allowing for adjustment along the optical axis (x'). The trapping beam is guided to the fiber-coupled trap optics assembly by the single-mode fiber-beamsplitter. The first lens has the task to collimate the beam and is therefore placed at a distance of $\Delta x' = f$ to the fiber output facet. The second lens then focuses the beam onto the resonator.

The divergence angle, α , of the Gaussian beam exiting the fiber is related to the mode field diameter, d_{MFD} , of the fiber⁷ via $\alpha \approx 2\lambda/\pi d_{\text{MFD}}$. A simple trigonometric consideration then yields for the waist of the beam incident onto the second lens

$$w'_0 \approx f \tan\left(\frac{2\lambda}{\pi d_{\text{MFD}}}\right) \approx 15 \text{ mm}. \quad (3.50)$$

For a given focal length f of the lens and wavelength λ of the transmitted light, which in our case is $\lambda = \lambda_{\text{trap}}$, the beam waist of the focused Gaussian beam, w_0 , is related to the beam waist of the incident Gaussian beam, w'_0 , via [66]

$$w_0 \approx \frac{\lambda f}{\pi w'_0}. \quad (3.51)$$

For our parameters, this expression predicts a waist of the focused laser beam of $w_0 \approx 2.5 \mu\text{m}$, in accordance with our initial requirement.

The $\lambda/2$ -waveplate in between the two lenses is used for polarization adjustment. In the measurements with single trapped atoms, which will be presented in Ch. 4, we used either \perp - or \parallel -polarized trap light (cf. Sec. 3.6.1). To facilitate the polarization adjustment, we temporarily insert a polarizer plus a large-sensor photodiode⁸ behind the $\lambda/2$ -waveplate, where the latter measures the intensity of the light transmitted through the polarizer. The polarizer is aligned so

⁶AL75150-B,Thorlabs

⁷FC780-90B-APC, Thorlabs; fiber-type: 780HP, with mode field diameter $d_{\text{MFD}} = 5.0 \pm 0.5 \mu\text{m}$.

⁸FDS10X10, Thorlabs

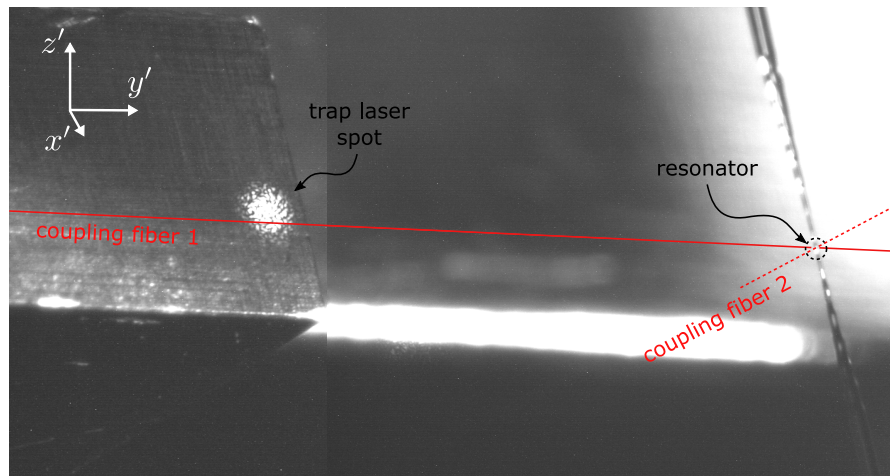


Figure 3.10: CCD-camera view through the large vacuum viewport into the vacuum chamber onto the edge of the coupling fiber holder and the fiber-resonator system, see Fig. 2.9 b). The two coupling fibers cross at the point of the resonator, which is indicated by the dashed black circle. Coupling fiber 1 lies behind the resonator from this perspective. The trapping beam is sent through the viewport as well and generates a bright spot on the fiber holder on the left. The height of the laser spot is adjusted to the height of coupling fiber 1, such that it can be easily translated from there to the resonator.

as to block the desired polarization. Then, by turning the $\lambda/2$ -waveplate, the optimal adjustment is reached when the transmitted intensity is minimized. Apart from focusing the trap light, the trap optics is also used to excite a trapped atom with a focused laser beam for fluorescence detection (cf. Sec. 4.5) and a second trap beam for compensation of the trap-induced light shift (cf. Ch. 5).

3.7.3 Positioning of the trapping beam onto the resonator surface

In order to obtain the desired trap potential and to yield an optimal trapping efficiency, the focus position of the trap beam has to be carefully adjusted with respect to the resonator mode in all three directions. For this purpose, the trap optics is mounted on a 3-axis translation stage⁹, which in turn is mounted on a 2-axis linear translation stage¹⁰. The latter provides micrometer screws in x' - and y' -direction with 13 mm travel range each. The different axes of the 3-axis translation stage are equipped with a manual micrometer screw (x'), a stepper motor actuator¹¹ (y') and a piezo-electric actuator as well as a manual micrometer screw (z').

After placing the trap optics in front of the vacuum viewport, the first goal is to locate the resonator inside the vacuum chamber with the trapping beam. For this coarse adjustment we have found that it is easy to locate the left edge of the coupling fiber mount, which is shown

⁹NanoMax300, Thorlabs

¹⁰XYT1, Thorlabs

¹¹M-232.17 High-resolution linear actuator with DC motor, Physik Instrumente

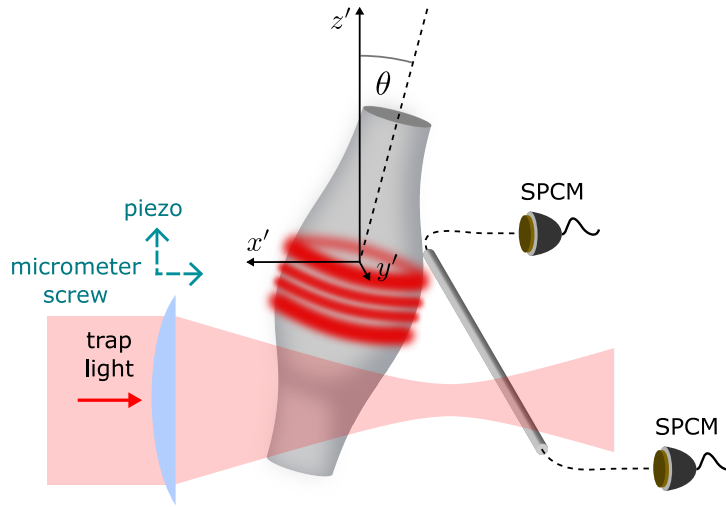


Figure 3.11: Illustration of the method for measuring the beam waist using the nanofiber as a probe. The trap optics, and with it the beam waist of the trapping beam, is moved across the nanofiber along the $-x'$ -direction using a manual micrometer screw and along the z' -direction by a piezo-electric actuator.

in Fig. 2.9 b). We send a small amount of trap light ($50\text{-}100\ \mu\text{W}$) through the trap optics into the vacuum chamber and observe the fiber mount with a CCD camera, see Fig. 3.10, while moving the beam. The camera is also mounted in front of the main vacuum viewport, i.e. it is approximately "looking" in $-x'$ -direction. On the camera image, coupling fiber 1 is slightly visible (highlighted in red in Fig. 3.10), such that, once we hit the fiber mount, we are able to adjust the height (z') of the trapping beam to the height of the fiber. Furthermore, focusing the laser spot onto the fiber mount already provides a coarse adjustment along the axial (x' -) direction. At this point we only have to move the trapping beam horizontally (y') along the coupling fiber toward the resonator. When the laser hits the resonator, we can also see the laser spot on the camera image at the position of the resonator. The subsequent fine adjustment will be described in the following.

x' -positioning and beam waist measurement

In x' -direction, the goal is to position the waist of the trapping beam on the resonator surface to minimize the trap extension. Thus, we first have to locate the beam waist inside the vacuum chamber. For this purpose, we exploit the presence of the nanofiber, which is an excellent tool to probe the intensity distribution of the trapping beam. Light that hits the nanofiber is partially coupled into the fiber, since it has some impurities on its surface that scatter incident light into the fiber-guided mode. The scattered photons can be detected with SPCMs on either side of the fiber, and thus the light intensity at a certain x' -position of the beam can be measured. Due to the small fiber diameter of $\geq 500\ \text{nm}$, this method provides a good resolution.

To measure the transverse beam profile as a function of x' , we send a small amount of trap

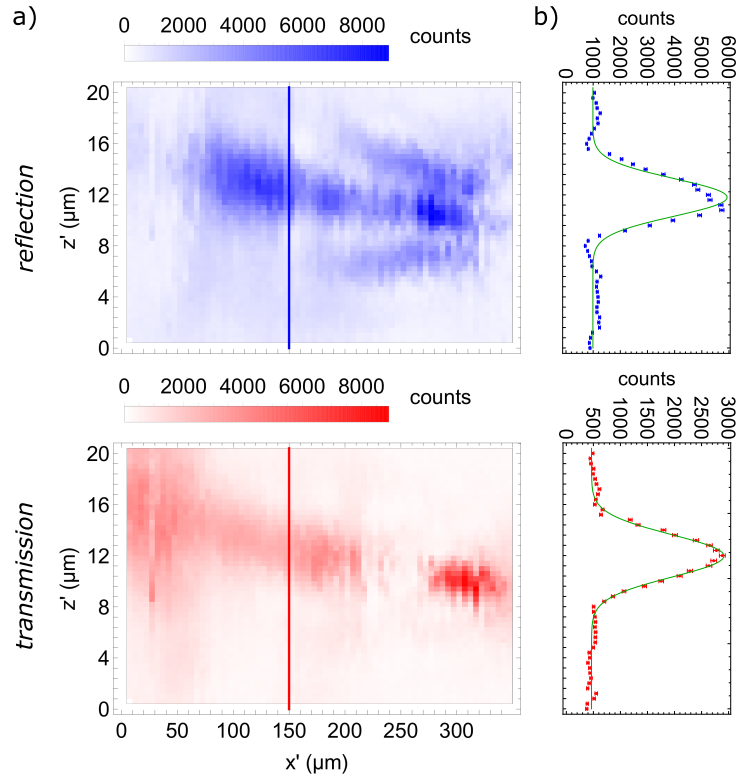


Figure 3.12: a) 2D intensity distribution in the focus region of the trapping beam, recorded by the SPCMs in reflection (blue) and transmission (red), respectively. The solid lines indicate the position $x' = 150 \mu\text{m}$, which was chosen to be aligned to the resonator surface. b) Transverse Gaussian beam profile, measured in reflection and transmission, respectively, at the position $x' = 150 \mu\text{m}$.

laser power ($\approx 100 \mu\text{W}$) through the trap optics onto the nanofiber, with a large enough offset in y' -direction to not hit the resonator, as illustrated in Fig. 3.11. We then move the beam across the nanofiber in z' -direction by applying a discrete voltage ramp consisting of 50 steps to the piezo-electric actuator of the 3-axis translation stage, which corresponds to a total travel range of $20 \mu\text{m}$. In order to perform a full scan of the focus region, we repeat the scan along z' for different values of x' .

Figure 3.12 a) shows the spatial intensity profile in the focus region of the trapping beam measured with the above described method. Here, we scanned over a length of about $350 \mu\text{m}$ in the $-x'$ -direction with a step size of $\Delta x' = 5 \mu\text{m}$. The blue and red photon counts were measured with the SPCMs in reflection and transmission (cf. Fig. 4.1), respectively. The two patterns differ from each other, which means that the impurities on the fiber surface do not scatter symmetrically into the clockwise and counter-clockwise propagating resonator modes, possibly due to polarization dependence. In both pictures, the intensity profiles deviate from the one of an ideal Gaussian beam. We observe two local maxima left and right of the central

intensity maximum, which are more pronounced in the reflection data. In three dimensions these correspond to an Airy pattern, which is known to occur in the focus of a laser beam passing through a lens with spherical aperture.

Due to these Airy rings it is difficult to identify the exact position of the beam waist. Therefore, we choose an axial position x' that exhibits a small beam radius, but does not have the ring structure. Figure 3.12 b) shows the transverse intensity profile at the position $x' = 150 \mu\text{m}$, which is marked in Fig. 3.12 a) by the solid lines. We fit the data with a Gaussian function of the form

$$C(z') = C_0 + Ae^{-\frac{2(z'-z'_0)}{w^2}}, \quad (3.52)$$

where w describes the radius of the beam. The fits yield beam radii at this x' -position of $w_{0,\text{transm}} = (3.3 \pm 0.1) \mu\text{m}$ for the transmitted counts and $w_{0,\text{refl}} = (2.9 \pm 0.1) \mu\text{m}$ for the reflected counts, respectively, which gives a mean value of $w_0 = (3.1 \pm 0.1) \mu\text{m}$.

In order to place the beam with the selected transverse profile on the resonator surface opposite to the nanofiber position, we translate the beam in $-y'$ -direction by the initial offset onto the resonator ($y' = 0$) and, then, in x' -direction by the resonator diameter of $\sim 37 \mu\text{m}$. For an ideal Gaussian beam with a waist radius of $w_0 \approx 3 \mu\text{m}$, the Rayleigh length would correspond to $x_R = \pi w_0^2 / \lambda_{\text{trap}} \approx 36 \mu\text{m}$. As this is as large as the resonator diameter, the adjustment in x' -direction is not very critical.

Resonator surface scan and (y', z') -positioning

Once the trapping beam is properly adjusted in x' -direction, we also fine-adjust the y' - and z' -positions. In y' -direction, the trap focus should be centered on the resonator ($y' = 0$), such that the beam is retroreflected and not deflected to the side due to the azimuthal curvature of the resonator. The optimal position of the trap focus in z' -direction along the resonator was identified in an independent measurement of the atom trapping efficiency as a function of the z' -position, see Sec. 4.4.1.

In order to facilitate the adjustment of the trap focus to the desired (y', z') -position, we create a 2D-map of the resonator surface and the nanofiber by measuring the position-dependent amount of light scattered into the nanofiber. For this purpose, we send a weak trap light ($\approx 50 \mu\text{W}$) through the trap optics and scan the beam focus across the fiber-resonator system (cf. Sec. 2.4.3) in an area of $\Delta z' \times \Delta y' = 20 \mu\text{m} \times 140 \mu\text{m}$. Trap photons are scattered off the resonator and the nanofiber and are partially coupled into the nanofiber, which allows us to detect them with the SPCMs at both ends of the fiber. To perform this scan, we apply discrete voltage ramps to the piezo-electric actuator to move the beam in z' -direction for each value of the y' -position. We scan the y' -position with a step size of typically 1 or 2 μm using a high-resolution linear actuator with DC motor¹².

A typical result of such a 2-dimensional scan is shown in Fig. 3.13 a) and b) recorded by the transmission- and reflection-SPCM (cf. Fig. 4.1), respectively. The darker red respective darker blue areas correspond to count rates higher than 10^4 . This color scale was chosen in order to

¹²M-232.17, Physik Instrumente

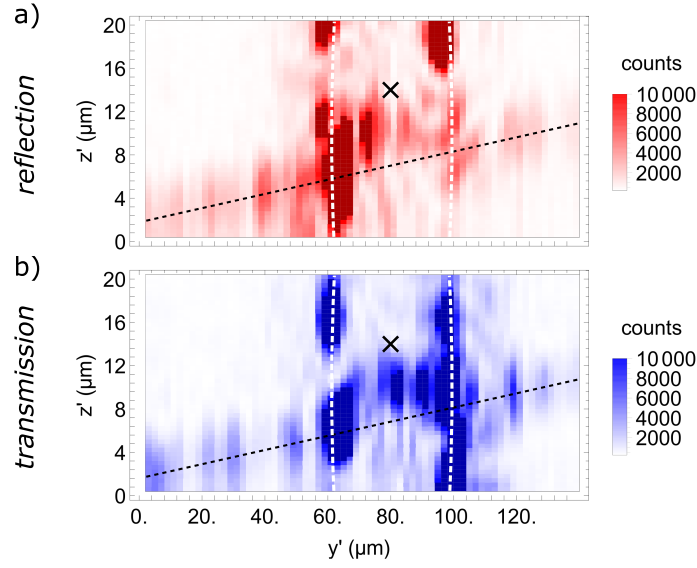


Figure 3.13: 2D map of the fiber–resonator system, recorded by the SPCMs in a) transmission and b) reflection. The dashed white lines indicate the approximate location of the resonator boundaries and the dashed black line indicates the nanofiber section of coupling fiber 1, which is lying behind the resonator from this perspective.

make structures visible with lower count rates, such as the nanofiber. The dashed white lines indicate the approximate location of the resonator boundaries. One can see that along these lines the count rates are significantly higher. When the trap light impinges tangentially onto the resonator boundaries, trap photons are probably coupled into the resonator and from there into the coupling fiber. It is also possible that trap light is being reflected from the boundaries and directly coupled into the fiber. Both effects might be enhanced by the presence of dust particles on the resonator surface, which would explain the spot-like structures. The distance between the spots of high count rates is compatible with the resonator diameter of $\sim 37 \mu\text{m}$. On the left and right side of the resonator boundaries we can see the nanofiber, which is indicated by the dashed black lines. It is less well resolved, because it is set back with respect to the front surface of the resonator and, therefore, lies behind the focal plane. It is possible that the higher count rates between the resonator boundaries are also caused by the nanofiber, although they are offset from the dashed black line. This could be because of refraction of the trap light, when it is transmitted through the resonator material.

We perform these scans always with a similar nanofiber–resonator distance, as well as similar trap power and wavelength. The choice of wavelength is important insofar, as it should not coincide with a resonance of the resonator. In such a case, the count rates are much higher and result in a blurred image. If the latter is avoided, the (y', z') -scans are very reproducible, that is they always exhibit the same recognizable structures and, therefore, provide a very good reference for positioning the trap focus in y' - and z' -direction. The optimum (y', z') -position is indicated by the black cross in Fig. 3.13 a) and b). In z' -direction it is offset by about $+7 \mu\text{m}$

from the interpolated nanofiber position, where we found the largest trapping efficiency in the measurement presented in Sec. 4.4.1. In Sec. 4.5.4 we will see that, when probing a trapped atom with resonant probe light through the trap optics, the above described position has to be adapted in order to yield minimum background counts.

Trapping single atoms close to the bottle resonator

After the design and experimental implementation of the optical dipole trap described in the previous chapter, we started to investigate whether we can actually trap single atoms from the atomic fountain in this trap potential. The first question was, how the presence of a trapped atom can be observed. Considering our scheme of detecting single atoms in the evanescent field (cf. Sec. 2.5.2), the obvious approach is to use the detection light for this task, which is sent into the coupling fiber. However, this light field is not resonant anymore with the atomic transition of a trapped atom due to the large trap-induced light shift (cf. Sec. 3.5). As we cannot shift the resonance frequency of the resonator fast enough to match the new atomic resonance frequency, the detection light can only be applied when the trap light field is off. Hence, our first attempt was to use a pulsed trapping scheme (cf. App. A.1.1). The idea is to switch the trap on and off in a fast fashion, such that the atom stays trapped and one can probe the atom whenever the trap light is off. In this way, we were able to observe for the first time atoms coupling to our bottle resonator beyond the typical interaction time of the free-falling atoms, but the signal decayed within a few microseconds. It is likely that the modulation of the trap in conjunction with the probing was heating the atoms out of the trap.

Consequently, we moved on to a scheme, where the trap light is sent onto the resonator in a continuous way. This chapter presents the development and application of techniques, which eventually allowed us to trap single atoms for a significant duration. First, we will describe the modifications of the experimental setup necessary for these experiments. We will show the general experimental sequence including the loading of the trap and the detection of trapped atoms. Besides the atom detection via the resonator field, we also investigate the detection via the observation of fluorescence photons. After presenting different parameter scans aiming at the improvement of the trapping and detection efficiency, characterization measurements will be shown, including a discussion of different heating mechanisms in the trap, which potentially limit the lifetime of the trapped atoms.

Parts of this chapter have been published in [149].

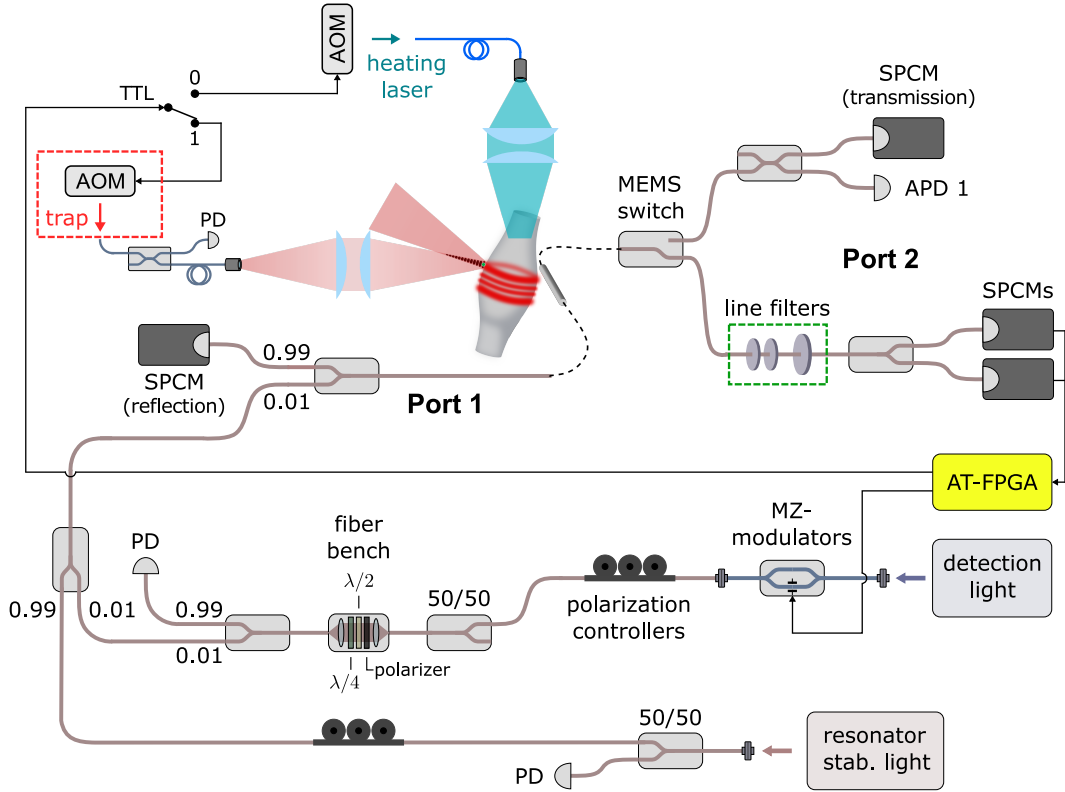


Figure 4.1: Schematic of the fiber network surrounding the bottle resonator, modified and upgraded to facilitate the trapping of single atoms close to the resonator. The dashed red box is a simplified representation for the optics setup shown in Fig. 4.2, which includes all light fields that are sent through the trap optics. The on/off-state of the trapping beam is controlled via the atom-trigger FPGA (AT-FPGA). The so-called *heating laser* has the inverse switching pattern to that of the trap beam and its function is explained in Sec. A.2. A set of line filters (dashed green box) was added to the setup to transmit resonant light at 780.24 nm, but efficiently block stray light from – in particular – the trapping beam.

4.1 Experimental setup for atom trapping

Figure 4.1 shows a scheme of the experimental setup, highlighting the parts that have been added to the original setup (cf. Fig. 2.11), in order to facilitate experiments with trapped atoms. The second coupling fiber is not shown in this scheme, as it was not used in the trapping measurements. The atom-trigger (AT) FPGA (cf. Sec. 2.5.2) now does not only control the on/off-state of the MZ-modulator of the detection light, but also the on/off-state of the AOMs that switch on and off the trap light and the heating laser beam, respectively. The task of the heating laser is to counteract thermal drifts of the resonator frequency that are induced by the illumination with the trap light (cf. App. A.2). To do this, the heating laser has exactly the inverse switching pattern to that of the trap beam, which in practice is accomplished using the radio frequency (RF)-driver

chain described in App. A.1.2 that supplies both AOMs.

Furthermore, a set of line filters (dashed green box) has been inserted in between the MEMS switch and the pair of SPCMs in Port 2 that measure the transmission through the coupling fiber. Its task is to transmit resonant photons at 780.24 nm while efficiently blocking background photons of other wavelengths, in particular at the trap wavelength ~ 783.7 nm and the compensation laser wavelength ~ 776.0 nm (cf. Ch. 5). We use two identical interference filters¹ with a very narrow bandwidth of 0.2 nm (FWHM). The center wavelength can be tuned by rotation of the filter. As those filters, however, still have a relatively large residual transmission of $\sim 1\%$ at 1 nm away from the center wavelength, we added an additional interference filter² with a typical bandwidth of 3 nm but with steeper slopes of the transmission band. With this combination we obtain an overall transmission of resonant light of $\sim 70\%$ and a suppression for the trap and compensation laser wavelengths on the order of 10^{-6} . To perform the (y', z') -scans that allow us to position the dipole trap onto the resonator before a measurement (cf. Sec. 3.7.3), we have placed an SPCM in the second arm of Port 2 (transmission) and of Port 1 (reflection) without filters, respectively.

In the course of chapters 4 and 5, we will discuss additional light fields that are sent through the trap optics. The different light fields are combined with each other and with the trapping beam in a free-space optics setup that is illustrated in Fig. 4.2. Besides the dipole trap laser, we use a so-called compensation laser, a fluorescence light and a repump light. The task of the compensation laser is to counteract the trap-induced light shift (cf. Sec. 3.5), which will be discussed in detail in Ch. 5. The fluorescence light allows us to externally probe and detect the trapped atom, see Sec. 4.5, and the repump beam is used to prevent potential depumping of the trapped atom to the $F = 2$ ground state, see below. These three additional beams are generated by separate laser sources and guided to the beam combination setup via polarization-maintaining (PM) single-mode fibers. First, the trap light is efficiently combined with the compensation light using a line filter. Then, this pair of beams is combined with the fluorescence light and the repump light on a 90:10 beam splitter cube. Subsequently, all light fields are transmitted through a PBS and a Berek compensator (BC) such that they enter the fiber-beam splitter with the same linear polarization. The 90%-port of the fiber-beam splitter is connected to the trap optics, while the 10%-port allows for measuring the individual beam powers. Typical powers of the trap, compensation, fluorescence and repump lights are 20 mW, ≤ 1 mW, ≤ 100 nW and 15 nW, respectively.

4.2 Trap loading

In order to trap single atoms in our standing-wave dipole potential, the basic structure of the experimental cycle, as explained in Sec. 2.5, is maintained. As before, the atomic fountain delivers a cloud of cold ^{85}Rb atoms to the bottle resonator, which spends about 100 ms in its close vicinity. Within this time window the FPGA-based detection and control system detects single atom transits through the evanescent field of the resonator mode in real time, which we will denote

¹Interference filter 780 nm, Radiant Dyes Laser & Accessories GmbH

²780 nm MaxLine laser clean-up filter, Semrock

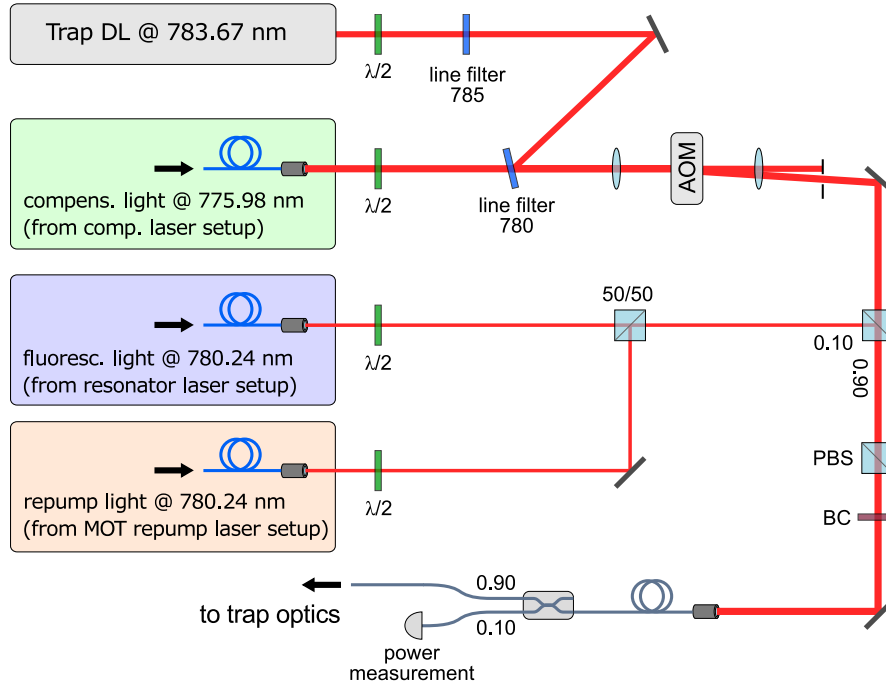


Figure 4.2: Scheme of the optics setup used for combining the trapping beam with the compensation, fluorescence and repumper beams (see text). All beams are coupled into the single-mode fiber-beam splitter, whose 90%-port is connected to the trap optics (cf. Fig. 3.9). The 10%-port of the fiber-beam splitter allows for measuring the individual laser powers.

as 1^{st} detection in the following. In the moment of the atom detection, the atom-trigger FPGA switches off the detection light and the trap light is switched on rapidly in order to capture the detected atom, if it is located inside the trapping volume.

In Fig. 2.17 we showed the time distribution of 1^{st} trigger events that indicate the arrival of atoms in the resonator mode, and it is again shown in Fig. 4.3 (red). One can see that we detect two classes of atoms that couple to the resonator on their way up and down, respectively. Here, we want to investigate, which of these atoms are more likely to be trapped.

The measurement has been performed at an earlier stage of our trapping investigations, where we used a pulsed trapping beam, see App. A.1.1. In order to probe the atom, the detection light was sent with the inverse switching pattern, such that it is on whenever the trap light is off. By analyzing the transmission of the detection light within the short time windows where the detection light is on, we are able to test the presence of a trapped atom. In this measurement, about 0.2 % of all atoms detected in the 1^{st} detection were trapped. We can plot the arrival times of these trapped atom events and compare it to the arrival time histogram of all initially detected atoms, see Fig. 4.3. For each case we normalize the number of atoms per millisecond, $N(t)$, by the total number of atom events N_{tot} . In the arrival time histogram of the trapped atom events (green), the later peak is now higher than the earlier one, indicating that atoms are more likely to

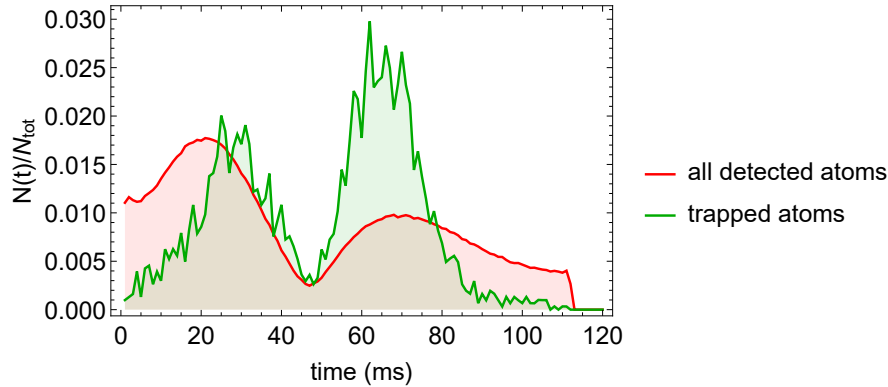


Figure 4.3: Comparison of the atom arrival time histograms of all atoms detected in the 1st detection (red; same data as in Fig. 2.17 a)) and of the trapped atoms (green). For better comparison, the histograms were normalized by the total number of initially detected atoms and trapped atoms, respectively.

be trapped when they are free falling after the turning point of the fountain trajectory. This seems plausible, considering the tilt direction of the resonator and the location of the dipole trap, see Fig. 3.2. Due to this, the resonator prevents – to some extent – the upward moving atoms from reaching the trap potential. Furthermore, the maxima of the green histogram are less separated in time with respect to each other than in the case of the red histogram. This means, that the atoms closer to the turning point of the trajectory, that is the slower atoms, are more likely to be trapped.

Based on this measurement, in the following we shortened the detection window during the experimental cycle and only analyzed events between $t = 40$ ms to $t = 120$ ms in order to only record the trapped atoms from the second peak. Furthermore, the shorter detection window helps preventing atom trigger cascades, which can occur due to the trap-induced heating of the resonator (cf. Sec. A.2).

4.3 Basic trapping sequence and data analysis

In all the trapping experiments presented in this thesis, we run the basic sequence depicted in Fig. 4.4 a), instead of the one in Fig. 2.16 b). Whenever an atom is detected in the resonator mode, the detection light is switched off and the dipole trap is switched on in order to catch the detected atom. In all experiments presented in this chapter, the trap light field was polarized perpendicular to the resonator axis (cf. Sec. 3.6.1), as indicated in Fig. 4.4 b). After a holding time, t_{hold} , the trap light is switched off and the detection light is switched on again. Thus, if the atom is still present after the trap phase, it will again be resonant with the resonator mode and can be detected via the transmission increase of the detection light. We denote the latter as *2nd detection*. With the detection light being switched on, the experiment is then ready again to detect the next atom transit event.

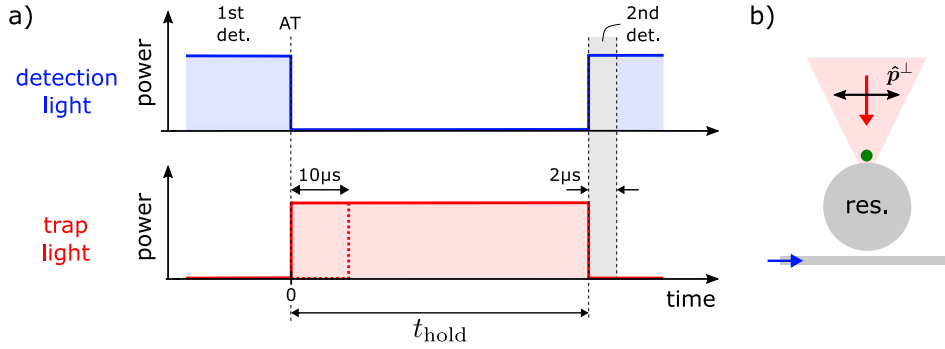


Figure 4.4: a) Key part of the experimental sequence for atom trapping. When an atom trigger (AT) event occurs (1st detection), the detection light is switched off and the trap light is switched on for a variable time duration t_{hold} . Afterwards, the trap is switched off and the detection light is switched on again. Thus, a potentially trapped atom is released from the trap and can be re-detected via the resonator field (2nd detection). b) Illustration of the propagation directions of the trap and the detection light fields. In all experiments presented in this chapter, the trap light field was \perp -polarized (cf. Sec. 3.6.1), as indicated by the black arrow.

We also perform a reference sequence without trapped atom by switching on the trap light with a delay of $10 \mu\text{s}$ after the atom detection, see dashed red line in Fig. 4.4 a). As transiting atoms leave the evanescent field within $1\text{-}2 \mu\text{s}$ (cf. Fig. 2.17 b)), a detected atom will not be trapped in this case. The reference sequence allows us to distinguish background photons from signal photons that originate from a trapped atom. After repeating the experimental cycle many times, we analyze the acquired data with respect to signatures of trapped atom events.

In the following, each part of the sequence and the data analysis will be discussed in more detail.

4.3.1 Sequence

Upon the detection of an atom, the trapping beam is switched on via the AOM in the trap setup, which has a switching delay of about 120 ns and a rise time of about 20 ns . As the reaction time of the atom-trigger FPGA is about 160 ns , the overall delay between atom detection and trapping is about 280 ns . This duration is much shorter than the average transit time of an atom through the evanescent field of the resonator mode and, thus, allows us to catch the detected atom.

As seen in Sec. 4.2, our trap loading mechanism has a rather low efficiency. However, when an atom is trapped upon being detected via the evanescent field of the resonator mode, it is most likely to be found in the trapping site closest to the resonator surface, as intended. There might be a possibility of trapping one or more atoms in trapping sites other than the first one. But already for the second trapping site at a distance of about 600 nm from the resonator surface, the atom-resonator coupling strength is close to zero and, thus, an atom located there would not affect the experiment. Due to the low density of the atomic cloud around the resonator

(cf. Sec. 2.5.1), the probability to trap multiple atoms in the first trapping site is negligibly low.

A trapped atom experiences a large light shift, as we have seen in Sec. 3.5. The resonator, however, is stabilized to the resonance of the unperturbed $(5S_{1/2}, F = 3) \rightarrow (5P_{3/2}, F' = 4)$ transition. Consequently, a trapped atom is strongly detuned from the resonator mode. A feed-forward of the resonator frequency could in principle compensate for the mean light shift of the atomic transition, but not for the broadening of the latter due to the position dependence of the light shift (cf. Sec. 3.6.4) in conjunction with the atomic motion in the trap. Furthermore, the experimental system for changing the resonator frequency only allows slow adjustments on the order of many tens of milliseconds. To tune the transition of the trapped atom back into resonance with the resonator, we ultimately implemented a light shift compensation scheme, which is discussed in Ch. 5.

During the holding time, the detection light that is incident on the resonator is switched off via the MZ-modulator and additionally with the AOM in the resonator laser setup (cf. Sec. 2.4.5). While the MZ-modulator provides fast switching on a sub-nanosecond time scale, the AOM ensures extinction of the light to better than 10^{-6} of the incident power. We take this measure, as in the presence of the detection light we observed a significantly reduced trapping signal. This is possibly linked to the fact that the $5P_{3/2}, F' = 3$ excited state is shifted closer to resonance due to the trap-induced light shift. The atom could be either heated via the $(5S_{1/2}, F = 3) \rightarrow (5P_{3/2}, F' = 4)$ transition, or it could decay into the $F = 2$ ground state level, where it is invisible for the detection light. For the latter reason, we implemented a repumper beam, which is also sent via the trap optics onto the atom, see Fig. 4.2. This beam is branched off from the repump laser source for the MOT (cf. Sec. 2.4.4). Hence, it is resonant to the unperturbed $(5S_{1/2}, F = 2) \rightarrow (5P_{3/2}, F' = 3)$ transition. To compensate for the light shift-induced detuning of the atomic repump transition to the repump light, we use an optical power corresponding to $10 - 20 I_{\text{sat}}$. This repump beam was applied over the full holding time in all the trapping measurements.

To detect a trapped atom via the resonator field, the detection light is switched on again. At the same time, the trap light needs to be switched off such that the light shift of the atomic transition vanishes. If an atom was trapped for the entire holding time, it is now released from the trap and spends about $1 \mu\text{s}$ in the evanescent field. In this time, it will interact again with the resonator field and thus lead to an increased transmission of detection light through the coupling fiber (cf. Sec. 2.5.2), which will be registered by the SPCMs. This detection method is destructive in the sense that the trapped atom is lost and, therefore, cannot be used for any further experiment. Later on we will, however, present a fluorescence detection method (cf. Sec. 4.5.1) that is compatible with detecting an atom while it is trapped.

4.3.2 Data analysis: trapped-atom statistics

With the resonator detection scheme described above, we can investigate the trapped atom statistics in our setup. For this purpose, we repeat the experimental cycle many times to collect a large number of atom trigger events (1st detection). All photon clicks associated with an atom trigger event are recorded by the pair of SPCMs in Port 2 (cf. Sec. 4.1), and they receive a time stamp

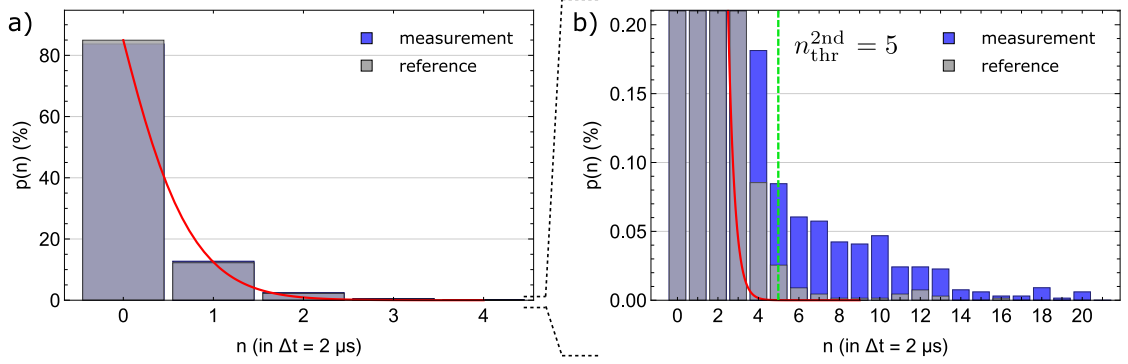


Figure 4.5: Photon number probability distribution of the transmission of the detection light within the $2 \mu\text{s}$ -long 2^{nd} detection window. a) Full histogram showing the result of both the actual (blue bars) and the reference measurement (gray bars). b) Zoom into the range of smaller probabilities of the histogram in (a). The red solid lines in both plots is a fit of a Poissonian function to the reference data. The dashed green line in (b) indicates the choice of a second trigger threshold, used to filter trapped atom events out of all atom trigger events (see text).

by the time tagger (TT) FPGA (cf. Sec. 2.6.1). We extended the photon recording window for the trapping measurements to cover $-5 \mu\text{s}$ to up to 2ms around an atom trigger event (instead of $\pm 25 \mu\text{s}$, which we used for the transiting atoms).

When the trap is switched off and the detection light is switched back on after t_{hold} , we count the number of photons registered in a $2 \mu\text{s}$ -long window, as indicated in Fig. 4.4 a). If no atom is present, the transmission of the detection light through the coupling fiber is nearly zero, and hence, we expect a low photon number. On the contrary, a trapped atom should give rise to a higher photon number due to strong resonant atom–resonator interaction. From the count results for all atom trigger events we generate a photon number histogram, that shows the probability

$$p(n) = \frac{N(n)}{N_{\text{tot}}}, \quad (4.1)$$

for registering n photons within the $2 \mu\text{s}$ as a function of n , see Fig. 4.5. Here, $N(n)$ is the number of atom trigger events, for which we detected n photons in $2 \mu\text{s}$ and N_{tot} is the total number of atom trigger events. In blue color we plot the histogram for the sequences potentially containing trapped atom cases (“measurement”) and in gray color the one obtained from the reference sequences (“reference”) where no atom was trapped. Figure 4.5 a) shows the full histograms plotted on top of each other, revealing that for small photon numbers ($n < 4$) they do not differ much from each other. More than 80 % of all atom trigger events show zero photons within the 2^{nd} detection window. The red solid line is a fit of a Poissonian function,

$$p(n) = A \frac{\lambda^n}{n!} e^{-\lambda}, \quad (4.2)$$

to the reference data, which yields an expectation value of $\lambda = 0.15$ photons per $2 \mu\text{s}$. This is compatible with the residual fiber transmission of the detection light of about 1 % in the absence

of an atom (cf. Sec. 2.5.2). Figure 4.5 b) shows the same histograms, but zoomed into a different range of the probability axis to better illustrate the distribution for higher photon numbers. We see that for $n > 4$ the blue histogram strongly deviates from the reference histogram, showing atom trigger events with larger photon numbers. This signal, which is absent in the reference data, most likely stems from trapped atoms. We also see a few such events in the reference data around $n \approx 12$, which we attribute to atoms from the atomic cloud accidentally transiting the evanescent field during the 2nd detection window.

Unfortunately, the probability distribution of the trapped atoms does not follow a Poissonian distribution, but rather merges into the reference distribution, which makes it difficult to clearly distinguish between trapped and non-trapped atom events. The reason is probably, that the distribution of atom–light coupling strengths in the 2nd detection window is rather broad. This underlines the importance of a reference measurement performed under the same experimental conditions. In the following, in order to identify a trapped atom, we choose a threshold value $n_{\text{thr}}^{2\text{nd}}$ for the 2nd detection, at which the measurement data clearly differs from the reference data. The fraction of trapped atoms that fulfill this condition is then given by the sum of all events fulfilling $n \geq n_{\text{thr}}^{2\text{nd}}$

$$\eta = \frac{1}{N_{\text{tot}}} \sum_{n=n_{\text{thr}}^{2\text{nd}}}^{\infty} N(n). \quad (4.3)$$

In the example measurement in Fig. 4.5 we could choose, e.g., $n_{\text{thr}}^{2\text{nd}} = 5$, which yields a fraction of trapped atoms of $\eta \approx 0.4 \%$. The predominant reason for this low value is the finite overlap of the trap volume with the resonator mode. Moreover, from all atom trigger events where the atom is inside the trapping volume in the moment of detection, only those atoms can be trapped whose total energy is smaller than the trap depth. The total energy of the atom is determined by its kinetic energy, which is dominated by the free fall of the atom, and its position with respect to the trap center at the moment the dipole trap switches on, which determines the initial potential energy in the trap. A third factor leading to a reduction of the trapping probability is the finite time delay between atom detection and switching on the trap of about 280 ns. Besides the trapping probability, the fraction η is also influenced by the efficiency of our second detection scheme, which is, however, difficult to estimate.

4.4 Investigation of trap loading and re-detection

During our first attempts to trap single atoms in the dipole trap, we observed typically very small or sometimes nearly vanishing trapping signals. Therefore, both the trap loading efficiency and the efficiency of the re-detection (2nd detection) had to be optimized, which is described in the following.

4.4.1 Optimization of the trap focus position

The probability for detecting a single atom in the resonator mode (1st detection) increases with the atom–light coupling strength g . As the latter is proportional to the atom’s position in the resonator mode (cf. Eq.(2.8)), the detection probability should be largest when the atom is at

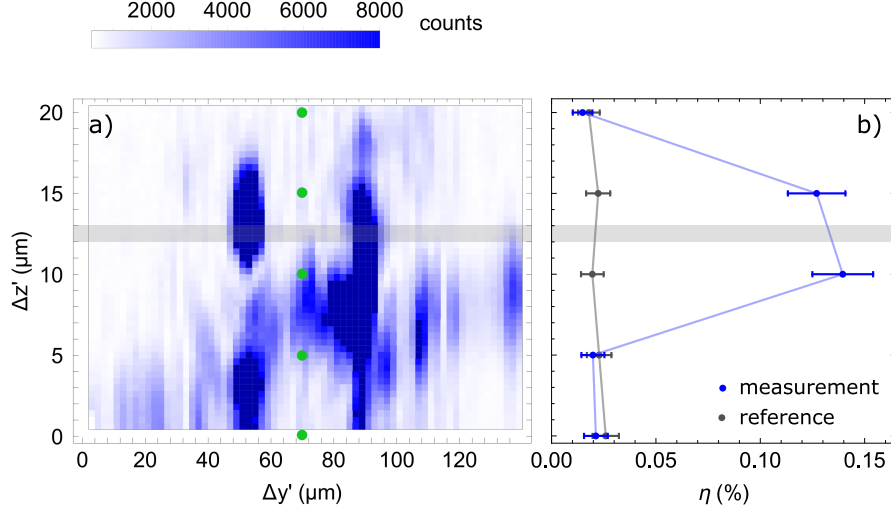


Figure 4.6: Dependence of the probability to trap and re-detect an atom on the trap focus position along the resonator axis. a) (y', z') -scan of the resonator surface, recorded as described in Sec. 3.7.3. b) Measured probability, η , for re-detecting a given detected atom after a time $t_{\text{hold}} = 100 \mu\text{s}$ via the resonator field, determined according to Eq. (4.3) for a second trigger threshold $n_{\text{thr}}^{\text{2nd}} = 7$. The solid lines are guides to the eye.

the caustic and near to the resonator surface. Consequently, in order to achieve a good trap loading efficiency, the trap should be positioned close to the caustic. In order to optimize the trap position, we therefore want to measure the probability, η , to trap and re-detect an atom, as a function of the axial (z') position of the trap focus along the resonator in the area of the caustic.

Unfortunately, as described in Sec. 2.4.6, the low scattering losses of the resonator make it hard to identify the exact axial quantum number of the used resonator mode, or the exact position of the caustics along the resonator axis. However, we know the approximate position of the caustic from the position of the coupling nanofiber, at which we optimize the fiber-resonator coupling. Therefore, we aim at scanning the trap focus around the position of the nanofiber. The latter we can find out, as described in Sec. 3.7.3, by performing a (y', z') -scan. The result of this scan is shown in Fig. 4.6 a). The z' -piezo of the trap optics translation stage has a full travel range of $20 \mu\text{m}$. Within this range we choose five discrete z' -positions for the trap focus – marked by the green dots in the (y', z') -scan – where we want to test the trap loading efficiency.

To perform the measurement, we run the basic trapping sequence as described in Sec. 4.3.1 with a holding time of $t_{\text{hold}} = 100 \mu\text{s}$. The trap power and wavelength were set to $P_{\text{trap}} = 18.9 \text{ mW}$ and $\lambda_{\text{trap}} = 783.65 \text{ nm}$, respectively. We repeat the sequence five times, where each time we change the position of the trap focus by $\Delta z' = 5 \mu\text{m}$. This is done automatically during the measurement by addressing the z' -piezo of the 3-axis translation stage of the trap optics. The block of five sequence parts is then repeated to obtain a set of measurements without trapped atoms, which is achieved by delaying the trap light by $10 \mu\text{s}$ after an atom detection event. The block of ten sequence parts is then repeated about 10000 times.

In total, we analyzed about 60000 atom trigger events per trap position, and we used a second trigger threshold of $n_{\text{thr}}^{\text{2nd}} = 7$. Figure 4.6 b) shows the measured probability, η , for trapping a given detected atom and re-detecting it after the holding time, for the different trap focus positions (blue) as well as the corresponding reference runs (gray). We observe a probability of $\eta(\Delta z') \approx 0.11\%$ for the third and fourth z' -position, while the probabilities for the other positions are indistinguishable from the reference results. The solid blue and gray lines are guides to the eye.

The measurement result suggests that the extension of the used resonator mode in z' -direction does not exceed $\Delta z' \approx 15\ \mu\text{m}$. The caustic positions of a resonator mode with an axial quantum number $q = 3$ have been determined to be $z_c \approx \pm 6.6\ \mu\text{m}$ [60]. Considering, that the trap focus has a diameter of $2w_{\text{trap}} \approx 7\ \mu\text{m}$, the above measurement is compatible with $q \lesssim 3$. Based on the measurement result of Fig. 4.6 b), in all following measurements presented in this thesis, we positioned the trap focus within the gray shaded area, which is about $+7\ \mu\text{m}$ offset from the interpolated nanofiber position (cf. Fig. 3.13).

4.4.2 Optimization of trap loading

Until now, in our experiments, the frequency of the resonator field was chosen to be resonant to the $(5S_{1/2}, F = 3, m_F = 3) \rightarrow (5P_{3/2}, F' = 4, m_{F'} = 4)$ atomic transition. In this case, the evanescent field does not exert a dipole force on the atoms in the cloud. If, however, the resonator frequency is detuned with respect to the atomic transition, the atoms feel a repulsive or attractive dipole force depending on whether the resonator–atom detuning $\Delta\omega_{\text{ra}} = \omega_r - \omega_a$ is > 0 or < 0 , respectively. The two cases are illustrated in Fig. 4.7 a), considering the short-range and attractive van der Waals force.

The effect of the resonator–atom detuning on the 1st detection of atoms was investigated in [59] by measuring the histogram of the atom detection times, as shown in Fig. 2.17, as a function of the detuning. It was found that for blue detuning ($\Delta\omega_{\text{ra}}/2\pi > 0$), the maxima of the two peaks in the arrival time histogram move away from each other and overall less atoms are detected. This indicates that slow atoms, i.e. atoms which arrive late in the first peak and early in the second peak are not noticed by the detection system. This confirms the repulsive force, as only the fast atoms are able to climb the potential hill toward the resonator surface and are able to couple sufficiently strong to the evanescent field to be detected. If the resonator field is red-detuned ($\Delta\omega_{\text{ra}}/2\pi < 0$), atoms are accelerated toward the resonator surface and are, thus, more likely to hit the surface. An investigation of the lifetime of the atoms in the evanescent field in Ref. [59] yielded, that a repulsive force increases the atom–light interaction time by about 50 % at $\Delta\omega_{\text{ra}}/2\pi = 3\ \text{MHz}$, while an attractive force reduces the interaction time by about 50 % at $\Delta\omega_{\text{ra}}/2\pi = -3\ \text{MHz}$, compared to the resonant case. In this section, we investigate the effect of the dipole force exerted by the resonator field on our trapped atom statistics.

We again use the basic trapping sequence shown in Fig. 4.4 with a holding time of $t_{\text{hold}} = 100\ \mu\text{s}$. The trap power was $P_{\text{trap}} = 20\ \text{mW}$ and the trap wavelength was $\lambda_{\text{trap}} = 783.68\ \text{nm}$. We repeat the sequence three times, where each time we simultaneously change the frequency of the detection light and the resonator. Both frequencies have to be identical in order to keep the transmission through the coupling fiber zero (in absence of an atom).

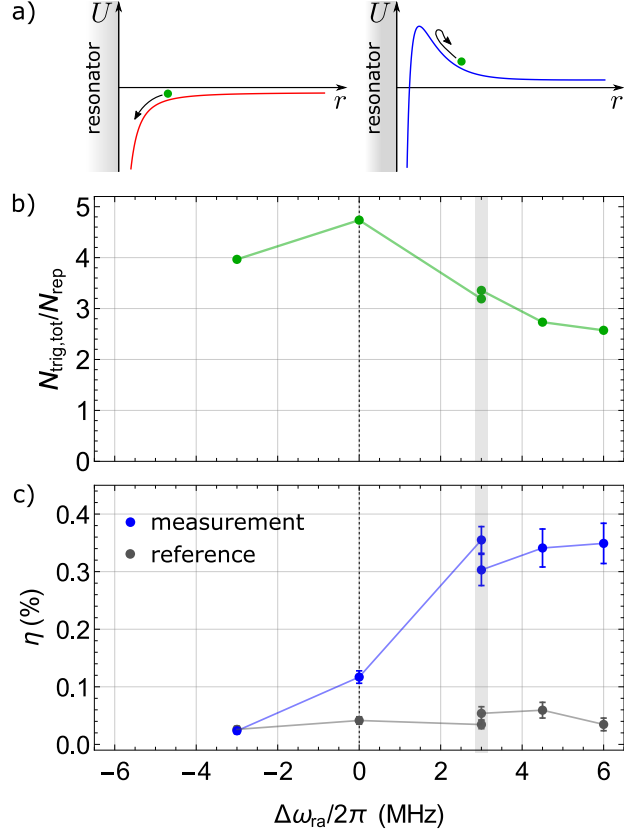


Figure 4.7: Dependence of the probability to trap and re-detect an atom on the resonator–atom detuning. a) Illustration of the dipole potentials associated with a red- and blue-detuned resonator field, considering the attractive van der Waals force. b) Number of detected atoms per sequence run in the 1st detection. Here, we normalized the total number of atom trigger events, $N_{\text{trig,tot}}$, by the number of sequence runs N_{rep} performed for a certain frequency setting. c) Measured probability, η , for re-detecting a given detected atom after a time $t_{\text{hold}} = 100 \mu\text{s}$ via the resonator field, determined according to Eq. (4.3) for a second trigger threshold of $n_{\text{thr}}^{\text{2nd}} = 6$.

In this way, we performed two independent measurements, with the settings for the detuning $\Delta\omega_{\text{ra}}/2\pi = \{-3, 0, +3\}$ MHz and $\Delta\omega_{\text{ra}}/2\pi = \{3, 4.5, 6\}$ MHz, respectively. Here, the +3 MHz setting was taken twice in order to judge the reproducibility between the two measurements. The results of both measurements are plotted together in Fig. 4.7. Panel (b) shows the measured dependence of the number of atoms detected in the 1st detection on the resonator–atom detuning. This quantity has a maximum for the resonant case with about 5 detected atoms per sequence run, and it decreases both for red and blue detuning of the resonator field. Panel (c) shows measured probability, η , for trapping and re-detecting an atom after the holding time t_{hold} , as a function of the resonator–atom detuning. A second trigger threshold of $n_{\text{thr}}^{\text{2nd}} = 6$ was applied. The blue data shows the measurement result and the gray data shows the reference result where no atom is trapped. When the resonator field is red-detuned with respect to the atom,

i.e. when it exerts an attractive force toward the resonator surface on the atom, the probability η for trapping the atom basically vanishes. On the other hand, for a blue-detuned resonator field, which exerts a repulsive force on the atom, the trapping probability increases even compared to the resonant case ($\Delta\omega_{\text{ra}}/2\pi = 0$). This is, on the one hand, most likely due to the longer atom–light interaction time. Furthermore, as the atoms are repelled from the resonator surface they are on average further away from the resonator, which favors the capturing of the atom in our trapping potential.

For all following measurements, we set the resonator–atom detuning to $\Delta\omega_{\text{ra}}/2\pi = +3$ MHz (gray bar), where the probability to trap an atom is larger by a factor of about 3 compared to the resonant case and we still detect a reasonable number of atoms per sequence run.

4.5 Fluorescence detection and probing of a trapped atom

To be able to see trapped atoms, we employed so far the re-detection scheme where we probe the system via the resonator field (cf. Sec. 4.3.1). A disadvantage of this method is that it cannot be applied in presence of the trap-induced light shift of the atomic transition, as it relies on resonant atom–resonator interaction. Thus, the trap light has to be switched off during detection, which results in the loss of the atom. For many experiments it would be advantageous to detect the atom non-destructively. Therefore, we introduce a different method, which relies on detecting the fluorescence of the trapped atom.

We use an additional light field, which we call *fluorescence light*. This light field is branched off from the resonator laser setup (cf. Sec. 2.4.5) and double-passes an AOM, which allows for switching and frequency tuning. Then it is coupled into a PM-fiber and guided to the laser beam combination setup shown in Fig. 4.2. We set the frequency of the light to be resonant to the resonator mode. When a trapped atom is illuminated with this light field via the trap optics, the atom elastically scatters photons. A fraction of these fluorescence photons is coupled into the resonator mode, out-coupled into the nanofiber and can then be detected with the SPCMs in transmission (Port 2).

4.5.1 Theoretical estimation of the fluorescence scattering rate

We want to estimate the number of fluorescence photons that can be detected with the SPCMs for a given incident power of the fluorescence light field, P_{fluor} . To do this, we start with the expression for the scattering rate into free space [111]

$$\Gamma_{\text{sc}}^{\text{fs}} = \Gamma \rho_{ee}, \quad (4.4)$$

where $\Gamma = 2\gamma$ is the natural decay rate of the excited state and ρ_{ee} is the excited state population. The latter can be derived from the optical Bloch equations [150] for a two-level atom in the steady state ($t \rightarrow \infty$), yielding [111]

$$\rho_{ee}(t \rightarrow \infty) = \frac{(\Omega/\Gamma)^2}{1 + 4(\Delta/\Gamma)^2 + 2(\Omega/\Gamma)^2}. \quad (4.5)$$

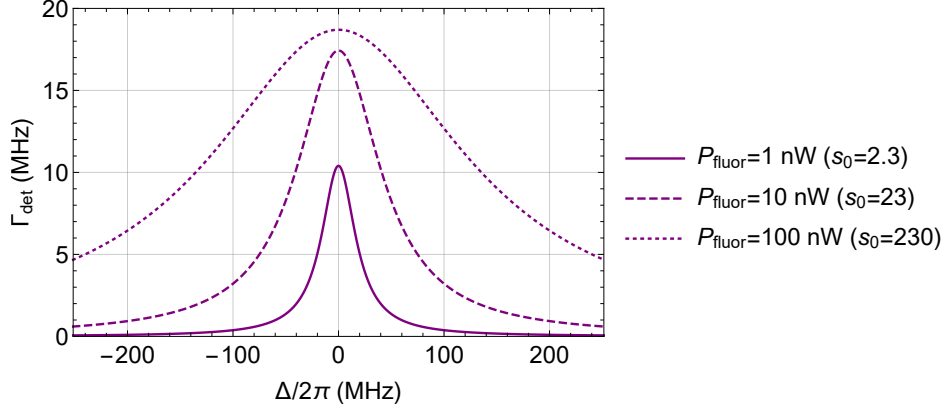


Figure 4.8: Theoretical estimation of the detection rate of fluorescence photons, Γ_{det} in the transmission port (Port 2) as a function of the atom–light detuning, when a resonator–coupled trapped atom is illuminated with fluorescence light of different powers, P_{fluor} , via the trap optics. The powers are also given in terms of the resonant saturation parameter defined by $s_0 = I/I_{\text{sat}}$ [19, 111].

Here, Ω is the resonant Rabi frequency and Δ is the atom–light detuning. As we are interested in the emission of photons into the resonator, we have to replace Γ in Eq. (4.4) by the Purcell-enhanced decay rate $2C\Gamma$ [31, 151] and in Eq. (4.5) by the total decay rate $(1 + 2C)\Gamma$, and thus obtain for the scattering rate into the resonator

$$\Gamma_{\text{sc}}^{\text{res}} = 2C\Gamma\rho_{ee} = C\Gamma \frac{(I/I'_{\text{sat}})}{1 + 4\left(\frac{\Delta}{(1+2C)\Gamma}\right)^2 + (I/I'_{\text{sat}})}, \quad (4.6)$$

with the cooperativity $C = g^2/2\kappa\gamma$. Furthermore, we inserted the relation between the Rabi frequency and the optical intensity [111]

$$\frac{I}{I'_{\text{sat}}} = 2\left(\frac{\Omega}{(1+2C)\Gamma}\right)^2, \quad (4.7)$$

where $I'_{\text{sat}} = (1 + 2C)^2 I_{\text{sat}}$ with $I_{\text{sat}} = 2.5 \text{ mW/cm}^2$ being the saturation intensity of the $(5S_{1/2}, F = 3) \rightarrow (5P_{3/2}, F' = 4)$ transition [111]. The ratio $s_0 = I/I_{\text{sat}}$ is also called saturation parameter [19].

To obtain a rough estimate for $\Gamma_{\text{sc}}^{\text{res}}$ we insert the values $\{g, \kappa, \gamma\} = 2\pi \{10, 10, 3\}$ MHz into Eq. (4.6), where the value for the coupling strength g was taken from Fig. 2.12 assuming the trapped atom to be located in the trap center at a distance of $x_0 \approx 205$ nm from the resonator surface. Moreover, we insert the intensity of the fluorescence beam at the trap center given by $I_{0,\text{fluor}} \approx f_{\perp}(x_0) \times 2P_{\text{fluor}}/\pi w_0^2$ where $f_{\perp}(x_0) = 1.43$ is given by Eq. (3.38). Since we want to know the photon detection rate, Γ_{det} , that we expect to observe on the SPCMs, we also have to take into account losses along the optical path between the resonator and the SPCMs:

$$\Gamma_{\text{det}} = \eta_{\text{ext}} \eta_{\text{SPCM}} \times \Gamma_{\text{sc}}^{\text{res}}. \quad (4.8)$$

Here, the factor $\eta_{\text{ext}} = 0.5$ accounts for the fact that for critical coupling only 50 % of the light is coupled into the nanofiber, as the other 50 % are dissipated by the resonator. Furthermore, $\eta_{\text{SPCM}} \approx 0.6$ is the approximate quantum efficiency of the SPCMs at a wavelength of 780 nm. In Fig. 4.8, the photon detection rate expected for our experiment Γ_{det} is plotted as a function of the atom–light detuning. For a power of, e.g., $P_{\text{fluor}} = 100$ nW and an average light shift-induced atom–light detuning $\Delta \approx 2\pi \times 200$ MHz (cf. Fig. 3.8 a)) we expect to register ~ 6 fluorescence photons in $1 \mu\text{s}$. As we used a position-independent fluorescence light intensity equal to the maximum intensity at the trap center in this derivation, the result in Fig. 4.8 should be regarded as an upper bound.

4.5.2 Experimental investigation of the fluorescence detection scheme

We now want to characterize how well we can see trapped atoms via the detection of fluorescence photons in the experiment. For this purpose, we have to illuminate the trapped atom with the fluorescence light field via the trap optics and measure the atomic fluorescence signal. We use the experimental sequence depicted in Fig. 4.9 a), where the dipole trap is loaded as described in Sec. 4.2. While the trap light is on, we send a strong fluorescence light pulse with variable pulse duration, Δt_{fluor} , onto the atom. This measurement should deliver information about the survival probability of a trapped atom in the presence of the fluorescence light pulse, depending on the pulse duration. Therefore, we also perform the 2nd detection via the resonator field, when the trap light switches off after a hold time of $t_{\text{hold}} = 100 \mu\text{s}$. We perform four measurement sequences for fluorescence pulse durations $\Delta t_{\text{fluor}} = \{0, 10, 30, 60\} \mu\text{s}$, as well as a reference sequence without trapped atoms for a fluorescence pulse duration of $\Delta t_{\text{fluor}} = 60 \mu\text{s}$. The fluorescence laser power was chosen to be $P_{\text{fluor}} \approx 100$ nW, corresponding to $I \approx 230 I_{\text{sat}}$, and the trap power was $P_{\text{trap}} \approx 20$ mW. Both the trap and the fluorescence light fields were \perp -polarized, as illustrated in Fig. 4.9 b).

In total, we analyzed about 115000 atom trigger events per sequence part. First, we want to know whether we are able to observe fluorescence photons scattered by trapped single atoms with the SPCMs, as described in the theoretical part of this section. For this purpose, we look at the photon number probability distribution, $p_{\text{fluor}}(n)$, within the first $10 \mu\text{s}$ of the fluorescence window, in the same way as we did so far for the 2nd detection window (cf. Sec. 4.3.2). The result is shown in Fig. 4.9 c) in purple color with the reference data plotted in gray. The red solid line is a Poisson fit of the reference data. We see a clear deviation between the purple and the gray histograms at higher photon numbers, meaning that we indeed see scattered fluorescence photons for some of the atom events. We filter the fluorescent atom events from the full data set by taking only those for which we detect " $n \geq n_{\text{thr}}^{\text{fluor}} = 6$ photons in $10 \mu\text{s}$ ", as indicated by the dashed green line in Fig. 4.9 c). We plot the time dependence of the fluorescence signal averaged over all filtered atom events in Fig. 4.9 d) (purple dots). The gray dots show the corresponding data for the atom events that were not trapped. The purple fluorescence signal reveals a photon detection rate of about 1.5 photons per $1 \mu\text{s}$, which is smaller by a factor of ~ 4 compared to the theoretically estimated value for an average atom–light detuning of $\Delta \approx 2\pi \times 200$ MHz (cf. Fig. 4.8). Furthermore, the signal decays with time, which means that atoms are lost from the trap under the influence of the fluorescence light. We fit an exponential function to the data (purple solid line), which yields a decay time of $(3.8 \pm 0.1) \mu\text{s}$. The latter can be understood

4. TRAPPING SINGLE ATOMS CLOSE TO THE BOTTLE RESONATOR

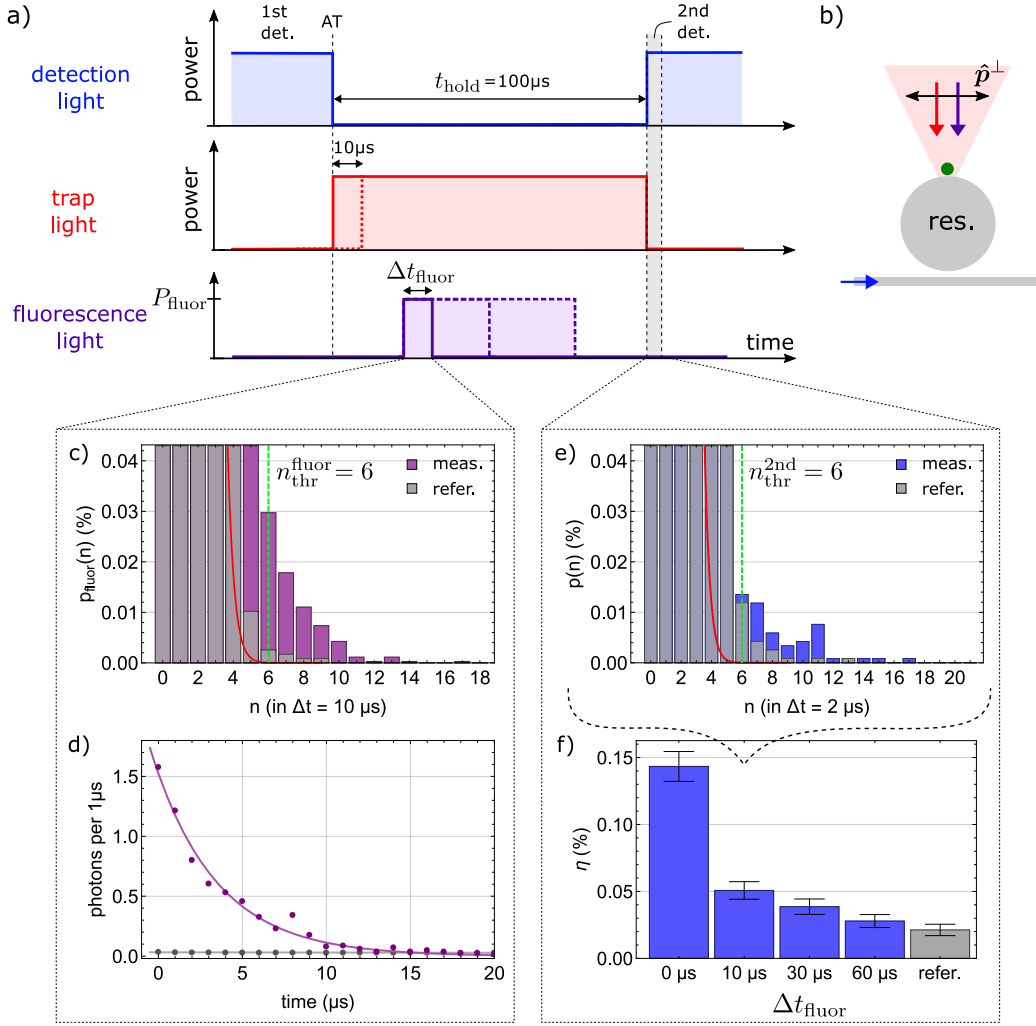


Figure 4.9: a) Experimental sequence for investigating the effect of a fluorescence beam sent via the trap optics onto the trapped atom. The sequence is performed for different durations of illumination with the fluorescence beam Δt_{fluor} . b) Illustration of the propagation direction of the involved light fields and the polarization direction of the trap and fluorescence beams. c) Photon number probability distribution of the first 10 μs of the fluorescence window with (purple bars) and without trapped atoms (gray bars). The dashed green line indicates the choice of the photon threshold to identify trapped atoms. d) Time dependence of the fluorescence signal after switching on the fluorescence light, averaged over the trapped atom events. The solid purple line is an exponential fit to the data, which yields a decay time of $(3.8 \pm 0.1) \mu\text{s}$. e) Photon number probability distribution of the 2nd detection window for the measurement (blue bars) and the reference data (gray bars). The dashed green line indicates the choice of the second trigger threshold, used to filter atom events that are trapped over the full holding time. f) Measured probability, η , for re-detecting a given detected atom after a time $t_{\text{hold}} = 100 \mu\text{s}$ via the resonator field, for a second trigger threshold $n_{\text{thr}}^{2\text{nd}} = 6$, as indicated in the photon number probability distribution in (e).

if we consider scattering-induced heating of the trapped atom. In particular, as we will discuss in Sec. 4.6.3, the trapped atom experiences a strong repulsive force in the excited state due to the position-dependent trap-induced light shift. We estimate for our experimental situation that the atom can scatter ~ 12 photons before it is lost. From the measured fluorescence photon detection rate of $\Gamma_{\text{det}}^{\text{meas}} = 1.5$ MHz, we can infer the expected total scattering rate of the atom in the trap, $\Gamma_{\text{sc}}^{\text{tot}} = \Gamma_{\text{sc}}^{\text{fs}} + \Gamma_{\text{sc}}^{\text{res}}$, using the expressions from Sec. 4.5.1, and obtain $\Gamma_{\text{sc}}^{\text{tot}} \approx 11.5$ MHz. The latter would correspond to a lifetime of the atom in the trap associated with this heating mechanism in the presence of the strong fluorescence light of $\sim 1 \mu\text{s}$. This value is compatible with the measured fluorescence decay time of $3.8 \mu\text{s}$, if we again consider that we are slightly overestimating the fluorescence light intensity seen by the atom by assuming the maximum intensity at the trap center for the calculation of $\Gamma_{\text{sc}}^{\text{tot}}$.

An alternative way to see whether atoms are lost from the trap during illumination with the fluorescence light, is to test their presence via the resonator field after the trap light switches off. For this purpose, we analyze the photon clicks detected within the 2nd detection window. Figure 4.9 e) shows the photon number probability distribution of the 2nd detection window, exemplarily for the sequence runs where the fluorescence pulse was sent for a duration of $\Delta t_{\text{fluor}} = 10 \mu\text{s}$. Applying a second trigger threshold of $n_{\text{thr}}^{2\text{nd}} = 6$ to the photon number probability distributions of all sequence parts, we obtain the probability, η , to trap and re-detect a given detected atom as a function of Δt_{fluor} . The result is shown in Fig. 4.9 f). The probability of $\eta \approx 0.15 \%$ for the runs without the fluorescence pulse ($\Delta t_{\text{fluor}} = 0$) is relatively low, because the measurement was still performed with a resonant instead of a blue-detuned resonator field (cf. Sec. 4.4.2). However, when the trapped atom is illuminated with the strong fluorescence pulse, the probability for re-detecting the atom at the end of the holding time is visibly reduced compared to the case without fluorescence light. Already after $10 \mu\text{s}$ of illumination the atom has very likely been heated out of the trap, which is in agreement with the result shown Fig. 4.9 d).

4.5.3 Non-destructive fluorescence detection

In the previous section we demonstrated the feasibility of the fluorescence detection, but the chosen power $P_{\text{fluor}} = 100$ nW was too high to keep the atom trapped despite the large trap-induced light shift, even for the smallest illumination time of $10 \mu\text{s}$. In the following measurement, we therefore reduce the fluorescence light power and increase the illumination time to investigate, whether we can perform a fluorescence detection of the atom without heating it out of the trap.

The corresponding experimental sequence is illustrated in Fig. 4.10 a). Compared to the previous measurement we extend the illumination time to $\Delta t_{\text{fluor}} = 960 \mu\text{s}$. We run four measurement sequences with fluorescence light powers $P_{\text{fluor}} = \{0, 0.25, 0.5, 1.0\}$ nW corresponding to about $\{0, 0.6, 1.2, 2.3\} I_{\text{sat}}$, as well as reference sequences without trapped atoms for the three non-zero power values.

We analyzed about 58000 atom trigger events per sequence part. First, we investigate the fluorescence window and determine the fraction of atom trigger events, η_{fluor} , for which we detect $n_{\text{thr}}^{\text{fluor}} = 6$ or more photons within the $960 \mu\text{s}$. We do this analogous to the analysis we performed so far for the 2nd detection window using Eq. (4.3). The result is shown in Fig. 4.10 c). Here, η_{fluor} gives information about the strength of the fluorescence signal, depending on the

4. TRAPPING SINGLE ATOMS CLOSE TO THE BOTTLE RESONATOR

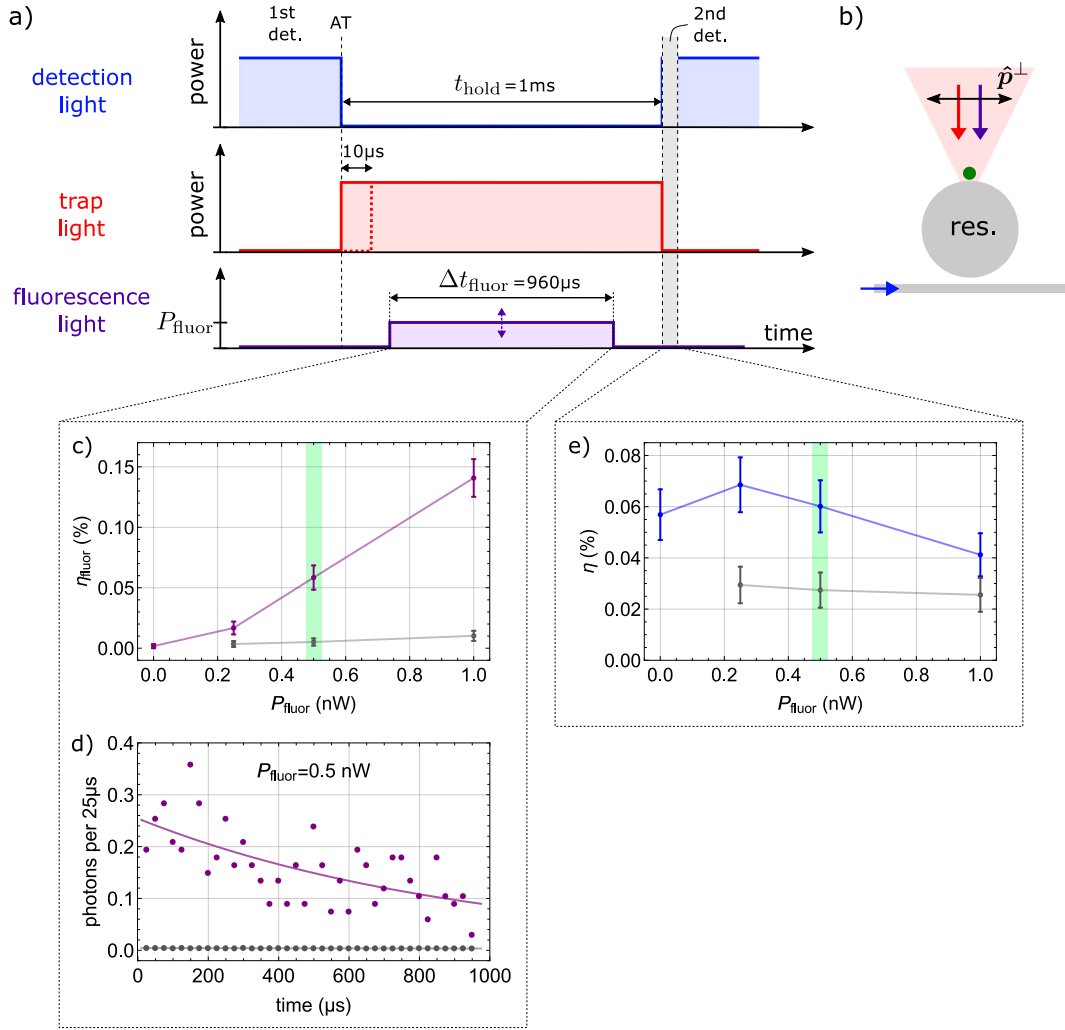


Figure 4.10: a) Experimental sequence for investigating the effect of a fluorescence beam sent via the trap optics onto the trapped atom. The sequence is performed for different fluorescence light powers $P_{\text{fluor}} = \{0, 0.25, 0.5, 1.0\}$ nW. b) Illustration of the propagation direction of the involved light fields and the polarization direction of the trap and fluorescence beams. c) Fraction of atom trigger events, η_{fluor} , for which we detect $n_{\text{thr}}^{\text{fluor}} = 6$ or more photons within the fluorescence window, calculated according to Eq. (4.3). The purple (gray) data points show the result for the measurement (reference) runs. d) Time dependence of the fluorescence signal after switching on the fluorescence light, averaged over the trapped atom events, for a fluorescence light power of $P_{\text{fluor}} = 0.5$ nW. The solid purple line is an exponential fit to the data, yielding a decay time of $(940 \pm 170) \mu\text{s}$. e) Measured probability, η , for re-detecting a given detected atom after a time $t_{\text{hold}} = 1$ ms via the resonator field, determined according to Eq. (4.3) for a second trigger threshold $n_{\text{thr}}^{\text{2nd}} = 7$. The blue (gray) data points show the result for the measurement (reference) runs. Panels c) and e) The solid lines are guides to the eye. The green bars indicate the optimal setting of the fluorescence light power, which allows us to see atoms *and* keep them trapped with a relatively large probability.

fluorescence light power, P_{fluor} . We see that the signal increases with increasing power. Now, to obtain information about the survival probability of a trapped atom, we also analyze the 2nd detection window. Figure 4.10 e) shows the probability, η , to re-detect a given detected atom after the holding time $t_{\text{hold}} = 1$ ms, as a function of the fluorescence light power, P_{fluor} . Overall, the signal-to-noise ratio is not as good as in the previous measurement, predominantly because the holding time is now on the order of the atomic lifetime in the trap (cf. Sec. 4.6.1). However, we do not observe a clear reduction of the atomic survival probability η for the two lower fluorescence light powers of 0.25 nW and 0.5 nW, indicating that the fluorescence light does not significantly heat the atom during the interrogation time.

In conjunction with the fluorescence signal strength shown in panel (c), the measurement suggests an optimal setting for the fluorescence light power of $P_{\text{fluor}} = 0.5$ nW, indicated by the green bars in the figure. At this power, we can both observe atomic fluorescence above the background *and* obtain a relatively large survival probability. In Fig. 4.10 d) we also plot the time dependence of the fluorescence signal averaged over the trapped atom events, for $P_{\text{fluor}} = 0.5$ nW. The purple solid line is an exponential fit to the data, which yields a decay time of (940 ± 170) μs . This decay time is comparable to the trap lifetime without applying fluorescence light (cf. Sec. 4.6.1). For comparison, for the case of the higher fluorescence light power $P_{\text{fluor}} = 1$ nW (not shown in Fig. 4.10) we obtain a decay time of (480 ± 40) μs .

4.5.4 Fluorescence background reduction

Since the fluorescence signal is relatively weak, it is essential to minimize the background photons reaching the SPCMs. When the fluorescence beam impinges on the resonator, not only the trapped atom scatters photons, which is the signal we want to detect, but photons of the incident beam also directly couple into the resonator. This effect is highly dependent on the adjustment of the trap optics. As these photons have the same frequency as the atomic fluorescence, they cannot be blocked with filters before reaching the SPCMs, as done for the trap light.

In order to minimize these scattered photons, we use the following procedure: First, we adjust the trap optics to the desired position via the (y', z') -scan, as described in Sec. 3.7.3. As a second step, we perform again a similar scan with 50-100 nW of fluorescence light. From this, we obtain the position dependence of the fluorescence background counts. We pick the position of minimum background close to the desired trap position, and we position the trap optics accordingly. After this positioning, we typically need to fine-adjust the trap optics position again to minimize the background counts, possibly due to slight hysteresis of the stepper motor and piezo-electric actuators. In this way, we achieve typical background count rates of $0.01 \mu\text{s}^{-1}$ for an incident fluorescence light power of ~ 100 nW.

4.5.5 Conclusion

We can conclude that the fluorescence beam sent via the trap optics allows us to detect the presence of an atom in the dipole trap in spite of the large trap-induced detuning between the atomic transition and the resonator. When using a fluorescence light power on the order of ~ 100 nW, the method is destructive, as the atom leaves the trap within several microseconds. However, while being destructive, the short and strong pulse yields a snap-shot information on

the presence of an atom in the trap. For this reason, we use this method for the detection of trapped atoms in the measurements presented in the remainder of this thesis.

In Sec. 4.5.3 we saw that a reduction of the fluorescence beam power in combination with a longer integration time allows us to see the trapped atom without heating it out of the trap. This offers the possibility for future trapped-atom experiments conditioned on the detection of an atom in the trap in real time.

Further benefits of the fluorescence detection method, compared to the detection via the resonator field, are the following: First, we directly talk to the trapped atom and thus do not detect atoms, which couple to the resonator mode at other positions around the resonator circumference. Second, the fluorescence method is less sensitive to a shift of the resonator frequency, e.g. induced by a temperature increase of the resonator material due to the illumination with the trapping beam, see Sec. A.2.

4.6 Characterization of the single trapped atoms

The measurements presented in Sec. 4.4 and 4.5 aimed at improving the trap loading efficiency and the efficiency to detect a trapped atom. Now we want to investigate the properties of the single trapped atoms, such as their average lifetime and temperature. Furthermore, we will discuss different mechanisms that lead to heating of the trapped atoms and give an estimate for the contribution of each mechanism.

4.6.1 Lifetime measurement

With the first measurement using the fluorescence detection scheme we studied the average lifetime of the single atoms in the trap potential.

The experimental sequence used for this measurement is shown in Fig. 4.11 a). We load the trap as in the previous sections. In order to test the survival probability of the atom in the trap as a function of time, we vary the waiting time t between switching on the trap and sending the fluorescence detection pulse. From now on, we denote the 20 μs -long fluorescence window with *2nd detection*. The power of the fluorescence pulse was set to $P_{\text{fluor}} \approx 100$ nW. The trap power was 19.5 mW. Both the trap and fluorescence light fields were \perp -polarized. We measured the survival probability for four different waiting times $t = \{0.1, 0.5, 1, 2\}$ ms and performed a reference measurement without trapped atoms for each time. To compensate for trap light-induced shifts of the resonator frequency, we employed the heating laser scheme described in Sec. A.2.2. Each of the eight sequence runs was repeated about 10000 times to yield good statistics.

In order to obtain the probability η for finding a single atom at a waiting time, t , after switching on the trap, we applied a threshold of $n_{\text{thr}}^{\text{2nd}} = 4$ to the photon number probability distributions of the detected fluorescence photons. The result is shown in Fig. 4.11 b). Here, we already subtracted the probabilities of accidental detection measured in the respective reference sequences. The red solid line is a fit of an exponential function to the data, $\eta(t) = \eta_0 \exp(-t/\tau_{\text{trap}})$. The fit yields a trap lifetime of $\tau_{\text{trap}} \approx 2.0$ ms. Furthermore, for this measurement we obtain a trapping probability of $\eta_0 \approx 0.7$ %.

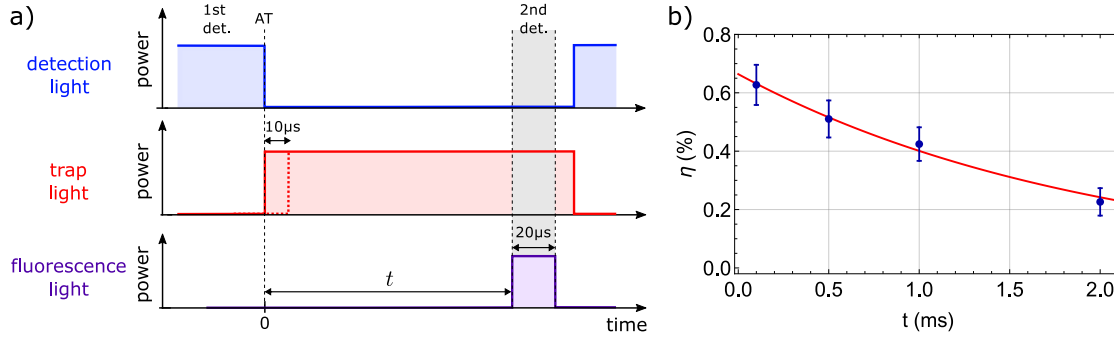


Figure 4.11: Measurement of the probability for finding a given detected single atom in the trap as a function of the waiting time t . a) Experimental sequence used to perform the measurement. b) Result of the measurement. The red line is an exponential fit, yielding a trap lifetime of $\tau_{\text{trap}} \approx 2$ ms.

The measured trap lifetime represents a thousandfold improvement of the previously typical interaction time of $1\text{-}2\ \mu\text{s}$ for atoms that are freely falling through the resonator field (cf. Fig. 2.17 b)). However, it is significantly smaller compared to the lifetimes reported for free-space standing-wave optical dipole traps for single atoms [117] and relatively small compared to standing-wave dipole traps formed either by nanofiber-guided light fields [44, 132, 133] or by retroreflection from the surface of a nanofiber [45]. As we will see later, this can be attributed to our trap loading mechanism and the likely presence of a heating mechanism in the trap.

4.6.2 Measurement of the energy distribution

We want to obtain an estimate of the average temperature of the single trapped atoms. For this purpose, we measure the energy distribution of the atoms using a method specifically suited for single atoms, which has been proposed and demonstrated in Refs. [117, 152].

The idea is to adiabatically lower the trap potential, starting from trap depth U_0 , and measure at which lowered depth U the atom leaves the trap. During the lowering, the energy of the atom is also reduced from its initial energy E_0 to E (“adiabatic cooling”), and the atom is lost when the trap depth becomes smaller than its energy, $U < E$. Repeating this procedure many times with a single atom in the trap would yield the energy distribution of the trapped atoms. However, it is experimentally not feasible to monitor the presence of a single atom in the trap in real time without modifying the atomic energy that is supposed to be measured. Instead, one has to lower the trap depth to a discrete value, U_{low} , and measure via many repetitions the fraction of atoms remaining in the lowered trap, as a function of U_{low} .

The trap depth is lowered by ramping down the trap laser power. This is illustrated in the experimental sequence shown in Fig. 4.12 a). The trap potentials corresponding to the initial power P_{trap}^0 and a certain reduced power $P_{\text{trap}}^{\text{low}}$ are drawn in panel (b). Not only the trap depth changes during the lowering, but also the slope of the potential and, with it, the atomic oscillation frequency $\omega(t)$. A criterion for adiabaticity of the trap lowering process is that the change of the

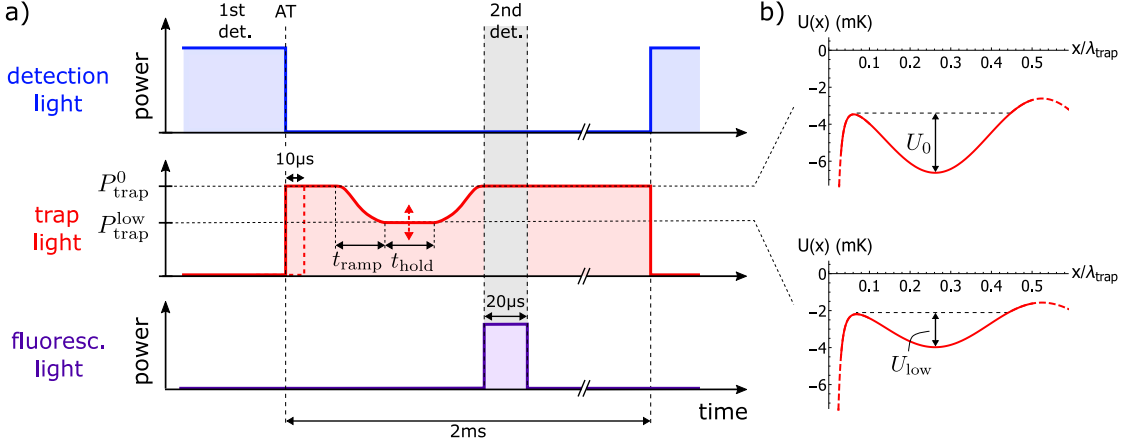


Figure 4.12: Measurement of the energy distribution of single trapped atoms. a) Experimental sequence used for the measurement. The trap laser power is adiabatically ramped down from $P_{\text{trap}}^0 = 20$ mW to $P_{\text{trap}}^{\text{low}}$ and, after a holding time t_{hold} , ramped up again. The power ramp is succeeded by a fluorescence detection pulse (2nd detection). We perform six sequences for the power ratios $P_{\text{trap}}^{\text{low}}/P_{\text{trap}}^0 = \{1, 0.8, 0.6, 0.4, 0.2, 0\}$, respectively, and two reference sequences with $P_{\text{trap}}^{\text{low}}/P_{\text{trap}}^0 = \{1, 0\}$. b) Trap potentials corresponding to the initial trap laser power value P_{trap}^0 and, exemplarily, for $P_{\text{trap}}^{\text{low}}/P_{\text{trap}}^0 = 0.6$.

oscillation frequency should be small at any time, t , compared to ω^2 , i.e.:

$$\dot{\omega}(t) \ll \omega^2(t). \quad (4.9)$$

For simplicity, we choose $\omega(t)$ to be a linear function, such that $\dot{\omega}(t) = \text{constant}$. Then, in harmonic approximation, the trap depth variation is a parabolic function

$$U(t) = \begin{cases} U_0 & \text{for } t \leq 0 \\ U_{\text{low}} + \frac{U_0 - U_{\text{low}}}{t_{\text{ramp}}^2} (t - t_{\text{ramp}})^2 & \text{for } 0 < t \leq t_{\text{ramp}}. \end{cases} \quad (4.10)$$

As we are limited by the lifetime of the trapped atoms, we have to find a trade-off between a ramp that is slow enough to fulfill adiabaticity and fast enough to yield a snap shot of the atomic temperature at a certain moment in time. Therefore, we choose a ramping time of $t_{\text{ramp}} = 75 \mu\text{s}$. With these choices, our trap depth variation fulfills the condition $\dot{\omega}(t) \approx 0.2 \omega^2(t)$ for the axial oscillation frequency, ω_x , until the lowered trap depth reaches $U_{\text{low},x} \approx 0.006 U_{0,x}$ and for the transverse oscillation frequencies, $\omega_{y/z}$, until $U_{\text{low},y/z} \approx 0.2 U_{0,y/z}$. This choice is justified, as we expect our atoms to be relatively hot due to the trap loading mechanism (cf. Sec. 4.2) and because the atoms are not actively cooled into the trap. After the down-ramp we hold the trap laser power constant for $t_{\text{hold}} = 50 \mu\text{s}$, as indicated in Fig. 4.12 a). The hold time is longer than the longest oscillation periods along the transverse axes, $2\pi/\omega_{y,z}$, thereby ensuring that an atom with a total energy $E > U_{\text{low}}$ indeed leaves the trap. Afterwards, we ramp up the trap power to the original value P_{trap}^0 with the time-reversed function. The experimental implementation of the trap laser power ramp is described in App. A.1.3.

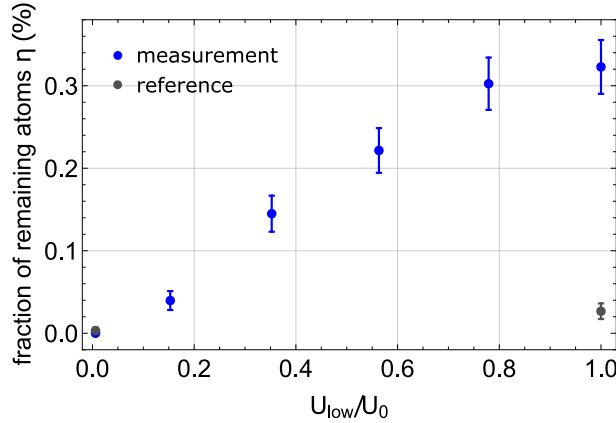


Figure 4.13: Measured fraction of atoms remaining in the lowered trap potential as a function of its depth U_{low} .

To perform the full temperature measurement, we run the experimental sequence illustrated in Fig. 4.12 for six trap powers with the power ratios $P_{\text{trap}}^{\text{low}}/P_{\text{trap}}^0 = \{1, 0.8, 0.6, 0.4, 0.2, 0\}$, respectively, where the initial trap power was chosen to be $P_{\text{trap}}^0 = 20$ mW. Furthermore, we run two reference sequences without trapped atoms, one without the trap power ramp ($P_{\text{trap}}^{\text{low}}/P_{\text{trap}}^0 = 1$) and one with the ratio $P_{\text{trap}}^{\text{low}}/P_{\text{trap}}^0 = 0$. The trap power ramp is succeeded by a fluorescence detection pulse to test the presence of the atom, see Fig. 4.12 a). The trap light was \perp -polarized.

In order to obtain the fraction η of atoms that are present after the trap lowering as a function of the trap depth U_{low} , we apply a second trigger threshold of $n_{\text{thr}}^{\text{2nd}} = 6$ to the fluorescence photon number probability distributions. The result is shown in Fig. 4.13. One can see, that η decreases with decreasing U_{low} . The atoms that contribute to this signal thus have an energy $E \leq E_{\text{max}} \equiv U_{\text{low}}$ in the lowered trap. The gray data points show the result of the reference sequences.

As stated before, an atom with initial energy E_0 is cooled to an energy E during the trap lowering. When the lowering is adiabatic, the action of the atom in the trap is conserved [117, 153], and, thus, there is a one-to-one mapping of the energy E to the corresponding E_0 . In order to connect the energy of the fraction of atoms that is lost when reducing the trap depth with the energy they possessed in the full potential, we assume that – if the trap lowering is adiabatic – the atoms will always stay in well-defined energy eigenstates. Comparing the eigenenergies of a given state for the different trap depths then allows us to calculate the initial energy of the lost atoms. For simplicity, we performed this calculation only in 1D along the axial direction (x). The resulting eigenenergies of the different trap eigenstates are shown in Fig. 4.14 a) as a function of the trap depth. The dashed line is a guide to the eye.

From this, together with a pointwise derivative ($\Delta\eta/\Delta U_{\text{low}}$) of the measured data in Fig. 4.13 we obtain an estimate of the energy distribution in the trap, which is shown in Fig. 4.14 b). As is apparent, the data cannot be described by a Boltzmann distribution, but is rather peaked toward higher energies. By fitting a Gaussian function to the data we find its maximum at an energy

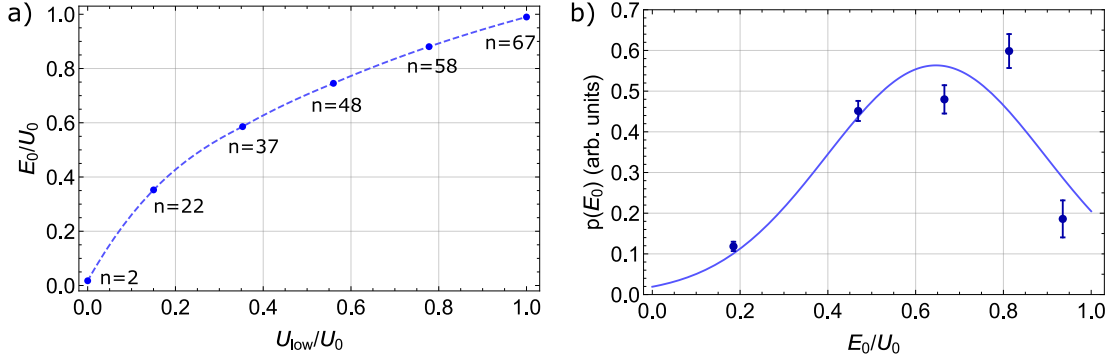


Figure 4.14: a) Eigenenergies of the different trap eigenstates in the original trap, E_0 , as a function of the trap depth. The dashed line is a guide to the eye. b) Energy distribution of the trapped atoms: derivative of the data in Fig. 4.13, where the abscissa was rescaled compared to that in Fig. 4.13 according to the one-to-one map of panel (a). The solid line is a Gaussian fit to the data.

$E_0 \approx 2/3 U_0 = k_B \times 1.8$ mK. This agrees with what we expect from our trap loading mechanism, where the energy of the trapped atom is predominantly determined by its kinetic energy due to the free fall and its position with respect to the trap center at the moment the dipole trap switches on. The resulting energy distribution is, thus, a convolution of the distributions of the kinetic energy and the potential energy due to these effects, respectively. In both cases, the probability for very cold atoms is small.

4.6.3 Heating mechanisms

In the previous section we found that the trapped atoms have a high energy after being trapped and we also observe a relatively short lifetime. In the following, we want to discuss several typical heating mechanisms present in optical dipole traps and estimate their contribution for our trap configuration and parameters.

Technical heating

Technical noise can result in a fluctuating trap potential. There are two types of fluctuations: fluctuations of the potential depth – and, hence, of the trap frequencies – and fluctuations of the trap center position. Both effects can have a strong influence on the oscillatory motion of the trapped atom and, thus, can lead to strong heating. When fluctuations of the first kind occur at twice a trap frequency it is called parametric heating. Fluctuations of the trap center position at a trap frequency lead to so-called resonant heating.

Parametric heating can be caused by fluctuations of the laser power $\Delta P_{\text{trap}} = P_{\text{trap}}(t) - \langle P_{\text{trap}} \rangle$ around the mean value $\langle P_{\text{trap}} \rangle$ (cf. Eq. (3.13)). The spectral density of the relative power

noise can be quantified by [154]

$$S_P(\nu)d\nu = \frac{\langle \Delta P_{\text{trap}}^2 \rangle_{d\nu}}{\langle P_{\text{trap}} \rangle^2} = \frac{\langle \Delta U^2 \rangle_{d\nu}}{\langle U \rangle^2} \quad (4.11)$$

In Ref. [155], the heating rate resulting from the laser power noise has been derived using a one-dimensional harmonic oscillator model to

$$\langle \dot{E} \rangle = \pi^2 \nu_i^2 S_P(2\nu_i) \langle E \rangle. \quad (4.12)$$

It shows that the average energy $\langle E \rangle$ increases exponentially for fluctuations occurring at the second harmonic of the trap frequency ν_i . Furthermore, the heating rate depends linearly on the average energy of the trapped atom.

In order to estimate the contribution of laser power fluctuations to the lifetime of our trapped atoms, we measured the relative power noise spectrum of the trap laser. For this purpose, the output of the fiber-beamsplitter in Fig. 3.9 was connected to a fast photodiode (PD). In this way, we capture possible power fluctuations originating from the laser itself or caused by the AOM driver. But also potential beam-pointing instabilities before the fiber-coupling will be translated into intensity fluctuations and would, thus, be measured as well. The electric signal of the PD was sent to an electronic spectrum analyzer³. Dividing the measured signal by the mean voltage of the PD signal and squaring the result yields the relative intensity noise, which is plotted in Fig. 4.15 a) (red data). The large peak at a frequency of 1 MHz stems from an artificially added modulation of the laser beam power, used to verify the proper function of the setup. The gray data has been taken for reference by blocking the trap laser beam.

In order to obtain the parametric heating rate, we first subtract the reference data from the actual data, and then apply Eq. (4.12) to the outcome. Here, we assume an average energy of the trapped atoms of $\langle E \rangle = 2/3 U_0$, corresponding to the result of our temperature measurement (cf. Sec. 4.6.2). The resulting parametric heating rate as a function of possible trap frequencies is shown in Fig. 4.15 b), where we have applied a binning with a bin width of $N_{\text{bin}} = 5$ data points. At twice our transverse trap frequencies, $2\nu_{y/z} = 142$ kHz (136 kHz) for \perp (\parallel -)polarized light, the corresponding heating rates amount to $0.8 U_{0,\perp}/s \approx 2.2$ $\mu\text{K}/\text{ms}$ ($0.6 U_{0,\parallel}/s \approx 1.1$ $\mu\text{K}/\text{ms}$). In case of the axial trap frequencies, $2\nu_x = 2.00$ MHz (1.72 MHz), the heating rates amount to $15 U_{0,\perp}/s \approx 41$ $\mu\text{K}/\text{ms}$ ($13 U_{0,\parallel}/s \approx 25$ $\mu\text{K}/\text{ms}$). In particular for the axial oscillation of the atom in the trap, the obtained heating rate is rather large. Given the assumed initial energy, it would correspond to a lifetime of about 18 ms (20 ms).

Resonant heating happens, when the trapping potential is shaken at the trap frequencies. One possibility for this to occur are beam-pointing instabilities originating from the laser. As mentioned above, in our setup such fluctuations of the beam position would be translated into power fluctuations due to the fiber coupling of the trap laser beam.

Since the trap standing wave is formed by retroreflection from the resonator surface, the relative phase between the incoming and the reflected beam is fixed and, consequently, the trap center position is fixed with respect to the resonator surface. In principle, vibrations of the

³DSA815, RIGOL

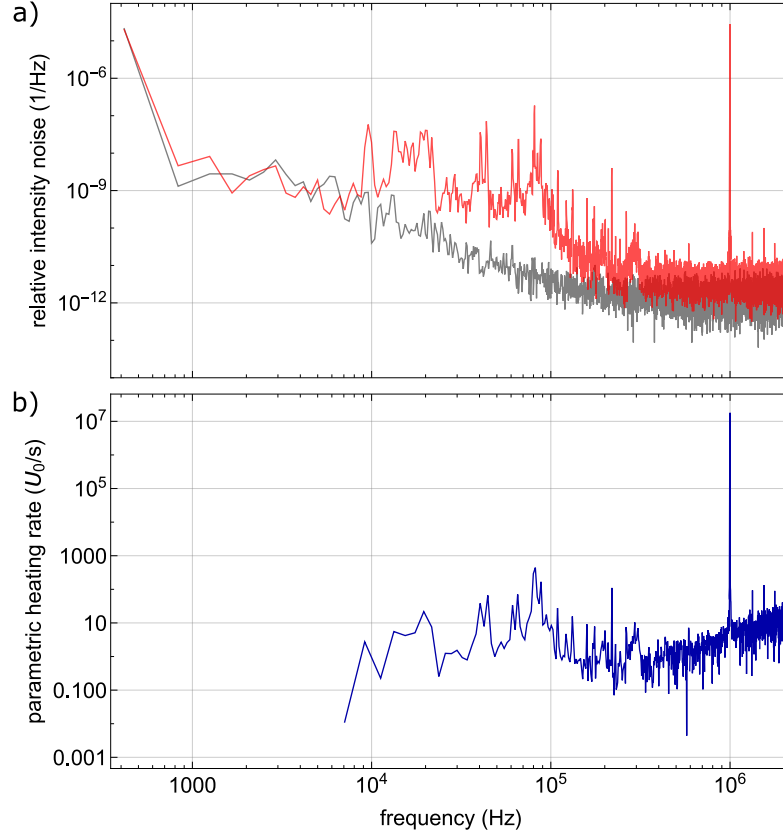


Figure 4.15: a) Relative intensity noise spectrum, $S_P(\nu)$, of the trap laser (red data). The gray data has been measured for reference with the laser beam blocked. The values of both data sets were determined from the measured raw data using Eq. (4.11). b) Parametric heating rate, obtained from the data in (a) using Eq. (4.12) and assuming an average energy of the trapped atoms of $\langle E \rangle = 2/3 U_0$. Here, the reference data has been subtracted from the actual laser-related data. Furthermore, the data has been smoothed by binning it with a bin width of $N_{\text{bin}} = 5$ data points.

resonator fiber itself could lead to shaking of the trapping potential. We can, however, practically exclude this possibility: we can infer from the typical residual transmission of light through the coupling fiber of 1-2 % (for the critically coupled empty resonator) that the fiber–resonator distance does not fluctuate by more than ~ 10 nm [59].

Recoil heating

A fundamental heating mechanism in an optical dipole trap is the energy gain of the atom associated with the spontaneous scattering of trap photons. Each scattering event transfers momentum to the atom due to the recoil, once when it is excited and once more when it decays. For scattering rates that are small with respect to the trap frequencies this leads to an average energy gain

of $2E_r$ per scattering event, and the corresponding average heating rate is therefore given by

$$\langle \dot{E} \rangle = 2E_r \Gamma_{sc}, \quad (4.13)$$

where $E_r = (\hbar k)^2 / 2m_{\text{Rb}}$ is the recoil energy with the wave number $k = 2\pi / \lambda_{\text{trap}}$ and the mass of the ^{85}Rb atom m_{Rb} . In far-detuned traps, the scattering rate – and consequently the heating rate – is typically small. We can calculate the scattering rate according to Eq. (3.11) for our trap parameters $\{P_{\text{trap}}, w_{\text{trap}}, \Delta_{\text{trap}}/2\pi\} = \{20 \text{ mW}, 3.5 \mu\text{m}, 1.68 \text{ THz}\}$ and obtain, at the center of the trap, $\Gamma_{sc} \approx 3.5 \text{ kHz}$. With that we can estimate the recoil heating rate to $\langle \dot{E} \rangle_{\text{rec}} = 1.3 \mu\text{K/ms}$. Assuming an initial energy of $2/3 U_0$, the atom should be able to scatter ~ 2500 (1700) photons before being heated out of the $\perp(\parallel)$ -polarized trap, which would correspond to a trap lifetime of $\sim 0.7 \text{ s}$ (0.5 s).

Scattering-induced dipole force fluctuations

In addition to technical issues, a fluctuating dipole potential can also originate – more fundamentally – from the different light shifts seen by the ground state and the excited state of the atomic dipole, respectively. In Fig. 3.8 we have plotted the position-dependent light shifts of the $5S_{1/2}$ ground state and of the $5P_{3/2}, m_{F'} = 0$ and $5P_{3/2}, m_{F'} = \pm 4$ excited state Zeeman levels. As is apparent, a trapped atom will experience a strong repulsive potential, when it is excited to the $5P_{3/2}$ state. Due to this effect, the inevitable scattering of trap photons will lead to additional heating of the trapped atom.

In the following, we want to estimate the average energy increase per scattering event due to this effect by analytically solving the classical equations of motion for the trapped atom. Since the heating is expected to be particularly large in strongly confining potentials, we restrict the calculation to one dimension, namely the x -axis. We assume harmonic potentials both for the ground and the excited state

$$U_g(x) = 1/2 m_{\text{Rb}} \omega_x^2 x^2 \quad (4.14)$$

$$U_e(x) = -1/2 m_{\text{Rb}} r \omega_x^2 x^2, \quad (4.15)$$

where $\omega_x = 2\pi \times 1.00(0.86) \text{ MHz}$ is the axial trap frequency for the $\perp(\parallel)$ -polarized trap (cf. Sec. 3.6.3) and r is the ratio of the light shifts. The tensor light shift of the excited state is considered only insofar that we average over the light shifts of the individual Zeeman sub-levels of the $F' = 4$ state. For our trap parameters we obtain for the ratio between the average excited state and ground state light shift at the trap center $r = \bar{\delta}_e / \delta_g \approx 0.72$.

In the classical picture, the atom oscillates in the ground state potential $U_g(x)$. At a random moment it is excited to the upper level by absorbing, e.g., a trap photon. The dipole force acts on the atom in the excited state according to Eq. (4.15), on average for a time duration equal to the excited state lifetime, before the atom decays back to the ground state. We can calculate the change in energy of the atom due to such an excitation event by analytically solving the equation of motion

$$-\frac{\partial U(x)}{\partial x} = m_{\text{Rb}} \ddot{x} \quad (4.16)$$

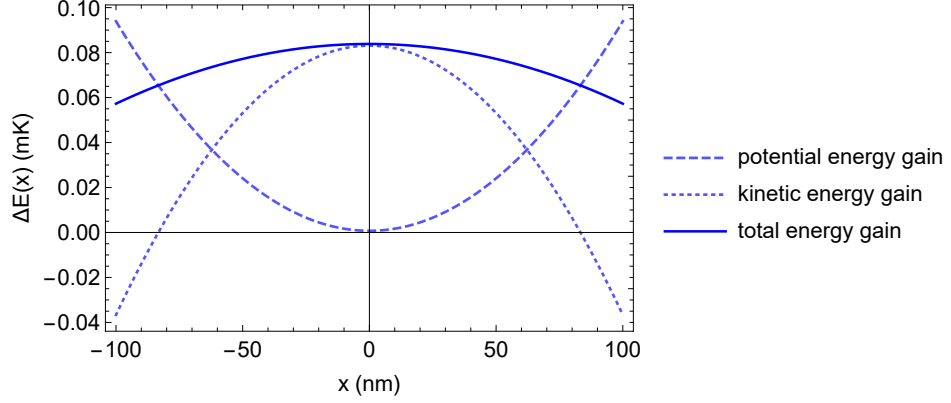


Figure 4.16: Energy increase per scattering event as a function of the atomic position in the trap, where the trap center is assumed to be at position $x = 0$. The dashed (dotted) line shows the gain in potential (kinetic) energy, and the solid line shows the total energy gain per scattering event. The result is plotted for an initial energy of $E_0 = 2/3 U_0$.

for an atom in the ground and the excited state potential, with the initial position $x(t = 0) = x_0$ and initial velocity $\dot{x}(t = 0) = v_0$. For each possible starting position x_0 , we calculate the potential and kinetic energy after the excited state lifetime for the rubidium atom of $\tau = 26.2$ ns [111]. Here, we also consider that, at each position x , the atom can be moving either in positive or negative x -direction, and we average over these two cases. The position-dependent velocity $v(x)$ is related to the oscillation amplitude x_{\max} , which in turn is determined by the initial energy E_0 of the atom in the trap, by

$$v(x) = \omega_x \sqrt{x_{\max}^2 - x^2}, \quad \text{with} \quad x_{\max} = \sqrt{2E_0/m_{\text{Rb}} \omega_x^2}. \quad (4.17)$$

Figure 4.16 shows the energy increase per scattering event for an initial energy of the trapped atom of $E_0 = 2/3 U_0$ as a function of the atomic position in the trap, where the trap center is assumed to be at $x = 0$. The dashed (dotted) line shows the gain in potential (kinetic) energy, and the solid line shows the total energy gain per scattering event. There is a net gain of the total energy for all positions in the trap. In the trap center, it is maximum and solely consists of kinetic energy. The position dependence is caused by the different slopes of the ground and excited state potentials due to the factor r in Eq. (4.15). The latter is also the reason for the loss of kinetic energy for the outer positions $|x| \gtrsim 60$ nm in the trap.

When averaging over all possible atomic positions in the trap, we obtain the average energy increase per scattering event as

$$\Delta E = E_0(1 + r) \sinh^2(\omega_x \tau \sqrt{r}). \quad (4.18)$$

Inserting our experimental parameters, the expression yields an energy increase per scattering event of $\Delta E = 0.034 E_0$ ($\Delta E = 0.025 E_0$) for the $\perp(\parallel)$ -polarized trap. For an initial energy of $E_0 = 2/3 U_0$, this corresponds to $\Delta E = 61 \mu\text{K}$ ($\Delta E = 32 \mu\text{K}$). From these heating rates

we estimate the number of photons that the atom can scatter before it is lost to 12 (16) for the $\perp(\parallel)$ -polarized trap. With a scattering rate of trap photons of $\Gamma_{sc} \approx 3.5$ kHz, this results in a lifetime of the atom in the trap of about 3.4 ms (4.6 ms), which is comparable with the lifetime measured in Sec. 4.6.1.

From the analysis in this section we can conclude that the largest contribution to heating of a single ^{85}Rb atom in our dipole trap originates from the light shift-induced repulsive excited state potential, which leads to a large energy increase each time the atom scatters a photon. As the corresponding heating rate increases linearly with the initial temperature of the atom, the effect is pronounced due to the high initial average temperature of the trapped atoms that we measured in Sec. 4.6.2. As a consequence, the relatively rare events of trap photon scattering lead to a corresponding lifetime that is on the order of the measured average lifetime (cf. Sec. 4.6.1).

Compared to this heating mechanism, the contribution of recoil heating is completely negligible. The expected trap lifetimes associated with laser power fluctuations in our setup are about an order of magnitude larger than the lifetime measured for our trapped atoms. Hence, we attribute the relatively short measured trap lifetime mostly to the scattering-induced heating via the repulsive dipole force in the excited state.

Compensation of the trap-induced light shift

In order to exploit the benefits of trapped single atoms in our experiment, we need to remove the large position-dependent light shift of the atomic transition introduced by the dipole trap (cf. Sec. 3.6.4). For some atomic species, a so-called magic wavelength exists [27, 156, 157]. A dipole trap operating at such a wavelength has the feature that the ground and excited state of the atomic transition are light-shifted in the same direction by the same amount, and thus the transition frequency remains unmodified. The idea of using magic wavelengths has been first proposed and experimentally demonstrated for the clock transition of strontium atoms in an optical lattice [156, 158] and shortly after for single dipole-trapped cesium atoms in the context of cavity quantum electrodynamics [27]. In the case of the D_2 line of the rubidium atom, there is no magic wavelength that would be suited for our experiment. Fundamentally, we require a trap wavelength that is red-detuned with respect to the D_2 line, such that the first intensity maximum of the standing wave near the resonator surface forms an attractive potential. Given this restriction, one magic wavelength at 791 nm was calculated for linearly polarized trap light [144]. The resulting light shifts, however, strongly depend on the magnetic sublevels of the excited state. Apart from that, red-detuned magic wavelengths have been found only at 1382 nm for circularly polarized light [159] and at 1397 nm for elliptically polarized trap light in combination with a magnetic field [160], both again unsuited for our experiment.

There is, however, a possibility to compensate for the transition shift even in the absence of a magic wavelength, which is to use an additional light field, that is superposed with the trap light field. With an appropriate choice of the optical power and detuning of this second light field, the trap-induced light shift of the excited state can be counteracted. Such a two-color scheme has been proposed and demonstrated in the context of RF spectroscopy and atomic clocks, where it managed to reduce the inhomogeneous frequency broadening in the hyperfine splitting of the ground state of optically trapped ^{85}Rb atoms [161]. In our experiment, we use a two-color light shift compensation scheme that has been experimentally demonstrated in [58]. There, it

has proven to suppress the inhomogeneous broadening of the optical transition frequency of an ensemble of trapped ^{85}Rb atoms.

In the first part of the chapter, the principle of this two-color light shift compensation scheme will be explained. Afterwards, we will theoretically evaluate the optimal working conditions for the light shift compensation and test the compensation scheme experimentally by measuring a fluorescence spectrum of single trapped atoms. Finally, the effects of the light shift compensation are further analyzed by measuring transmission spectra of the trapped atom–resonator system in the presence and absence of the additional light field.

The main experimental results of this chapter were published in [149].

5.1 Principle of light shift compensation

The energy level shifts of a ^{85}Rb atom exposed to the trap light field with power, P_{trap} , and detuning to the $5S_{1/2} \rightarrow 5P_{3/2}$ fine-structure transition, Δ_{trap} , have been determined in Sec. 3.5. For our experiment, the situation is illustrated in Fig. 5.1. We are mostly interested in the $(5S_{1/2}, F = 3) \rightarrow (5P_{3/2}, F' = 4)$ transition, as the resonator is locked to the unperturbed frequency of this transition, ω_0 , indicated by the blue arrow. In the presence of the red-detuned trap light, the energy levels of the $5S_{1/2}, F = 3$ ground state and the $5P_{3/2}, F' = 4$ excited state are pushed away from each other, thereby strongly detuning the atomic transition with respect to the resonator mode. For linear polarization of the trap light, the ground state exhibits only a scalar light shift, while for the excited state both the scalar and tensor polarizabilities, according to Eq. (3.16), contribute to the light shift. Due to the tensor light shifts the detuning of each $|Fm_F\rangle \rightarrow |F'm_{F'}\rangle$ transition depends on $|m_{F'}|$ (cf. Eq. (3.27)).

In order to efficiently interface the trapped atom with the resonator in the presence of this light shift, we have to compensate for the latter. This has to be achieved in a way, however, such that the ground state light shift remains mostly unaffected, as it is the basis for forming the trapping potential. The general idea is, therefore, to "push" the excited state levels down toward lower energies until the unperturbed transition frequency is recovered. This can be realized by exposing the atom to an additional light field – from now on called compensation light field. Its frequency, ω_c , is chosen such that it has a small red detuning, $\Delta_c \sim 1$ GHz, to the transition from the excited state $5P_{3/2}$ to the higher lying excited state $5D_{5/2}$, as depicted in Fig. 5.1 a). According to Eq. (3.8), the compensation light field then induces a relatively large light shift on the energy levels of this transition, even for small powers. The detuning of the compensation laser with respect to the D_2 transition, however, is large compared to Δ_c , due to the ~ 4 nm wavelength difference between the two fine-structure transitions. Hence, the compensation laser-induced light shift of the $5S_{1/2}$ energy level will be small. The compensation laser polarization is chosen to be aligned with the linear polarization of the trap field. Consequently, it will also induce a scalar and tensor light shifts in the $5P_{3/2}$ hyperfine manifold.

The green column in Fig. 5.1 a) illustrates the effect of increasing the compensation laser intensity, I_c , on the atomic levels in the presence of a fixed intensity, I_{trap} , of the trapping light field. With increasing I_c , both scalar and tensor light shifts of the $F' = 4$ excited states reduce, until the light shifts of the excited state Zeeman levels become equal to the shift of the ground state, indicated by the dashed blue line. Here, the trap-induced light shift of the

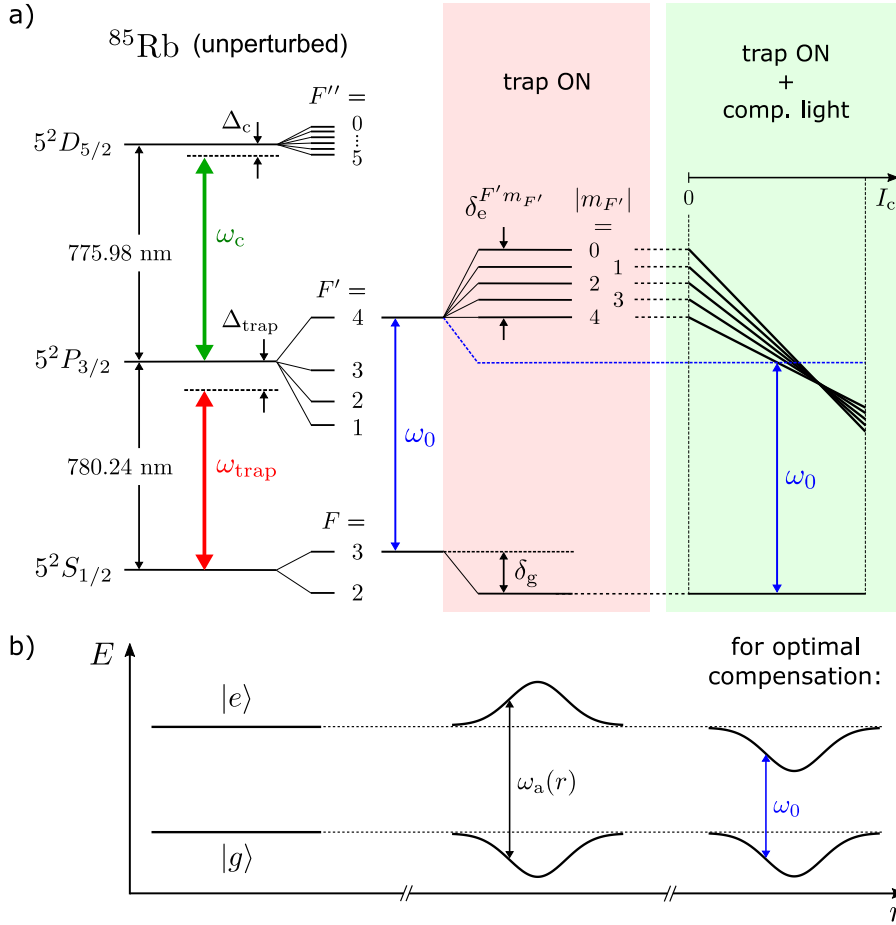


Figure 5.1: Illustration of the light shift compensation principle. a) The left-most panel shows the ^{85}Rb energy level structure relevant for the compensation scheme. The middle panel illustrates the light shift of the $(5S_{1/2}, F=3) \rightarrow (5P_{3/2}, F'=4)$ atomic transition, induced by the trap light with frequency ω_{trap} , for a fixed intensity I_{trap} . The right-most panel depicts how the $F'=4$ Zeeman levels are tuned across resonance, when increasing the intensity, I_c , of the compensation laser, in the presence of the trap light. b) Illustration of the spatial energy variation of the ground and excited state of a representative two-level atom, assuming a Gaussian trapping field, for the three different scenarios shown in panel (a).

$(5S_{1/2}, F=3) \rightarrow (5P_{3/2}, F'=4)$ transition is compensated and the unperturbed transition frequency, ω_0 , is recovered. However, due to the tensor light shifts, perfect compensation cannot be achieved simultaneously for all $F'=4$ Zeeman sublevels.

In practice, the trap light field has a three-dimensional intensity distribution (cf. Sec. 3.6.1), $I_{\text{trap}}(\mathbf{r})$, which causes the light shifts of the atomic ground and excited states to be dependent on the atomic position \mathbf{r} in the trap (cf. Sec. 3.6.4). This is illustrated in Fig. 5.1 b) for a two-level atom and a one-dimensional Gaussian intensity profile. In the presence of just the trap

light field, the atomic transition frequency is position-dependent: $\omega_a(r)$. The strength of the light shift compensation scheme now is, that it allows to counteract the spatial dependence of the trap-induced light shifts, if the compensation laser beam exhibits the same spatial intensity distribution as the trap field.

5.2 Calculation of the two-color light shifts

In this section, we want to quantify the influence of the compensation laser beam on the light shifts as a function of the intensity of the compensation field, I_c . With the formalism used in Sec. 3.5, we will therefore again calculate the energy shifts of the $5S_{1/2}, F = 3$ ground state and the $5P_{3/2}$ excited state manifold of a trapped atom, with the difference that the atom is now subject to both the trap and the compensation light fields. In order to find the new energy eigenvalues for a fine-structure state $|nJ\rangle$ of the atom, we thus have to diagonalize the interaction Hamiltonian

$$H_{\text{int}} = V_{\text{Stark}}^{\text{trap}} + V_{\text{Stark}}^c + V_{\text{hfs}} , \quad (5.1)$$

which describes the atom–light interaction with the two light fields as well as the hyperfine interaction. The Stark operator, V_{Stark} , and the non-zero matrix elements, $\langle nJFM | V_{\text{hfs}} | nJFM \rangle$, of the hyperfine interaction operator are given in Eqs. (3.15) and (3.24), respectively.

We have to evaluate Eq. (5.1) for the ground state, $|n, J\rangle = |5, 1/2\rangle$, and the excited state, $|n, J\rangle = |5, 3/2\rangle$. In the calculation of the polarizabilities $\alpha_{5,1/2}^{(K)}$ and $\alpha_{5,3/2}^{(K)}$ according to Eq. (3.16), we take the coupling to the same fine-structure states $|n'J'\rangle$ into account as described in Sec. 3.5.1 and Sec. 3.5.2, respectively. We assume that the polarization of the two light fields is linear and identical, and, therefore, insert the polarization vector $\mathbf{u} = (0, 0, 1)$ into Eq. (3.17). In this case, the contribution of the vector polarizability to the light shift is zero: $\alpha_{n,J}^{(K=1)} = 0$. As the tensor polarizability vanishes for $J = 1/2$ states (cf. Sec. 3.5.1), the $5S_{1/2}$ ground state only experiences a scalar light shift, i.e. all Zeeman levels are shifted by the same amount, δ_g . When diagonalizing the Hamiltonian in Eq. (5.1) for the excited state, $5P_{3/2}$, we first obtain the total frequency offset for each $|F'm_{F'}\rangle$ level from the $5P_{3/2}$ state in the absence of Stark and hyperfine interaction

$$\delta_{\text{tot}}^{F'm_{F'}}(I_c, I_{\text{trap}}) = \delta_{\text{hfs}}^{F'} + \delta_e^{F'm_{F'}}(I_c, I_{\text{trap}}) , \quad (5.2)$$

consisting of the F' -dependent frequency shift, $\delta_{\text{hfs}}^{F'}$, due to the hyperfine interaction and the F' - and $m_{F'}$ -dependent as well as intensity-dependent light shift, $\delta_e^{F'm_{F'}}(I_c, I_{\text{trap}})$. This is the same expression as in Eq. (3.25) for the trap-induced light shift, but now with an additional I_c -dependence. Accordingly, the shift of each $m_{F'}$ level with respect to the unperturbed energy of the $F' = 4$ level, which we are mainly interested in, is given by

$$\delta_{\text{tot}}^{F'm_{F'}}(I_c, I_{\text{trap}}) - \delta_{\text{hfs}}^{F'=4} . \quad (5.3)$$

The detuning of each $|Fm_F\rangle \rightarrow |F'm_{F'}\rangle$ transition with respect to the unperturbed frequency of the $(5S_{1/2}, F = 3) \rightarrow (5P_{3/2}, F' = 4)$ transition is then

$$\delta\nu(I_c, I_{\text{trap}}) = \delta_{\text{tot}}^{F'm_{F'}}(I_c, I_{\text{trap}}) - \delta_{\text{hfs}}^{F'=4} - \delta_g(I_c, I_{\text{trap}}) , \quad (5.4)$$

with $\delta_{\text{hfs}}^{F'=4} = 100.205 \text{ MHz}$ [111].

Based on the calculation procedure described above, we want to obtain a theoretical estimate for the light shift compensation in our dipole trap, which we will later compare to the experimental investigation presented in Sec. 5.5. To obtain absolute numbers for the ground and excited state two-color light shifts, we have to insert the expected trap and compensation laser intensities at the position of the atom into the Stark matrix elements given by Eq. (3.15). For now we will restrict this calculation to the case of an atom located at the trap center: $(x_0, y_0, z_0) = (205 \text{ nm}, 0, 0)$. The intensity distribution of the trap light has been calculated in Sec. 3.6.1 and, as both light fields are sent through the same fiber-coupled trap optics and have near-identical wavelengths ($\lambda_c \approx \lambda_{\text{trap}}$), we will assume the same distribution for the compensation laser beam. Then, according to Eq. (3.40) the trap and compensation laser intensities at the trap center are given by

$$I_l = \frac{2P_l}{\pi w_l^2} \times f_p(x_0), \quad (5.5)$$

where the index $l = \{\text{trap}, \text{c}\}$ indicates the trap or the compensation light, and $f_p(x_0)$ with $p = \{\perp, \parallel\}$ describes the intensity modulation in x -direction due to the partial standing-wave pattern given by Eqs. (3.38) and (3.39). We perform this calculation for linear polarization pointing along the y -axis (\perp -polarization) for both light fields, for which $f_{\perp}(x_0) = 1.43$. Furthermore, we use the following experimental values¹ for the trap power, the beam waist and the detunings: $\{P_{\text{trap}}, w_{\text{trap}} = w_c, \Delta_{\text{trap}}/2\pi, \Delta_c/2\pi\} = \{18.7 \text{ mW}, 3.5 \mu\text{m}, 1.68 \text{ THz}, 930 \text{ MHz}\}$. Δ_{trap} and Δ_c are taken with respect to the atomic fine-structure transitions as indicated in Fig. 5.1.

Figure 5.2 shows the results for the ground state light shift, δ_{g} , and the excited state level shifts, $\delta_{\text{tot}}^{F' m_{F'}} - \delta_{\text{hfs}}^{F'=4}$, as a function of the compensation laser power, P_c , since this parameter will be varied in the corresponding measurement (cf. Sec. 5.5). The ground state light shift is plotted in red, and the shift of the excited state is plotted in blue for the $F' = 4$ -level and in gray for the levels with $F' < 4$. The plot shows that the ground state light shift is independent of $m_{F'}$ and almost constant over the range of compensation laser powers, as intended. It amounts to

$$\delta_{\text{g}, \perp} \approx -129 \text{ MHz}. \quad (5.6)$$

For the $F' = 4$ excited state (blue), both scalar and tensor light shifts reduce with increasing compensation laser power, until the light shifts of the $m_{F'=4}$ levels sequentially become equal to the ground state light shift around a compensation laser power of about 0.25 mW. At these points, the unperturbed transition frequency, ω_0 , is recovered. When further increasing the power of the compensation laser, a setting occurs at which all Zeeman levels of $F' = 4$ intersect, indicated by the vertical dashed green line. For this power, the tensor light shift of the $5P_{3/2}$ excited state vanishes. The dotted gray lines show the shifts of the Zeeman levels of the $F' = 3, 2, 1$ manifolds. Some of these levels become resonant to the unperturbed transition frequency for lower compensation laser powers.

Based on the same calculation, we plot the transition shifts according to Eq. (5.4) for the individual excited state Zeeman levels. The result is shown in Fig. 5.3 for three discrete values

¹The given value for the beam waist, which is slightly larger than the measured beam waist (cf. Sec. 3.7.3), accounts for imperfect alignment of the trap optics and drifts of the latter.

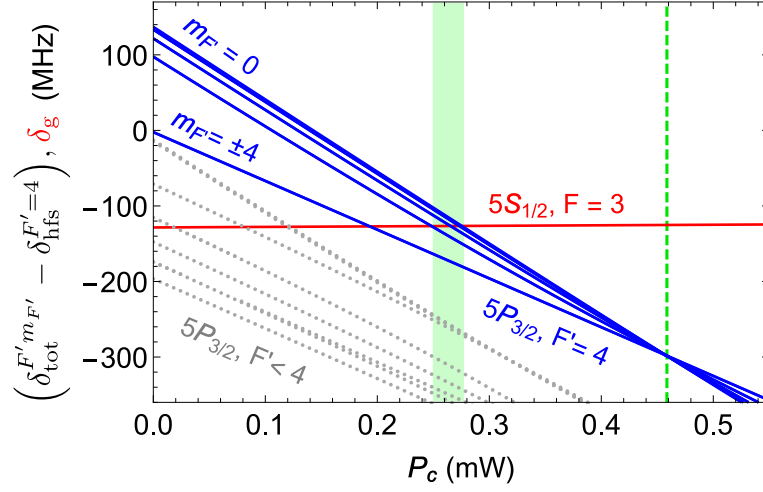


Figure 5.2: Calculation of the two-color light shifts of the $5S_{1/2}, F = 3$ ground state (red) and the $5P_{3/2}, F' = 4$ excited state (blue), for an atom located at the center of the trap and as a function of the compensation laser power, P_c . The trap and compensation laser beams are linearly polarized perpendicular to the plane of incidence (\perp -polarization, see Sec. 3.6.1). For \parallel -polarized light, the light shifts are about 10 % smaller (cf. Fig. 3.7). The calculation is performed for the parameters $\{P_{\text{trap}}, w_{\text{trap}} = w_c, \Delta_{\text{trap}}/2\pi, \Delta_c/2\pi\} = \{18.7 \text{ mW}, 3.5 \mu\text{m}, 1.68 \text{ THz}, 930 \text{ MHz}\}$. The dotted gray lines show the shifts of the lower lying F' -levels of the excited state.

of the compensation laser power. If $P_c = 0 \text{ mW}$, the detuning is solely caused by the trap light. For $P_c = 0.193 \text{ mW}$, both scalar and tensor contributions to the light shift are reduced. The cycling transitions to the outermost Zeeman levels are shifted back to the unperturbed transition frequency. At a power of $P_c = 0.457 \text{ mW}$, the tensor light shifts vanish, and the original excited state hyperfine structure is recovered, although now at a detuning of about 170 MHz from the unperturbed transition frequency.

For the above calculations, we assumed the atom to be at a fixed position, namely in the center of the trap. However, in Sec. 4.6.2 we experimentally found that the single trapped atoms have a high average energy in the trap potential, and in Sec. A.3 we simulate the corresponding position distribution of the atoms based on the measured energy distribution. Thus, the knowledge of the light shifts at other positions than the trap center will be relevant for the understanding of the experimental results.

Let us first again assume that the intensity distributions of the trap and the compensation light fields are identical, as desired. In this case, the intensities of both light fields are maximum in the trap center, i.e. the corresponding two-color light shifts represent an upper bound. At other atomic positions, $\mathbf{r} = (x, y, z)$, in the trap, the intensities of both light fields are smaller and, thus, the light shifts are smaller. However, the ratio $I_{\text{trap}}(\mathbf{r})/I_c(\mathbf{r})$ is independent of the position. This means, that the point of optimal compensation – where the excited state light

5.3. Residual mismatch of the intensity distributions and resulting position dependence of the two-color light shifts

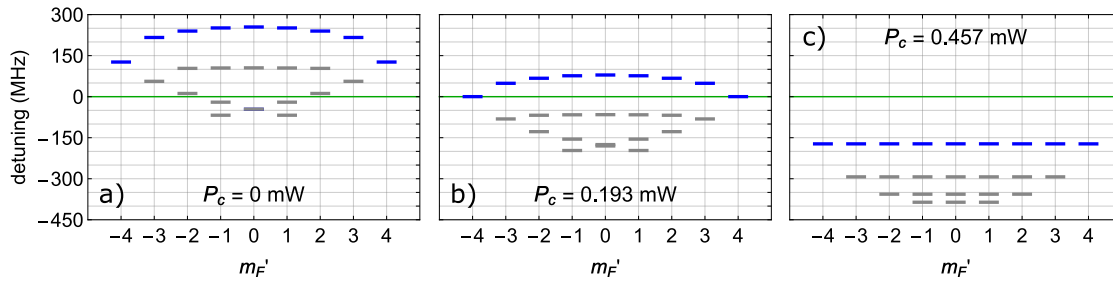


Figure 5.3: Detunings of the light-shifted transition frequencies between the $5S_{1/2}$, $F = 3$ ground state and the $5P_{3/2}$ excited state manifold with respect to ω_0 , for $\{P_{\text{trap}}, w_{\text{trap}} = w_c, \Delta_{\text{trap}}/2\pi, \Delta_c/2\pi\} = \{18.7 \text{ mW}, 3.5 \mu\text{m}, 1.68 \text{ THz}, 930 \text{ MHz}\}$ and three different values of the compensation laser power: a) in absence of the compensation laser, b) for the case where the light shift of the cycling transition is canceled ($P_c = 0.193 \text{ mW}$), c) for the case of vanishing tensor light shifts ($P_c = 0.457 \text{ mW}$).

shifts are equal to the ground state light shift – remains the same as in Fig. 5.2. In other words, if the power of the compensation field, P_c , is adequately chosen, the trap-induced scalar light shift of the transition can be canceled in the entire trapping volume, i.e. independently of the atomic position in the trap.

In the course of our measurements, however, it became apparent that the intensity distributions of the trap and compensation laser fields did not perfectly match. The reasons and the consequences of this will be described in the following section.

5.3 Residual mismatch of the intensity distributions and resulting position dependence of the two-color light shifts

In our experiment, we send the trap and compensation laser beams simultaneously through our fiber-coupled trap optics (cf. Sec. 4.1). The two light fields have similar, but not identical, wavelengths $\lambda_{\text{trap}} = 783.68 \text{ nm}$ and $\lambda_c = 775.98 \text{ nm}$, respectively. Due to the small wavelength difference of $\sim 4 \text{ nm}$, the respective periodicities of the trap and compensation laser standing waves – given by $\lambda/2 \cos \theta$ – slightly differ from each other. At the location of our trap potential, the resulting mismatch between the two standing waves is, however, negligible.

A more significant mismatch is caused by chromatic aberrations of our trap optics. Chromatic aberration is a lens effect that arises from dispersion, i.e. from the wavelength-dependence of the refractive index $n(\lambda)$ of the lens material. As a consequence, the focal length of the lens differs for light beams of different wavelengths and, thus, their foci are displaced with respect to each other along the beam axis. The refractive index of the lenses in our trap optics (N-BK7 glas) increases with decreasing wavelength in the visible range. Thus, the compensation laser beam ($\lambda_c = 775.98 \text{ nm}$) is refracted more strongly than the trapping beam ($\lambda_{\text{trap}} = 783.68 \text{ nm}$), i.e. its focus is closer to the lens than the trap focus, as depicted in the inset of Fig. 5.4 a). We estimated the displacement between the trap and compensation laser foci via a ray tracing

calculation to about $\Delta x_{\text{chrom}} \approx 95 \mu\text{m}$, where we took the two lenses and the vacuum viewport into account. If we assume the two light fields to be ideal Gaussian beams [66], each with a waist of $w_0 \approx 3.5 \mu\text{m}$, this displacement would be equivalent to almost two Rayleigh lengths ($x_{\text{R}} = \pi w_0^2 / \lambda \approx 50 \mu\text{m}$). Such a large displacement would mean that the radius of the compensation laser beam at the position of the trap waist is enlarged to up to $\sim 7.5 \mu\text{m}$.

We want to analyze the influence of the foci displacement on the two-color light shifts as a function of the position. Here, we assume that the trap waist is positioned onto the resonator surface ($w_{\text{trap}}(x=0) = w_0$), as depicted in the inset of Fig. 5.4 a). The trap and compensation laser beams are reflected from the surface, each forming a standing wave (not shown in the inset), and the atoms are trapped in the first intensity maximum of the trap light standing wave. As the trap center is only about 200 nm away from the resonator surface, we can approximate the intensity distributions of the two light fields at the position of the atom, analogous to Eq. (3.40), by

$$I_{\text{trap}}(x, \rho) = \frac{2P_{\text{trap}}}{\pi w_0^2} \times f_p(x) e^{-2\rho^2/w_0^2}, \quad (5.7)$$

$$I_{\text{c}}(x, \rho, P_{\text{c}}) = \frac{2P_{\text{c}}}{\pi w_{\text{c}}(x)^2} \times f_p(x) e^{-2\rho^2/w_{\text{c}}(x)^2}. \quad (5.8)$$

The first terms in the product are the intensity magnitudes $I_{0,\text{trap}}$ and $I_{0,\text{c}}$, respectively. The function $f_p(x)$ with $p = \{\perp, \parallel\}$ is given in Eq. (3.38) and describes the standing-wave intensity modulation in axial direction for the case of linear polarization perpendicular (\perp) or parallel (\parallel) to the plane of incidence (x - z -plane). In transverse direction ($\rho = \sqrt{y^2 + z^2}$) the two beams have Gaussian intensity profiles, described by the last terms in Eqs. (5.7) and (5.8), respectively.

In the above expressions, the intensity modulations of the trap and the compensation laser are assumed to be identical in axial direction (x). This is not perfectly true due to their small wavelength difference of $\sim 4 \text{ nm}$, as discussed above, but Eqs. (5.7) and (5.8) are sufficiently good approximations. In transverse direction (ρ), however, the Gaussian beam profiles of the two light fields do not perfectly overlap, if there is a mismatch between the beam radii at the position of the atoms due to chromatic aberrations, i.e. if $w_{\text{c}}(x \approx 0) > w_0$, see Fig. 5.4 a). As a consequence, the position dependence of the trap-induced light shift of the atomic transition cannot be fully eliminated by the compensation laser beam. In other words, there is no setting of the compensation laser power, for which the unperturbed transition frequency, ω_0 , is recovered everywhere in the trap potential.

To illustrate this, we calculate the two-color light shifts as a function of the compensation laser power as we did it in Fig. 5.2 for the trap center, but now also taking the position dependence into account by employing the above expressions for the intensity distributions. For this calculation, we assume both light fields to be \perp -polarized. Furthermore, we insert the same parameter values for the trap and compensation laser beams as in Fig. 5.2. As the only difference, we assume a beam radius ratio at the position of the atoms of $w_{\text{c}}(x \approx 0)/w_0 \approx 1.5$, which is a result of the experimental investigation of the light shift compensation that will be described in Sec. 5.5.

5.3. Residual mismatch of the intensity distributions and resulting position dependence of the two-color light shifts

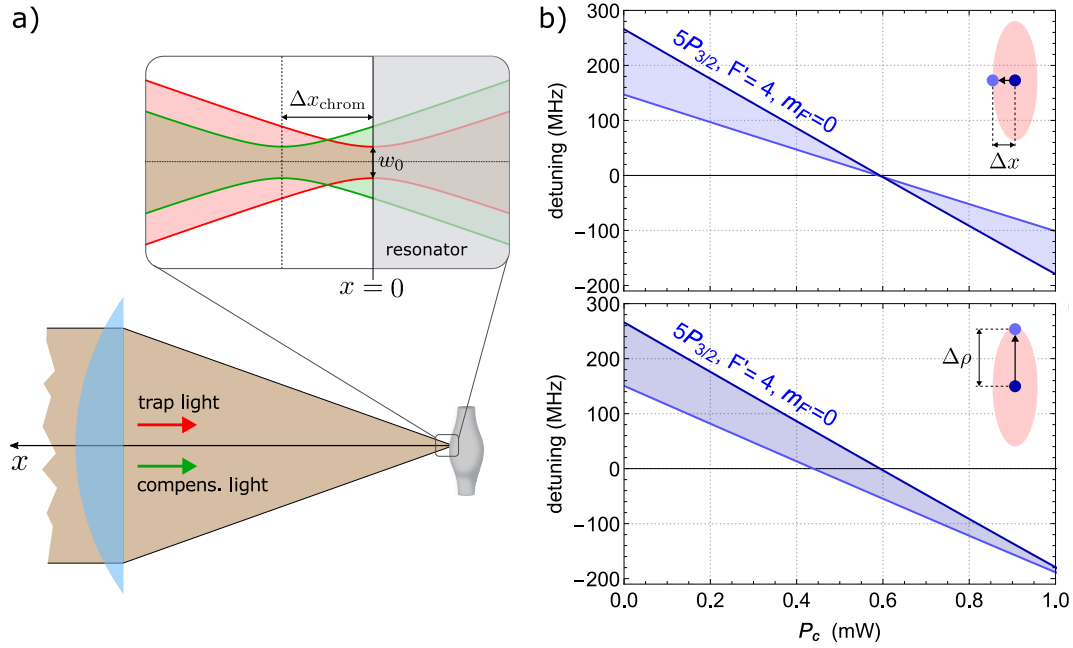


Figure 5.4: Illustration of the effect of the chromatic aberrations of our focusing optics. a) The compensation laser beam (green) is focused a few tens of micrometer closer to the lens than the trap beam (red). b) Position dependence of the detuning of the $(5S_{1/2}, F = 3) \rightarrow (5P_{3/2}, F' = 4, m_{F'} = 0)$ atomic transition with respect to its unperturbed value, according to Eq. (5.4), for an atom moving from the trap center to the trap potential boundary along the axial (upper plot) and the transverse direction (lower plot), respectively.

Figure 5.4 b) shows the calculated distribution of the position-dependent detuning of the atomic transition due to the two-color light shifts, $\delta\nu$, according to Eq. (5.4). For better visibility, only the result for the $(F' = 4, m_{F'} = 0)$ level is shown. We plot here, for illustration purpose, the detuning corresponding to the possible positions of a trapped atom on the x -axis (upper plot) and on a transverse axis (lower plot), as depicted in the insets. The dark blue solid lines show the detuning for an atom in the trap center and are, thus, equal to the difference between the light shift of the $(F' = 4, m_{F'} = 0)$ level and the ground state light shift in Fig. 5.2. The light blue solid lines correspond to the outermost positions in the trap, which we define by the maximum possible potential energy due to the van der Waals interaction, see Sec. 3.6.2. This allows maximum distances from the trap center in the two directions of $\Delta x = 150$ nm and $\Delta \rho = 1.85$ μ m, respectively. The shaded areas between the solid lines show the light shifts for the intermediate positions.

In the absence of the compensation laser ($P_c = 0$), the detuning is the same along both directions. The width of the plotted detuning band illustrates the maximum inhomogeneous broadening of the atomic transition frequency due to the position-dependent light shift induced by the trap light field. As in x -direction the trap and compensation laser intensity patterns match, in the upper plot this broadening reduces with increasing compensation laser power,

until it vanishes at a power of $P_c \approx 600 \mu\text{W}$. This optimal compensation laser power is now larger than in Fig. 5.2, because we assumed a larger compensation laser beam radius. However, the two-color light shifts behave differently in transverse direction, where the Gaussian intensity profiles of the trap and the compensation laser do not match because $w_c \neq w_0$. With increasing compensation laser power, the broadening reduces less significantly and there is no single P_c -value for which the position dependence of the detuning is completely canceled. The effect of this non-optimal compensation of the trap-induced light shifts on our experimental results will be discussed in Sec. 5.5 and Sec. 5.6.

5.4 Compensation laser setup and offset-lock

Figure 5.5 shows the compensation laser setup. The laser source is a widely tunable diode laser², whose lasing wavelength is set to about 776 nm. It has an output power of about 50 mW, which is split into two parts using a $\lambda/2$ -waveplate and a polarizing beamsplitter (PBS) cube. The reflected beam passes through an absorption spectroscopy setup, which will be explained below, and the transmitted beam is the main beam that will be employed for the measurement. It passes an acousto-optical modulator (AOM), which allows for independent switching of the light field and controlling its power. Then, the beam is coupled into a polarization-maintaining (PM) fiber after passing through a Berek compensator (BC). The PM fiber guides the compensation light from the laser table to the experiment table, where it is combined with the trap light (cf. Fig. 4.2) and subsequently coupled into the trap optics.

The task of the compensation laser is to induce a light shift predominantly on the $5P_{3/2}$ excited state, while not affecting the $5S_{1/2}$ ground state. To achieve this, we choose a small red detuning to the $5P_{3/2} \rightarrow 5D_{5/2}$ transition ($\Delta_c/2\pi < 1$ GHz). This, however, means that drifts of the laser frequency of just a few tens of MHz would considerably change the induced light shift. Thus, the compensation laser frequency has to be actively stabilized with the desired detuning to the frequency of the $5P_{3/2} \rightarrow 5D_{5/2}$ atomic transition. For this purpose, we perform absorption spectroscopy of this transition using rubidium atoms in a heated vapor cell, which will provide a reference signal and is explained in the following.

5.4.1 Two-photon spectroscopy

The setup for the absorption spectroscopy is also shown in Fig. 5.5. We use a two-step excitation scheme along the lines of [162, 163]. As a first step, atoms in a rubidium (Rb) vapor cell are excited to the $5P_{3/2}$ state by a 780 nm pump laser (ω_{pump}), which is locked close to resonance with respect to the $5S_{1/2}, F = 3 \rightarrow 5P_{3/2}$ transition of the ^{85}Rb atom, see Fig. 5.6 a). This pump beam is derived from our MOT-laser setup (cf. Sec. 2.4.4) and we use an optical power of about 10 mW. For the second excitation step, we use about 2 mW of the counter-propagating 776 nm probe laser beam that is derived from the Velocity laser (ω_{probe}). Atoms that are excited to the $5P_{3/2}$ state by the pump beam can absorb probe light and be excited on the $5P_{3/2} \rightarrow 5D_{5/2}$ transition. Both the pump and probe beams are linearly polarized, but orthogonal with respect to each other.

²New Focus, Velocity TLB 6700

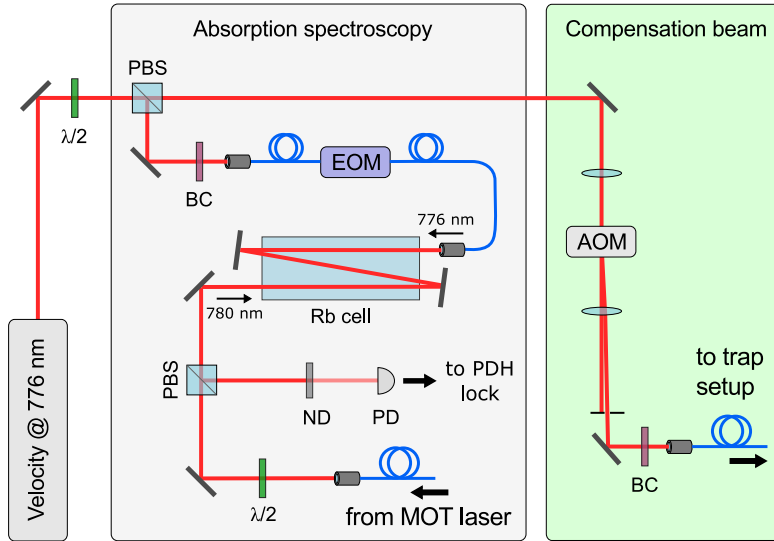


Figure 5.5: Laser setup for the generation of the frequency-stabilized compensation light field. The light from a commercial tunable diode laser (Velocity laser) with an output power of 50 mW, tuned to 776 nm, is split into two branches: one that goes as a probe beam into a setup for absorption spectroscopy of the excited state and one that provides the main beam for the experiment. The pump light at 780 nm required for the two-photon spectroscopy is derived from the MOT laser (cf. Sec. 2.4.4) and sent through the rubidium (Rb) vapor cell from the opposite side (see details in the main text). The transmission signal of the probe beam, measured with the photodiode (PD), is sent to the Pound-Drever-Hall (PDH) frequency stabilization setup, see Fig. 5.7 a).

In order to obtain the absorption spectrum of the probe beam, we scan its frequency across the $5P_{3/2} \rightarrow 5D_{5/2}$ atomic resonance and measure its transmission through the vapor cell with a photodiode (PD). From this, we obtain an absorption spectrum as the one shown in Fig. 5.6 b). To improve the absorption signal, we heat the vapor cell to between 50 and 60 °C. For this purpose, we surround the cell with an aluminium tube that is closed on each side by a glass window. A current-carrying heating wire is wound around the aluminium tube, such that the cell is heated uniformly. This increases the vapor pressure inside the cell and, thus, the number of atoms absorbing the probe light. Here it is important not to increase the temperature too much, as beyond 60 °C two-body collisions of rubidium atoms will lead to a depletion of the population in the $5P_{3/2}$ state, resulting in a decreased absorption on the $5P_{3/2} \rightarrow 5D_{5/2}$ transition [163]. As an additional measure to increase the absorption signal, we send the laser beams along multiple passes through the cell, which further increases the number of atoms interacting with the light.

In the transmission signal four dips are visible (see Fig. 5.6 b)), which correspond to the absorption via the two-photon transitions between the $5S_{1/2}, F = 3$ state and the $F'' = \{5, 4, 3, 2\}$ hyperfine levels of the $5D_{5/2}$ state of the ^{85}Rb atom. One would also expect a dip corresponding to the two-photon transition to the $F'' = 1$ level. A transmission dip corresponding to a transition to the $F'' = 0$ level is not visible, because the transition is forbidden according to the selection rules for electric-dipole transitions, as will be discussed below. The solid line is

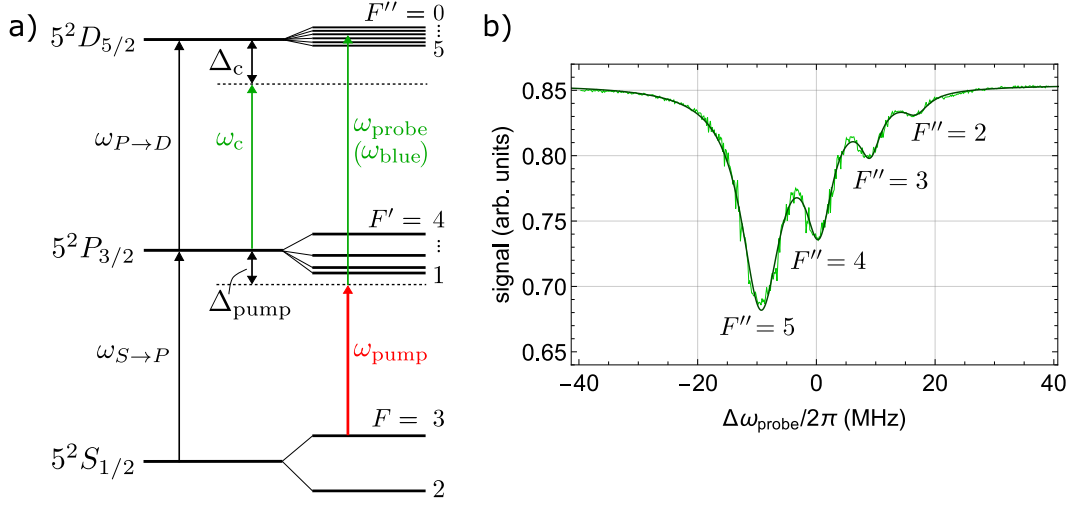


Figure 5.6: Two-photon spectroscopy. a) Energy level scheme of the ^{85}Rb atom. b) Measured absorption signal of the $5P_{3/2} \rightarrow 5D_{5/2}$ transition. The depth of the absorption dip amounts to $\sim 20\%$ of the full transmission.

a fit of a sum of Lorentzian absorption dips. Using the dip positions resulting from the fit and the hyperfine splittings of the $5D_{5/2}$ state reported in [162], we can approximately rescale the abscissa to show the probe detuning ($\Delta\omega_{\text{probe}}$).

To better understand the measured absorption signal, let us have a closer look at the mechanism of the two-step excitation. It starts with the first excitation step from the $F = 3$ ground state. As the frequency of the pump laser is fixed, it has different detunings to each intermediate hyperfine level F' of the $5P_{3/2}$ hyperfine manifold. However, due to the thermal motion of the atoms in the vapor cell, the pump laser becomes resonant with the transitions to the different F' -levels for certain velocity classes of atoms. Considering the selection rules for electric-dipole transitions, $\Delta F = 0, \pm 1$, the pump laser can only excite the $F' = \{4, 3, 2\}$ levels and the probe laser can further excite those atoms to the $F'' = \{5, 4, 3, 2, 1\}$ levels. This means, that the two-photon resonances corresponding to the different F'' levels, thus, have contributions from excitation paths via three F' -levels. Here, the strength of the contribution depends on the respective transition strengths as well as the number of atoms belonging to a certain velocity class [162]. As the probe beam is counter-propagating with respect to the pump beam, the Doppler shift of the two-photon resonance is nearly canceled, except for a small Doppler mismatch due to the small wavelength difference between the two exciting beams: ~ 780 nm and ~ 776 nm, respectively. For the most probable (mp) velocity of the ^{85}Rb atoms in the heated cell of $v_{\text{mp}} = \sqrt{2k_B T/m_{\text{Rb}}} \approx 250$ m/s [19] this mismatch is about 1-2 MHz.

5.4.2 Frequency offset lock

The absorption spectroscopy provides a reference signal for stabilizing the frequency of the compensation laser to the $5P_{3/2} \rightarrow 5D_{5/2}$ atomic transition. However, as described before, we

need to lock the laser with a small frequency offset

$$\Delta_c = \omega_{P \rightarrow D} - \omega_c, \quad (5.9)$$

to this transition. Here, ω_c denotes the output frequency of the Velocity laser and $\omega_{P \rightarrow D}$ is the transition frequency between the fine-structure levels $5P_{3/2}$ and $5D_{5/2}$, see also Fig. 5.6 a). To enable the offset locking, the probe light is sent through an electro-optical modulator (EOM) before entering the Rb vapor cell, see Fig. 5.5. The EOM modulates the phase of the probe light with its RF-driving frequency, which we choose to be $\omega_{\text{EOM}} = 2\pi \times 1.24$ GHz. As a consequence, the light interacting with the atoms contains (predominantly) three frequency components: one at the laser output frequency frequency, ω_c , and two first-order sideband frequencies, $\omega_c \pm \omega_{\text{EOM}}$. When the probe light is scanned across resonance, we thus observe three copies of the absorption signal of Fig. 5.6 b). The idea now is to stabilize the laser to the absorption of the "blue" sideband with frequency

$$\omega_{\text{blue}} = \omega_c + \omega_{\text{EOM}}. \quad (5.10)$$

In this case, the laser frequency ω_c will be red-detuned to the $5P_{3/2} \rightarrow 5D_{5/2}$ transition, as desired. Note, that in our experiment the resulting detuning is, however, not equal to the driving frequency of the EOM: $\Delta_c \neq \omega_{\text{EOM}}$. The reason is that our pump laser is not exactly resonant with the $(5S_{1/2}, F = 3) \rightarrow 5P_{3/2}$ transition, but has a non-zero detuning

$$\Delta_{\text{pump}} = \omega_{S \rightarrow P} - \omega_{\text{pump}}, \quad (5.11)$$

as indicated in Fig. 5.6 a). Here, $\omega_{S \rightarrow P}$ is the transition frequency between the fine-structure levels $5S_{1/2}$ and $5P_{3/2}$. The two-photon resonance condition, thus, requires for the blue sideband frequency

$$\omega_{\text{blue}} = \omega_{P \rightarrow D} + \Delta_{\text{pump}}. \quad (5.12)$$

Inserting Eq. (5.10) and (5.12) into Eq. (5.9), we obtain

$$\Delta_c = \omega_{\text{EOM}} - \Delta_{\text{pump}}. \quad (5.13)$$

The 780 nm pump laser beam is branched off at the output of the MOT laser. Thus, the pump detuning Δ_{pump} is determined by the setup and the locking scheme of the MOT laser system (cf. Sec. 2.4.4) and it amounts to $\Delta_{\text{pump}}/2\pi \approx 310$ MHz. Equation (5.13) then yields the compensation laser detuning

$$\Delta_c/2\pi \approx 930 \text{ MHz}, \quad (5.14)$$

which is the value that we also used for the theoretical predictions in the previous section.

To stabilize the frequency of the blue sideband to the $5P_{3/2} \rightarrow 5D_{5/2}$ atomic resonance, we use the well-established Pound-Drever-Hall (PDH) technique [108]. Originally, it was proposed for stabilizing the frequency of a laser to a (more) stable optical cavity [164]. But it works analogously when the reference is provided by an atomic resonance, as in our case. We saw in Fig. 5.6 b) that the F'' -hyperfine levels lie very close to each other, and hence the individual absorption lines are not very well resolved. We will thus take the full absorption spectrum as a reference for the stabilization.

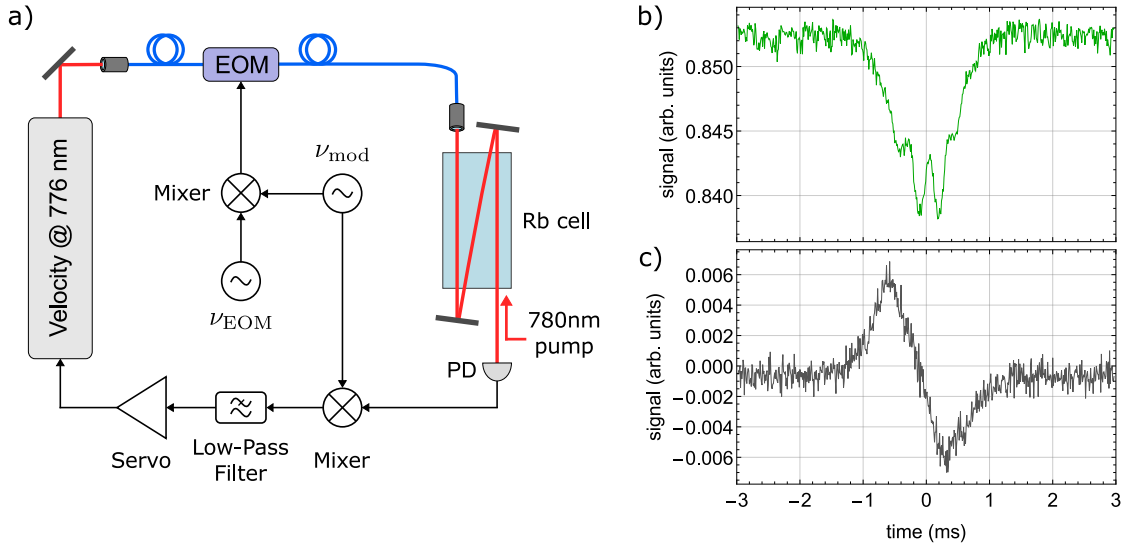


Figure 5.7: Frequency offset lock. a) Schematic of the setup for the Pound-Drever-Hall frequency stabilization scheme. b) Measured absorption of the blue sideband on the $5P_{3/2} \rightarrow 5D_{5/2}$ transition. c) Corresponding error signal, generated by the setup depicted in panel (a).

Key to counteracting deviations of the laser frequency from resonance is to know to which side of the resonance the laser is momentarily drifting. The absorption signal itself does not give this information, as it is symmetric around resonance. The frequency-dependent phase of the light interacting with the atoms, however, is antisymmetric. The problem is that this phase cannot be measured directly, but the PDH technique provides a way to indirectly measure it. The idea is to modulate sidebands onto the light to be stabilized, which provide a phase reference [108].

Figure 5.7 a) shows a simplified scheme of the used setup. Remember, that in our case the light to be stabilized is the blue sideband with frequency $\omega_{\text{blue}} = \omega_c + \omega_{\text{EOM}}$. To modulate sidebands onto this light, we drive the same EOM additionally with a frequency $\omega_{\text{mod}} \ll \omega_{\text{EOM}}$, provided by a local oscillator. We choose the modulation frequency to be $\omega_{\text{mod}} \approx 5$ MHz, which is smaller than the spectral width of the $5D_{5/2}$ hyperfine structure. When the light, which now has frequency components $\omega_{\text{blue}} \pm \omega_{\text{mod}}$, interacts with the atoms, we observe an absorption signal on the PD as shown in Fig. 5.7 b). It looks different than in Fig. 5.6 b) because it is a sum of the absorption of the carrier and the two sidebands. Apart from this intensity signal, the PD detects beat signals between the sidebands, as well as between the carrier and the sidebands. We are only interested in the latter, which oscillate at the modulation frequency, as they contain information on the frequency offset. This beat signal can be isolated by mixing the PD signal with the local oscillator and low-pass filtering the mixer output signal. This yields the so-called error signal, which is shown in Fig. 5.7 c). It is antisymmetric around resonance and, thus, serves well to give proper feedback to the laser. In practice, the feedback is provided by an electronic PID controller (servo), which acts on the piezo-electric actuator controlling the lasing frequency of the laser.

5.5 Experimental verification of the light shift compensation

With the compensation laser being set up, we can now test the light shift compensation scheme explained in Sec. 5.1 and 5.2. We do this by measuring fluorescence of the trapped atom as a function of the compensation laser power.

Figure 5.8 a) depicts the experimental sequence used to perform this measurement. When an atom is detected in the evanescent field of the resonator mode via the detection light, the FPGA-based detection system triggers the detection light to switch off and the trap light to switch on. Additionally, we now sent the compensation light with variable power, P_c , onto the atom via the trap optics. In the presence of both trap and compensation light we send a weak fluorescence probe light for 100 μs through the trap optics, which is resonant to the resonator and the unperturbed atom. Fluorescence photons emitted by a trapped atom are detected with the pair of SPCMs in Port 2, see Fig. 4.1. Directly after the probing, a strong fluorescence pulse is applied to test the presence of the atom. The compensation laser is switched off after the probing, such that the fluorescence detection is performed under the same conditions in each sequence part. We expect the fluorescence rate in the probing window to depend on the power setting of the compensation laser, and it should peak at the point of optimal light shift compensation. In order to not heat the atom out of the trap during probing, we limit the probe power to $P_{\text{probe}}^{\text{fluor}} \approx 1 \text{ nW}$, corresponding to about $2 I_{\text{sat}}$. This power is low enough such that a large fraction of the trapped atoms survive the probing, which most likely can be explained by the non-optimal light shift compensation that we discussed in Sec. 5.3. The pulses for the fluorescence probing and detection were generated from the same laser beam. In order to enable fast switching between the two different optical powers we used a home-built AOM-driver, which is described in App. A.4.1. The above described sequence is executed for a set of compensation laser powers $P_c = \{0, 275, 365, 455, 545, 635, 725, 815\} \mu\text{W}$, respectively, and for reference with a 10 μs -long trap delay at $P_c = 815 \mu\text{W}$ in order to prevent the loading of an atom into the trap.

In this measurement, we chose linear polarization perpendicular to the plane of incidence (cf. Sec. 3.6.1), for all light fields sent through the trap optics, as indicated by the vector $\hat{\mathbf{p}}^\perp = (0, 1, 0)$ in Figure 5.8 b). In this case, the polarization of the reflected beam is the same as the one of the incoming beam. Thus, the polarization is approximately equal everywhere in the trap. This choice, however, has implications for the atom–probe interaction in this measurement. To simplify the description, it is convenient to choose the quantization axis to point along the polarization direction of the trap optics fields, i.e. along the y -direction. This means, however, that we use a different atomic eigenbasis than compared to the optical pumping process during the atom detection, see Sec. 2.5.2. With respect to the new basis, the atomic population is not concentrated in the outermost Zeeman level after the atom is detected. Instead, the $(F = 3, m_F = +3)$ level with respect to the z -axis, which is prepared during atom detection, can be expressed as a superposition of the new magnetic sublevels $-3 \leq m_F \leq +3$ of the $F = 3$ manifold for the quantization axis aligned along y . As a consequence, the atomic population is initially distributed over all magnetic sublevels. Furthermore, with respect to the new quantization axis, the probe light will predominantly drive π -transitions to the $(F' = 4, |m_{F'}| \leq 3)$ levels, as illustrated in Fig. 5.8 c). Also transitions to the $F' = 3$ - and $F' = 2$ -manifolds are

5. COMPENSATION OF THE TRAP-INDUCED LIGHT SHIFT

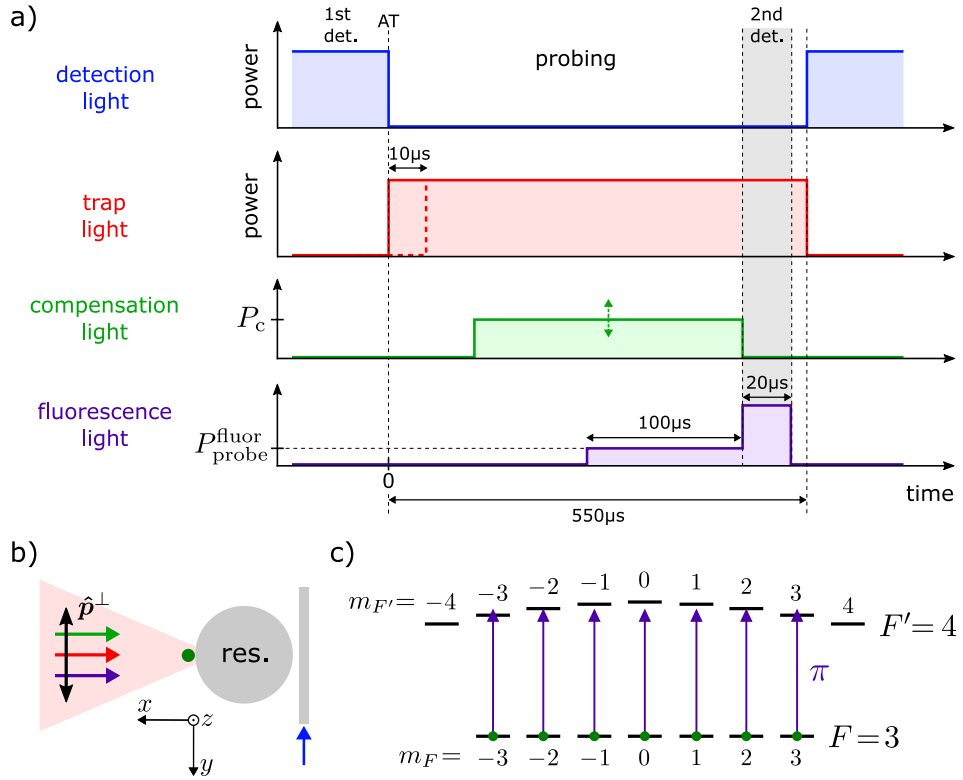


Figure 5.8: a) Experimental sequence for the verification of the light shift compensation. In the different sequence parts the compensation laser power, P_c , is set to different values, see main text. The fluorescence beam with a power corresponding to $\sim 2 I_{\text{sat}}$ is sent onto the atom for a probing time of $100 \mu\text{s}$. When the compensation laser switches off, the fluorescence light power is increased corresponding to $\sim 100 I_{\text{sat}}$ to perform the usual detection of the trapped atom. b) Illustration of the propagation directions of the involved light fields and the polarization direction of the light fields sent through the trap optics. c) Coupled transitions, for the case of \perp -polarized fluorescence probe light.

allowed according to the selection rule, $\Delta F = 0, \pm 1$, and for low compensation laser powers those transitions even become resonant to the probe light, see Fig. 5.2. The corresponding transition strengths are, however, much smaller than those for the $F' = 4$ -manifold [111]. As a consequence of the choice of polarization, we expect that the probe light will induce fluorescence predominantly via the transitions to the ($F' = 4, |m_{F'}| \leq 3$) levels. The fluorescence signal is, thus, expected to be broadened due to the tensor light shift of the $F' = 4$ -manifold, as indicated by the green bar in Fig. 5.2.

After repeating the experimental sequences many times, we analyze the photon statistics in the fluorescence probing and detection windows. Figure 5.9 a) shows the fraction, η , of atom trigger (AT) events where an atom was present in the trap after the probing window, as a function

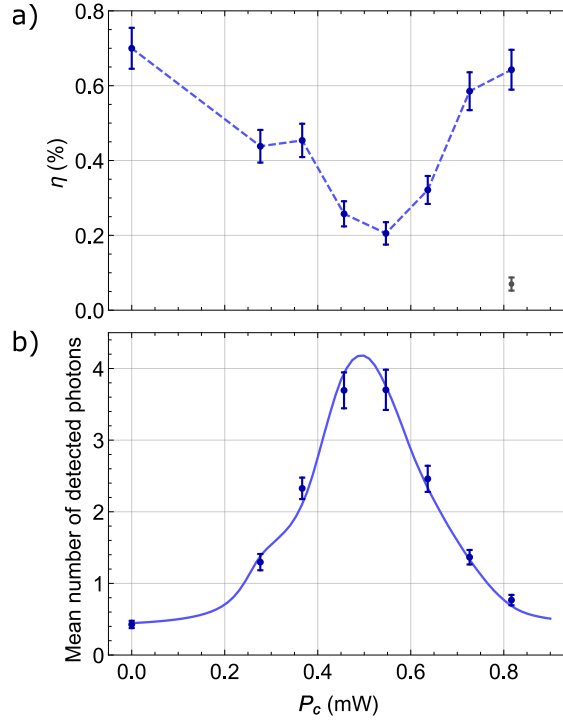


Figure 5.9: a) Fraction of atom events that are re-detected in the fluorescence detection window (2nd detection) by fulfilling the criterion of " $n \geq n_{\text{thr}}^{2\text{nd}} = 3$ detected photons in $20 \mu\text{s}$ " and are, therefore, counted as trapped atoms. The dashed blue line is a guide to the eye. b) Mean number of detected fluorescence photons in the presence of the trap and the compensation laser, as a function of compensation laser power P_c . The solid blue line is a theoretical fit, which is explained in Sec. 5.5.2.

of the compensation laser power. We count a detection event as a trapped atom if we detected a number $n \geq n_{\text{thr}}^{2\text{nd}} = 3$ of the photons scattered into the resonator mode within the $20 \mu\text{s}$ -long fluorescence detection window. The same selection criterion is applied to the reference run where no atom was loaded (gray data point), for which we find $\eta < 0.1 \%$. For the measurement runs (blue data points) one can see, that the fraction of surviving atoms is significantly reduced around the compensation laser power of $\sim 550 \mu\text{W}$. This indicates that the atom is closer to resonance with the probe light for this power, and thus it is more likely to be heated out of the trap. For each atom trigger event that fulfills the above selection criterion, i.e. for all atoms that stayed trapped over the full probing window, we then count the photons detected during the $100 \mu\text{s}$ of probing. The average photon number detected in the probing window is plotted as a function of the compensation laser power in Fig. 5.9 b). We observe a clear maximum of about four photons for the power $P_c^{\text{max}} = 500 \pm 50 \mu\text{W}$. This increased fluorescence rate confirms that the atom is tuned into resonance with the probe light around the compensation laser power P_c^{max} , thereby demonstrating the successful compensation of the trap-induced light shift. The solid blue line is a theoretical fit, which we will explain below. As an addition, the

photon number probability distribution of the probing window is shown for each value of the compensation laser power in App. A.4.1. These photon probability distributions again illustrate the increased atomic fluorescence for the intermediate compensation laser powers.

5.5.1 Discussion

If we compare the result of the fluorescence measurement with the theoretical prediction in Fig. 5.2, we can identify two main differences: First, we calculated optimal light shift compensation for a compensation laser power of about $P_c^{\text{max,th}} \approx 0.25$ mW (green bar) and, therefore, initially expected to observe the maximum fluorescence around this power. Instead, the measured mean number of fluorescence photons peaks at about twice the predicted compensation laser power, indicating that the compensation laser intensity at the position of the atom was smaller than expected. Second, the measured resonance is significantly broadened compared to the expectation.

These deviations from the theory are predominantly caused by the chromatic aberrations of our trap optics, which we discussed in Sec. 5.3. This effect leads to a slight mismatch between the focus positions of the trap and the compensation laser beam along the optical axis, such that the beam radius of the compensation laser is larger than the radius of the trapping beam at the position of the atom ($w_c > w_0$). This explains the reduced compensation laser intensity and the resulting shift of the measured resonance toward a higher compensation laser power.

Since the atoms are moving in the trap potential due to their relatively high average energy (cf. Sec. 4.6.2), the measured fluorescence spectrum in Fig. 5.9 b) is an average over the range of possible atomic positions in the trap (cf. Sec. A.3). The chromatic aberrations, thus, lead to a broadening of the measured spectrum, as for a wider range of P_c -values the trap-induced light shift is canceled only at certain positions in the trap.

5.5.2 Theoretical model

In this section, we explain how we derive the theoretical model for the data in Fig. 5.9 b). In order to obtain a realistic description, the model must include the effect of the motion of the atoms in the trap in conjunction with the position-dependent two-color light shifts caused by the displacement between the trap and compensation laser beam foci, as discussed in the preceding section. The theory is based on the model of the interaction between a two-level atom and a single resonator mode using the master equation approach (cf. Sec. 2.3.2).

In the measurement, the trapped atom is probed with an external resonant light field ("atom-drive"), which is sent through the trap optics. A certain fraction of the photons that are scattered by the atom is coupled into the resonator mode and from the resonator into the coupling fiber with the rate κ_{ext} . The resonator field, outcoupled into the nanofiber, is given by

$$\langle \hat{a}_{\text{out}}^{\text{fluor}} \rangle = -i\sqrt{2\kappa_{\text{ext}}} \langle \hat{a} \rangle, \quad (5.15)$$

where $\langle \hat{a} \rangle$ is the expectation value of the photon annihilation operator for the resonator field.

The Hamiltonian that describes the external excitation of the atom is

$$\hat{H}_{\text{drive}}^{\text{fluor}} = i\hbar \frac{\Omega}{2} (\hat{\sigma}_- - \hat{\sigma}_+), \quad (5.16)$$

where Ω is the Rabi frequency of the external probe laser. Inserting this driving term into Eq. (2.34) and solving the master equation for the case of weak driving allows us to derive a steady-state solution for the outcoupled power in first approximation:

$$|\langle \hat{a}_{\text{out}}^{\text{fluor}} \rangle|^2 = 2\kappa_{\text{ext}} \left| \frac{g\Omega/2}{g^2 + (\gamma + i\Delta_{\text{ap}})(\kappa_{\text{tot}} + i\Delta_{\text{rp}})} \right|^2. \quad (5.17)$$

The resonator–probe detuning, $\Delta_{\text{rp}} = \omega_{\text{r}} - \omega_{\text{probe}}$, was set to $2\pi \times 10 \text{ MHz}^3$ in the measurement. The atom–probe detuning, $\Delta_{\text{ap}} = \omega_{\text{a}} - \omega_{\text{probe}}$, is predominantly determined by the detuning, $\delta\nu$, of the light-shifted atomic transition frequency with respect to ω_0 . According to Eq. (5.4) and considering the chromatic aberrations of our trap optics (cf. Sec. 5.3), this detuning depends on the trap and compensation laser intensities as well as on the position $\mathbf{r} = \{x, y, z\}$ of the atom in the trap, such that $\Delta_{\text{ap}} := 2\pi \delta\nu(I_{\text{trap}}, I_{\text{c}}, \mathbf{r})$.

Also the Rabi frequency of the probe light, $\Omega(\mathbf{r})$, and the atom–resonator coupling strength, $g(\mathbf{r})$, depend on the atomic position. Since the probe light is sent through the trap optics, the corresponding distribution of the Rabi frequencies can be described analogous to Eq. (3.40):

$$\Omega = \Omega_0 f_{\perp}(x) e^{-2\rho^2/w_{\text{fluor}}^2}, \quad (5.18)$$

with $\Omega_0 = 2\gamma\sqrt{I/2I_{\text{sat}}} \approx 40 \text{ MHz}$ [111]. Due to the chromatic aberrations and $\lambda_{\text{fluor}} = 780.24 \text{ nm}$, the fluorescence beam focus must be located between the trap and compensation laser foci. Thus, we estimate the radius of the fluorescence beam at the position of the atom to $w_{\text{fluor}} \approx 4 \mu\text{m}$. The position dependence of the atom–resonator coupling strength $g(\mathbf{r})$ is determined by the intensity distribution of the resonator mode and is given in Sec. 2.4.7. Here, we assume that the trap center lies at the caustic of the resonator mode.

Evaluating Eq. (5.17) for P_{c} -values $\in [0, 0.9] \text{ mW}$ yields a theoretical fluorescence spectrum. To fit the measured fluorescence spectrum, we first calculate fluorescence spectra for an atom at a certain position, \mathbf{r} , for each of the driven transitions depicted in Fig. 5.8 c). For simplicity, we equally average those spectra, which yields a spectrum that is slightly broadened due to the tensor shifts of the $F' = 4$ Zeeman manifold. We do this for a large set of positions and then average the resulting spectra over the position distribution of the atoms in the trap potential formed by the \perp -polarized trap light field. The latter we derived from the measured energy distribution by calculating classical trajectories of the atom in the trap potential (cf. Sec. A.3).

When performing the fit using as free parameters the beam radius of the compensation laser at the position of the trap, w_{c} , and the maximum mean number of detected photons, we find that the FWHM-width of the measured fluorescence spectrum of $\sim 300 \mu\text{W}$ cannot be fully explained by the tensor shifts and the chromatic aberration. For this reason, we also include that the polarization vector of the trap and compensation fields might contain residual elliptical

³The fluorescence light frequency was supposed to be resonant to the resonator frequency ($\Delta_{\text{rp}} = 0$), but we missed to change the setting after a different measurement, which we performed prior to the presented measurement.

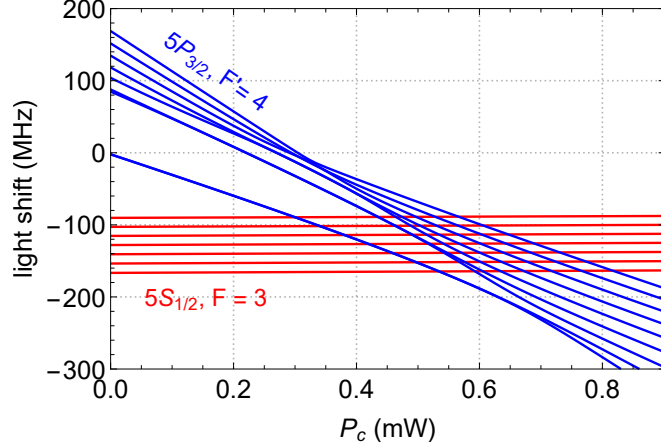


Figure 5.10: Calculation of the two-color light shifts of the $5S_{1/2}, F = 3$ ground state (red) and the $5P_{3/2}, F' = 4$ excited state (blue), for an atom in the center of the trap, for the elliptical polarization vector $\mathbf{u} = (u_x, u_y, u_z) = (0, 0.98, 0.20i)$ and a mismatch of the beam radii at the position of the atom ($w_c/w_{\text{trap}} \approx 1.5$).

components. Such elliptical components can be present, even if the incident polarization was perfectly adjusted to linear, for instance due to stress-induced birefringence of the large vacuum viewport.

To model this, we use for the calculations of the two-color light shifts a normalized polarization vector of the form $(0, 1, \varepsilon i) / \sqrt{1 + \varepsilon^2}$. Note that, here, we implicitly chose the y -axis as the quantization axis for the light shift formalism. The calculated light shifts are shown in Fig. 5.10, for an atom at the trap center and for the polarization vector $\mathbf{u} = (0, 0.98, 0.20i)$, for which we yield the best fitting final spectrum. The red (blue) solid lines are the light shifts for the $5S_{1/2}, F = 3$ ground state ($5P_{3/2}, F' = 4$ excited state) Zeeman manifold. Due to the elliptical polarization component, the vector polarizability of the atom now also contributes to the light shifts: $\alpha_{n,J}^{(K=1)} \neq 0$. Thus, also the ground state light shifts depend now on the Zeeman state. Note that, due to the elliptical polarization components, the $m_{F^{(\prime)}}$ quantum numbers of the hyperfine basis $\{|nJFm_F\rangle\}$ are no good quantum numbers anymore, leading to substantial level mixing. Therefore, we do not label the plotted energies with these numbers anymore. In the excited state, we observe level mixing even between the F' -manifolds. In this situation it is difficult to define a transition frequency. For this reason, for simplicity, we eventually consider all $7 \times 9 = 63$ combinations for the transition energy between the ground and the excited states in our fitting procedure. The averaging of the resulting spectra is done as described before.

In this way, we fit the data in Fig. 5.9 b) with w_c, ε as well as the maximum mean number of detected photons and obtain the blue solid line, which agrees very well with the data. This fit yields a compensation laser beam radius of $w_c = 5.13 \mu\text{m}$, corresponding to a ratio of the trap and compensation laser beam radii of $w_c/w_{\text{trap}} = 1.47$. The fit result for the polarization vector \mathbf{u} was given before already with $\mathbf{u} = (0, 0.98, 0.20i)$. We can compute the overlap of

this polarization with π -polarization described by the unit vector $e_\pi := e_y = (0, 1, 0)$ and yield

$$|\mathbf{u} \cdot \mathbf{e}_\pi^*|^2 / |\mathbf{u}|^2 \approx 0.96. \quad (5.19)$$

This means that, according to the fit results, the polarization of the trap optics beams had a reduced overlap with linear polarization of about 96 %.

5.6 Spectroscopy of the atom–resonator system

In Sec. 5.5 we measured the fluorescence of a trapped atom in the presence of the compensation light and observed an increased scattering rate peaking at the power $P_c^{\max} = 500 \pm 50 \mu\text{W}$. This strongly suggests that the atom has been tuned into resonance with the probe light and, thus, with the resonator. In this situation, it should be possible to observe resonant interaction between the resonator and the trapped atom. One way to test this is to measure a transmission spectrum of the coupled atom–resonator system, which at the same time allows us to measure the atom–resonator coupling strength.

We measure transmission spectra in the presence and absence of light shift compensation, using the experimental sequence illustrated in Fig. 5.11 a). After an atom is detected in the resonator mode and possibly loaded into the trap, we send a 400 μs -long probe pulse through the coupling fiber and vary its detuning, $\Delta\omega = \omega_{\text{probe}} - \omega_0$. The compensation laser beam is set to a fixed power value, P_c . The probe beam is provided by the same light source as the detection light used for the 1st detection, however, with reduced power to not heat the atom out of the trap during probing. This condition is fulfilled for a detection laser power of $P_{\text{probe}}^{\text{res}} \approx 16 \text{ fW}$, which we determined in a separate measurement (cf. App. A.4.2). After the probing, the latter is switched off and a strong fluorescence pulse is sent to test the presence of a trapped atom. We perform in total twenty-two measurement sequences, each for a different detuning, $\Delta\omega$, within the range of $\pm 40 \text{ MHz}$ around the resonance frequency ω_0 .

In contrast to all previously shown measurements, here, we align the linear polarization, $\hat{\mathbf{p}}^{\parallel}$, of the trap and the compensation light approximately along the resonator axis, as depicted in Fig. 5.11 b). With respect to this axis, the driven resonator mode is approximately σ^+ -polarized. As the atom is prepared in the outermost Zeeman level ($F = 3, m_F = 3$) by the 1st detection (cf. Sec. 2.5.2), it interacts with the probe light predominantly via the strong ($F = 3, m_F = 3$) \rightarrow ($F' = 4, m_{F'} = 4$) cycling transition, see Fig. 5.11 c).

Figure 5.12 shows the transmission spectra in presence ($P_c = 330 \pm 30 \mu\text{W}$) and absence ($P_c = 0$) of the compensation laser, respectively. The spectra show the transmission within the 400 μs -long probing window as a function of the probe–resonator detuning $\Delta\omega$. The blue data corresponds to the atom trigger events where an atom was present in both 1st and 2nd detection ($n \geq n_{\text{thr}}^{2\text{nd}} = 5$ detected photons in 20 μs). The gray data shows the transmission corresponding to the other atom trigger events, i.e. the events where no atom was loaded into the trap as well as the events where the atom was lost during probing. The latter show – as expected – the empty resonator spectrum. The gray dashed line is a fit of a Lorentzian function to the data with a HWHM-width of about 11 MHz.

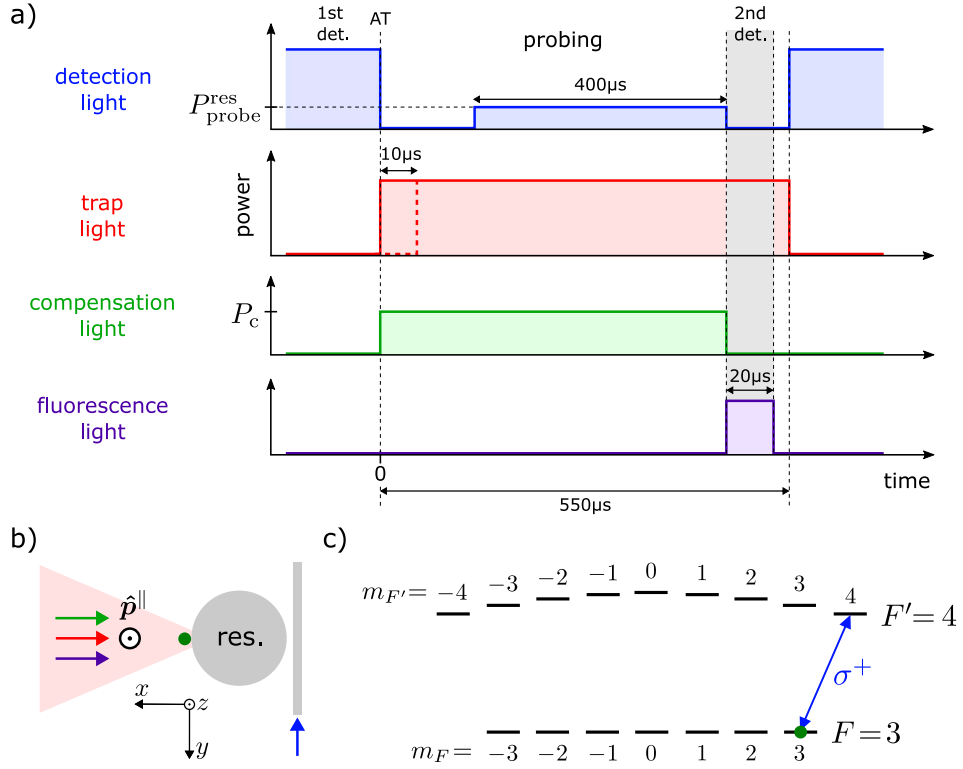


Figure 5.11: a) Experimental sequence for the spectroscopy of the coupled trapped atom–resonator system. The trapped atom is probed for $400 \mu\text{s}$ via the resonator field using the detection light. In the in total twenty-two sequence parts, the detuning of the probe light with respect to the resonator, $\Delta\omega$, is varied. After the probing the presence of the trapped atom is tested by sending a strong fluorescence pulse. b) Illustration of the propagation directions of the involved light fields and the polarization direction of the light fields that are sent through the trap optics. c) Predominantly probed transition by the detection light.

The trapped atom events in Fig. 5.12 a) (blue data) show a clear vacuum Rabi splitting. This demonstrates, for the first time, strong resonant coupling between a single trapped atom and the bottle microresonator. Note, that we measured the Rabi splitting at a smaller compensation laser power than the one for which we observed the maximum fluorescence ($P_c^{\text{max}} \approx 500 \mu\text{W}$). This is expected, because the cycling transition features a smaller light shift compared to the transitions to the other Zeeman levels of the $F' = 4$ excited state, which were involved in the fluorescence measurement (cf. Fig. 5.2). Thus, the cycling transition should already be compensated for a compensation laser power of $\sim 0.75 P_c^{\text{max}}$. The measured difference between the two values of $\approx 34 \%$ agrees with this prediction within the error of $\pm 10 \%$ of P_c^{max} , which we determined from Fig. 5.9 b). The blue solid line in Fig. 5.12 a) is a theoretical prediction, which is discussed in detail in the next section. We can, however, already infer the mean trapped atom–resonator coupling strength from the theoretical model to be $\bar{g}_{\text{trap}}/2\pi \approx 10 \text{ MHz}$.

For comparison, the Rabi splitting measured for the case of transiting atoms in Fig. 2.18

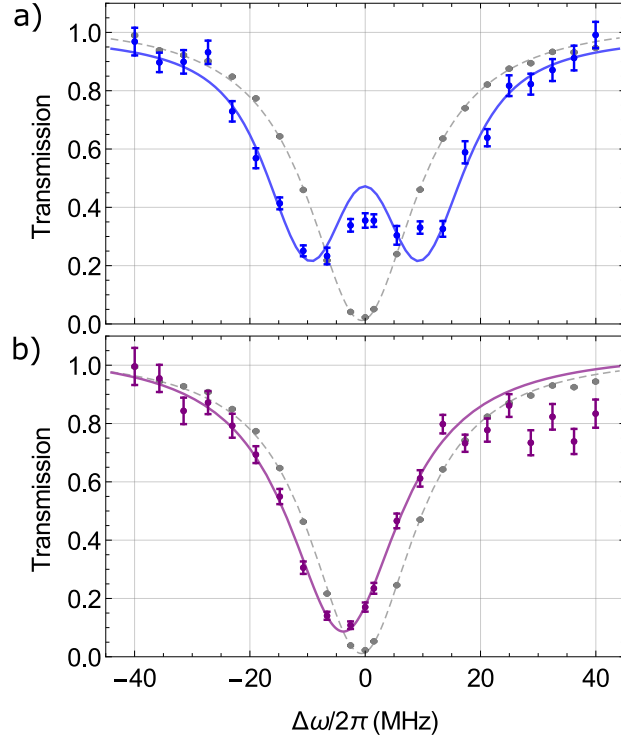


Figure 5.12: Normalized transmission spectra of the atom–resonator system a) in presence ($P_c = 330 \pm 30 \mu\text{W}$) and b) absence of the compensation laser. Each plot shows the average spectrum of single trapped atoms (blue and purple, respectively), as well as the empty resonator spectrum when no atom was trapped (gray). The error bars of the gray data points are smaller than the point size. The solid line in (a) is a theoretical prediction (see Sec. 5.6.1). The solid line in (b) is a fit of a Lorentzian function to the data as a guide to the eye, excluding the six right-most data points. The dashed lines are fitted Lorentzians with a HWHM-width of about 11 MHz.

revealed a mean coupling strength of $\bar{g}_{\text{transit}}/2\pi = 17 \text{ MHz}$, which is a factor of 1.7 larger than in the trapped atom case. Both measurements have been performed with the same resonator mode and under the condition of critical coupling for the empty resonator. Accordingly, the mode volume V , and with it the coupling strength according to Eq. (2.8), were equal. Therefore, the difference in the measured mean coupling strengths must be a consequence of the probability distributions of the atomic positions and their respective overlap with the resonator mode for the two cases. It is, thus, likely that the trapped atoms are on average further away from the resonator surface than the transiting atoms.

For comparison with the vacuum Rabi splitting in Fig. 5.12 a), panel (b) shows the transmission spectrum of the trapped atoms in the absence of light shift compensation. Due to the large atom–resonator detuning caused by the trap-induced light shift (cf. Sec. 3.5), we only observe a small dispersive shift of the resonator resonance. The purple solid line is a fit of a Lorentzian

function to the data excluding the points taken for the detunings $\Delta\omega/2\pi = +20$ to $+40$ MHz. We suspect that the deviation of these data points from the Lorentzian shape is caused by the coupling of the probe light to the states of the $F' \neq 4$ manifolds, which are shifted into resonance for $P_c = 0$, see Fig. 5.2. We also measured transmission spectra for the values of $P_c \approx 370 \mu\text{W}$ and $P_c \approx 410 \mu\text{W}$, which are shown in App. A.4.2.

5.6.1 Theoretical prediction

In order to describe the experimental situation theoretically, we again include the atomic motion together with the position-dependent coupling strength and light shift of the atomic transition. We had found residual position dependence of the two-color light shifts even for the optimal compensation laser power, caused by imperfect mode-matching of the trap and the compensation laser beams (cf. Sec. 5.3). For simplicity, we neglect in this description the possible presence of elliptical polarization components.

In Sec. 2.3.2 we derived the expression for the transmission through the coupling fiber using the master equation approach (cf. (Eq. 2.39)):

$$T = \frac{|\langle \hat{a}_{\text{out}} \rangle|^2}{|\langle \hat{a}_{\text{in}} \rangle|^2} = \left| \frac{g^2 + (\gamma + i\Delta_{\text{ap}}) (\kappa_0 - \kappa_{\text{ext}} + i\Delta_{\text{rp}})}{g^2 + (\gamma + i\Delta_{\text{ap}}) (\kappa_0 + \kappa_{\text{ext}} + i\Delta_{\text{rp}})} \right|^2. \quad (5.20)$$

Here, $\Delta_{\text{rp}} = -\Delta\omega$ is the resonator–probe detuning plotted on the abscissa in Fig. 5.12. The atom–probe detuning Δ_{ap} is now a sum of the detuning $\Delta\omega$ and the position-dependent detuning of the two-color light shifted atomic transition frequency with respect to its unperturbed value, such that $\Delta_{\text{ap}} = -\Delta\omega + 2\pi \delta\nu(I_{\text{trap}}, I_c, \mathbf{r})$. For the calculation of the two-color light shifts we use the intensity distributions given in Eq. (5.7) and (5.8), but with the corresponding standing-wave pattern for \parallel -polarization described by $f_{\parallel}(x)$ (cf. Eq. (3.39)). In these expressions we also insert the beam radii $w_{\text{trap}} = 3.5 \mu\text{m}$ and $w_c = 5.13 \mu\text{m}$, where the latter value was obtained from the fit to the measured fluorescence spectrum in Sec. 5.5.2. For the atom–resonator coupling strength, $g(\mathbf{r})$, we again consider the position dependence given in Sec. 2.4.7, with the assumption that the trap center lies at the caustic of the resonator mode.

Based on the expression in Eq. (5.20), we can model the measured vacuum Rabi splitting. Evaluating this expression as a function of $\Delta\omega$ yields a theoretical transmission spectrum. We calculate such spectra for each of the positions that were considered for the calculated position distribution (cf. Sec. A.3). In contrast to the fluorescence model, here we only consider the coupling to the $(F = 3, m_F = 3) \rightarrow (F' = 4, m_{F'} = 4)$ cycling transition. The resulting spectra are then averaged over the position distribution of the atoms in the trap to yield the final spectrum plotted in Fig. 5.12 a). Averaging the coupling strengths over the position distribution of the atoms in the trap potential for the case of \parallel -polarized trap light, yields an average coupling strength of $g^{\text{th}}/2\pi = 9.3$ MHz with a standard deviation of $\sigma_g^{\text{th}}/2\pi = 6.1$ MHz, in good agreement with our expectations.

In this modeling, we leave the compensation laser power P_c as a free parameter in order to find the most symmetric spectrum. The solid line in Fig. 5.12 a) was obtained for a theoretical

power of $P_c^{\text{th}} = 400 \mu\text{W}$. As mentioned earlier, the discrepancy between this theoretical value and the experimental value of $P_c = 330 \pm 30 \mu\text{W}$ probably comes from the uncertainty of the P_c^{max} -value, determined from the fluorescence measurement. This uncertainty impacts our estimation of the ratio of the compensation and trap laser beam radii, w_c/w_{trap} , which also enters as a parameter in this model for the Rabi-splitting.

We can apply the presented model also to the transmission spectrum of Fig. 5.12 b) by simply setting the compensation laser power to $P_c^{\text{th}} = 0$. However, by doing so, we find a theoretical spectrum that is almost identical to the empty resonator case. In contrast, the measured data shows a clear shift with respect to the pure resonator resonance. We think that for an adequate description, one would need to take into account the coupling of the resonator mode to transitions other than the $F = 3 \rightarrow F' = 4$ cycling transition, which are shifted closer to resonance for $P_c = 0$, as visible in Fig. 5.2.

Summary and Outlook

Summary

In the framework of this thesis, different options for trapping single rubidium atoms in the resonator mode of a whispering-gallery-mode bottle microresonator have been considered. Thereby, we identified a retroreflected optical tweezer trap as the most promising trapping scheme and integrated such a trap into our CQED experiment.

In order to load a single atom into the trap, we bring a cloud of laser-cooled ^{85}Rb atoms to the resonator via an atomic fountain. Upon real-time detection of a single atom in the evanescent field of the resonator mode, we rapidly switch on the trap laser in order to capture the atom. We experimentally verified that, in this way, we can catch atoms and hold them inside the optical potential. A trap loading probability of about 1% was found, which is compatible with what we expect from geometrical consideration of our loading scheme. In our experiment we measured an average lifetime of the trapped atoms of about 2 ms. This constitutes a significant increase compared to previously demonstrated interaction times for free-falling atoms coupled to WGM resonators. However, it is relatively small compared to the lifetimes reported for standing-wave dipole traps used in conjunction with, e.g., optical nanofibers. We attribute the measured lifetime mostly to scattering-induced heating where the large repulsive excited state potential gives rise to a large temperature increase per scattering event due to the relatively high initial temperature of the trapped single atoms.

The ground and the excited state of the trapped rubidium atoms are shifted into opposite directions under the influence of the trap light, which results in a strong position dependence of the atomic transition frequencies. Since in the red-detuned regime no magic wavelength exists for rubidium, we implemented a light shift compensation scheme in order to resonantly couple the trapped single atoms to the resonator mode. In this scheme, we superimpose the trapping beam with a second laser beam, which is red-detuned to the transition between the excited state and a higher-lying state. We experimentally demonstrated the working principle of this compensation scheme. Making use of the light shift compensation, we could tune the atom back to resonance with the unperturbed transition. This allowed us to measure a vacuum Rabi splitting

of trapped single atoms coupled to a WGM resonator, which revealed an average atom–resonator coupling strength of $\bar{g}_{\text{trap}}/2\pi \approx 10$ MHz. This result constitutes the first demonstration of strong coupling of a single trapped atom to a WGM resonator.

With the improved control over the atomic motion, more complex applications and quantum information protocols are now possible with our system. For example, we could implement a photon–photon gate as suggested in Ref. [65] or prepare our quantum optical circulator [55] in a superposition of its operation directions to create Schrödinger cat states of light.

Outlook

As our system provides a fully fiber-integrated interface between a trapped single atom and a single photon, it is ideally suited for integration into an optical quantum network as a network node. Performing quantum computations, long-distance quantum communication or quantum simulations requires to construct large-scale quantum networks consisting of many network nodes. In such a network, quantum operations as, e.g., the distribution of entanglement across the network or the teleportation of quantum states between network nodes [37], demand a large degree of control, in particular, over the external and internal degrees of freedom of the atoms. To allow this, in each network node, the atom needs to be coupled deterministically to the resonator and for a significant amount of time.

In our experiment, one possibility to make the loading of the dipole trap more efficient and deterministic, is to first load atoms from the atomic fountain into a MOT near the resonator. Then, a single atom can be transferred from the MOT into an optical tweezer trap by exploiting the collisional blockade effect [137]. After a successful loading, which can be verified via fluorescence detection, the atom can be transported close to the resonator by moving the focus of the optical tweezer trap toward the resonator surface. This has to be done in such a way, however, that the atom is transferred from the initial free-space tweezer potential into the minimum of the emerging partial standing-wave potential, which is closest to the resonator surface. In a recent proposal [165] it is suggested to use a coherent superposition of radial Laguerre-Gauss beams to create the dipole trap. This configuration is expected to yield a strong suppression of the standing-wave pattern, which originates from the interference between the incoming and the reflected trapping beam, for distances from the dielectric surface larger than $\sim \lambda_{\text{trap}}$. Thus, essentially only the trap minimum closest to the resonator remains, into which the atom can be loaded.

To increase the storage time, the trapped atom needs to be cooled inside the trap. With a trap loading mechanism as described before, the initial average temperature of the trapped single atoms should already be reduced compared to the one resulting from our current scheme. However, during the execution of quantum protocols the atom will always be illuminated with probe or control fields, which inevitably leads to heating and eventually to loss of the atom. In order to prevent this, a cooling mechanism with a sufficiently large cooling rate will thus be needed for future applications. In the past two decades, extensive theoretical and experimental research has been conducted on laser cooling of trapped ions and neutral atoms. Cavity-based cooling techniques are, e.g., feedback cooling [166, 167], cavity cooling [24, 168, 169] and Ra-

man sideband cooling [25, 26]. By making use of the mutually orthogonal circular polarization of counter-propagating WGMs in our system, we could possibly implement a cooling scheme that combines polarization gradient cooling with cavity cooling [170]. With an efficient cooling mechanism in place, the lifetime of the trapped atoms should further increase by several orders of magnitude.

The scalability of quantum optical architectures can be significantly improved by employing optical chip technology (e.g. [171] and references therein). Hence, there is also a trend to realize atom–light interfaces on the basis of such platforms [125, 126]. Already in the early 2000s, microtoroids have been fabricated in linear arrays on a silicon chip motivated by the same idea [37, 76, 172]. The scheme of coupling single trapped atoms to a WGM microresonator demonstrated within this thesis can also be applied to on-chip disk or ring resonators [173]. Combining such integrated optical resonators with deterministically coupled atoms, possibly in large arrays or networks, has a great potential for future applications in quantum optics. In particular, new quantum protocols and functionalities may profit from the chiral atom–light interaction present in the type of system that has been described in this thesis.

Appendices

A.1 Supplementary Information: Trapping single atoms close to the bottle resonator

A.1.1 Trapping single atoms with a pulsed trap

In our first attempts to trap atoms in the standing-wave dipole trap, we sought for real-time observation of the single trapped atoms. As the large trap-induced light shift renders atom detection via the resonator problematic, the first idea was to employ a pulsed trap. This means that the trapping beam is periodically switched on and off, such that the trapped atom can be resonantly probed during the off-times. In order for the atom to stay trapped nevertheless, the switching frequency has to be much larger than the largest atomic oscillation frequency. In this case, the atom should always "see" a time-averaged trapping potential.

Due to the tight confinement of the atom along the axial direction in our dipole trap, the corresponding oscillation frequency is ~ 1 MHz (cf. Sec. 3.6.3). Therefore, we aimed at a switching period of not more than 100-200 ns. Upon detection of an atom in the evanescent field at time $t = 0$, we switched on the trapping beam, see Fig. A.1.1 a). After a hold time of $5 \mu\text{s}$, which ensures that non-trapped atoms have left the evanescent field, we started the interrogation phase. In that, the trap was periodically switched on and off, while the detection beam was sent onto the resonator with the inverse switching pattern, such that it is on whenever the trap is off. For the generation of the pulse sequences of both beams we employed an ADwin system (Jäger Computergesteuerte Messtechnik). We also accounted for delays due to electronic or optical path length differences in order to yield the desired pulse timings at the position of the atom.

In order to test the presence of the atoms during the pulse sequence, we analyzed the transmission of the detection light during the detection light pulses. To extract a lifetime from this data, we divided the sequence into bundles, each containing 30 pulses, and integrated the transmitted photons over the 30 pulses for each bundle. Figure A.1.1 b) shows an example of such a lifetime measurement. We fit an exponential function to the data and obtain a decay constant

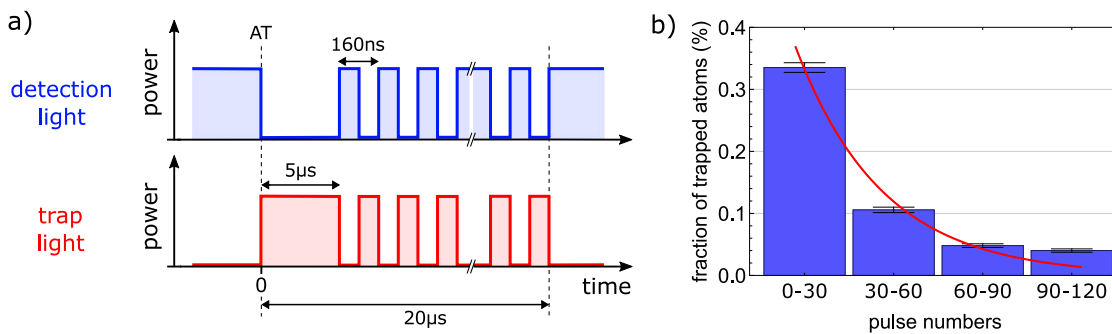


Figure A.1.1: Trapping and detection of atoms in the standing-wave dipole potential using a pulsed trapping scheme. a) Sketch of the experimental sequence showing the inversely phased pulse patterns of the detection and trap light. b) Lifetime measurement of single atoms in the pulsed trap. The solid red line is an exponential fit, yielding a decay constant of about 30 pulses, corresponding to a lifetime of about $4.8 \mu\text{s}$.

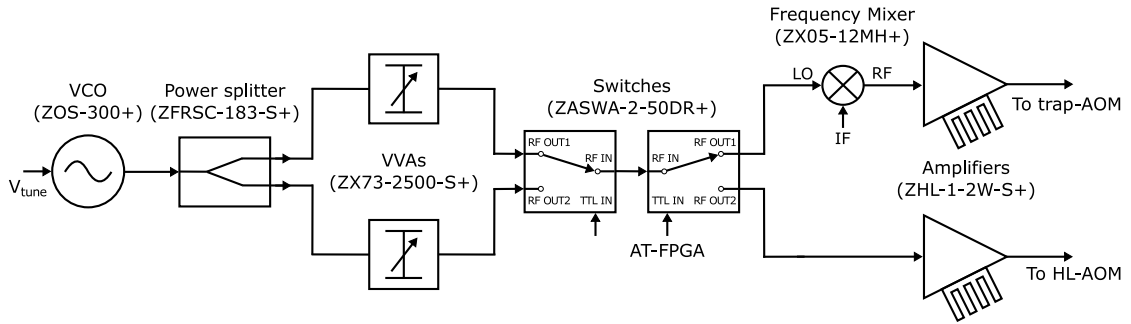


Figure A.1.2: Simplified scheme of the RF-driver chain that supplies the AOMs in the trap and heating laser (HL) paths. The individual Mini-Circuits[®] RF-components are labeled and their respective model number is given in brackets.

of ~ 30 pulses corresponding to a lifetime of about $4.8 \mu\text{s}$. Thus, in these measurements we already observed a response of trapped atoms during the detection windows, but the signal decayed within the first few microseconds. Most probably, the atoms were heated out of the trap by the trap modulation in conjunction with the interaction with the detection light. Furthermore, due to the limited response time of our AOMs and control electronics, additional heating effects occurred. For this reason, we moved on to the approach of a continuous trapping beam and started investigating different options of probing the trapped atom, which is described in Ch. 4.

A.1.2 RF-driver for trap and heating laser control

The main task of this radio frequency (RF) driver is to enable fast on/off-switching of the trap laser. This is essential in our experiment, as we want to capture free-falling atoms in the trapping potential, after they have been detected in real time in the evanescent field of the resonator mode. The original RF-driver was assembled and characterized within the framework of a Bachelor thesis, where details can be found about the individual components [174]. However, in the course of our measurements, certain components were added to this RF-driver to allow for additional functions.

In Fig. A.1.2 a scheme of the RF-driver is depicted, showing only the main components. The RF-source is a voltage-controlled oscillator (VCO), whose output frequency can be tuned between 150 MHz and 280 MHz via a tuning voltage V_{tune} . Next comes a power splitter, which splits the signal into two branches. Each of the branches has a voltage-variable attenuator (VVA), which allows one to adjust the RF-power via a control voltage. The VVAs are followed by an RF-switch that allows fast switching between the two branches by means of a TTL signal. The two-branch structure offers the possibility to rapidly switch between different RF-powers. The TTL input of the second switch in the chain is supplied by the atom-trigger FPGA, which thus determines the on/off-state of the trap-AOM and the on/off-state of the heating laser (HL-) AOM. More specifically, with the arrangement shown in Fig. A.1.2, the driver generates exactly inversely phased on/off-switching patterns of the trap and HL beams. We use this feature to counteract the trap-induced resonator heating described in Sec. A.2. Between the second switch

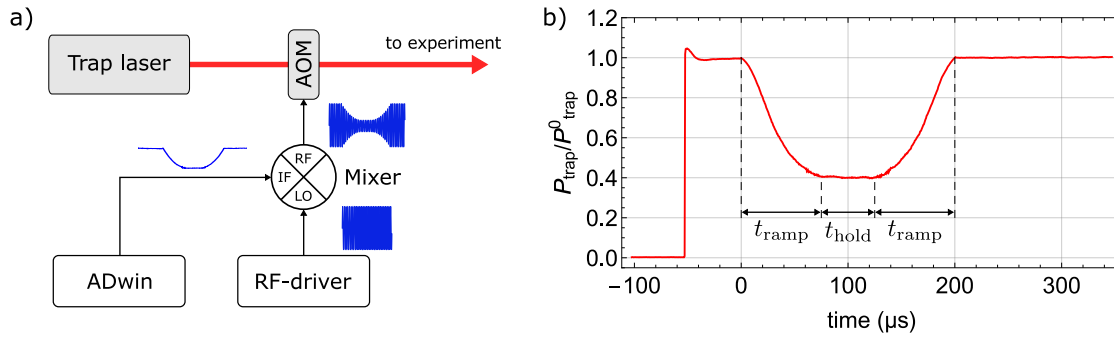


Figure A.1.3: Experimental implementation of the adiabatic trap depth variation for the temperature measurement described in Sec. 4.6.2. a) Scheme of the optical and electronic components involved in modulating the amplitude of the RF-signal and, thus, the trap power. The RF-signal is generated by the driver discussed in App. A.1.2. b) Resulting optical signal of the trap light measured behind the trap-AOM with a photodiode, exemplarily for the final trap power $P_{\text{trap}}^{\text{low}} = 0.4 P_{\text{trap}}^0$.

and the high-power amplifier in the upper RF-path we inserted a mixer, which enables us to drive a predefined trap power ramp in the measurement of the temperature of the trapped single atoms, described in Sec. 4.6.2.

A.1.3 Measurement of the energy distribution

Experimental implementation of the trap laser power ramp

The variation of the trap laser power in the measurement of the energy distribution of the trapped single atoms (cf. Sec. 4.6.2) is implemented by modulating the amplitude of the RF-driving signal for the trap-AOM. For this purpose, we inserted a frequency mixer into the RF-driver chain that supplies the AOM (cf. Fig. A.1.2). A simplified scheme of the setup is shown in Fig. A.1.3 a). We chose to use a mixer, as it provides both fast and linear response. For this application we use the local oscillator (LO) port and the intermediate frequency (IF) port of the mixer as input ports and the RF port as output port. The original RF-driving signal is sent into the LO port. The IF port is supplied with a time-dependent quasi-analog DC-voltage signal according to the function given in Eq. (4.10). This analog signal was generated by our ADwin system¹. For each sequence part with a different U_{low} -value a separate ramp was programmed in the ADbasic programming language. The mixer then simply multiplies the two input signals, giving rise to the modulation of the RF-amplitude. The resulting optical signal is shown in Fig. A.1.3 b), exemplarily for the case where the trap depth is lowered to 40 % of its initial value. The ADwin input function is very well mapped onto the optical signal, thereby showing that both the mixer and the AOM were operating approximately in their linear regimes.

¹ADwin, Jäger Computergesteuerte Messtechnik

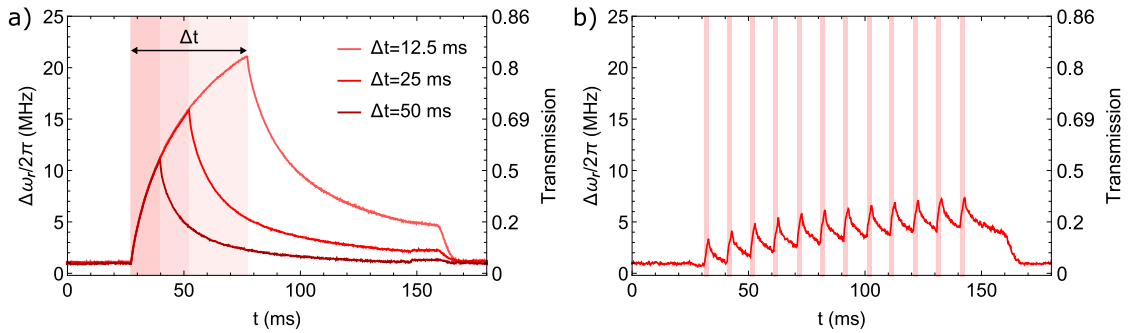


Figure A.2.4: Trap-induced heating of the resonator. a) Frequency shift $\Delta\omega_r$ and transmission increase for light initially resonant with the resonator, for the case that the resonator is illuminated with the trap light field for different durations Δt . b) Same quantities for the case of several successive short periods of trap illumination ($\Delta t = 2$ ms).

A.2 Resonator heating effect

A.2.1 Trap-induced heating of the resonator material

When the trapping beam impinges on the resonator, a small fraction of the trap power is absorbed, which causes the resonator temperature to slightly increase. As a consequence, the refractive index of the resonator material (silica) and the resonator diameter change. Both effects lead to a shift of the resonator mode frequency, which is detrimental to our experiments.

Since, in our measurements, the coupling fiber is critically coupled to the empty resonator and the resonator frequency is not stabilized during the detection window (cf. Sec. 2.5), the frequency shift manifests itself in a transmission increase of the light through the coupling fiber. We demonstrate this in two measurements shown in Fig. A.2.4. We use the same experimental cycle as in a usual measurement, however, with the differences that we do not launch the atomic fountain and we do not send any detection light. Instead, we keep the resonator stabilization light on during the detection window, during which the resonator lock is off, and measure the stabilization light transmission through the coupling fiber while letting the trap light impinge on the resonator with our typical trapping parameters ($P_{\text{trap}} = 20$ mW, $\lambda_{\text{trap}} = 783.68$ nm).

In Fig. A.2.4 a) the transmission of the stabilization light and the corresponding frequency shift are shown as a function of the illumination time, for the case that the trap light switches on at the beginning of the detection window for time durations $\Delta t = \{12.5, 25, 50\}$ ms. In Fig. A.2.4 b) the same signal is shown, however, for a situation more similar to an actual measurement: we send several short pulses ($\Delta t = 2$ ms) of the trap light onto the resonator, thereby imitating atom detection events. In both plots, the red shaded areas indicate when the trap light is on and, thus, when the resonator heats up. In plot (a) we see a steep increase of the transmission when the trap laser is switched on, which saturates for longer times. After the laser is switched off, the resonator frequency returns to its steady state value on a time scale of ~ 15 to 35 ms, depending on the illumination time. At time $t \approx 165$ ms we see an abrupt step in the transmission. Here, the resonator lock kicks in and thus pulls the resonator frequency back into

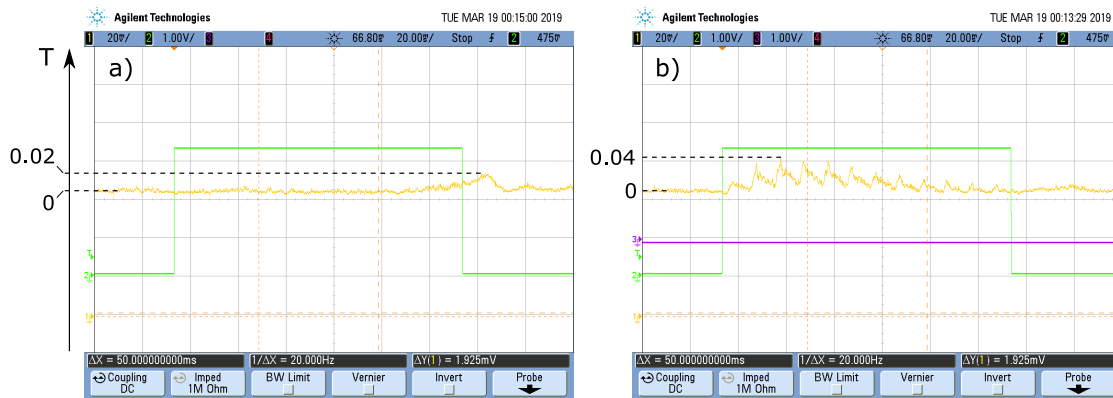


Figure A.2.5: Suppression of the trap-induced heating of the resonator using the interleaved heating laser. a) and b) Oscilloscope screenshots of the measured transmission, T , of light initially resonant with the resonator (yellow trace), for several successive pulses of trap light ($\Delta t = 2$ ms) as in Fig. A.2.4 b), but now with additional heating laser illumination with the inverse switching pattern as compared to the trap laser. a) Single shot with best-case suppression of the heating-induced transmission increase. b) Single shot with worst-case suppression.

resonance with the stabilization light. In plot (b) we observe a fast temperature-induced shift of the resonator frequency of up to 2-3 MHz, whenever the trap light switches on. The subsequent cooling after switching the trap off has a larger time constant than the heating, such that the resonator does not cool down completely after each illumination. Therefore, we also observe a slow accumulative drift of the resonator frequency over time.

As described in Sec. 2.5.2, our real-time atom detection scheme relies on the large transmission increase from about 0 to $\sim 70\%$ associated with the strong coupling of an atom to the resonator mode. Consequently, the heating-induced transmission increase of the empty resonator discussed here, can lead to false detection events. When multiple atom events occur successively within a short time, i.e. the trap is quasi-continuously on, this can even lead to a cascade of spurious detection events, which will prevent us from seeing actual atoms coupling to the resonator. Without taking any countermeasures, this limits the time duration Δt for trapping the atom to about 200 μs . Consequently, we have to counteract the heating effect.

A.2.2 Counteracting the heating effect

To counteract the heating, we send an additional laser beam onto the resonator, which we call "heating laser", see Fig. 4.1. This laser has the inverse on/off-switching pattern compared to the trap light, such that it is always on when the trap light is off and vice versa. We achieve this by using the RF-driver chain depicted in Fig. A.1.2.

The heating laser has a wavelength of 980 nm, a power of up to 100 mW and a focus diameter of about 50 μm . It is sent onto the resonator along the $-z'$ -direction, as illustrated in Fig. 4.1. In this way, it does not affect the trapping of the atom. Since the heating laser beam impinges at a different position onto the resonator and has different properties than the trap light, the resulting

dynamics of the heating (cooling) of the resonator, when the laser switches on (off), are different. As a consequence, we can counteract the slow accumulative drift of the resonator frequency relatively well, but we cannot fully eliminate the short-term frequency drift. This can be seen in Fig. A.2.5 a) and b), which shows two single shots of the experimental cycle, respectively. In plot (a) close-to-optimal suppression of the temperature-dependent drift is achieved, while plot (b) shows another single shot, where the suppression is worse and the residual transmission increase still goes up to $\sim 4\%$.

As an additional measure to avoid the cascade effect explained in Sec. A.2.1, we introduce a dead time of typically 2 ms for the AT-FPGA after a trigger event has occurred. Thereby, the resonator always has some time to cool down before a new atom can be detected.

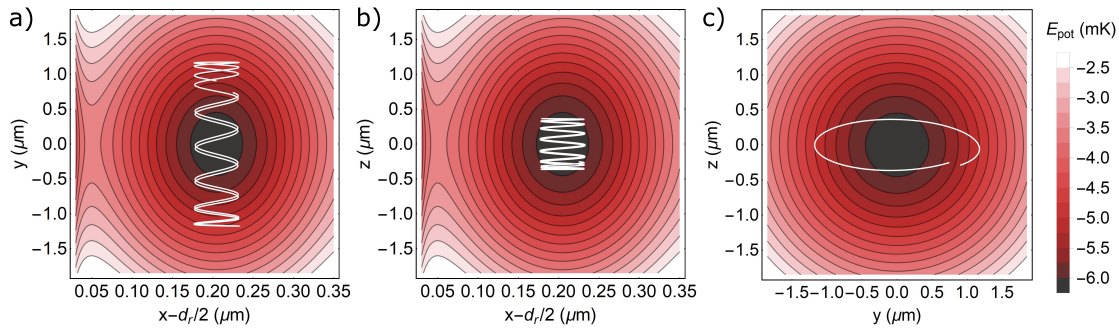


Figure A.3.6: Example trajectory of a trapped atom in the trapping potential, for the case of a \perp -polarized trap with the parameters $\{P_{\text{trap}}, w_{\text{trap}}, \Delta_{\text{trap}}/2\pi\} = \{18.7 \text{ mW}, 3.5 \mu\text{m}, 1.68 \text{ THz}\}$. One transverse oscillation period ($T_{y/z} \approx 15 \mu\text{s}$) of the trajectory is shown, projected onto the a) x - y -plane, b) x - z -plane and c) y - z -plane, respectively. The coordinate system is chosen in accordance with Fig. 3.2.

A.3 Position distribution of the trapped atoms

In Sec. 4.6.2 we have seen that the single trapped atoms have on average a rather high energy corresponding to approximately two thirds of the trap depth ($E_0 \approx 2/3U_0$). Accordingly, the atoms are expected to occupy a large part of the trapping volume. As a consequence, the atomic transition frequency is not only shifted due to the trap-induced light shift, but also substantially broadened. Here, we are interested in the position distribution, i.e. the probability $p(\mathbf{r})$ of the atom to be found at a certain position in the trap, from which we can then calculate the distribution of the atomic transition frequency. As E_0/\hbar is much larger than the oscillation frequencies $\omega_{y/z}$ and ω_x in the trap, we can imagine the atoms as classical particles oscillating in the trap potential. Thus, to find out the probability distribution of the atomic positions, we calculate classical trajectories of a single trapped atom for different total energies, E_0 , sampled over the energy distribution in Fig. 4.14 c).

The first step to simulate an atomic trajectory is to pseudo-randomly generate a start position within the trapping volume. Here, the boundaries of the trapping volume are defined by the maximum possible potential energy, $E_{\text{max}} = U_0$, which corresponds to the local maximum of the potential, before it steeply drops toward the resonator surface due to the van der Waals-interaction (cf. Fig. 3.7). The generated start position is associated with a potential energy, E_{pot} . In consideration of energy conservation, $E_0 = E_{\text{pot}} + E_{\text{kin}}$, the remaining kinetic energy E_{kin} is then randomly distributed onto the three components of the velocity vector. Given these starting conditions, we numerically solve the equations of motion in the trapping potential given by Eq. (3.44). The size of the time steps is chosen small enough such that the fast oscillation of the atom in longitudinal direction (x) is properly sampled. Furthermore, the temporal length of each trajectory is chosen to be about three times longer than the longest oscillation period in transverse direction ($T_{y/z} \approx 15 \mu\text{s}$). Figures A.3.6 a)-c) show exemplarily one such calculated trajectory in the potential landscape, projected onto the x - y -plane, x - z -plane and y - z -plane, respectively. Here, the trap light was chosen to be \perp -polarized and the trap parameters were

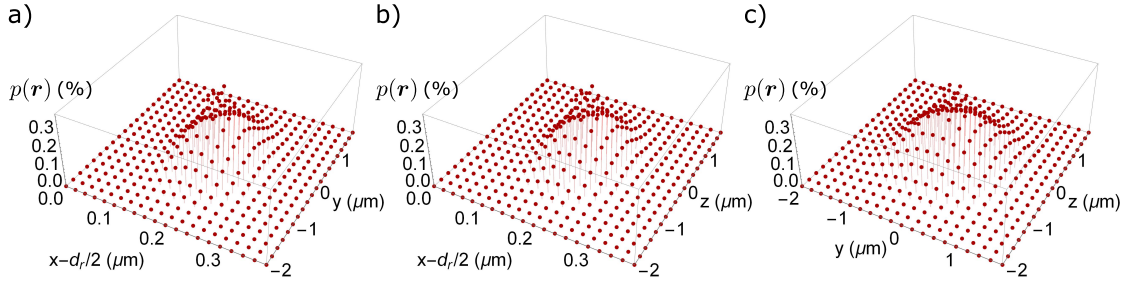


Figure A.3.7: Position distribution, $p(\mathbf{r})$, obtained by averaging simulated classical atomic trajectories over the Gaussian energy distribution in Fig. 4.14 b) (see details in the text). Panels (a) to (c) show the distribution along two axes, respectively.

$\{P_{\text{trap}}, w_{\text{trap}}, \Delta_{\text{trap}}/2\pi\} = \{18.7 \text{ mW}, 3.5 \mu\text{m}, 1.68 \text{ THz}\}$, chosen in accordance with the experimental parameters used in the measurement presented in Sec. 5.5. For better visibility, we plot only one oscillation period, $T_{y/z}$, of the slow transverse oscillation. In this particular example, the atom moves relatively far away from the trap center in transverse y -direction, while the oscillation amplitude in x -direction is rather small.

The above describe procedure is performed for ~ 30 discrete energy values, E_0 , evenly sampled over the Gaussian energy distribution of Fig. 4.14 b). For each energy we calculate 500 trajectories and histogram the occurring positions, $\mathbf{r} = \{x, y, z\}$, in $20^3 = 8000$ three-dimensional bins of size $\Delta x \times \Delta y \times \Delta z = (20 \times 100 \times 100) \text{ nm}^3$ around the trap center. To obtain the final normalized position distribution, we average the resulting histograms taking into account the corresponding weighting factors from the normalized Gaussian energy distribution, $P(E_0)$. Note, that we have to rescale the energy distribution from Sec. 4.6.2, which was measured for a trap power $P_{\text{trap}} = 20 \text{ mW}$, to the present case where we consider a slightly lower power of 18.7 mW. For this, we assume that the relative energy distribution does not change in a shallower trap, as it is probably a characteristic of our trap loading mechanism. The resulting position distribution for the parameters mentioned above is plotted in Figs. A.3.7 a)-c) for all directions, respectively. The highest probability of about 0.3 % is found for an atom located at the trap center $\mathbf{r}_0 = \{d_r/2 + 0.205, 0, 0\} \mu\text{m}$.

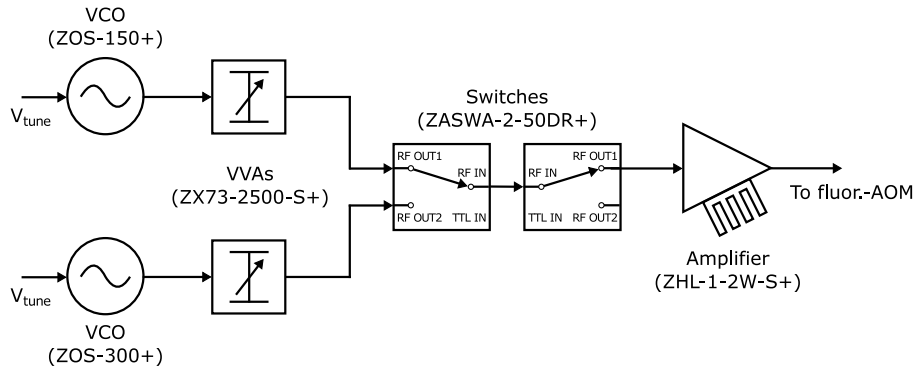


Figure A.4.8: Simplified scheme of the RF-driver chain that supplies the AOM in the fluorescence light path. It enables fast switching between fluorescence light pulses of different powers, which was used in the measurement presented in Sec. 5.5. The individual Mini-Circuits® RF-components are labeled and their model number is given in brackets.

A.4 Supplementary Information: Compensation of the trap-induced light shift

A.4.1 Experimental verification of the light shift compensation

RF-driver for fluorescence light control

In Fig. 5.8 a) we show the experimental sequence that we used for the measurement to verify the working principle of the light shift compensation scheme (cf. Sec. 5.5). In order to rapidly switch between the fluorescence light pulses of different powers we assembled a dedicated AOM-driver, which is schematically shown in Fig. A.4.8. Here, two independent RF-signals with different powers are connected to two fast switches in series. The first switch is operated in reversed direction, such that the two RF-branches can be connected to its two output ports. Hence, by sending a TTL-signal to the first switch, we can decide which of the two RF-signals should be transmitted. The second switch enables to turn the transmitted signal on or off, depending on its TTL input-level. Each of the two RF-branches possesses a voltage-controlled oscillator (VCO) as RF-source and a voltage-variable attenuator (VVA). The latter allows to adjust the RF-power. A VVA alone, however, could not have served for the power switching task in our measurement, as it has a typical switching time of $20 \mu\text{s}$. In contrast, the RF-switch has a switching time of only $\sim 10 \text{ ns}$.

Additionally, this AOM-driver allows one to switch between RF-signals with different frequencies, which could be useful for future experiments, e.g. for testing schemes to cool the trapped atom.

Photon statistics of the fluorescence probing window for trapped-atom events

Here, we show the photon number probability distributions of the fluorescence probing window in the measurement presented in Sec. 5.5. For this purpose, we considered only the traces

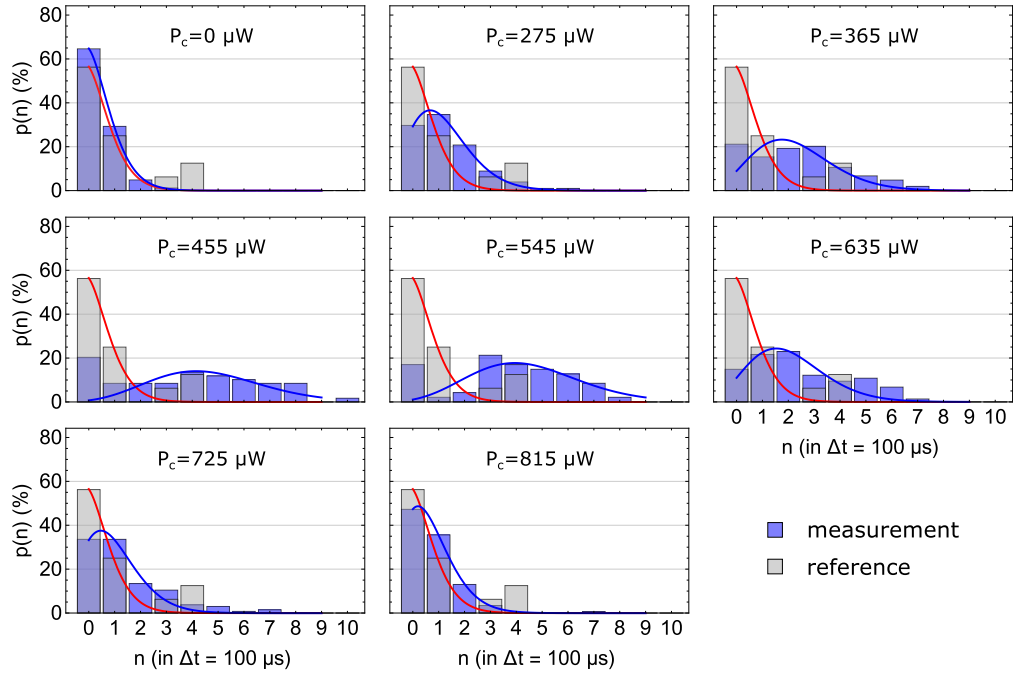


Figure A.4.9: Photon number probability distributions for the different compensation laser powers, P_c , used in the measurement. The gray bars show the reference data, where no atom is trapped. The blue (red) solid lines are fits of a Poisson function according to Eq. (4.2) to the measurement (reference) data.

where the atom stayed trapped over the full probing window, i.e. the runs where the second trigger criterion " $n \geq n_{\text{thr}}^{2\text{nd}} = 3$ photons in $20 \mu\text{s}$ " is fulfilled, see Sec. 5.5. We then histogram the scattered fluorescence photons that were registered with the SPCMs for each value of the compensation laser power, P_c , used in the measurement.

The result is shown in Fig. A.4.9. The blue histograms correspond to the runs with trapped atoms for the different compensation laser powers, as indicated. The gray histogram, which is the same in each plot, shows the result for the reference run, where no atom is loaded into the trap. The blue (red) solid lines are fits of a Poisson function according to Eq. (4.2) to the measurement (reference) data. The measurements clearly illustrate the increased number of scattered fluorescence photons for the intermediate compensation laser powers, where the atoms are tuned close to resonance. The average photon numbers are plotted as a function of the compensation laser power in Fig. 5.9 b).

A.4.2 Spectroscopy of the atom–resonator system

Detection power scan

In preparation for the measurements of the transmission spectra, presented in Sec. 5.6, we performed a short measurement to find a suited power of the detection light for probing. The power

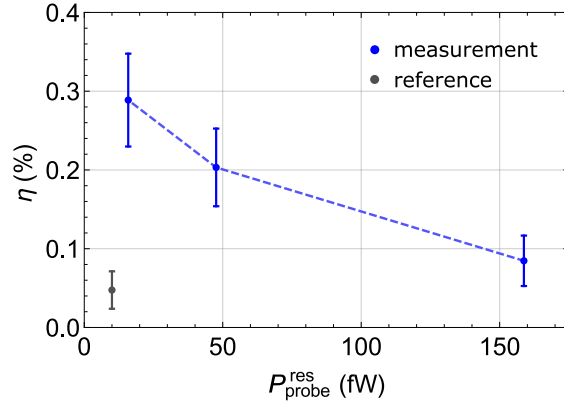


Figure A.4.10: Fraction of atom events that stay trapped over the full 400 μs -long probing window (blue data points), as a function of the probe power $P_{\text{probe}}^{\text{res}}$. The dashed blue line is a guide to the eye. The gray data point was measured for reference without trapped atoms.

should be low enough such that the atom is not heated out of the trap and, thus, the transmission is stable over the full 400 μs -long probing window.

The timings of the experimental sequence that we use for this measurement are identical to the one in Fig. 5.11. However, instead of varying the probing frequency, we set three different values of the probe power: $P_{\text{probe}}^{\text{res}} \approx \{16, 48, 160\}$ fW (femto watts). For comparison, the power used for detecting an atom in the evanescent field is about 1.6 pW. In addition to the three sequence parts with different powers, we include one reference sequence. With the fluorescence pulse at the end of the sequence we can determine the fraction of atoms surviving the interrogation with the probe light. Figure A.4.10 shows the result. We find the largest survival probability for the lowest probe power of $P_{\text{probe}}^{\text{res}} \approx 16$ fW. Accordingly, we chose to use this power in the transmission measurement. For the largest of the tested power values of 160 fW the survival probability is close to zero.

Transmission spectra for different compensation powers

In addition to the transmission spectra shown in Fig. 5.12, we measured two more spectra for the compensation laser powers $P_c = 370 \pm 35 \mu\text{W}$ and $P_c = 410 \pm 40 \mu\text{W}$, respectively. The spectra are shown in Fig. A.4.11. The solid lines are theoretical predictions, which were generated as described in Sec. 5.6.1 for compensation laser powers of $P_c^{\text{th}} = 440 \mu\text{W}$ and $P_c^{\text{th}} = 490 \mu\text{W}$, respectively, which were chosen so as to give a similar ratio of P_c^{th}/P_c as for the spectrum in Fig. 5.12 a), described in Sec. 5.6.1. Note that these spectra were measured at higher compensation laser powers, i.e. in a situation where the transitions to the other Zeeman levels of the $F' = 4$ manifold are close to the unperturbed transition frequency, while the cycling transition is already detuned, see Fig. 5.2. Thus, the two-level atom approximation in our theory model does not fully apply anymore, and, as a consequence, the agreement between the measured data and the theoretical prediction is not as good as for the compensated spectrum in Fig. 5.12 a).

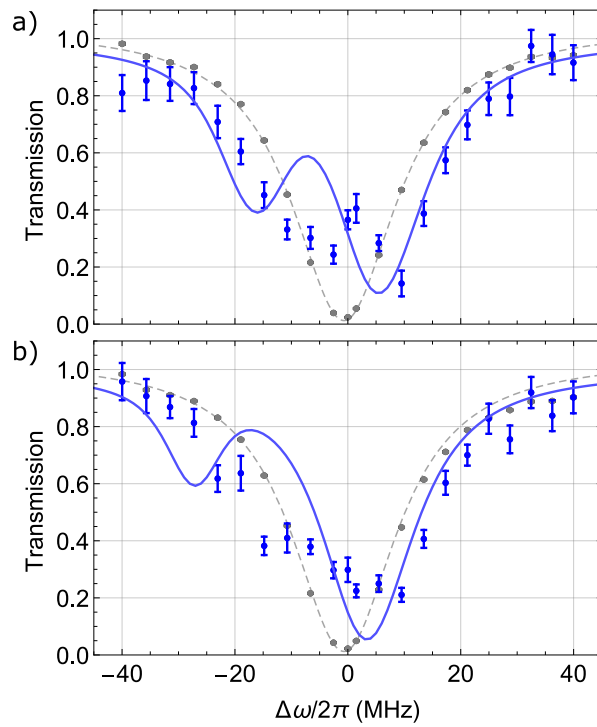


Figure A.4.11: Normalized transmission spectra for compensation laser powers of a) $P_c = 370 \pm 35 \mu\text{W}$ and b) $P_c = 410 \pm 40 \mu\text{W}$. The solid lines are theoretical predictions, see text.

List of Acronyms

AOM acousto-optical modulator

APD avalanche photodiode

AT atom trigger

BC Berek compensator

BS beam splitter

CQED cavity quantum electrodynamics

DDS direct digital synthesizer

ECDL external cavity diode laser

EOM electro-optical modulator

FBS fiber-beam splitter

FM frequency modulation

FP Fabry-Pérot

FSR free spectral range

FPGA field programmable gate array

LO local oscillator

MEMS micro electro-mechanical system

MOT magneto-optical trap

MZ Mach-Zehnder

PBS polarizing beam splitter

PD photodiode

PDH Pound-Drever-Hall

PGC polarization gradient cooling

PID proportional, integral, derivative

PM polarization-maintaining

Rb Rubidium

RF radio frequency

SPCM single-photon counting module

TA tapered amplifier

TE transverse-electric

TM transverse-magnetic

TTL transistor-transistor logic

WGM whispering-gallery mode

Bibliography

- [1] S. Haroche and D. Kleppner. Cavity quantum electrodynamics. *Physics Today*, 42(1):24–30, 1989.
- [2] G. Gabrielse and H. Dehmelt. Observation of inhibited spontaneous emission. *Physical Review Letters*, 55(1):67, 1985.
- [3] R. G. Hulet, E. S. Hilfer, and D. Kleppner. Inhibited spontaneous emission by a Rydberg atom. *Physical Review Letters*, 55(20):2137, 1985.
- [4] W. Jhe, A. Anderson, E. A. Hinds, D. Meschede, L. Moi, and S. Haroche. Suppression of spontaneous decay at optical frequencies: Test of vacuum-field anisotropy in confined space. *Physical Review Letters*, 58(7):666, 1987.
- [5] F. De Martini, G. Innocenti, G. R. Jacobovitz, and P. Mataloni. Anomalous spontaneous emission time in a microscopic optical cavity. *Physical Review Letters*, 59(26):2955, 1987.
- [6] D. J. Heinzen, J. J. Childs, J. E. Thomas, and M. S. Feld. Enhanced and inhibited visible spontaneous emission by atoms in a confocal resonator. *Physical Review Letters*, 58(13):1320, 1987.
- [7] D. J. Heinzen, J. J. Childs, J. E. Thomas, and M. S. Feld. Erratum: Enhanced and inhibited visible spontaneous emission by atoms in a confocal resonator [Physical Review Letters 58, 1320 (1987)]. *Physical Review Letters*, 58(20):2153, 1987.
- [8] P. Goy, J. M. Raimond, M. Gross, and S. Haroche. Observation of cavity-enhanced single-atom spontaneous emission. *Physical Review Letters*, 50(24):1903, 1983.
- [9] M. Fox. *Quantum optics*. Oxford University Press, 2012.
- [10] D. Meschede, H. Walther, and G. Müller. One-atom maser. *Physical Review Letters*, 54(6):551, 1985.
- [11] G. Rempe, H. Walther, and N. Klein. Observation of quantum collapse and revival in a one-atom maser. *Physical Review Letters*, 58(4):353, 1987.
- [12] M. Brune, J. M. Raimond, P. Goy, L. Davidovich, and S. Haroche. Realization of a two-photon maser oscillator. *Physical Review Letters*, 59(17):1899, 1987.

- [13] J. M. Raimond, M. Brune, and S. Haroche. Manipulating quantum entanglement with atoms and photons in a cavity. *Reviews of Modern Physics*, 73(3):565, 2001.
- [14] M. Brune, F. Schmidt-Kaler, A. Maali, J. Dreyer, E. Hagley, J. M. Raimond, and S. Haroche. Quantum Rabi oscillation: A direct test of field quantization in a cavity. *Physical Review Letters*, 76(11):1800, 1996.
- [15] M. Brune, E. Hagley, J. Dreyer, X. Maitre, A. Maali, C. Wunderlich, J. M. Raimond, and S. Haroche. Observing the progressive decoherence of the “meter” in a quantum measurement. *Physical Review Letters*, 77(24):4887, 1996.
- [16] A. Rauschenbeutel, G. Nogues, S. Osnaghi, P. Bertet, M. Brune, J. M. Raimond, and S. Haroche. Coherent operation of a tunable quantum phase gate in cavity QED. *Physical Review Letters*, 83(24):5166, 1999.
- [17] G. Nogues, A. Rauschenbeutel, S. Osnaghi, M. Brune, J. M. Raimond, and S. Haroche. Seeing a single photon without destroying it. *Nature*, 400(6741):239–242, 1999.
- [18] R. J. Thompson, G. Rempe, and H. J. Kimble. Observation of normal-mode splitting for an atom in an optical cavity. *Physical Review Letters*, 68(8):1132, 1992.
- [19] H. J. Metcalf and P. Van der Straten. Laser cooling and trapping, 1999.
- [20] H. Mabuchi, Q. A. Turchette, M. S. Chapman, and H. J. Kimble. Real-time detection of individual atoms falling through a high-finesse optical cavity. *Optics Letters*, 21(17):1393–1395, 1996.
- [21] M. Hennrich, T. Legero, A. Kuhn, and G. Rempe. Vacuum-stimulated Raman scattering based on adiabatic passage in a high-finesse optical cavity. *Physical Review Letters*, 85(23):4872, 2000.
- [22] P. Münstermann, T. Fischer, P. Maunz, P. W. H. Pinkse, and G. Rempe. Dynamics of single-atom motion observed in a high-finesse cavity. *Physical Review Letters*, 82(19):3791, 1999.
- [23] J. Ye, D. W. Vernooy, and H. J. Kimble. Trapping of single atoms in cavity QED. *Physical Review Letters*, 83(24):4987, 1999.
- [24] P. Maunz, T. Puppe, I. Schuster, N. Syassen, P. W. H. Pinkse, and G. Rempe. Cavity cooling of a single atom. *Nature*, 428(6978):50–52, 2004.
- [25] A. D. Boozer, A. Boca, R. Miller, T. E. Northup, and H. J. Kimble. Cooling to the ground state of axial motion for one atom strongly coupled to an optical cavity. *Physical Review Letters*, 97(8):083602, 2006.
- [26] A. Reiserer, C. Nölleke, S. Ritter, and G. Rempe. Ground-state cooling of a single atom at the center of an optical cavity. *Physical Review Letters*, 110(22):223003, 2013.

- [27] J. McKeever, J. R. Buck, A. D. Boozer, A. Kuzmich, H.-C. Nägerl, D. M. Stamper-Kurn, and H. J. Kimble. State-insensitive cooling and trapping of single atoms in an optical cavity. *Physical Review Letters*, 90(13):133602, 2003.
- [28] R. Miller, T. E. Northup, K. M. Birnbaum, A. Boca, A. D. Boozer, and H. J. Kimble. Trapped atoms in cavity QED: coupling quantized light and matter. *Journal of Physics B: Atomic, Molecular and Optical Physics*, 38(9):S551, 2005.
- [29] J. McKeever, A. Boca, A. D. Boozer, R. Miller, J. R. Buck, A. Kuzmich, and H. J. Kimble. Deterministic generation of single photons from one atom trapped in a cavity. *Science*, 303(5666):1992–1994, 2004.
- [30] A. Boca, R. Miller, K. M. Birnbaum, A. D. Boozer, J. McKeever, and H. J. Kimble. Observation of the vacuum Rabi spectrum for one trapped atom. *Physical Review Letters*, 93(23):233603, 2004.
- [31] A. Reiserer and G. Rempe. Cavity-based quantum networks with single atoms and optical photons. *Reviews of Modern Physics*, 87(4):1379, 2015.
- [32] S. Ritter, C. Nölleke, C. Hahn, A. Reiserer, A. Neuzner, M. Uphoff, M. Mücke, E. Figueroa, J. Bochmann, and G. Rempe. An elementary quantum network of single atoms in optical cavities. *Nature*, 484(7393):195–200, 2012.
- [33] B. Hacker, S. Welte, G. Rempe, and S. Ritter. A photon–photon quantum gate based on a single atom in an optical resonator. *Nature*, 536(7615):193, 2016.
- [34] S. Daiss, S. Langenfeld, S. Welte, E. Distanto, P. Thomas, L. Hartung, O. Morin, and G. Rempe. A quantum-logic gate between distant quantum-network modules. *Science*, 371(6529):614–617, 2021.
- [35] G. Rempe, R. J. Thompson, H. J. Kimble, and R. Lalezari. Measurement of ultralow losses in an optical interferometer. *Optics Letters*, 17(5):363–365, 1992.
- [36] T. Aoki, B. Dayan, E. Wilcut, W. P. Bowen, A. S. Parkins, T. J. Kippenberg, K. J. Vahala, and H. J. Kimble. Observation of strong coupling between one atom and a monolithic microresonator. *Nature*, 443(7112):671, 2006.
- [37] H. J. Kimble. The quantum internet. *Nature*, 453(7198):1023–1030, 2008.
- [38] J. Volz, R. Gehr, G. Dubois, J. Estève, and J. Reichel. Measurement of the internal state of a single atom without energy exchange. *Nature*, 475(7355):210–213, 2011.
- [39] M. Steiner, H. M. Meyer, C. Deutsch, J. Reichel, and M. Köhl. Single ion coupled to an optical fiber cavity. *Physical Review Letters*, 110(4):043003, 2013.
- [40] J. Gallego, W. Alt, T. Macha, M. Martinez-Dorantes, D. Pandey, and D. Meschede. Strong Purcell effect on a neutral atom trapped in an open fiber cavity. *Physical Review Letters*, 121(17):173603, 2018.

- [41] M. Brekenfeld, D. Niemietz, J. D. Christesen, and G. Rempe. A quantum network node with crossed optical fibre cavities. *Nature Physics*, pages 1–5, 2020.
- [42] J. D. Thompson, T. G. Tiecke, N. P. de Leon, J. Feist, A. V. Akimov, M. Gullans, A. S. Zibrov, V. Vuletić, and M. D. Lukin. Coupling a single trapped atom to a nanoscale optical cavity. *Science*, 340(6137):1202–1205, 2013.
- [43] A. Goban, C.-L. Hung, J. D. Hood, S.-P. Yu, J. A. Muniz, O. Painter, and H. J. Kimble. Superradiance for atoms trapped along a photonic crystal waveguide. *Physical Review Letters*, 115(6):063601, 2015.
- [44] S. Kato and T. Aoki. Strong coupling between a trapped single atom and an all-fiber cavity. *Physical Review Letters*, 115(9):093603, 2015.
- [45] K. P. Nayak, J. Wang, and J. Kelothe. Real-time observation of single atoms trapped and interfaced to a nanofiber cavity. *Physical Review Letters*, 123(21):213602, 2019.
- [46] C. Junge, D. O’Shea, J. Volz, and A. Rauschenbeutel. Strong coupling between single atoms and nontransversal photons. *Physical Review Letters*, 110(21):213604, 2013.
- [47] I. Shomroni, S. Rosenblum, Y. Lovsky, O. Bechler, G. Guendelman, and B. Dayan. All-optical routing of single photons by a one-atom switch controlled by a single photon. *Science*, 345(6199):903–906, 2014.
- [48] D. W. Vernooy, A. Furusawa, N. P. Georgiades, V. S. Ilchenko, and H. J. Kimble. Cavity QED with high-Q whispering gallery modes. *Physical Review A*, 57(4):R2293, 1998.
- [49] K. Y. Bliokh, F. J. Rodríguez-Fortuño, F. Nori, and A. V. Zayats. Spin–orbit interactions of light. *Nature Photonics*, 9(12):796–808, 2015.
- [50] A. Aiello, P. Banzer, M. Neugebauer, and G. Leuchs. From transverse angular momentum to photonic wheels. *Nature Photonics*, 9(12):789–795, 2015.
- [51] P. Lodahl, S. Mahmoodian, S. Stobbe, A. Rauschenbeutel, P. Schneeweiss, J. Volz, H. Pichler, and P. Zoller. Chiral quantum optics. *Nature*, 541(7638):473, 2017.
- [52] D. O’Shea, C. Junge, J. Volz, and A. Rauschenbeutel. Fiber-optical switch controlled by a single atom. *Physical Review Letters*, 111(19):193601, 2013.
- [53] J. Volz, M. Scheucher, C. Junge, and A. Rauschenbeutel. Nonlinear π phase shift for single fibre-guided photons interacting with a single resonator-enhanced atom. *Nature Photonics*, 8(12):965–970, 2014.
- [54] C. Sayrin, C. Junge, R. Mitsch, B. Albrecht, D. O’Shea, P. Schneeweiss, J. Volz, and A. Rauschenbeutel. Nanophotonic optical isolator controlled by the internal state of cold atoms. *Physical Review X*, 5(4):041036, 2015.

- [55] M. Scheucher, A. Hilico, E. Will, J. Volz, and A. Rauschenbeutel. Quantum optical circulator controlled by a single chirally coupled atom. *Science*, 354(6319):1577–1580, 2016.
- [56] O. Bechler, A. Borne, S. Rosenblum, G. Guendelman, O. E. Mor, M. Netser, T. Ohana, Z. Aqua, N. Drucker, R. Finkelstein, et al. A passive photon–atom qubit swap operation. *Nature Physics*, 14(10):996, 2018.
- [57] Y. Louyer, D. Meschede, and A. Rauschenbeutel. Tunable whispering-gallery-mode resonators for cavity quantum electrodynamics. *Physical Review A*, 72(3):031801, 2005.
- [58] A. P. Hilton, C. Perrella, A. N. Luiten, and P. S. Light. Dual-color magic-wavelength trap for suppression of light shifts in atoms. *Physical Review Applied*, 11:024065, Feb 2019.
- [59] D. O’Shea. *Cavity QED experiments with a whispering-gallery-mode bottle resonator*. PhD thesis, Vienna University of Technology, 2013.
- [60] C. Junge. *Cavity Quantum Electrodynamics with Non-transversal photons*. PhD thesis, Vienna University of Technology, 2013.
- [61] T. D. Ladd, F. Jelezko, R. Laflamme, Y. Nakamura, C. Monroe, and J. L. O’Brien. Quantum computers. *Nature*, 464(7285):45–53, 2010.
- [62] N. Gisin and R. Thew. Quantum communication. *Nature Photonics*, 1(3):165–171, 2007.
- [63] V. Giovannetti, S. Lloyd, and L. Maccone. Quantum-enhanced measurements: beating the standard quantum limit. *Science*, 306(5700):1330–1336, 2004.
- [64] J. I. Cirac, P. Zoller, H. J. Kimble, and H. Mabuchi. Quantum state transfer and entanglement distribution among distant nodes in a quantum network. *Physical Review Letters*, 78(16):3221, 1997.
- [65] M. Scheucher. *Single-atom cavity quantum electrodynamics with whispering-gallery-modes: Single-photon nonlinearity and nonreciprocity*. PhD thesis, Vienna University of Technology, 2017.
- [66] B. E. A. Saleh and M. C. Teich. *Fundamentals of photonics*. John Wiley & Sons, 2019.
- [67] H. J. Kimble. Strong interactions of single atoms and photons in cavity QED. *Physica Scripta*, 1998(T76):127, 1998.
- [68] D. A. Steck. *Quantum and Atom Optics*. <http://steck.us/teaching> (revision 0.13.4, 24 September 2020), 2020.
- [69] M. Pöllinger, D. O’Shea, F. Warken, and A. Rauschenbeutel. Ultrahigh-Q tunable whispering-gallery-mode microresonator. *Physical Review Letters*, 103(5):053901, 2009.
- [70] M. Pöllinger. *Bottle microresonators for applications in quantum optics and all-optical signal processing*. PhD thesis, Johannes Gutenberg-Universität Mainz, 2010.

- [71] K. J. Vahala. Optical microcavities. *Nature*, 424(6950):839–846, 2003.
- [72] Lord Rayleigh. The problem of the whispering gallery. *The London, Edinburgh, and Dublin Philosophical Magazine and Journal of Science*, 20(120):1001–1004, 1910.
- [73] V. B. Braginsky, M. L. Gorodetsky, and V. S. Ilchenko. Quality-factor and nonlinear properties of optical whispering-gallery modes. *Physics Letters A*, 137(7-8):393–397, 1989.
- [74] D. W. Vernooy, V. S. Ilchenko, H. Mabuchi, E. W. Streed, and H. J. Kimble. High-Q measurements of fused-silica microspheres in the near infrared. *Optics Letters*, 23(4):247–249, 1998.
- [75] B. Gayral, J. M. Gérard, A. Lemaitre, C. Dupuis, L. Manin, and J. L. Pelouard. High-Q wet-etched GaAs microdisks containing InAs quantum boxes. *Applied Physics Letters*, 75(13):1908–1910, 1999.
- [76] D. K. Armani, T. J. Kippenberg, S. M. Spillane, and K. J. Vahala. Ultra-high-Q toroid microcavity on a chip. *Nature*, 421(6926):925–928, 2003.
- [77] S. M. Spillane, T. J. Kippenberg, K. J. Vahala, K. W. Goh, E. Wilcut, and H. J. Kimble. Ultrahigh-Q toroidal microresonators for cavity quantum electrodynamics. *Physical Review A*, 71(1):013817, 2005.
- [78] M. Sumetsky. Whispering-gallery-bottle microcavities: the three-dimensional etalon. *Optics Letters*, 29(1):8–10, 2004.
- [79] A. B. Matsko and V. S. Ilchenko. Optical resonators with whispering-gallery modes-part I: basics. *IEEE Journal of selected topics in quantum electronics*, 12(1):3–14, 2006.
- [80] T. J. Kippenberg, S. M. Spillane, and K. J. Vahala. Demonstration of ultra-high-q small mode volume toroid microcavities on a chip. *Applied Physics Letters*, 85(25):6113–6115, 2004.
- [81] M. Pöllinger, D. O’Shea, F. Warken, and A. Rauschenbeutel. Ultrahigh-Q tunable whispering-gallery-mode microresonator. *Physical Review Letters*, 103(5):053901, 2009.
- [82] F. Warken. *Ultradünne Glasfasern als Werkzeug zur Kopplung von Licht und Materie*. PhD thesis, Rheinische Friedrich-Wilhelms-Universität Bonn, 2007.
- [83] M. Scheucher, A. Rauschenbeutel, and J. Volz. Cavity quantum electrodynamics and chiral quantum optics. *arXiv:2012.06546*, 2020.
- [84] S. M. Spillane, T. J. Kippenberg, O. J. Painter, and K. J. Vahala. Ideality in a fiber-taper-coupled microresonator system for application to cavity quantum electrodynamics. *Physical Review Letters*, 91(4):043902, 2003.

- [85] R. Garcia-Fernandez, W. Alt, F. Bruse, C. Dan, K. Karapetyan, O. Rehband, A. Stiebeiner, U. Wiedemann, D. Meschede, and A. Rauschenbeutel. Optical nanofibers and spectroscopy. *Applied Physics B*, 105(1):3–15, 2011.
- [86] J. E. Hoffman, S. Ravets, J. A. Grover, P. Solano, P. R. Kordell, J. D. Wong-Campos, L. A. Orozco, and S. L. Rolston. Ultrahigh transmission optical nanofibers. *AIP advances*, 4(6):067124, 2014.
- [87] J. C. Knight, G. Cheung, F. Jacques, and T. A. Birks. Phase-matched excitation of whispering-gallery-mode resonances by a fiber taper. *Optics Letters*, 22(15):1129–1131, 1997.
- [88] E. T. Jaynes and F. W. Cummings. Comparison of quantum and semiclassical radiation theories with application to the beam maser. *Proceedings of the IEEE*, 51(1):89–109, 1963.
- [89] H. I. Yoo and J. H. Eberly. Dynamical theory of an atom with two or three levels interacting with quantized cavity fields. *Physics Reports*, 118(5):239–337, 1985.
- [90] A. Messina, S. Maniscalco, and A. Napoli. Interaction of bimodal fields with few-level atoms in cavities and traps. *Journal of Modern Optics*, 50(1):1–49, 2003.
- [91] H. J. Carmichael. *Statistical Methods in Quantum Optics 1: Master Equations and Fokker-Planck Equations*. Springer Berlin Heidelberg, Berlin, Heidelberg, 2002.
- [92] C. C. Gerry and P. L. Knight. *Introductory quantum optics*. Cambridge university press, 2005.
- [93] M. O. Scully and M. S. Zubairy. *Quantum optics*, 1999.
- [94] J. J. Sanchez-Mondragon, N. B. Narozhny, and J. H. Eberly. Theory of spontaneous-emission line shape in an ideal cavity. *Physical Review Letters*, 51(7):550, 1983.
- [95] T. J. Kippenberg, S. M. Spillane, and K. J. Vahala. Modal coupling in traveling-wave resonators. *Optics Letters*, 27(19):1669–1671, 2002.
- [96] B. Dayan, A. S. Parkins, T. Aoki, E. P. Ostby, K. J. Vahala, and H. J. Kimble. A photon turnstile dynamically regulated by one atom. *Science*, 319(5866):1062–1065, 2008.
- [97] J. L. Hall, M. Zhu, and P. Buch. Prospects for using laser-prepared atomic fountains for optical frequency standards applications. *Journal of the Optical Society of America B*, 6(11):2194–2205, 1989.
- [98] M. A. Kasevich, E. Riis, S. Chu, and R. G. DeVoe. rf spectroscopy in an atomic fountain. *Physical Review Letters*, 63(6):612, 1989.
- [99] P. Münstermann, T. Fischer, P. W. H. Pinkse, and G. Rempe. Single slow atoms from an atomic fountain observed in a high-finesse optical cavity. *Optics Communications*, 159(1-3):63–67, 1999.

- [100] C. Hauswald. Aufbau und Charakterisierung eines Atom-springbrunnens für ein Resonator-QED-Experiment mit Flüstergaleriemoden-Mikroresonatoren. Diplomarbeit, Johannes Gutenberg-Universität Mainz, 2010.
- [101] T. Aoki, A. S. Parkins, D. J. Alton, C. A. Regal, B. Dayan, E. Ostby, K. J. Vahala, and H. J. Kimble. Efficient routing of single photons by one atom and a microtoroidal cavity. *Physical Review Letters*, 102(8):083601, 2009.
- [102] E. L. Raab, M. Prentiss, A. Cable, S. Chu, and D. E. Pritchard. Trapping of neutral sodium atoms with radiation pressure. *Physical Review Letters*, 59(23):2631, 1987.
- [103] S. Chu, L. Hollberg, J. E. Bjorkholm, A. Cable, and A. Ashkin. Three-dimensional viscous confinement and cooling of atoms by resonance radiation pressure. *Physical Review Letters*, 55(1):48, 1985.
- [104] P. D. Lett, W. D. Phillips, S. L. Rolston, C. E. Tanner, R. N. Watts, and C. I. Westbrook. Optical molasses. *Journal of the Optical Society of America B*, 6(11):2084–2107, 1989.
- [105] C. J. Foot. Atomic physics, 2005.
- [106] R. Wynands and S. Weyers. Atomic fountain clocks. *Metrologia*, 42(3):S64, 2005.
- [107] E. A. Donley, T. P. Heavner, F. Levi, M. O. Tataw, and S. R. Jefferts. Double-pass acousto-optic modulator system. *Review of Scientific Instruments*, 76(6):063112, 2005.
- [108] E. D. Black. An introduction to Pound–Drever–Hall laser frequency stabilization. *American Journal of Physics*, 69:79, 2001.
- [109] B. Schlederer. Description of a bottle resonator evanescently coupled to a waveguide. Master’s thesis, Technische Universität Wien, 2013.
- [110] J. Dalibard and C. Cohen-Tannoudji. Laser cooling below the Doppler limit by polarization gradients: simple theoretical models. *Journal of the Optical Society of America B*, 6(11):2023–2045, 1989.
- [111] D. A. Steck. Rubidium 85 D line data, revision 2.1.4, 23 December 2010.
- [112] K. Friebe. Strong coupling of single atoms to a whispering-gallery-mode resonator of ultrahigh quality. Diplomarbeit, Johannes Gutenberg-Universität Mainz, 2011.
- [113] R. Grimm, M. Weidemüller, and Yu. B. Ovchinnikov. Optical dipole traps for neutral atoms. In *Advances in atomic, molecular, and optical physics*, volume 42, pages 95–170. Elsevier, 2000.
- [114] A. L. Migdall, J. V. Prodan, W. D. Phillips, T. H. Bergeman, and H. J. Metcalf. First observation of magnetically trapped neutral atoms. *Physical Review Letters*, 54(24):2596, 1985.

- [115] A. M. Kaufman, B. J. Lester, and C. A. Regal. Cooling a single atom in an optical tweezer to its quantum ground state. *Physical Review X*, 2(4):041014, 2012.
- [116] A. Cooper, J. P. Covey, I. S. Madjarov, S. G. Porsev, M. S. Safronova, and M. Endres. Alkaline-earth atoms in optical tweezers. *Physical Review X*, 8(4):041055, 2018.
- [117] W. Alt, D. Schrader, S. Kuhr, M. Müller, V. Gomer, and D. Meschede. Single atoms in a standing-wave dipole trap. *Physical Review A*, 67(3):033403, 2003.
- [118] S. Nussmann, M. Hijlkema, B. Weber, F. Rohde, G. Rempe, and A. Kuhn. Submicron positioning of single atoms in a microcavity. *Physical Review Letters*, 95(17):173602, 2005.
- [119] K. M. Fortier, S. Y. Kim, M. J. Gibbons, P. Ahmadi, and M. S. Chapman. Deterministic loading of individual atoms to a high-finesse optical cavity. *Physical Review Letters*, 98(23):233601, 2007.
- [120] M. Khudaverdyan, W. Alt, I. Dotsenko, T. Kampschulte, K. Lenhard, A. Rauschenbeutel, S. Reick, K. Schörner, A. Widera, and D. Meschede. Controlled insertion and retrieval of atoms coupled to a high-finesse optical resonator. *New Journal of Physics*, 10(7):073023, 2008.
- [121] H. Mabuchi and H. J. Kimble. Atom galleries for whispering atoms: binding atoms in stable orbits around an optical resonator. *Optics Letters*, 19(10):749–751, 1994.
- [122] D. W. Vernooy and H. J. Kimble. Quantum structure and dynamics for atom galleries. *Physical Review A*, 55(2):1239, 1997.
- [123] F. Le Kien, V. I. Balykin, and K. Hakuta. Atom trap and waveguide using a two-color evanescent light field around a subwavelength-diameter optical fiber. *Physical Review A*, 70(6):063403, 2004.
- [124] E. Vetsch, S. T. Dawkins, R. Mitsch, D. Reitz, P. Schneeweiss, and A. Rauschenbeutel. Nanofiber-based optical trapping of cold neutral atoms. *IEEE Journal of Selected Topics in Quantum Electronics*, 18(6):1763–1770, 2012.
- [125] M. E. Kim, T.-H. Chang, B. M. Fields, C.-A. Chen, and C.-L. Hung. Trapping single atoms on a nanophotonic circuit with configurable tweezer lattices. *Nature Communications*, 10(1):1647, 2019.
- [126] X. Zhou, H. Tamura, T.-H. Chang, and C.-L. Hung. Subwavelength precision optical guiding for trapped atoms coupled to a nanophotonic resonator. *arXiv:2111.01119*, 2021.
- [127] F. Le Kien, P. Schneeweiss, and A. Rauschenbeutel. Dynamical polarizability of atoms in arbitrary light fields: general theory and application to cesium. *The European Physical Journal D*, 67(5):92, 2013.

- [128] L. Allen and J. H. Eberly. *Optical resonance and two-level atoms*, volume 28. Courier Corporation, 1987.
- [129] R. J. Cook and R. K. Hill. An electromagnetic mirror for neutral atoms. *Optics Communications*, 43(4):258–260, 1982.
- [130] Yu. B. Ovchinnikov, S. V. Shul’ga, and V. I. Balykin. An atomic trap based on evanescent light waves. *Journal of Physics B: Atomic, Molecular and Optical Physics*, 24(14):3173, 1991.
- [131] A. D. McLachlan. Van der Waals forces between an atom and a surface. *Molecular Physics*, 7(4):381–388, 1964.
- [132] E. Vetsch, D. Reitz, G. Sagué, R. Schmidt, S. T. Dawkins, and A. Rauschenbeutel. Optical interface created by laser-cooled atoms trapped in the evanescent field surrounding an optical nanofiber. *Physical Review Letters*, 104(20):203603, 2010.
- [133] A. Goban, K. S. Choi, D. J. Alton, D. Ding, C. Lacroûte, M. Pototschnig, T. Thiele, N. P. Stern, and H. J. Kimble. Demonstration of a state-insensitive, compensated nanofiber trap. *Physical Review Letters*, 109(3):033603, 2012.
- [134] J.-B. Béguin, E. M. Bookjans, S. L. Christensen, H. L. Sørensen, J. H. Müller, E. S. Polzik, and J. Appel. Generation and detection of a sub-poissonian atom number distribution in a one-dimensional optical lattice. *Physical Review Letters*, 113(26):263603, 2014.
- [135] B. Gouraud, D. Maxein, A. Nicolas, O. Morin, and J. Laurat. Demonstration of a memory for tightly guided light in an optical nanofiber. *Physical Review Letters*, 114(18):180503, 2015.
- [136] J. Lee, J. A. Grover, J. E. Hoffman, L. A. Orozco, and S. L. Rolston. Inhomogeneous broadening of optical transitions of ^{87}Rb atoms in an optical nanofiber trap. *Journal of Physics B: Atomic, Molecular and Optical Physics*, 48(16):165004, 2015.
- [137] N. Schlosser, G. Reymond, and P. Grangier. Collisional blockade in microscopic optical dipole traps. *Physical Review Letters*, 89(2):023005, 2002.
- [138] S. Kuhr, W. Alt, D. Schrader, M. Müller, V. Gomer, and D. Meschede. Deterministic delivery of a single atom. *Science*, 293(5528):278–280, 2001.
- [139] D. J. Alton. *Interacting single atoms with nanophotonics for chip-integrated quantum networks*. PhD thesis, 2013.
- [140] D. J. Alton, N. P. Stern, T. Aoki, H. Lee, E. Ostby, K. J. Vahala, and H. J. Kimble. Strong interactions of single atoms and photons near a dielectric boundary. *Nature Physics*, 7(2):159–165, 2011.

- [141] M. Rosenblit, Y. Japha, P. Horak, and R. Folman. Simultaneous optical trapping and detection of atoms by microdisk resonators. *Physical Review A*, 73(6):063805, 2006.
- [142] J. E. Sansonetti. Wavelengths, transition probabilities, and energy levels for the spectra of rubidium (Rb I through Rb XXXVII). *Journal of physical and chemical reference data*, 35(1):301–421, 2006.
- [143] A. A. Voronin and A. M. Zheltikov. The generalized sellmeier equation for air. *Scientific reports*, 7:46111, 2017.
- [144] B. Arora, M. S. Safronova, and C. W. Clark. Magic wavelengths for the np – ns transitions in alkali-metal atoms. *Physical Review A*, 76:052509, Nov 2007.
- [145] G. L. Pollack and D. R. Stump. *Electromagnetism*. Addison-Wesley, 2002.
- [146] H. B. G. Casimir. On the attraction between two perfectly conducting plates. In *Proc. Kon. Ned. Akad. Wet.*, volume 51, page 793, 1948.
- [147] F. Intravaia, C. Henkel, and M. Antezza. Fluctuation-induced forces between atoms and surfaces: The Casimir–Polder interaction. In *Casimir Physics*, pages 345–391. Springer, 2011.
- [148] E. Hecht. *Optik*. Oldenbourg Wissenschaftsverlag, 2005.
- [149] E. Will, L. Masters, A. Rauschenbeutel, M. Scheucher, and J. Volz. Coupling a single trapped atom to a whispering-gallery-mode microresonator. *Physical Review Letters*, 126(23):233602, 2021.
- [150] R. Loudon. *The quantum theory of light*. OUP Oxford, 2000.
- [151] E. M. Purcell. Spontaneous emission probabilities at radio frequencies. *Physical Review*, 69(681), 1946.
- [152] W. Alt, D. Schrader, S. Kuhr, M. Mueller, V. Gomer, and D. Meschede. Erratum: Single atoms in a standing-wave dipole trap [Physical Review A 67, 033403 (2003)]. *Physical Review A*, 71(1):019905, 2005.
- [153] L. D. Landau and E. M. Lifshitz. *Quantum mechanics* butterworth, 1981.
- [154] E. Vetsch. *Optical Interface Based on a Nanofiber Atom-Trap*. PhD thesis, Johannes Gutenberg-Universität Mainz, 2010.
- [155] T. A. Savard, K. M. O’Hara, and J. E. Thomas. Laser-noise-induced heating in far-off resonance optical traps. *Physical Review A*, 56(2):R1095, 1997.
- [156] H. Katori, T. Ido, and M. Kuwata-Gonokami. Optimal design of dipole potentials for efficient loading of Sr atoms. *Journal of the Physical Society of Japan*, 68(8):2479–2482, 1999.

- [157] J. Ye, H. J. Kimble, and H. Katori. Quantum state engineering and precision metrology using state-insensitive light traps. *Science*, 320(5884):1734–1738, 2008.
- [158] M. Takamoto and H. Katori. Spectroscopy of the $1S_0 - 3P_0$ clock transition of ^{87}Sr in an optical lattice. *Physical Review Letters*, 91(22):223001, 2003.
- [159] B. Arora and B. K. Sahoo. State-insensitive trapping of Rb atoms: Linearly versus circularly polarized light. *Physical Review A*, 86(3):033416, 2012.
- [160] S. Singh, B. K. Sahoo, and B. Arora. Magnetic-sublevel-independent magic wavelengths: Application to Rb and Cs atoms. *Physical Review A*, 93(6):063422, 2016.
- [161] A. Kaplan, M. F. Andersen, and N. Davidson. Suppression of inhomogeneous broadening in rf spectroscopy of optically trapped atoms. *Physical Review A*, 66(4):045401, 2002.
- [162] T. T. Grove, V. Sanchez-Villicana, B. C. Duncan, S. Maleki, and P. L. Gould. Two-photon two-color diode laser spectroscopy of the Rb $5D_{5/2}$ state. *Physica Scripta*, 52(3):271, 1995.
- [163] A. Yu. Kalatskiy, A. E. Afanasiev, P. N. Melentiev, and V. I. Balykin. Frequency stabilization of a diode laser on the $5P \rightarrow 5D$ transition of the Rb atom. *Laser Physics*, 27(5):055703, 2017.
- [164] R. W. P. Drever, J. L. Hall, F. V. Kowalski, J. Hough, G. M. Ford, A. J. Munley, and H. Ward. Laser phase and frequency stabilization using an optical resonator. *Applied Physics B*, 31(2):97–105, 1983.
- [165] J.-B. Béguin, J. Laurat, X. Luan, A. P. Burgers, Z. Qin, and H. J. Kimble. Reduced volume and reflection for bright optical tweezers with radial Laguerre–Gauss beams. *Proceedings of the National Academy of Sciences*, 117(42):26109–26117, 2020.
- [166] A. Kubanek, M. Koch, C. Sames, A. Ourjoumtsev, P. W. H. Pinkse, K. Murr, and G. Rempe. Photon-by-photon feedback control of a single-atom trajectory. *Nature*, 462(7275):898–901, 2009.
- [167] M. Koch, C. Sames, A. Kubanek, M. Apel, M. Balbach, A. Ourjoumtsev, P. W. H. Pinkse, and G. Rempe. Feedback cooling of a single neutral atom. *Physical Review Letters*, 105(17):173003, 2010.
- [168] P. Horak, G. Hechenblaikner, K. M. Gheri, H. Stecher, and H. Ritsch. Cavity-induced atom cooling in the strong coupling regime. *Physical Review Letters*, 79(25):4974, 1997.
- [169] M. Wolke, J. Klinner, H. Keßler, and A. Hemmerich. Cavity cooling below the recoil limit. *Science*, 337(6090):75–78, 2012.
- [170] M. Gangl and H. Ritsch. Cavity-enhanced polarization gradient cooling. *Journal of Physics B: Atomic, Molecular and Optical Physics*, 35(22):4565, 2002.

- [171] A. Politi, J. C. F. Matthews, M. G. Thompson, and J. L. O'Brien. Integrated quantum photonics. *IEEE Journal of Selected Topics in Quantum Electronics*, 15(6):1673–1684, 2009.
- [172] M. Hossein-Zadeh and K. J. Vahala. Free ultra-high-Q microtoroid: a tool for designing photonic devices. *Optics Express*, 15(1):166–175, 2007.
- [173] T.-H. Chang, B. M. Fields, M. E. Kim, and C.-L. Hung. Microring resonators on a suspended membrane circuit for atom–light interactions. *Optica*, 6(9):1203–1210, 2019.
- [174] F. Steiner. Assembly and characterization of a diode laser for an optical dipole trap. Bachelor thesis, Technische Universität Wien, 2018.

Danksagung

An erster Stelle möchte ich mich bei meinem Betreuer Arno Rauschenbeutel bedanken, der mir die Möglichkeit gegeben hat, an diesem spannenden Forschungsprojekt zu arbeiten. Bereits während einer Vorlesung in meiner Studienzeit in Mainz bewunderte ich seine Fähigkeit, komplexe physikalische Zusammenhänge bildlich und einfach darzustellen. Wann immer nötig, stand er mir mit Rat und Tat zur Seite.

Mein größter Dank auf fachlicher Seite gilt, ohne Zweifel, Jürgen Volz. Sein physikalisches Verständnis und seine unendliche Geduld bei der Beantwortung von Fragen und Diskussionen physikalischer Sachverhalte, haben entscheidend zum Gelingen der Experimente und dem Zustandekommen dieser Arbeit beigetragen.

Ich möchte Christian Junge und Danny O’Shea danken, obwohl ich mit ihnen keinen zeitlichen Überlapp in der Gruppe hatte. Sie haben bei dem Entwurf und Aufbau des CQED-Experiments eine beeindruckende Leistung vollbracht, und damit auch den Grundstein für diese Arbeit gelegt. Natürlich sind Forschungsergebnisse, wie die hier beschriebenen, das Resultat einer Team-Anstrengung. Ich möchte daher meinem langjährigen Kollegen Michael Scheucher danken, dessen zielorientierte Arbeitsweise unser Team und das Experiment oft entscheidend vorangebracht haben. Luke Masters danke ich für die gute Zusammenarbeit, besonders in den letzten Monaten vor dem Umzug nach Berlin. Adèle Hilico danke ich für ihren Einsatz in der Anfangsphase der Atomfallen-Experimente.

Auch allen anderen Mitgliedern der Arbeitsgruppe danke ich für die gemeinsame Zeit, z.B. bei lustigen Kaffee- und Kuchenpausen, sowie für die gegenseitige Hilfsbereitschaft.

Mein Dank gilt auch dem Doktoratskolleg CoQuS, für finanzielle Unterstützung und, insbesondere, für die Bereitstellung eines einzigartigen wissenschaftlichen und sozialen Umfelds. In diesem Zusammenhang bedanke ich mich auch bei Markus Arndt, der mir als Mentor beratend und unterstützend zur Seite stand.

Ich danke der Administration am Atominstitut, insbesondere Barbara Stros, Brigitta Buchberger, Stephan Schneider und Helmut Richter. Sie waren jederzeit sehr hilfsbereit bei organisatorischen Angelegenheiten, sowie Fragen zur Labor-Infrastruktur und IT-Fragen.

Ich möchte meinen Freunden in Wien danken, die die Zeit neben der Arbeit unvergesslich gemacht haben, und dem TU Chor für viele gemeinsame musikalische Jahre. Ich danke meinen Freundinnen aus der Heimat dafür, dass sie mich schon so lange auf meinem Lebensweg begleiten. Ganz besonders möchte ich Adarsh danken, der immer für mich da ist.

Zu guter Letzt danke ich, von Herzen, meiner Familie. Ihr großes Vertrauen und unermüdlicher Zuspruch haben mir, trotz vieler Herausforderungen, die nötige Energie für diese Arbeit gegeben.

LEBENS LAUF

Elisa Maria Will
Hörnesgasse 4/16
1030 Wien
Österreich

Persönliche Daten

Geburtsdatum: 2. Juli 1988
Geburtsort: Limburg a. d. Lahn, Deutschland
Staatsangehörigkeit: deutsch

Ausbildung

seit 03/2014	Technische Universität Wien, Doktorandin in Technischer Physik
10/2007 – 07/2013	Johannes Gutenberg-Universität Mainz, Deutschland Diplomstudium in Physik
1998 – 2007	Gymnasium "Marienschule", Limburg a. d. Lahn
1994 – 1998	Grundschule "Lindenschule", Limburg a. d. Lahn